Ultrafast Hydration Dynamics Near Extended Macromolecular Interfaces

by

Ved Prakash Roy

A dissertation submitted in partial fulfillment
of the requirements for the degree of
Doctor of Philosophy
(Chemistry)
in the University of Michigan
2019

Doctoral Committee:

Professor Kevin J. Kubarych, Chair
Professor Emeritus Ari Gafni
Professor Eitan Geva
Professor Roseanne Sension

Ved Prakash Roy

vproy@umich.edu

ORCID iD: 0000-0002-8089-6286

To my grandparents

Acknowledgements

First and foremost, I would like to thank my advisor Prof. Kevin Kubarych for his guidance and support which enabled me to work on a range of projects during my graduate career. Kevin has been very encouraging, even when experiments, equipments or computer programs did not work as expected. I am very grateful to have him as my advisor. His enthusiasm for science and clarity in explaining difficult concepts kept me motivated and helped me grasp new ideas quickly. This also allowed me to hone many experimental and computational skills described in this dissertation. Academic writing is an integral part of doing science. Kevin's attention to details and thoughtful suggestions has positively influenced my writing style. I hope to imbibe his scientific curiosity and fearless attitude towards life.

My graduate committee members have been very encouraging throughout my graduate education. I thank Prof. Ari Gafni, Prof. Roseanne Sension and Prof. Eitan Geva for their continued support. Their scientific and academic advices have been very valuable. I would also like to take this opportunity to thank my undergraduate mentor, Dr. Arindam Ghosh who instilled in me a sense of self-worth as a physical chemist and motivated me to pursue doctoral studies.

Current and former co-workers have played an important role in shaping not only my academic life but also social one. I would like to thank Josef Dunbar for explaining meticulous details of the optical layout in our 2D-IR setup and optomechanical components. Evan, Kim, Laura, Lindsay, Rong, Joseph Meadows and Joseph Mastron have been kind in helping me navigate various social norms in the United States in addition to being great colleagues. I am very glad to have mentored many undergraduate students, many of whom where students in my teaching discussions earlier. Jaeyoon, Nick, Hyun and Anna are some of the smartest

undergraduate students I worked with and wish them success for their future endeavors. I also have had the opportunity to interact with members from Ogilvie group in Physics. I am grateful to Prof. Jennifer Ogilvie for making me a part of LUMOS during its initial years. I have had many interesting and thoughtful discussions about science and life with Vivek, Orko, Yassel and Yin over lunch and will cherish them for years to come.

I would like to acknowledge the Department of Chemistry and Rackham Graduate school for various research fellowships and travel grant at different stages of my graduate studies. University of Michigan has some of the best academic support systems in place to assist graduate students to develop as a scholar. English language institute has been very instrumental in shaping my teaching skills ever since I moved to Michigan. Their summer course on GSI training for international students helped me overcome various pedagogical challenges I faced during my initial years of teaching. I have always enjoyed ELI courses taught by Christine Feak who is probably the most effective instructor, and I wish I can learn her art of public speaking.

My life has been deeply enriched by the presence of Sonisilpa in it and I consider myself extremely fortunate to have met her. She has stood strong by my side during my darkest days and has unconditionally encouraged and supported me, thereby forging a timeless bond between us.

I consider myself blessed to have parents who have been very supportive in my decisions regarding career and life choices. I am very grateful for their upbringing and wonderful childhood memories. I would like to express my sincere thanks to my elder sister, Gargi for always having my back and uplifting me. My adorable nieces, Tanuja and Tvisha always brought joy whenever I video called home.

Table of Contents

List of Figures

List of Tables

List of Abbreviations

1D: One dimensional
2D: Two dimensional
2D-IR: Two-dimensional infrared spectroscopy
AGS: Silver gallium sulfide
ATP: Adenosine triphosphate
B3LYP: Becke's three-parameter/ Lee Yang Parr
BBO: beta-barium borate
CPU: Chirped pulse upconversion
DCM: Dichloromethane
DFG: Difference frequency mixing
DFT: Density functional theory
DNA: Deoxyribonucleic acid
DTAB: Dodecyltrimethylammonium bromide
FFCF: Frequency frequency correlation function
FT-IR: Fourier transform infrared (spectroscopy)
HEWL: Hen Egg White Lysozyme
IR: Infrared
IVR: Intramolecular vibrational redistribution
MC: Monte Carlo
MCT: Mercury cadmium telluride (detector)
MD: Molecular dynamics
MMDS: Multispectral Multidimensional Spectrometer
MSD: Mean square displacement
nm: Nanometer (10^{-9} m)
NMR: Nuclear Magnetic Resonance (spectroscopy)
ns: Nanosecond (10^{-9} s)
OPA: Optical Parametric Amplifier
PEG: Polyethylene glycol (Polyethylene oxide)
ps: Picosecond (10^{-12} s)
RMSF: Root mean square fluctuation
SDS: Sodium dodecyl sulfate
SPC/E: Extended SPC
SPC: 3-site rigid water model
VDOS: Vibrational density of states

Abstract

Liquid water is arguably the most complex, but interesting chemical, enabling development and sustenance of life. The tetrahedral geometry of the water molecule allows the formation of a dense network of hydrogen bonds which undergoes rapid fluctuations at picosecond timescales. This ultrafast making and breaking of hydrogen bonds near an extended macromolecular interface may govern various biochemical kinetics, such as enzymatic activity, protein folding and membrane formation and disruption. Having a better understanding of interfacial hydration dynamics has implications to tune enzymatic activity, design targeted drugs and develop efficient desalination techniques. This dissertation elucidates the complex origin of the slowdown in hydration dynamics near the interfaces of micelle, protein and polymer.

To completely capture the timescale and perturbation of hydration dynamics by an extended interface, surface charge cannot be excluded. Using the thiocyanate anion (SCN^-) as a vibrational probe in the infrared and in conjunction with magnetic resonance spectroscopy, we find that the thiocyanate anion strongly associates with an interfacial model system of dodecyltrimethylammonium bromide (DTAB) micelles. Ultrafast two-dimensional infrared (2D-IR) spectroscopy of the SCN^- probe in a range of DTAB micelle sizes shows little if any size dependence to the time scale for spectral diffusion, which is found to be ~3.5 times slower compared to bulk water (both D_2O and H_2O). We conclusively find that the SCN^- spectral dynamics in cationic micelles is largely dominated by hydration contributions and offers a promising probe for interfacial hydration near positively charged interfaces.

Graph theoretical analysis of water hydrogen bond network is implemented to map its network topology obtained using molecular dynamic simulations in confined protein (Hen Egg White Lysozyme) geometries. The observed power-law dependence for average path length on system size reveals that the bulk hydrogen bond networks cannot be considered

random, but rather consists of a giant lattice-like component. At small protein separations (5-10 Å) with reduced hydrogen bond connectivity, similar global network structures are observed, indicating the maintenance of a completely unperturbed network topology. A Monte Carlo simulation on square lattices devoid of surface heterogeneity of real proteins reveals that the slowdown in hydration dynamics falls off exponentially near flat interfaces and converges within 2-3 shells with no evidence of cooperative effects. However, we conclusively find that protein surface residues become significantly slow when crowded and remains decoupled with interfacial hydration dynamics. The long-range collective influences by an interface may be due to complex chemical patterning of the surface.

Poly(ethylene oxide) is well known for its water structuring ability and bio-compatibility by forming strong a rigid hydration shell. In small poly(ethylene oxide) polymers, high charge density cations slaves PEG-200 to adopt a cyclic conformation, even at low salt concentrations. Probing the CN stretching frequency of the thiocyanate counter anion shows significantly slow spectral diffusion (∼5-fold) time scale offering evidence for direct interactions between the polymer and cations contrary to currently accepted water mediated mechanism. The lack of correlation with the Hofmeister ordering of the cations implies that PEG-cation interactions are highly specific. While complete maintenance of bulk-like dynamics in concentrated DNA duplex confirms weak DNA-water interactions.

The diverse range of dynamical timescales for water fluctuations near macromolecular interfaces may require simultaneous probing of chemical groups present on macromolecular interfaces and water directly, a feat that is now possible using the recently developed broadband mid-infrared light source.

Chapter 1
Introduction

1.1. Macromolecular hydration dynamics

Water is known to play a crucial role in maintaining structure and functioning of various macromolecules within the complex and highly crowded cellular milieu of an organism. It provides the necessary driving force for hydrophobic pockets to glue together while directly interacting with hydrophilic regions. During a binding event, such as between an enzyme and its cofactor, understanding the details of macromolecular conformational changes have received significant interest in the past due to the notion that functionality of a biomolecule

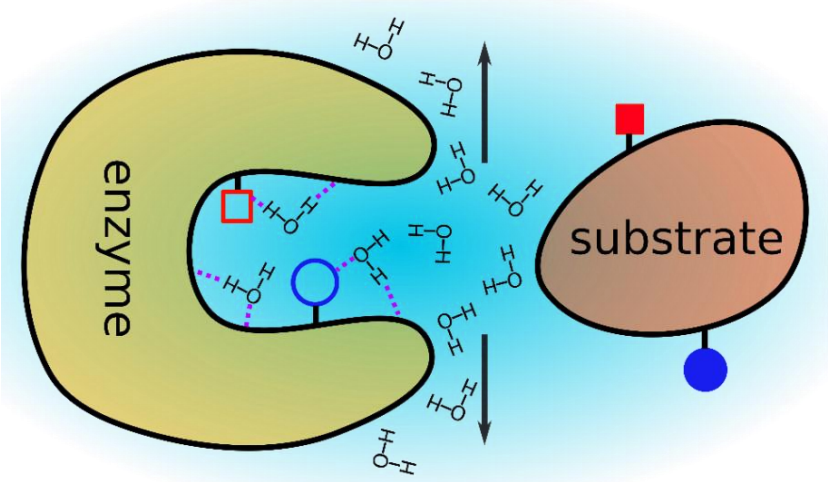

Figure 1.1. Illustration showing an interacting macromolecular assembly of enzyme substrate binding event. In addition to conformational changes needed for the macromolecules to successfully bind, surface and buried waters are inevitably expelled (as shown by arrows). Water molecules can also bind to specific chemical groups on the surface of the enzyme or substrate (shown in purple) that are sufficiently hydrophilic. Major contribution to the free energy of binding includes energy associated with conformational changes, breaking surface-water hydrogen bonds and ultrafast solvent reorganization. Additional energetic cost is incurred if water molecules beyond the first shell from an interface are have high dynamical constraint. It is therefore of interest to understand the role of water and its fluctuations near a variety of interfacial heterogeneity.

is governed by itself only.[1-4] Despite advancement in our understanding of structure function relationship, biochemical reactions involving macromolecules inevitably also involve

removal of surface bound water, but only to an extent that would preserve the native structure of the interacting macromolecule (**Figure 1.1**). Having an accurate and reliable prediction of enzyme kinetics, osmosis, wetting properties, and heat management in physiologically relevant conditions holds substantial practical implications such as, but not limited to, developing targeted drugs[5, 6], tune enzymatic activity[7] and purify water[8, 9].

At an ecological level, life has figured out how to exploit the anomalous properties of water for its survival. Marine life thrives in freezing cold conditions[10], water strider utilizes the high surface tension of water to skate on its surface[11] while arid plants effectively recycle water to avoid osmotic shock. Water is also recognized to participate in various biochemical reactions such as the evolution of oxygen via photosynthesis in plants[12], ion pumps in cellular membranes[9], and hydrolysis of ATP[13]. Such an elaborate management of water by any biological machinery would thus also involve an extensive molecular level interaction between them. Severe effects can result from altered hydration structure and dynamics between a macromolecule and its associated water. For example, a single mutation in a protein that is a major component of the human eye lens can drastically alter its optical properties from being transparent to translucent (resulting in cataracts).[14] Hence, a direct connection between the macromolecular structure and its hydration environment is of fundamental scientific interest. To access the inherently ultrafast time and ultrashort length scales, spectroscopists have the option to employ molecular probes and time resolved spectroscopy, supported by theoretical formalism and computer simulations.

Time resolved spectroscopy measurements spanning different wavelength ranges have found that the dynamics of surface water in crowded macromolecular solutions is slow, but the magnitude of this slowdown is still vigorously debated.[15] In addition, a wide range[16, 17] of observed slowdown in hydration dynamics often raises questions about the validity of the method being employed. This dissertation focuses on understanding the extent to which crowding, and the heterogeneity imposed by macromolecular interfaces influences hydration dynamics timescales. In addition, the degree to which conformational flexibility of a protein surface residues get restricted by a nearby interface has also been characterized using classical molecular dynamic simulations.

Biologically relevant water such as the environment of the cellular cytoplasm is viscous and contains a vast array of ions and macromolecules such as proteins, lipids and

nucleic acids. A typical average distance between macromolecules in the cytoplasm is about 10 Å, which can accommodate, at most, two layers of water molecules between the individual interfaces.[18] Investigations of ultrafast dynamics of concentrated biomacromolecular solutions estimate that roughly 10-25% of water in the cell is significantly slowed[19, 20], which often implies that "biological water" should be considered different than that of the bulk liquid. Contrary to these speculations, water in biological environments has long been regarded just as a passive matrix for solubilization and transport of a variety of small and large biochemical components.

Despite being the most abundant compound in our planet, water is riven with numerous disputes, both political and scientific. Though discussion in this dissertation focuses on resolving divergent scientific views, it bears keeping in mind that the molecular challenges, such as efficient and selective desalination, can also have a positive influence on water's societal challenges. Significant efforts have been expended to accurately determine the molecular arrangements of hydrogen bonded water by itself and near a hydrophobic interface. Experimentally observed slowdown in water dynamics near an interface to an extent have been rationalized to arise from amorphous ice-like nature of liquid water at room temperature. Instead, many conflicting arguments stem from the pursuit of deciphering liquid "water structure" while also recognizing its dynamical and fluid nature.

Based on Kauzmann's description[21], water rearranges itself around a hydrophobic interface by forming a "clathrate" type of structure that compensates hydrophobic attraction within macromolecules with the entropic ordering of water. In the gas phase, various polyhedron structures of water have been characterized,[22-24] prompting the search for similar structures in the liquid phase as well. Numerous molecular dynamics simulations and experiments at room temperature, however, are yet to find a completely static ordering of water in a hydration environment.[25-27] Instead, water has been found to exhibit considerable translational and orientational slowdowns relative to the pure liquid, which is consistent with a specific cross-over length proposed by Lum, Chandler and Weeks.[28] This active pursuit of finding super-slow clathrate-like water has preserved the enthusiasm of physical chemists for over four decades.

It is the fluctuating nature of liquid water that further complicates the interpretation of various spectroscopic observables probing interfaces and the bulk liquid.[29-31] The typical

timescales of water diffusion, orientation and dynamical fluctuations span from second to picosecond. Such a diverse range of timescales is almost impossible to probe using a single technique, therefore different experimental methods such as fluorescence, NMR, neutron scattering, ultrafast IR and terahertz spectroscopy are often implemented and are assumed to be complimentary. Some efforts[32] have been made to bridge this gap but more such experiments are needed to verify and constitute an overall, consistent picture. Apart from recognizing the heterogeneous nature of hydration dynamics near a biomacromolecular interfaces, the wide range of reported timescales has also fueled complex debates[33-38], particularly about the spatial extent and degree of the interface's perturbation of the hydration water dynamics. Hydrogen bonded water molecules at the immediate vicinity (i.e. the first shell) of an interface has significantly broken network structures and a reduced fraction of available water neighbors.

There is one school of thought which argues that since the second and higher shell water molecules can effectively achieve full coordination, there is no reason for their structure and dynamics to be different from the bulk.[39] Water's high dielectric constant effectively screens charges, further reducing the overall magnitude of electrostatic interactions (coulomb, dipole and polarizability),[40] suggesting that its influence should be local. Experimental evidence using neutron scattering on green fluorescent proteins strongly favors short ranged perturbation[41] (within two hydration shells).

On the other hand, due to the collective nature of hydrogen bonding and the correlation of multiple water molecule dipole moments, it is reasonable to expect that water's perturbation extends over greater distances. Observations, particularly in the terahertz community,[42, 43] have consistently argued that the spatial correlation extent of water dynamical perturbation near an interface is long-ranged (>40 Å).[43-46] Terahertz spectroscopy (<1000 cm^{-1}) is particularly sensitive to the collective hydrogen bonded water motions involving more than one water molecule. It is widely accepted that the structural perturbation experienced by first-shell water molecules can somehow propagate to the neighboring shells and beyond, inducing a long-range dynamical correlation. An important fact to consider which is often unstated is that the low frequency collective (fast librational motions of hydrogen bonds, <100 cm^{-1}) modes of water significantly overlap with the librational modes of protein surface residues as well. Hence measurements that access

primarily the magnitude or frequency (i.e. THz spectroscopy) are likely confounded the contributions from both motions of the water and the protein.

1.1.1. What is meant by "hydration dynamics"?

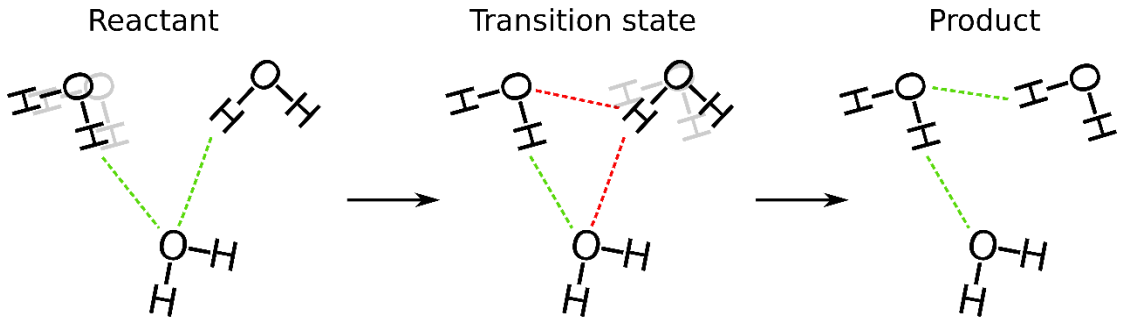

Figure 1.2. Water molecules in the bulk can rapidly switch its hydrogen bonding partner to another favorable neighbor via the three-body angular jump mechanism proposed by Laage et. al. The reactant configuration includes two water molecules which are hydrogen bonded to a common neighboring water molecule. During the initiation step of this termolecular reaction, the oxygen atom of one the water extends its electron density to the hydrogen of another water molecule in its vicinity which is already thereby forming a transition state. A key step in switching hydrogen bond involves an angular jump by the constrained water molecule in the direction away from its original neighbor. The product state appears release of the original hydrogen bond and formation of a new one with another neighboring water.

Water molecules can form an extended network of hydrogen bonds due to its ability to donate and accept hydrogen bonds simultaneously. Contrary to the static arrangement of water as in case of ice, liquid water molecules are constantly fluctuating. Besides translational diffusion, water molecules also undergo rotation and angular jumps that result in the breaking of a hydrogen bond with one neighbor and the formation with another (**Figure 1.2**). The energy needed to break a typical hydrogen bond (10-20 kJ/mol) is much greater than k_BT (2.5 kJ/mol), yet the typical lifetime of a hydrogen bond is roughly a picosecond. The fast fluctuations and rearrangements of the hydrogen bond network implies that any given dangling (i.e. broken) bond is present for only a very brief time.[47] A key mechanism by which water switches its hydrogen bond is via the three-bond angular jump,[48] but in presence of an interface, the availability of favorable neighbors is depleted and hence the probability of switching decreases. The term "dynamics" in this dissertation will refer to the fundamental hydrogen bond switching and orientational motion of water molecules either in bulk or near an extended interface. It is worth mentioning, however, that there are changes in kinetics, such as the rates of hydrogen bond rearrangements, that are caused by entropic modulations of the free energy barrier. These kinds of kinetic perturbations are not

readily interpreted as being truly dynamic, since they do not arise from changes in the microscopic motion, but rather to the statistics of switching probabilities induced by the excluded volume of switching partners.

1.2. Two-dimensional infrared spectroscopy (2D-IR)

The principal experimental method used in the work that comprises this dissertation is nonlinear, ultrafast two-dimensional infrared spectroscopy. The interaction of a low-intensity light wave with a medium creates a macroscopic polarization at the resonance frequency of the absorber (eg. a solute). The radiated first order signal field destructively interferes with the incident beam at the detector. By scanning the frequency of the incident wave and measuring the intensity drop one can construct the one-dimensional absorption spectrum of the molecule. Unfortunately, the underlying complex chemical dynamics of the solute and its surrounding medium can only be partially characterized using a linear absorption spectrum and is highly model-dependent. An infrared spectrum of a single molecule would appear sharp but is still somewhat broadened. Such broadening in the linewidth is homogeneous in nature, arising from finite lifetime of the excited vibrational state[49]. However, in solution, the infrared spectrum of a molecular oscillator experiences a variety of forces and environments such as covalent/non-covalent interactions and polar/non-polar interfaces. The spectra of molecules in such complex environments are significantly broadened, and typically the major contribution in the liquid phase has inhomogeneous character. These contributions arise from diverse transient interactions and environmental fluctuations that can span a vast range of time scales. Interrogating the local dynamics in the vicinity of a solute requires unique experimental methods that can effectively separate various contributions at high time and spatial resolutions. Frequency domain lineshape profiles, to a certain extent, provide information about the underlying broadening mechanisms. Homogenous broadening is usually characterized by a Lorentzian lineshape which essentially a result of Fourier transform of an exponential dephasing. On the other hand, inhomogeneous broadening mechanisms arise from an ensemble distribution of molecular interactions and is often modeled using a gaussian function (such as doppler broadening which has gaussian speed distributions). For nearly all the systems, the lineshape function is often convoluted due to contributions from both homogenous and

inhomogeneous broadening mechanism. Therefore, a Voigt profile is a convenient, but nonunique, function commonly used to model spectra with both sources of broadening.

As a concrete example, the hydrogen bond of water has a typical lifetime of about a picosecond. Ultrafast transient absorption techniques have previously been applied to probe

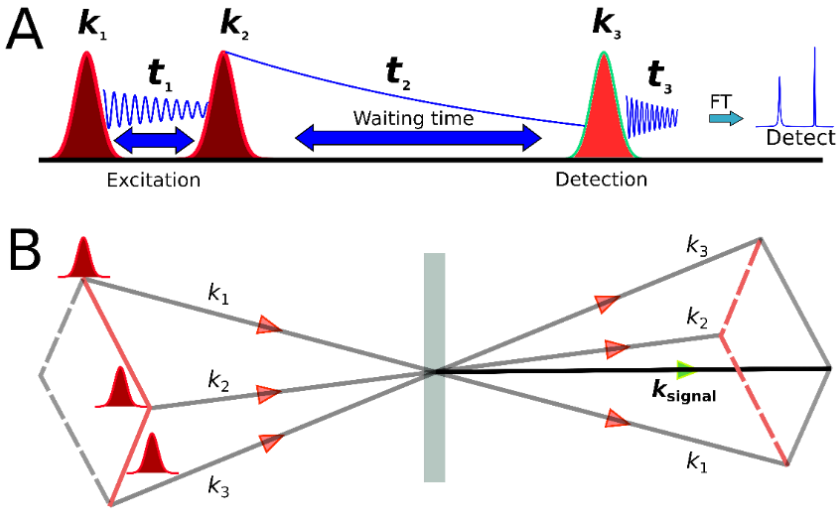

Figure 1.3. (A) 2D-IR pulse sequence involving interaction of three mid-infrared pulses with wave vectors k_1, k_2 and k_3 and time intervals of t_1, t_2 and t_3. Scanning the waiting time delay between the first two excitation and detection pulses enables the observation of underlying dynamics within a system. First and third time delays are Fourier transformed which results in a frequency domain spectrum. (B) Schematic representation of the box geometry implemented which spatially separates the three pulses along the three corners of a box. Emitted signal field appears on the fourth corner which is essentially background free.

various microscopic environments in systems of micelles, proteins and lipids either indirectly using fluorescent probes[50-53] or in the infrared by directly sensing the water or by detecting the hydration environment using probe solute vibrations[54-56]. To capture true equilibrium fluctuations underlying a vibrational mode, ultrafast 2D-IR offers a promising approach. The nonlinear interaction of three mid-infrared pulses with the sample creates a third-order signal field (**Figure 1.3**). The two-dimensional spectrum is accessible by altering the spatial and temporal ordering of these pulses and Fourier transforming the time dependent signal.

The 2D-IR spectrometer (**Figure 1.4**) used for the experiments described in this dissertation consists of two independently tuned, dual stage optical parametric amplifiers (OPA) based on β-barium borate (BBO) crystals pumped with 100 fs, 800 nm pulses provided by a Ti-sapphire regenerative amplifier. The OPAs are seeded using a white light continuum generated via self-phase modulation of a weak 800 nm beam focused on a YAG

crystal. The signal (~1400 nm) and idler (~1900 nm) outputs are then combined in separate GaSe crystals for difference frequency mixing to generate 2 μJ mid-infrared pulses centered around 2000 cm^{-1}. The mid-IR outputs are split into excitation (with wave vectors $\boldsymbol{k}_1$ and $\boldsymbol{k}_2$),

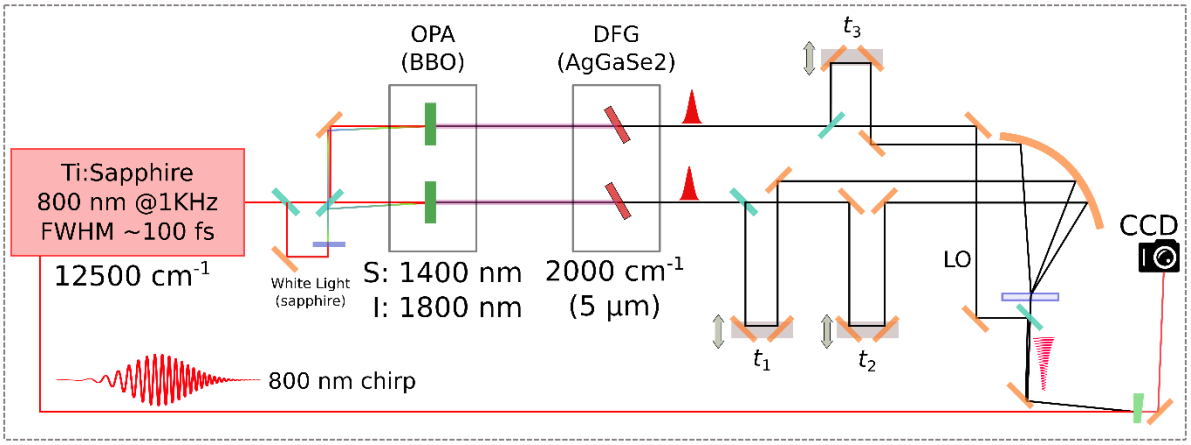

Figure 1.4. Schematic for 2D-IR setup consisting of two independent optical parametric amplifier and difference frequency generation segment which enables down conversion of 100 fs, 800 nm output from our regenerative amplifier to mid-IR wavelengths. DFG output is split to create excitation and detection pulses.

detection ($\boldsymbol{k}_3$) and reference local oscillator (LO) beams. The excitation and detection pulses are overlapped noncollinearly at the sample in a box geometry. The background-free emitted signal is combined with the local oscillator and upconverted in a 5% MgO:$LiNbO_3$ crystal into the visible region using a chirped pulse centered at 800 nm provided by the uncompressed output of the regenerative amplifier. The visible sum-frequency field is detected on a charge coupled device array (PI Acton, PIXIS). The samples are placed in a cell formed by two calcium fluoride windows (25.4 mm diameter and 3 mm thick) separated by a Teflon spacer.

1.2.1. Rephasing and non-rephasing 2D-IR spectrum

The emitted third-order signal field encodes the response function[57] of the system being studied. In the background-free beam geometry, scanning the time delay between the excitation pulses results in capturing only one of the components of the total response function. Given the wave vectors' spatial arrangements in our 2D-IR apparatus, either the rephasing ($\boldsymbol{k}_R = -\boldsymbol{k}_1 + \boldsymbol{k}_2 + \boldsymbol{k}_3$) or the non-rephasing ($\boldsymbol{k}_N = \boldsymbol{k}_1 - \boldsymbol{k}_2 + \boldsymbol{k}_3$) signal is emitted along the fourth corner of the box geometry. In a later section, we will explore how vibrational dynamics of a probe can be measured using two separately acquired 2D spectra, rephasing and non-rephasing. Let's first examine how the two spectra are acquired and the physical interpretation behind them. In practical implementation, at time-zero (i.e. $t_1 = t_2 = 0$) all three spatially overlapped pulses are identical. The distinction between first second and third

pulse begins to manifest once the coherence time delay (t_1) is scanned from the reference zero position. A pulse whose time delay is being scanned becomes the excitation pulse with wave vector k_1 (first pulse) while the static pulse becomes the second pulse with wave vector k_2. The emitted signal direction is dictated by the phase matching conditions for rephasing and non-rephasing. Individual scanning of the excitation pulses is analogous to switching the

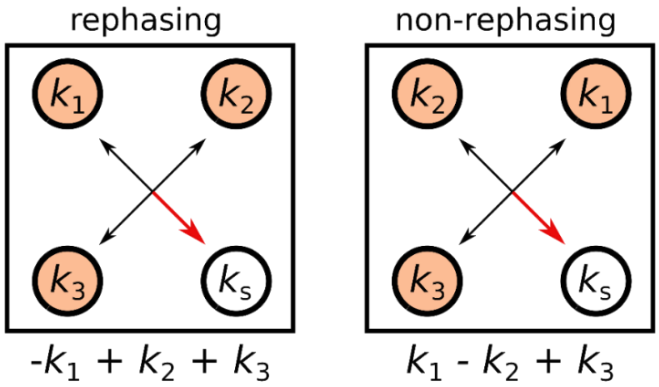

Figure 1.5. Vector diagram showing the direction of emitted field for rephasing and non-rephasing signal. The two contribution to the response function is acquired individually as a separate 2D signal. Each mid-infrared beam is represented by the four corners of the box. The direction of the emitted field is governed by the phase matching conditions for a given response function. By swapped the time-ordering of the two excitation pulses without changing the physical positions rephasing and non-rephasing spectra can be acquired.

wave vector positions for k_1 and k_2 in the box diagram shown in **Fig. 1.5**. This approach enables rephasing and non-rephasing signals to be measured in the same direction without changing the position of the detector by simply switching the time ordering between the two excitation pulses.[57]

In order fully appreciate the physical insight regarding the nature of rephasing and non-rephasing signal, we first explicitly represent the response function for each of them mathematically.

$$R_{rephasing}(t_1, t_2, t_3) = 2e^{-\Gamma_{11}t_2} \times |V_{10}|^4 e^{-\Gamma_{10}t_3 - \Gamma_{10}t_1} \times e^{i\omega_{10}(t_3 - t_1)}$$

$$R_{non-rephasing}(t_1, t_2, t_3) = 2e^{-\Gamma_{11}t_2} \times |V_{10}|^4 e^{-\Gamma_{10}t_3 - \Gamma_{10}t_1} \times e^{i\omega_{10}(t_3 + t_1)}$$

In the expression shown above, ω_{10} represents the transition frequency of a two-level system, Γ_{11} and Γ_{10} represents the population and dephasing decay rates respectively and $|V_{10}|$ is the transition dipole moment operator (responsible for the signal intensity). The signal corresponding to both rephasing and non-rephasing pathways oscillates with the frequency corresponding to the energy gap between the ground and first excited state. In the

case of the non-rephasing signal, the time evolution of the signal evolves as the sum of the preparation and detection times, and the decay rate simply corresponds to the vibrational lifetime and dephasing rate of the mode. But in the case of the rephasing signal, the signal evolves as the difference between the preparation (t_1) and detection (t_3) times. Such time evolution implies that the detected signal creates an echo at time $t_3 = t_1$ which essentially undoes the dephasing corresponding to different microscopic environments in the system. This "undoing" of dephasing is characteristic of different solvent organization and configurations around the molecular probe which corresponds to the inhomogeneity in the system. By separately acquiring rephasing and non-rephasing spectra and referencing them to the non-rephasing spectrum, the dynamic fluctuations of solvent rearrangements can be extracted.

1.2.2. Spectral Diffusion

Dynamical fluctuations of the environment in the vicinity of a vibrational probe can be accessed by quantifying the spectral diffusion responsible for the decay of the correlations of frequency fluctuations. The rephasing spectrum, which contains the dynamical

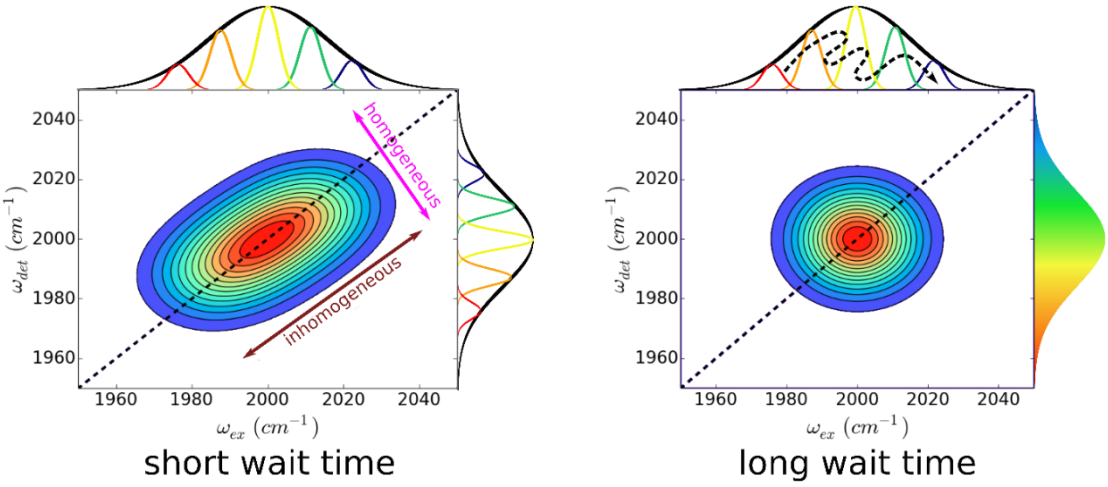

Figure 1.6. A schematic representation of a 2D-IR spectra for a vibrational mode centered around 2000 cm^{-1}. At early waiting times (t_2) between the excitation detection pulses, the spectrum appears sufficiently broadened along the diagonal due to inhomogeneous broadening. At later waiting times, the system effectively samples the available microscopic environments which results in a loss of correlation between excited and detected frequencies (indicated by the dashed wiggly curve). This change in the shape or slope of the spectrum is characterizes the spectral diffusion, which is the main observable from 2D-IR experiments.

information about the loss of reversibility, provides a means of detecting the frequency-fluctuation correlation function (FFCF). At early waiting times, the vibrational probe cannot entirely sample the available micro-environments resulting in the 2D spectrum appearing

elongated along the diagonal, indicating a high degree of correlation between excited and detected frequencies. While at large waiting times, due to scrambling of the vibrational mode frequencies due to sampling other micro-environments, the 2D spectrum becomes symmetrical, indicating loss of correlation between the two frequencies (**Figure 1.6**).

Two-dimensional infrared (2D-IR) spectroscopy facilitates measurement of the inhomogeneity index, which quantifies the loss in correlation resulting from structural dynamics. The inhomogeneity index is related to the frequency fluctuation correlation function which is the main observable in 2D-IR spectroscopy. By measuring the amplitude of a diagonal peak for a given vibrational mode in the rephasing (A_r) and non-rephasing (A_{nr}) spectrum, the inhomogeneity index (II)[58] can be computed:

$$II(t) = \frac{A_r - A_{nr}}{A_r + A_{nr}}$$

The transformation, $C(t) = \sin[\pi II(t)/2]$ can be implemented for systems with a high value of inhomogeneity index and long correlation decay times.

1.2.3. Vibrational lifetime

At equilibrium, nearly all molecules remain in the ground vibrational state as the transition energy is greater than the available room temperature thermal energy. Molecules promoted to higher vibrational state using excitation pulses eventually relax back to the ground state. The decay curve (usually a sum of exponentials) corresponding to this population relaxation has an associated time constant, referred as the vibrational lifetime. Lifetimes of vibrational modes can last up to 1 ns in non-polar solvents[59] due to the reduced number of accessible solvent and weak interaction with the solute. Probes studied in this work have vibrational lifetime of at most 30 ps in aqueous solutions. In the gas phase, much longer vibrational lifetimes are observed due to the lack of available modes for rapid energy dissipation. In the liquid state, vibrational modes can sufficiently couple with solvent's local and collective modes thus enhancing the rate of energy dissipation (**Figure 1.7**).[60] In addition to solvent coupling, molecules with a greater number of degrees of freedom (modes) can also dissipate energy localized on an excited vibrational mode to another mode via intra-molecular vibrational redistribution or IVR.

2D-IR spectroscopy offers the advantage to easily visualize such coupling between any two modes as time dependent changes in the cross-peak amplitudes. In this dissertation, which focuses solely on solvent dynamics, molecules with mostly a single IR-active

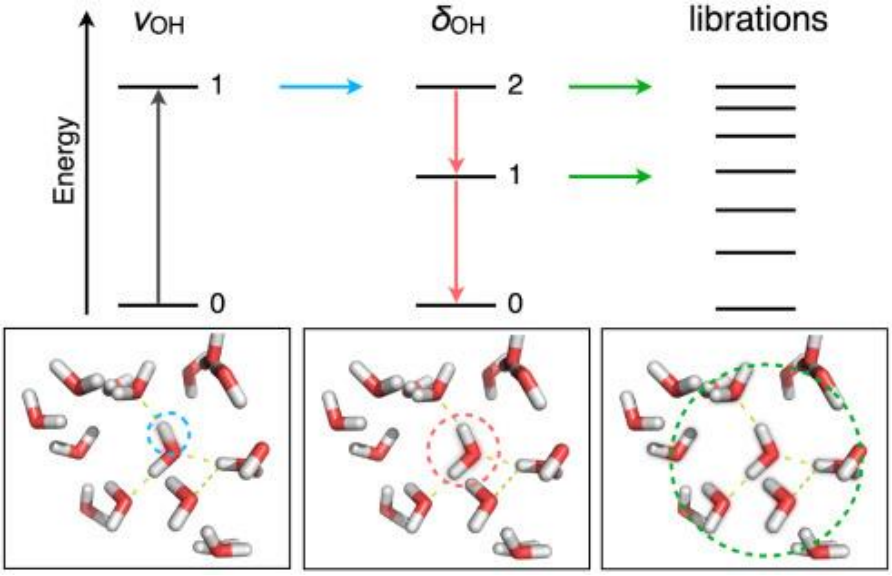

Figure 1.7. Initial excitation of a single water molecule from the ground to the first vibrational level in the OH stretching frequency (~3400 cm^{-1}) mode. The excited molecule then relaxes to the ground state at ultrafast timescales by coupling itself with the overtone band of the bend mode manifold. Eventually, the delocalized energy is further dissipated into the librational modes of hydrogen bonded water molecules. Both stretch and bend modes of water lie in the infrared region of the spectrum (1000 – 3000 cm^{-1}), while librational mode lie in the much lower energy THz region (<200 cm^{-1}) of the electromagnetic spectrum.

vibrational mode were studied in aqueous medium. Isotopic substitution (D_2O vs H_2O) did yield changes in the vibrational lifetime. In pure H_2O the bend-librational combination band is more pronounced because the individual component of this band corresponds to the light hydrogen atom motions in the hydrogen bond which is shifted to much lower frequency in D_2O.[61]

1.2.4. Continuous scanning of coherence time (t_1)

A key experimental difference between 2D-IR and other third-order experiments such as pump-probe is that two excitation pulses are scanned independent of the dynamical waiting time (t_2). The coherence time (t_1) scan in 2D-IR can be achieved either using an optical pulse shaper[62, 63] or by moving motors attached to an optical delay. Typically, delays of ~10 ps are sufficient to scan the coherent oscillations of a vibrational mode and achieve suitable spectral resolution. In our experimental setup, instead of discretely stepping the motors, they are scanned continuously. Such rapid scanning of motors during experiments has enabled faster spectral acquisition as well as development of methods for quick acquisition

of multidimensional spectra.[64, 65] A traditional approach is to set the optical delay stages to a predetermined position and step them in discrete time steps. Instead, they are run at their maximum speed while simultaneously recording their positions on a shot-to-shot basis using a fast encoder counter trigged by the regenerative amplifier. Due to inherent instability of even highest precision motor, and imperfections in the wedges used to change the optical pathlength, positions deviate from linearity, but this deviation can easily be corrected using post-processing methods. This fluctuation in the motor position from ideal linearity manifests as wobbling of peak in the frequency spectrum. Therefore, before performing any 2D-IR spectral acquisition, the delay stage motors are calibrated by measuring the interference fringe pattern between a static and moving pulse and corrected to remove any artefacts. The non-linear response is subtracted by fitting the reference peak with combination of linear, polynomial and sinusoidal functions.

1.3. Computational modeling of water using classical mechanics

Extracting a molecular picture from experiments alone is an arduous task, therefore a combination of theory and computer simulations are often needed to supplement physical observations.[66, 67] The hydrogen bond between water molecules does not have an explicit empirical expression due to the high number of degrees of freedom and polarizable nature of the bond, therefore numerical simulations are needed. Quantum mechanical calculations using various approximations have been developed to compute the electron density between a pair of hydrogen bonded water molecules. Density functional theory and *ab initio* methods which consider nuclear quantum corrections[68] have been applied to compute key macroscopic parameters of bulk water[69] with good accuracy. Such high-level calculations are inherently complex and have associated high computational cost. Instead, classical molecular dynamics simulations are well-suit to the problems studied by biophysicists and physical chemists, particularly when studying water and its interaction with macromolecules to calculate various transport and dynamical properties. It is remarkable that many physical properties of water such as density, diffusion coefficient and melting properties can be captured using very simple static point charge water models such as SPC[70], SPC/E[71], TIP3P[72], TIP4P[72] and the Mercedes-Benz[73]. Classical Molecular Dynamics (MD) simulations evolve the system of molecules by treating interactions between any pair,

triplets, etc. of atoms using a potential energy function. The potential energy function can depend on the distance or angle between the system of atoms. A harmonic potential is used for atoms connected via a bond without considering bond breaking. While non-bonded interactions are treated using short ranged potentials such as van der Waals and Lennard-Jones. The force on each particle is computed at each time step and the trajectory is obtained by numerically integrating Newton's equation of motion, yielding a trajectory of particle positions and velocities.

An unequivocal idea of hydrogen bond "networks" is often introduced to explain seemingly inconsistent and surprising observations of water near a macromolecular interface or concentrated salt solutions[74, 75]. It is often stated, almost as an article of faith, that the global connectivity of water becomes perturbed by an interface, but the direct application of techniques from network theory to the hydrogen-bonded network of water has not been investigated. In this dissertation, we will implement ideas and concepts from network science to explicitly characterize the hydrogen bond network's local and global topologies. Analysis based on graph theorical methods, it is found that the hydrogen bond networks cannot be considered simply as a random connection between any given water molecule. Instead, the most novel findings of this works is that the hydrogen bond connectivity is arranged in a rigid framework and show striking similarity with networks arranged in a square lattice. Due to dense connectivity pattern of hydrogen bond networks, the local and global network characteristics remains unaltered in conditions ranging from dilute to crowded. Beyond first hydration shell, nearby macromolecular interfaces are unable to disrupt the hydrogen bond network and the fast collective librational motions of water show bulk-like dynamics.

There is a relatively established tradition of constructing simplified models of water that can capture and predict various thermodynamic and transport properties without explicitly considering the detailed structure of water. Using an Ising-like model on a square lattice, a new simulation model is described in chapter 5 of this dissertation. The developed which effectively captures the four-coordinate hydrogen bonding network in liquid water. Metropolis Monte Carlo was used to simulate the switching dynamics of water which mimics the jumping events responsible for hydrogen bond rearrangements. The model explores the spatial extent of perturbations to the switching dynamics near an idealized hydrophobic

interface. The central finding of the work is that one can reproduce the spatial mapping of hydration dynamics slowdown under crowding as a simple sum of dilute interfacial perturbations. In other words, no evidence for cooperative hydrogen bond slowdown within the thermodynamic ansatz was observed. These results indicate that cooperative hydration dynamics under confinement must arise from dynamical perturbations that are distinct from the entropic, excluded volume contribution.

1.4. Thesis Outline

The essential theme of this research is to understand the nature, extent and timescale of the perturbation of the hydrogen bond jumping dynamics of water and its network structures near a macromolecular interface, or by itself (**Figure 1.8**).

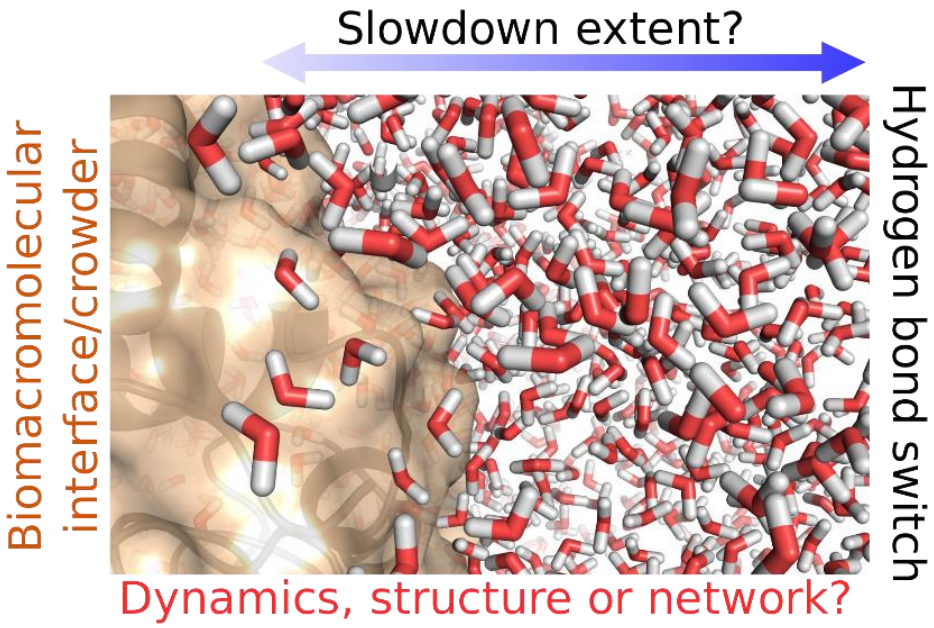

Figure 1.8. Illustration depicting the scope of this dissertation. Apart from differences in the magnitude of the slowdown, we still lack an agreement regarding the length scale for the extent of slowdown from the interface. The present work aims to provide quantitative evidence for the observed dynamical slowdown with local structure and global hydrogen bond network properties of water near a variety of interfaces with different chemical and structural heterogeneity as well as explores the extent of this perturbation.

This chapter provides an outlook to various scientific questions and approaches in the experimental and theoretical communities to understand and characterize the nature of water dynamics. This chapter also discusses the past and ongoing debates concerning the structural and dynamical aspects of water. Such disagreements in results and methods are necessary to advancing our scientific understanding but holding onto an extreme viewpoint prevents a scientific debate from ever being resolved.

The main body of this dissertation focuses on experimental and simulation approaches applied to studying hydration dynamics on a variety of macromolecular interfaces with different chemical and surface topologies.

Chapter 2 highlights our recent findings of interfacial hydration using the thiocyanate anion (SCN^-) as a vibrational probe in cationic micelles of different size factors and curvatures. The study aims to probe the hydration dynamics near surfactant interfaces solely without requiring averaging contributions from the bulk and the interface. This study is the first of its kind to simultaneously probe ultrafast dynamics of water using 2D-IR and provide accurate structural characterization of surfactant interfaces using the well-established spectroscopic tool of NMR.

Chapter 3 takes a defensive approach to resolve the long-standing debate on the spatial extent of perturbation of the hydrogen bond network in crowded environments. Graph theoretical analysis was used in conjunction with molecular dynamics simulations of binary proteins in water mimicking different degrees of crowding. Water-water hydrogen bonds were treated explicitly and characterized using the metrics of network science. To our surprise, and contrary to past findings we observe only short-ranged perturbation to the hydrogen bond network. A strong correlation of retarded fluctuations in protein residues emerges when macromolecular interfaces become significantly crowded. Motivated by our simulation results we tested the validity of long-range slowdown in hydration dynamics without labeling the protein and observe a bulk-like timescale, thereby highlighting the limitations of studying crowding induced slowdown using surface-labeled probes.

Chapter 4 focuses on an alternative approach to the computer simulation of water. Instead of using molecular dynamics we have developed a simple Monte Carlo based two-dimensional lattice model of hydrogen bond rearrangements of interfacial water in conditions ranging from dilute to crowded. The present simplified model attempts to determine whether the excluded volume picture of hydrogen bond perturbation supports long-range cooperativity that has been observed in several experiments. It is remarkable that this simulation model captures quantitatively the interface-induced excluded volume

slowdown originally identified using purely entropic contribution to the free energy landscape. This modeling approach is well suited to a systematic study of interfacial topology contributions that are difficult to control in realistic, atomistic simulations.

Chapter 5 presents an experimental investigation into the effect of ions on the hydration dynamics of poly(ethylene oxide) and deoxyribonucleic acids (DNA) solutions. This chapter investigates the direct interaction mechanism between Hofmeister cations and short PEG polymers. Capturing a complete picture of hydration dynamics near extended interfaces requires modelling the interaction of ions with water and interfaces. 2D-IR spectral diffusion measurements of thiocyanate with PEG-200 show significant retardation in dynamics compared to bulk with additional slowdown for potassium ion specifically. Instead of trying to directly compare the effect of different thiocyanate salts to their fixed ranking in the Hofmeister series, we take an outward approach to rationalize the experimental findings aided by optimized structure calculations. While hydration dynamics for long strand DNA duplex remains bulk like, these results highlight the specific nature of cations to induce conformational transition in polymers.

Chapter 6 describes the development of a light source in the mid-infrared which can be interfaced with other light sources simultaneously developed to perform multispectral multidimensional spectroscopy spanning ultraviolet to terahertz frequencies. Once fully implemented the setup would enable probing ultrafast dynamics from ultrafast femtosecond timescales to second timescale in a single experiment. This chapter will primarily discuss the design principles and methods to implement a non-collinear difference frequency mixing approach for generation of tunable broadband mid-infrared frequency.

The final chapter of the dissertation will recapitulate and summarize the experimental and computational findings. A brief discussion and suggestions for future experiments will also be highlighted in this chapter.

1.5. References

1. Shoichet, B. K.; Baase, W. A.; Kuroki, R.; Matthews, B. W., A Relationship Between Protein Stability And Protein Function. *Proceedings of the National Academy of Sciences of the United States of America* **1995,** *92* (2), 452-456.
2. Dikic, I.; Wakatsuki, S.; Walters, K. J., Ubiquitin-binding domains - from structures to functions. *Nature Reviews Molecular Cell Biology* **2009,** *10* (10), 659-671.
3. Gutteridge, A.; Thornton, J., Conformational change in substrate binding, catalysis and product release: an open and shut case? *Febs Letters* **2004,** *567* (1), 67-73.
4. Henzler-Wildman, K. A.; Thai, V.; Lei, M.; Ott, M.; Wolf-Watz, M.; Fenn, T.; Pozharski, E.; Wilson, M. A.; Petsko, G. A.; Karplus, M.; Hubner, C. G.; Kern, D., Intrinsic motions along an enzymatic reaction trajectory. *Nature* **2007,** *450* (7171), 838-U13.
5. Mancera, R. L., Molecular modeling of hydration in drug design. *Current Opinion in Drug Discovery & Development* **2007,** *10* (3), 275-280.
6. Jeszenoi, N.; Balint, M.; Horvath, I.; van der Spoel, D.; Hetenyi, C., Exploration of Interfacial Hydration Networks of Target Ligand Complexes. *Journal of Chemical Information and Modeling* **2016,** *56* (1), 148-158.
7. Daniel, R. M.; Dunn, R. V.; Finney, J. L.; Smith, J. C., The role of dynamics in enzyme activity. *Annual Review of Biophysics and Biomolecular Structure* **2003,** *32*, 69-92.
8. Kocsis, I.; Sorci, M.; Vanselous, H.; Murail, S.; Sanders, S. E.; Licsandru, E.; Legrand, Y. M.; van der Lee, A.; Baaden, M.; Petersen, P. B.; Belfort, G.; Barboiu, M., Oriented chiral water wires in artificial transmembrane channels. *Science Advances* **2018,** *4* (3).
9. Decker, K.; Page, M.; Aksimentiev, A., Nanoscale Ion Pump Derived from a Biological Water Channel. *Journal of Physical Chemistry B* **2017,** *121* (33), 7899-7906.
10. Davies, P. L.; Hew, C. L., Biochemistry of Fish Antifreeze Proteins. *Faseb Journal* **1990,** *4* (8), 2460-2468.
11. Bai, F.; Wu, J. T.; Gong, G. M.; Guo, L., Biomimetic "Water Strider Leg" with Highly Refined Nanogroove Structure and Remarkable Water-Repellent Performance. *Acs Applied Materials & Interfaces* **2014,** *6* (18), 16237-16242.
12. Yachandra, V. K.; Sauer, K.; Klein, M. P., Manganese cluster in photosynthesis: Where plants oxidize water to dioxygen. *Chemical Reviews* **1996,** *96* (7), 2927-2950.
13. Lodish, H. F., *Molecular cell biology*. W.H. Freeman and Co.: New York, 2013.
14. Huang, K. Y.; Kingsley, C. N.; Sheil, R.; Cheng, C. Y.; Bierma, J. C.; Roskamp, K. W.; Khago, D.; Martin, R. W.; Han, S., Stability of Protein-Specific Hydration Shell on Crowding. *Journal of the American Chemical Society* **2016,** *138* (16), 5392-5402.
15. Calero, C.; Stanley, H. E.; Franzese, G., Structural Interpretation of the Large Slowdown of Water Dynamics at Stacked Phospholipid Membranes for Decreasing Hydration Level: All-Atom Molecular Dynamics. *Materials* **2016,** *9* (5).
16. Qiu, W. H.; Kao, Y. T.; Zhang, L. Y.; Yang, Y.; Wang, L. J.; Stites, W. E.; Zhong, D. P.; Zewail, A. H., Protein surface hydration mapped by site-specific mutations. *Proceedings of the National Academy of Sciences of the United States of America* **2006,** *103* (38), 13979-13984.
17. Mattea, C.; Qvist, J.; Halle, B., Dynamics at the protein-water interface from ^{17}O spin relaxation in deeply supercooled solutions. *Biophysical Journal* **2008,** *95* (6), 2951-2963.
18. Ball, P., Water is an active matrix of life for cell and molecular biology. *Proceedings of the National Academy of Sciences of the United States of America* **2017,** *114* (51), 13327-13335.

19. Persson, E.; Halle, B., Cell water dynamics on multiple time scales. *Proceedings of the National Academy of Sciences of the United States of America* **2008,** *105* (17), 6266-6271.
20. Jasnin, M.; Moulin, M.; Haertlein, M.; Zaccai, G.; Tehei, M., Down to atomic-scale intracellular water dynamics. *Embo Reports* **2008,** *9* (6), 543-547.
21. Kauzmann, W., Some Factors In The Interpretation of Protein Denaturation. *Advances in Protein Chemistry* **1959,** *14*, 1-63.
22. Keutsch, F. N.; Saykally, R. J., Water clusters: Untangling the mysteries of the liquid, one molecule at a time. *Proceedings of the National Academy of Sciences of the United States of America* **2001,** *98* (19), 10533-10540.
23. Gregory, J. K.; Clary, D. C.; Liu, K.; Brown, M. G.; Saykally, R. J., The water dipole moment in water clusters. *Science* **1997,** *275* (5301), 814-817.
24. Liu, K.; Cruzan, J. D.; Saykally, R. J., Water clusters. *Science* **1996,** *271* (5251), 929-933.
25. Blokzijl, W.; Engberts, J., Hydrophobic Effects - Opinions and Facts. *Angewandte Chemie-International Edition* **1993,** *32* (11), 1545-1579.
26. Duboue-Dijon, E.; Laage, D., Characterization of the Local Structure in Liquid Water by Various Order Parameters. *Journal of Physical Chemistry B* **2015,** *119* (26), 8406-8418.
27. Dang, L. X.; Chang, T. M., Molecular dynamics study of water clusters, liquid, and liquid-vapor interface of water with many-body potentials. *Journal of Chemical Physics* **1997,** *106* (19), 8149-8159.
28. Lum, K.; Chandler, D.; Weeks, J. D., Hydrophobicity at small and large length scales. *Journal of Physical Chemistry B* **1999,** *103* (22), 4570-4577.
29. Scatena, L. F.; Brown, M. G.; Richmond, G. L., Water at hydrophobic surfaces: Weak hydrogen bonding and strong orientation effects. *Science* **2001,** *292* (5518), 908-912.
30. Limmer, D. T.; Willard, A. P.; Madden, P.; Chandler, D., Hydration of metal surfaces can be dynamically heterogeneous and hydrophobic. *Proceedings of the National Academy of Sciences of the United States of America* **2013,** *110* (11), 4200-4205.
31. Willard, A. P.; Chandler, D., Instantaneous Liquid Interfaces. *Journal of Physical Chemistry B* **2010,** *114* (5), 1954-1958.
32. Charkhesht, A.; Regmi, C. K.; Mitchell-Koch, K. R.; Cheng, S.; Vinh, N. Q., High-Precision Megahertz-to-Terahertz Dielectric Spectroscopy of Protein Collective Motions and Hydration Dynamics. *Journal of Physical Chemistry B* **2018,** *122* (24), 6341-6350.
33. Jungwirth, P., Biological Water or Rather Water in Biology? *Journal of Physical Chemistry Letters* **2015,** *6* (13), 2449-2451.
34. Mondal, S.; Mukherjee, S.; Bagchi, B., Protein Hydration Dynamics: Much Ado about Nothing? *Journal of Physical Chemistry Letters* **2017,** *8* (19), 4878-4882.
35. Furse, K. E.; Corcelli, S. A., The dynamics of water at DNA interfaces: Computational studies of Hoechst 33258 bound to DNA. *Journal of the American Chemical Society* **2008,** *130* (39), 13103-13109.
36. Halle, B., Reply to "Comment on 'Hydration and Mobility of Trehalose in Aqueous Solution'". *Journal of Physical Chemistry B* **2014,** *118* (36), 10806-10812.
37. Heyden, M.; Schwaab, G.; Hayenith, M., Comment on "Hydration and Mobility of Trehalose in Aqueous Solution". *Journal of Physical Chemistry B* **2014,** *118* (36), 10802-10805.
38. Winther, L. R.; Qvist, J.; Halle, B., Hydration and Mobility of Trehalose in Aqueous Solution. *Journal of Physical Chemistry B* **2012,** *116* (30), 9196-9207.
39. Persson, F.; Soderhjelm, P.; Halle, B., The spatial range of protein hydration. *Journal of Chemical Physics* **2018,** *148* (21).

40. Despa, F.; Fernandez, A.; Berry, R. S., Dielectric modulation of biological water. *Physical Review Letters* **2004,** *93* (22).
41. Perticaroli, S.; Ehlers, G.; Stanley, C. B.; Mamontov, E.; O'Neill, H.; Zhang, Q.; Cheng, X. L.; Myles, D. A. A.; Katsaras, J.; Nickels, J. D., Description of Hydration Water in Protein (Green Fluorescent Protein) Solution. *Journal of the American Chemical Society* **2017,** *139* (3), 1098-1105.
42. Martin, D. R.; Forsmo, J. E.; Matyushov, D. V., Complex Dynamics of Water in Protein Confinement. *Journal of Physical Chemistry B* **2018,** *122* (13), 3418-3425.
43. Born, B.; Kim, S. J.; Ebbinghaus, S.; Gruebele, M.; Havenith, M., The terahertz dance of water with the proteins: the effect of protein flexibility on the dynamical hydration shell of ubiquitin. *Faraday Discussions* **2009,** *141*, 161-173.
44. Ebbinghaus, S.; Kim, S. J.; Heyden, M.; Yu, X.; Heugen, U.; Gruebele, M.; Leitner, D. M.; Havenith, M., An extended dynamical hydration shell around proteins. *Proceedings of the National Academy of Sciences of the United States of America* **2007,** *104* (52), 20749-20752.
45. Heyden, M.; Tobias, D. J.; Matyushov, D. V., Terahertz absorption of dilute aqueous solutions. *Journal of Chemical Physics* **2012,** *137* (23).
46. Novelli, F.; Pour, S. O.; Tollerud, J.; Roozbeh, A.; Appadoo, D. R. T.; Blanch, E. W.; Davis, J. A., Time-Domain THz Spectroscopy Reveals Coupled Protein-Hydration Dielectric Response in Solutions of Native and Fibrils of Human Lysozyme. *Journal of Physical Chemistry B* **2017,** *121* (18), 4810-4816.
47. Eaves, J. D.; Loparo, J. J.; Fecko, C. J.; Roberts, S. T.; Tokmakoff, A.; Geissler, P. L., Hydrogen bonds in liquid water are broken only fleetingly. *Proceedings of the National Academy of Sciences of the United States of America* **2005,** *102* (37), 13019-13022.
48. Laage, D.; Hynes, J. T., A molecular jump mechanism of water reorientation. *Science* **2006,** *311* (5762), 832-835.
49. Hollas, J. M., *Modern spectroscopy*. 4th ed.; J. Wiley: Chichester ; Hoboken, NJ, 2004; p xxvii, 452 p.
50. Abbyad, P.; Childs, W.; Shi, X. H.; Boxer, S. G., Dynamic Stokes shift in green fluorescent protein variants. *Proceedings of the National Academy of Sciences of the United States of America* **2007,** *104* (51), 20189-20194.
51. Qin, Y. Z.; Wang, L. J.; Zhong, D. P., Dynamics and mechanism of ultrafast water-protein interactions. *Proceedings of the National Academy of Sciences of the United States of America* **2016,** *113* (30), 8424-8429.
52. Yang, Y.; Qin, Y. Z.; Ding, Q.; Bakhtina, M.; Wang, L. J.; Tsai, M. D.; Zhong, D. P., Ultrafast Water Dynamics at the Interface of the Polymerase-DNA Binding Complex. *Biochemistry* **2014,** *53* (33), 5405-5413.
53. Pal, S. K.; Peon, J.; Zewail, A. H., Biological water at the protein surface: Dynamical solvation probed directly with femtosecond resolution. *Proceedings of the National Academy of Sciences of the United States of America* **2002,** *99* (4), 1763-1768.
54. Lee, J.; Maj, M.; Kwak, K.; Cho, M., Infrared Pump-Probe Study of Nanoconfined Water Structure in Reverse Micelle. *Journal of Physical Chemistry Letters* **2014,** *5* (19), 3404-3407.
55. Loparo, J. J.; Roberts, S. T.; Tokmakoff, A., Multidimensional infrared spectroscopy of water. I. Vibrational dynamics in two-dimensional IR line shapes. *Journal of Chemical Physics* **2006,** *125* (19).

56. Piletic, I. R.; Tan, H. S.; Fayer, M. D., Dynamics of nanoscopic water: Vibrational echo and infrared pump-probe studies of reverse micelles. *Journal of Physical Chemistry B* **2005,** *109* (45), 21273-21284.
57. Hamm, P.; Zanni, M., *Concepts and Methods of 2D Infrared Spectroscopy*. Cambridge University Press: Cambridge, 2011.
58. Roberts, S. T.; Loparo, J. J.; Tokmakoff, A., Characterization of spectral diffusion from two-dimensional line shapes. *Journal of Chemical Physics* **2006,** *125* (8).
59. Heilweil, E. J.; Cavanagh, R. R.; Stephenson, J. C., Population Relaxation of CO(ν=1) Vibrations In Solution Phase Metal Carbonyl Complexes. *Chemical Physics Letters* **1987,** *134* (2), 181-188.
60. Kubarych, K.; Roy, V. P.; Daley, K. R., Interfacial Water Dynamics. In *Encyclopedia of Interfacial Chemistry*, Wandelt, K., Ed. Elsevier: Oxford, 2018; pp 443-461.
61. Czurlok, D.; Gleim, J.; Lindner, J.; Vohringer, P., Vibrational Energy Relaxation of Thiocyanate Ions in Liquid-to-Supercritical Light and Heavy Water. A Fermi's Golden Rule Analysis. *Journal of Physical Chemistry Letters* **2014,** *5* (19), 3373-3379.
62. Shim, S. H.; Zanni, M. T., How to turn your pump-probe instrument into a multidimensional spectrometer: 2D IR and Vis spectroscopies via pulse shaping. *Physical Chemistry Chemical Physics* **2009,** *11* (5), 748-761.
63. Shim, S. H.; Strasfeld, D. B.; Ling, Y. L.; Zanni, M. T., Automated 2D IR spectroscopy using a mid-IR pulse shaper and application of this technology to the human islet amyloid polypeptide. *Proceedings of the National Academy of Sciences of the United States of America* **2007,** *104* (36), 14197-14202.
64. Dunbar, J. A.; Osborne, D. G.; Anna, J. M.; Kubarych, K. J., Accelerated 2D-IR Using Compressed Sensing. *Journal of Physical Chemistry Letters* **2013,** *4* (15), 2489-2492.
65. Osborne, D. G.; Kubarych, K. J., Rapid and Accurate Measurement of the Frequency-Frequency Correlation Function. *Journal of Physical Chemistry A* **2013,** *117* (29), 5891-5898.
66. Stillinger, F. H.; Rahman, A., Improved Simulation of Liquid Water by Molecular Dynamics. *Journal of Chemical Physics* **1974,** *60* (4), 1545-1557.
67. Stillinger, F. H., Water Revisited. *Science* **1980,** *209* (4455), 451-457.
68. Xantheas, S. S., Ab-Initio Studies of Cyclic Water Clusters $(H_2O)_n$, n=1-6 .2. Analysis of Many-Body Interactions. *Journal of Chemical Physics* **1994,** *100* (10), 7523-7534.
69. Pestana, L. R.; Marsalek, O.; Markland, T. E.; Head-Gordon, T., The Quest for Accurate Liquid Water Properties from First Principles. *Journal of Physical Chemistry Letters* **2018,** *9* (17), 5009-5016.
70. Toukan, K.; Rahman, A., Molecular Dynamics Study of Atomic Motions in Water. *Physical Review B* **1985,** *31* (5), 2643-2648.
71. Berendsen, H. J. C.; Grigera, J. R.; Straatsma, T. P., The Missing Term In Effective Pair Potentials. *Journal of Physical Chemistry* **1987,** *91* (24), 6269-6271.
72. Jorgensen, W. L.; Chandrasekhar, J.; Madura, J. D.; Impey, R. W.; Klein, M. L., Comparison of Simple Potential Functions for Simulating Liquid Water. *Journal of Chemical Physics* **1983,** *79* (2), 926-935.
73. Silverstein, K. A. T.; Haymet, A. D. J.; Dill, K. A., A simple model of water and the hydrophobic effect. *Journal of the American Chemical Society* **1998,** *120* (13), 3166-3175.
74. Tielrooij, K. J.; Garcia-Araez, N.; Bonn, M.; Bakker, H. J., Cooperativity in Ion Hydration. *Science* **2010,** *328* (5981), 1006-1009.

75. Giammanco, C. H.; Wong, D. B.; Fayer, M. D., Water Dynamics in Divalent and Monovalent Concentrated Salt Solutions. *Journal of Physical Chemistry B* **2012,** *116* (46), 13781-13792.

Chapter 2

Chaotropicity of Thiocyanate anion Enables Probing of Interfacial Hydration Dynamics in Cationic Micelles

The work presented in this chapter has been published in the following article:
Roy, V. P.; Kubarych, K. J., Interfacial Hydration Dynamics in Cationic Micelles Using 2D-IR and NMR. *J.Phys. Chem. B* **2017,** *121*, 9621-9630.

2.1. Introduction

Since membranes are essential components of biological machinery, there has been substantial effort devoted to measuring ultrafast dynamics in model systems such as lipid bilayers and reverse micelles. Coupled with ultrafast infrared spectroscopy, it has been possible to measure hydration dynamics by probing the water vibrations directly,[1-5] and access to the surfactant head groups has been achieved using either phosphate transitions,[6] or the C=O units of ester-containing lipids.[7] The interior of lipid bilayers has been investigated using transition metal carbonyl probes which are largely insoluble in water.[8] Hydration dynamics at the interface with a model bilayer was studied using a transition metal carbonyl derivatized cholesterol probe,[9] as well as approaches using multiple probes.[10] At a molecular level, the surface of proteins and nucleic acids exhibit both chemical

and topological heterogeneity. From relatively flat membranes to sharp grooves in biomolecules, varying degrees of curvature is likely to influence hydration dynamics differently. Hence, many aspects of membrane structure likely influence both the membrane and hydration dynamics.

As mentioned in the earlier chapter, apart from imposing structural constraints on hydration water, the reduced availability of hydrogen bonding partners at extended interfaces also modifies water's translational and orientational dynamics[11]. The altered hydration dynamics can, in turn, influence the structural dynamics of the biomacromolecules through a coupling commonly denoted "slaving."[12] Additionally, slowed water has material properties that differ from the bulk, most notably the dielectric response $\varepsilon(\omega)$, which is the Fourier transform of the dipole moment time correlation function.[13] Hence, electrostatic interactions at extended hydration interfaces may be attenuated differently than would be predicted using bulk water parameters.[14] Such restricted dynamics of the hydration shell has been proposed to play crucial roles in many biological processes including enzyme catalysis,[15, 16] protein folding and aggregation,[17] DNA photoprotection,[18] proton transfer in proton pumps,[19] as well as membrane formation and disruption.[20, 21] In cells, where crowded environments predominate, hydration dynamics are expected to be dictated by the collective influence of these interfacial constraints,[22] which may extend to relatively long distances (>20 Å) based on both experiment and simulation results.[23-26]

Here, we employ a tunable model system of reverse micelles where relative hydration levels can be adjusted by changing the volume and morphology of the encapsulated water. Dissolved NaSCN provides a vibrational probe through the strong CN stretch of the thiocyanate anion,[27-33] which we show here strongly associates with the cationic $N(CH_3)_3^+$ head groups of the DTAB (dodecyltrimethylammonium bromide) surfactant. The concentration ratio of water to surfactant (w_0 = [water]/[surfactant]) determines the micelle diameter, while additives can be introduced to change the morphology.[34, 35] Previous studies on intermediate (~4 nm) to large (~10 nm) reverse micelles have led to a picture of confined water dynamics being composed of a weighted sum of interfacial and bulk-like contributions.[4, 36] The dynamics of nanoconfined systems are expected to be highly dispersed, exhibiting motions on a wide range of time scales[37]. A limitation of probing

intrinsic vibrational transitions such as the phosphates,[6] carbonyls, and water's OH stretch is that all have rather short vibrational lifetimes ranging from 0.3 to 2 ps, limiting the temporal dynamical range. In principle, a vibrational probe with a longer lifetime should provide access to slower phases of dynamics that are expected to stretch out to very long μs to ms time scales.[37] In D_2O, SCN^- has a comparatively longer vibrational lifetime of roughly 30 ps, compared with ~2 ps in H_2O.[38] Besides SCN^-, it is also possible to use CN^- as a vibrational probe[39-41] since the lifetime can be very long, particularly for the case of $^{13}C^{15}N^-$ in D_2O, where the lifetime is 120 ps. Previous work by Owrutsky *et al*. has found population and orientational relaxation of SCN^- and other pseudohalides to depend on the presence and size factor of reverse micelles composed of nonionic surfactants.[42, 43] Dynamics inside reverse micelles composed of surfactants with anionic head groups have been investigated using the somewhat larger anion tricyanometanide; there, two spectroscopic species are evident reflecting the head-group region and the bulk.[44] In these previous studies, the vibrational probes were not found to preferentially interact with the head groups due to the lack of favorable electrostatic attraction between anionic spectroscopic reporters and either neutral or anionic head groups.

2.1.1. Two-Dimensional Spectroscopy and Spectral Diffusion.

Ultrafast vibrational spectroscopy provides local dynamical information through several distinct, but often complementary observables.[45] Vibrational energy relaxation yields the excited state lifetime, transient absorption anisotropy can generally be related to orientational diffusion, and, using 2D-IR spectroscopy, time dependent line shape changes can reveal solvation dynamics. There are situations where vibrational relaxation is linked to structural dynamics, such as solvent environment fluctuations and orientational motion, but there are also many examples where the lifetime is uncorrelated with structural dynamics.[46-48] The decoupling is probably most apparent when the vibrational excitation itself is not the principal trigger of the resulting dynamics. In water and other hydrogen bonded liquids, for example, exciting the OH stretch causes hydrogen bond breaking, and therefore plays a role in launching nonequilibrium dynamics.[49-52] In vibrational systems with long (>10 ps) lifetimes, it is quite common to see little to no correlation between, for example, vibrational relaxation and spectral diffusion. In these cases, it is more likely that the vibrational

excitation is negligibly responsible for the dynamics the probe senses.[46, 48, 53-55] To access the molecular dynamical fluctuations in the vicinity of a probe chromophore, we employ 2D-IR spectroscopy to extract the frequency-fluctuation correlation function (FFCF) for the CN stretch in D_2O solutions in order to have the best chance to observe equilibrium fluctuations of the surroundings.

Using an anionic vibrational probe, such as SCN^-, offers the possibility to sense preferentially the cationic head group region. Whether or not a given ion is likely to associate strongly with a charged head group is largely dictated by the ion's position in the Hofmeister series.[56] The ordering of Hofmeister ions was originally based on a given ion's tendency to stabilize or destabilize the folded state of proteins. Apart from altering the physical properties of solvents, such as surface tension, other physical aspects of solutes are also modulated, such as enzymatic activity, protein-protein interactions, as well as structural properties including optical rotation of sugars and amino acids.[57, 58] Although the fundamental mechanisms underlying Hofmeister effects are not yet fully understood, and there may be different mechanisms for different processes,[59] it seems that a consensus is growing in favor of direct interaction between the ions and the macromolecular solutes.[56] For example, using surface specific sum-frequency spectroscopy, which is limited to planar interfaces, the tendencies of different anions to adsorb at the interface of a positively charged surfactant have been observed to follow the Hofmeister series;[60] a selection of anions is shown below:

(kosmotropes) $Cl^- < NO_3^- < Br^- < I^- < ClO_4^- < SCN^-$ (chaotropes)

In the present work, we use DTAB as a micellar surfactant, having a positively charged head group, in conjunction with an anionic vibrational probe (SCN^-), which is on the extreme chaotropic end of the Hofmeister series. The anion would be expected to localize preferentially at the surfactant-water interface of cationic micelles, making it an interface selective probe capable of sensing local dynamics. If it can be established that the probe localizes near the head group region, it should be possible to access primarily interfacial dynamics at any micelle size, and hence yield measurements that are independent of the micelle curvature. When studying water directly, micelle size controls the relative fractions of interface and bulk water, as well as the micelle curvature. Provided the SCN^- associates with the interfacial region, we can expect little contribution from bulk-like dynamics,

effectively decoupling the micelle size and curvature from the observed dynamics. Moreover, by using SCN^- in D_2O, the dynamic range of our experiment can be increased by roughly an order of magnitude relative to the OD stretch in D_2O or HOD. There have been various interface-specific experiments observing excess surface concentration of low charge density anions, such as thiocyanate[61] and various halides[62] at the hydrophobic water interfaces. The present work contributes to this long-range research goal of formulating a complete understanding of the nature of interactions at charged interfaces.

2.2. Experimental Methods

2.2.1. Preparation of Reverse and Normal Phase Micelles.

Reverse and normal phase micelles were prepared using DTAB as the surfactant layer between the water and the organic phase. The positive charge on the head group of the surfactant is water exposed in the reverse micelles while the long hydrocarbon tail faces the organic phase. Different size factors (w_0) of reverse micelles were prepared by mixing appropriate concentrations of surfactant and water in an organic phase of dichloromethane (DCM). Water and DCM are inherently immiscible, but addition of the surfactant spontaneously favors self-assembly of reverse micelles which results in a clear one phase solution. The thiocyanate probe in H_2O or D_2O was introduced as NaSCN at a concentration of 125 mM to facilitate improved signal to noise ratio in our 2D-IR spectrometer for the smallest size factor (w_0 = 4), and we kept the SCN^- concentration constant for all larger micelles. Competing ion studies with thiocyanate were also performed using different ratios of counter anions (Cl^- and I^-) which were introduced in addition to the thiocyanate probe inside the water nanopool.

Normal phase micelle samples were prepared by directly dissolving DTAB in an aqueous solution of sodium thiocyanate. The concentration of the probe in water was also kept at 125 mM, which is the same as that used for the reverse micelle experiments. The concentration of surfactant was chosen to be higher than the critical micelle concentration[63, 64] to allow spontaneous formation of micelles in water. Micelle samples for study were freshly prepared on the day of the experiments.

2.2.2. NMR Experiments

NMR studies were performed on a 500 MHz Varian spectrometer. 100 mM DTAB samples were prepared in D_2O along with different stoichiometric ratios of thiocyanate. The sample was spin locked using the deuterium peak in D_2O. In another set of separate experiment, sodium salts of different halides along with DTAB were studied to observe selective perturbation due to anions only at the interface of micelles. Proton NMR experiments were averaged over 16 scans and post processed using the standard method of baseline and phase correction to produce absorptive spectra. Peaks were calibrated using the solvent residual peak and integration values were referenced to the most intense trimethylamine protons.

2.3. Results and Discussion

2.3.1. Thiocyanate Probe for Interfacial Hydration Dynamics

A key finding of this study is that the SCN^- anion is tightly associated with the positively charged head group of the surfactant through a specific noncovalent interaction. Attempts to displace SCN^- with competitive anions showed no evidence of freeing the SCN^- from the head groups. A rigorous quantification of this strong head group/SCN^- association has been made using different experimental methods.

Sodium thiocyanate in bulk water shows an intense but broad peak at 2065 cm^{-1} corresponding to the CN stretch mode. Linear FT-IR measurements (**Fig. 2.1**) indicate a

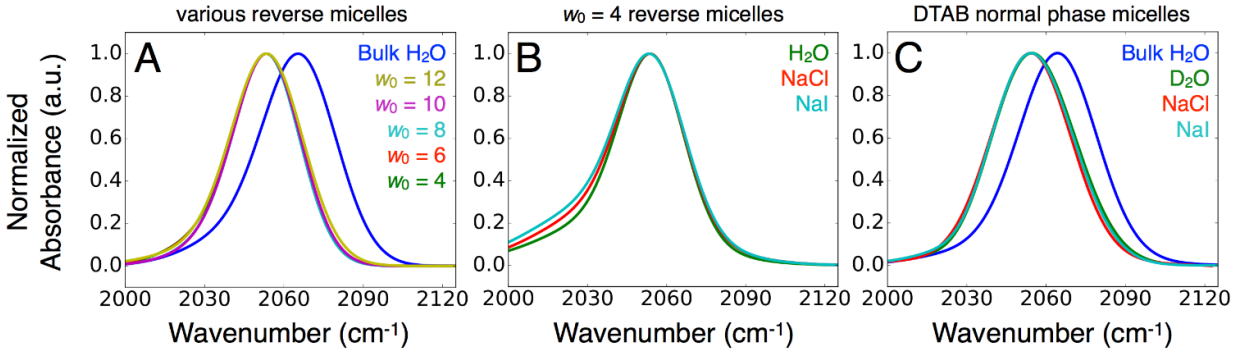

Figure 2.1. (A) Linear FT-IR spectra of the CN stretching mode of thiocyanate in reverse micelles of varying size factors and in bulk water. The CN stretch in reverse micelles is red shifted by 10-12cm^{-1} relative to that in bulk water. (B) FT-IR spectra of thiocyanate in reverse micelles (w_0 = 4, green) and in presence of different competing anions of chloride (red) and iodide (cyan) show that the additional ions result in a growth on the red side of the absorption spectrum. (C) FT-IR spectra of sodium thiocyanate in normal phase micelles shows that addition of competing anions does not alter the thiocyanate absorption spectrum.

pronounced 10-12 cm^{-1} red shift in the vibrational stretching frequency of thiocyanate in

reverse micelles relative to bulk water. Earlier work[1, 3] using the OD stretch of water in reverse micelles also found spectral shifts, where the depletion of hydrogen bonds due to the interface causes a blue shift. For our SCN^- probe, we find a red shift using DFT calculated frequencies in the presence of a bare positive charge as well as near trimethylamine cations with truncated alkane chains, indicating the proximity of our probe to the positively charged surfactant head group (see discussion in the SI). This origin of the red shift is significant because SCN^-, like most CN stretches, blue shifts upon hydrogen bonding.[65, 66] Hence, the observed red shift can arise from a combination of at least two factors: proximity to cations, and the depletion of hydrogen bonds to water.

The CN stretching bands exhibit slight asymmetry on the red side of the spectra. Previous studies using selenocyante as well as thiocyanate attributed the existence of the shoulder to contributions from weak hydrogen bonds in cyanates with water[67, 68] which alters the triple bond character of the CN. Introduction of thiocyanate inside the reverse micelles appears to enhance the red side of the CN stretch mode at 2055 cm^{-1}, and as already noted above, while reduced hydrogen bonding to water in reverse micelles also hints at thiocyanate's proximity to the interface. The position and line width of the thiocyanate band in reverse micelles are insensitive to the encapsulated water radius in size factors ranging from w_0 = 4 to w_0 = 12. At the thiocyanate concentrations used, no distinct distributions corresponding to core and shell regions were observed in our experiments.

Next, we tested the influence of adding different ions to the thiocyanate-probed reverse micelles. **Figure 2.1**(B) shows the FT-IR spectrum of thiocyanate in w_0 = 4 reverse micelles, with and without added chloride or iodide. Introduction of Cl^- or I^- does not alter the stretching frequency mode of thiocyanate in reverse micelles, but we do observe a new feature on the red side (~2020 cm^{-1}) of the main thiocyanate band, which increases proportionally to the concentration of the competing salts. Iodide causes a greater increase in this new band relative to chloride. We can attribute this observation to further breaking of hydrogen bonds when other competing ions are introduced.

In order to eliminate the confinement of reverse micelles, and to significantly alter the interfacial curvature, we investigated normal phase micelles **(Fig. 2.1**(C)**)** at a minimum concentration of 160 mM for the surfactant. A very similar red shift in the CN stretching frequency is observed relative to the bulk water, suggesting that the SCN^- preferentially

associates with the head groups even when the water concentration is very high, and the interfacial curvature apparently has little influence over the CN stretch. The absence of a curvature dependence suggests that, in reverse micelles, the CN stretch frequency would not be expected to exhibit a micelle size dependence. As with the reverse micelle case, the SCN^- vibrational spectrum in normal phase micelles is not substantially altered by adding competitive chloride or iodide anions.

2.3.2. Ultrafast 2D-IR Spectroscopy of SCN^- in Micelles

Considering the evidences from FT-IR indicating strong head group association by SCN^- (**Fig. 2.2**(A)), we turn to 2D-IR spectroscopy to measure vibrational dynamics in several conditions. **Figure 2.2**(B) shows absorptive 2D-IR spectra of the thiocyanate probe in bulk

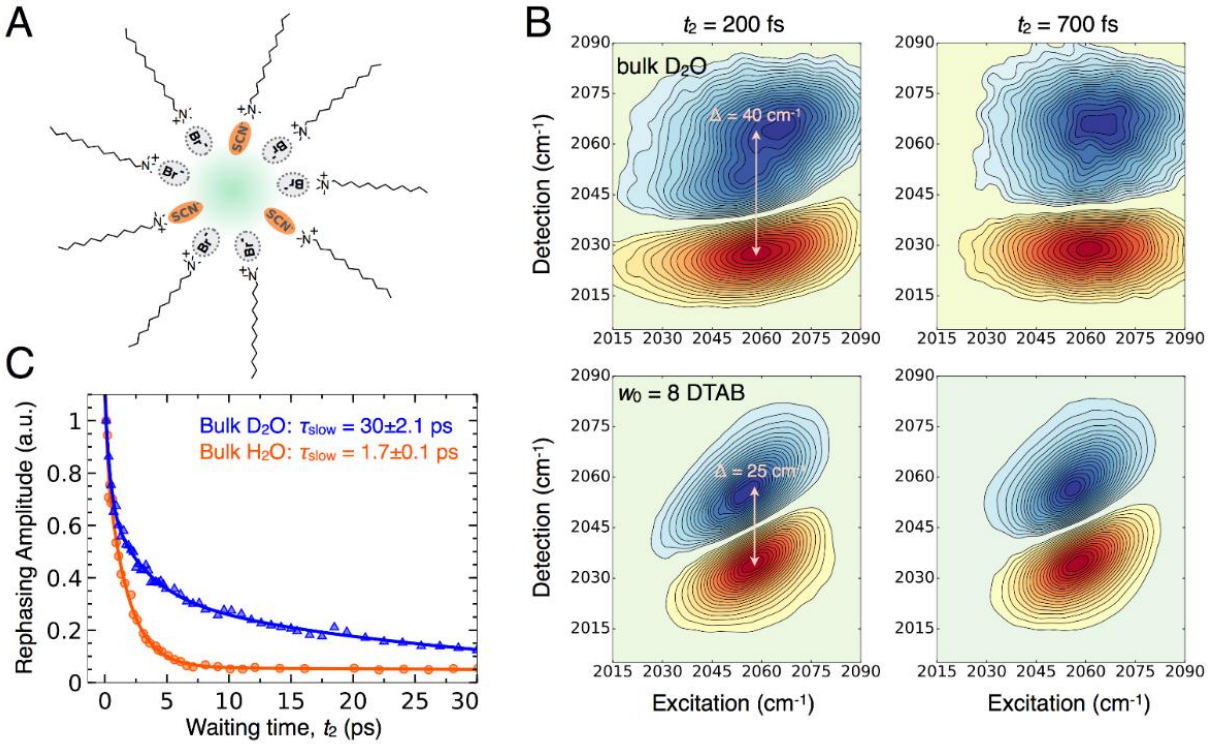

Figure 2.4. (A) Cartoon representation of reverse micelles studied in this work using DTAB as surfactant and thiocyanate anion as a vibrational probe which we find to have preferential association with the positively charged interface of the surfactant. (B) Absorptive 2D-IR spectra of sodium thiocyanate in bulk D_2O and in reverse micelles of w_0 = 8 at early (200 fs) and later (700 fs) waiting times. Diagonal elongation of the peak in reverse micelles persists for much longer that in bulk water indicating slower spectral diffusion. The observed anharmonicity in for thiocyanate in reverse micelles is found to be 25 cm^{-1} while in bulk water it is determined to be 40 cm^{-1}. Perturbation to the vibrational potential suggest proximity of thiocyanate to the charged surfactant interface. (C) Decays of the rephasing amplitudes of thiocyanate using the 0-1 transition in different isotopes of bulk water shows an order of magnitude longer vibrational lifetime for thiocyanate in D_2O compared to that in H_2O. Lifetimes values were obtained via fitting the rephasing data using three exponentials and the longest time constant is reported here.

D_2O and in w_0 = 8 reverse micelles at different waiting times between excitation and

detection. The single CN stretch vibrational mode exhibits a doublet in the 2D-IR spectrum, where the blue peaks are the ground state bleach and stimulated emission at the 0-1 frequency, and the red peaks are excited state absorption from 1-2. The difference between the 0-1 and 1-2 transitions measures the anharmonicity of the potential. In bulk D_2O the anharmonicity is ~40 cm^{-1}, whereas in reverse micelles, the anharmonicity is ~25 cm^{-1}. The substantial 15 cm^{-1} change in anharmonicity indicates perturbation of the vibrational potential which can be attributed to a combination of factors including clustering[33, 69, 70] and proximity to the positively charged interface. Previous studies of thiocyanate in various aqueous solutions show similar results for free SCN^- and SCN^- complexed with cations.[33, 69, 70] Our study, described below, on normal phase micelles suggests that proximity to cations is the dominant factor shaping the vibrational potential of thiocyanate in micelles.

A key observable from 2D-IR spectra is the diagonal elongation of two-dimensional peak shapes at early waiting times, indicating inhomogeneity arising from spectroscopically distinct micro-environments. For thiocyanate in bulk D_2O, the 2D-IR spectra show diagonal elongation at an early waiting time of 200 fs that is promptly lost by 700 fs due fast hydrogen bond fluctuations in the liquid.[71, 72] Similar diagonal elongation also exists at early waiting time for thiocyanate probed inside reverse micelles, but the loss of correlation is clearly much slower

In addition, the anti-diagonal width, which can provide a measure of homogeneous broadening, is significantly reduced relative to the bulk water case. It is noteworthy that the widths of the FT-IR spectra in bulk water and in micelles are very similar, highlighting the limitations of 1D spectroscopy to disentangle the microscopic origins of broadening.

The overall signal amplitude decay is ultimately determined by vibrational relaxation. Fitting the decay of the diagonal band of the rephasing spectrum (**Fig. 2.2**(C)), we can estimate the vibrational lifetimes of SCN^- in D_2O and in H_2O. In our experiments, performing the dynamics measurements in D_2O is preferable due to the order of magnitude longer vibrational lifetime for the CN stretch of the thiocyanate compared to that in H_2O.[38]

2.3.3. Variation in Micelle Size and Curvature

Figure 2.3(A) shows the FFCFs for thiocyanate in reverse and normal phase micelles. Spectral diffusion time constants for thiocyanate in bulk D_2O and H_2O are ~1 ps, reflecting

the bulk water dynamical fluctuations that have been measured using 2D-IR of neat isotope substituted water, as well as numerous probes.[9, 46, 73, 74] Actually, the time scales are slightly faster than bulk water, which reflects the moderately large negative (–0.07) value of the B coefficient for SCN^-, which is similar to I^- (–0.08) and ClO_3^- (–0.08). Laage *et al*. have shown a correlation between the B coefficient and the time scale for hydrogen bond reorientations.[75] Observation of dynamics slower than this bulk water time scale indicates a slowdown due to the interface, which is likely a combination of contributions due to the

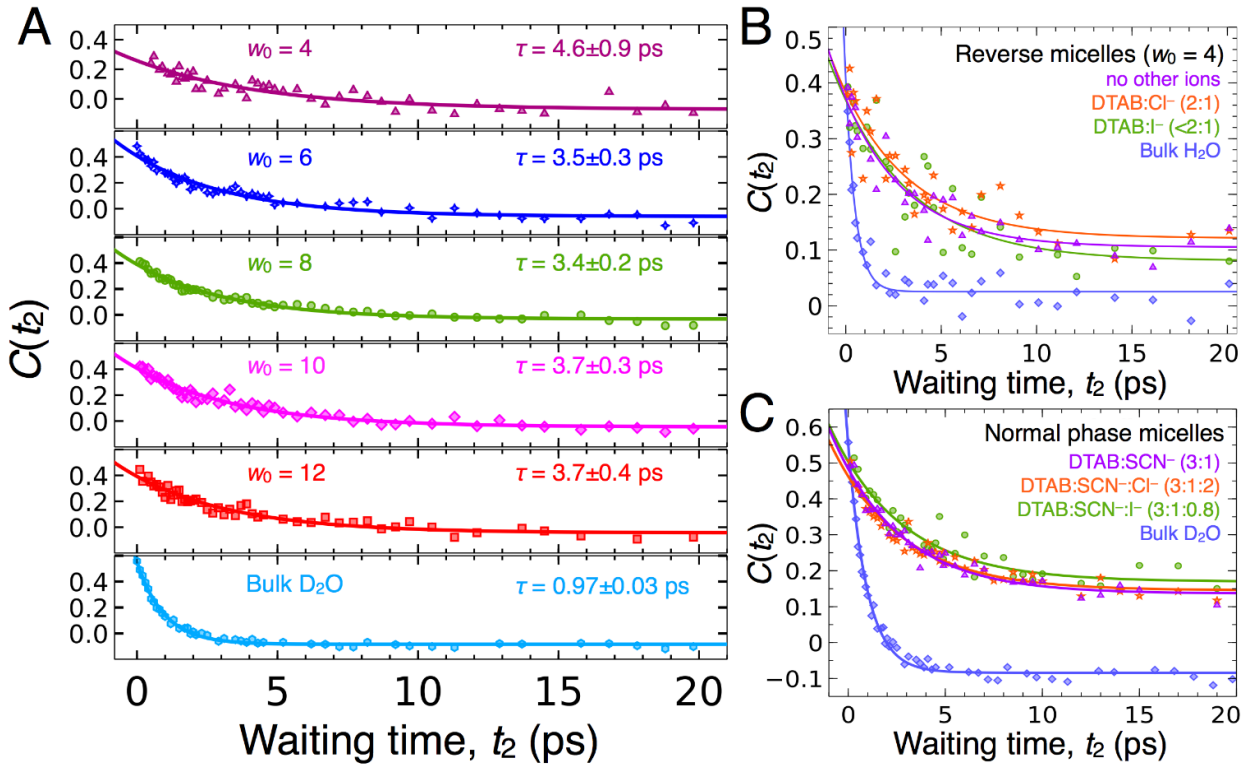

Figure 2.7. (A) Frequency-frequency correlation function, $C(t_2)$ for the CN stretch mode (at 2055 cm^{-1}) in reverse micelles of different size factors up to w_0 = 12. Time constants have been obtained by fitting experimental data to a single exponential function with an offset. Errors reported here are one standard deviation from the fit. The smallest reverse micelles (w_0 = 4) data is prone to scatter due to inherently low signal amplitude. Overall, we find a roughly 3-5 times slowdown compared to bulk water, which is appears to be independent of the size of water nanopool. (B) Comparing FFCF decays for thiocyanate in reverse micelles (w_0 = 4) with and without added chloride and iodide. In H_2O, the spectral diffusion time constant of 0.5 ± 0.07 ps is obtained consistent with bulk water dynamics. The spectral diffusion time constant in w_0 = 4 reverse micelles in H_2O was found to be 3.2 ± 0.5 ps, while in the presence of chloride and iodide the time constants are 3.6 ± 0.9 ps and 3.9 ± 1.1 ps, respectively. Such similar values indicate no displacement of thiocyanate from the interface due to additional anions. (C) The FFCF decay for thiocyanate in normal phase micelles in D_2O with and without the competitive anions again indicates no displacement of the probe from the interface.

hydration water and the surfactant molecules. Within the reverse micelles, which contain bulk as well as interfacial water, the thiocyanate spectral diffusion time constants are greater

than roughly 3.5 ps (in D_2O), with the slowest 4.6±0.9 ps measured in the smallest (w_0 = 4) reverse micelles. We note that in the smallest reverse micelles, the reduced concentration of thiocyanate results in smaller signal amplitude and increased fitting error bars.

To assess the expected contribution of the surfactant dynamics to the observed FFCF decays, we consider previous 2D-IR investigations of 1,2-dioleoyl-*sn*-glycero-3-phosphocholine (DOPC) phospholipid micelles.[6] The phosphate spectral diffusion was found to exhibit one fast (~300 fs) and one slow (>10 ps) time scale. The authors attributed the fast time scale to a wobbling-in-a-cone motion of the head group in the electrostatic field of the charged interface. The much slower time scale was assigned to the very strongly hydrogen bonded water molecules tightly associated with the zwitterionic head groups.

Although the present DTAB and the previous study of DOPC involve different molecules, they share an ammonium cationic moiety in the head group region. Given that our measured spectral diffusion time scales are all roughly 3-5 ps, the most likely explanation for the time scale is that it arises primarily from hydration dynamics. Given an approximate slowdown factor of 3-4 relative to the bulk liquid, the excluded volume mechanism for the suppression of large angular jumps of interfacial water suggests that the thiocyanate and the hydration water it is sensing is buried to some degree within the head group region.[76] For reference, at a flat interface which removes one-half of the water molecules available for hydrogen bond switching, there is a reduction in transition state entropy by a factor of 2, which translates to a two-fold slowdown of hydrogen bond switching events. Here we find a greater magnitude of slowdown, which may reflect large entropy loss.

The penetration of water into the head group region of normal and reverse phase micelles is supported by experimental[60, 77] and simulation evidence.[78-81] Using the technique of Raman multivariate curve resolution on different alkyl chain lengths, Ben-Amotz and co-workers[77] report that the hydrophobic trail region near the trimethylamine cation in normal phase micelles remains significantly hydrated. Given the lower probability that burred water in micelles may form hydrogen bonds, our increased 3-4 fold slowdown suggests contributions from these water molecules. In our previous study of a DOPC interface using a transition metal carbonyl derivatized cholesterol probe, we also found a slightly greater than two-fold slowdown in hydration dynamics.[9]

2.3.4. Addition of Competing Anions

We attempted to alter the dynamics sensed by thiocyanate in reverse micelles by further addition of chloride and iodide ions. **Figure 2.3**(B) shows the spectral diffusion dynamics for thiocyanate in bulk water, reverse micelles (w_0 = 4), and (**Fig. 2.3**(C)) in normal phase micelles with added NaCl or NaI. In our experiments the spectral diffusion time scales of thiocyanate in different isotopes of water was found to be similar, though the substantially reduced lifetime limits the signal to noise ratio. We obtain a spectral diffusion time constant of 3.2±0.5 ps for thiocyanate in reverse micelles when H_2O is used as the polar phase. Similar time constants of 3.6±0.9 ps and 3.9±1.1 ps are obtained for the reverse micelles in the presence of chloride and iodide as competitive anions, respectively. Within fitting error the timescales are not significantly different. Nearly identical spectral diffusion time constants are obtained for normal phase micelles in D_2O (**Fig. 2.3**(C)), irrespective of different competing anions introduced. The spectral diffusion time scale for thiocyanate in normal phase micelles in D_2O is 3.5±0.3 ps. In the presence of chloride and iodide, we find time constants of 3.6±0.4 ps and 3.7±0.6 ps, respectively. Viewed collectively, the data indicate that there is no curvature dependence to the dynamics sensed by the SCN^- probe, which also lends support to the hydration origin, since previous work has found that surfactants fluctuate differently in such different packing conditions.[8]

2.3.5. Comparison with an Anionic Surfactant

The experimental data described above show that adding chloride and iodide, which are less chaotropic than SCN^-, does not influence the spectral diffusion timescales in micelles, suggesting these ions are incapable of displacing thiocyanate from the charged interface. To test the role of the cationic head group, we carried out experiments in normal phase micelles containing two different surfactants, DTAB and SDS. DTAB contains a trimethylammonium cation as a headgroup, while SDS contains an anionic sulfate headgroup. **Figure 2.4**(A) shows the FT-IR spectrum of thiocyanate in bulk D_2O and in normal phase micelles. Compared with the red shift found in the DTAB micelle case, SCN^- in the presence of SDS micelles is indistinguishable from bulk D_2O. We observe the same trend using 2D-IR (**Fig. 2.4**(B)), where the spectral diffusion found for thiocyanate in SDS micelles is consistent with bulk water dynamics. This finding is perhaps not particularly surprising since we do not

expect the SCN^- to associate with the anionic headgroup of SDS. A recent study of AOT reverse micelles, which have the same sulfate headgroup as SDS, reported slow (12-13 ps)

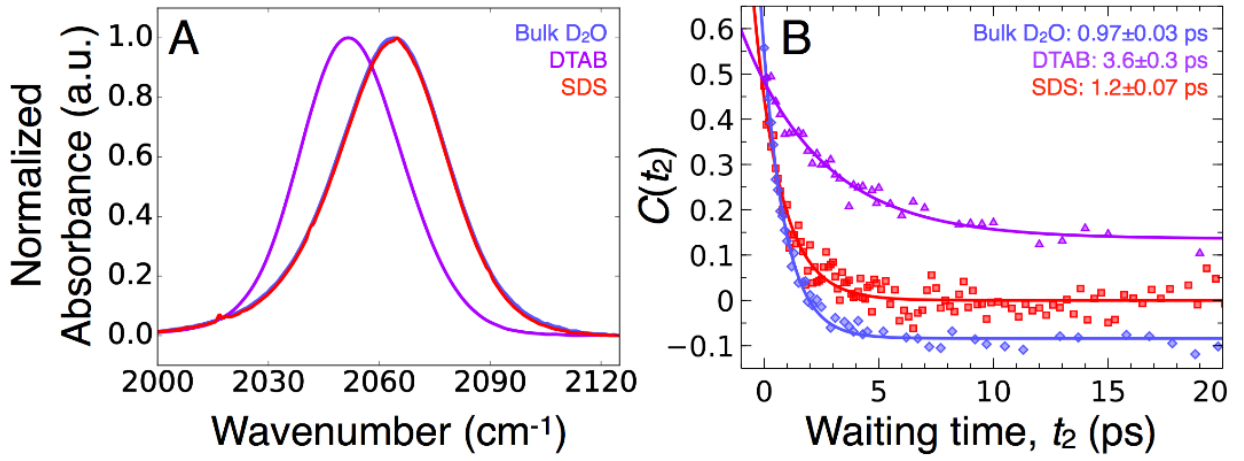

Figure 2.10. (A) FT-IR spectrum for thiocyanate in bulk water, in regular micelles using DTAB as surfactant and in regular micelles again with SDS as surfactant. The CN stretching frequency for thiocyanate appears at 2055 cm^{-1} when DTAB is used. When sodium dodecyl sulfate (SDS) as surfactant is used, which has a negatively charged headgroup, the CN stretch is consistent with bulk water environment. (B) 2D-IR FFCFs comparing the dynamics of thiocyanate in bulk D_2O and surfactants containing positive (DTAB) and negative (SDS) headgroups. Spectral dynamics for thiocyanate in SDS are consistent with bulk D_2O indicating that the probe is displaced from the interface of the surfactant. Experimental data points have been fitted to single exponentials with an offset. For the SDS case the offset has been set to zero for comparison.

orientational dynamics and spectral diffusion of an anionic SeCN probe.[82] Motived by the recent study using selenocyanate in large reverse micelles ($w_0 \geq 16$)[82] probing the interfacial boundary layer water, we also attempted to fit of our spectral diffusion data for thiocyanate in SDS normal phase micelles using a bi-exponential function. The longest time constant that we could obtain was 1.67±0.76 ps, which is within the uncertainty of the fits, suggesting the contribution is exclusively from bulk water. The missing slow phase of spectral diffusion likely reflects both the absence of confinement induced slowdown in normal phase micelles as well as a lack of interaction with the headgroups.

2.3.6. Structural Characterization of DTAB Surfactant Using ^1H NMR

To understand the specific interaction of the SCN^- vibrational probe with surfactant head groups, we also carried out proton NMR experiments to characterize perturbations to surfactant molecule chemical shifts. Normal phase micelles in D_2O were studied using ^1H NMR in the presence of a series of SCN^- concentrations (**Fig. 2.5**). Protons in the alkyl tail of the surfactant show chemical shifts consistent with other alkanes around 2 ppm. Protons attached to the primary and secondary carbons connected to the quaternary amine of the

headgroup experiences significant deshielding, shifting them further downfield to around 3 ppm. Spectrum prediction algorithms used to assign protons in the surfactant molecule agree with assignments based on peak integration values.

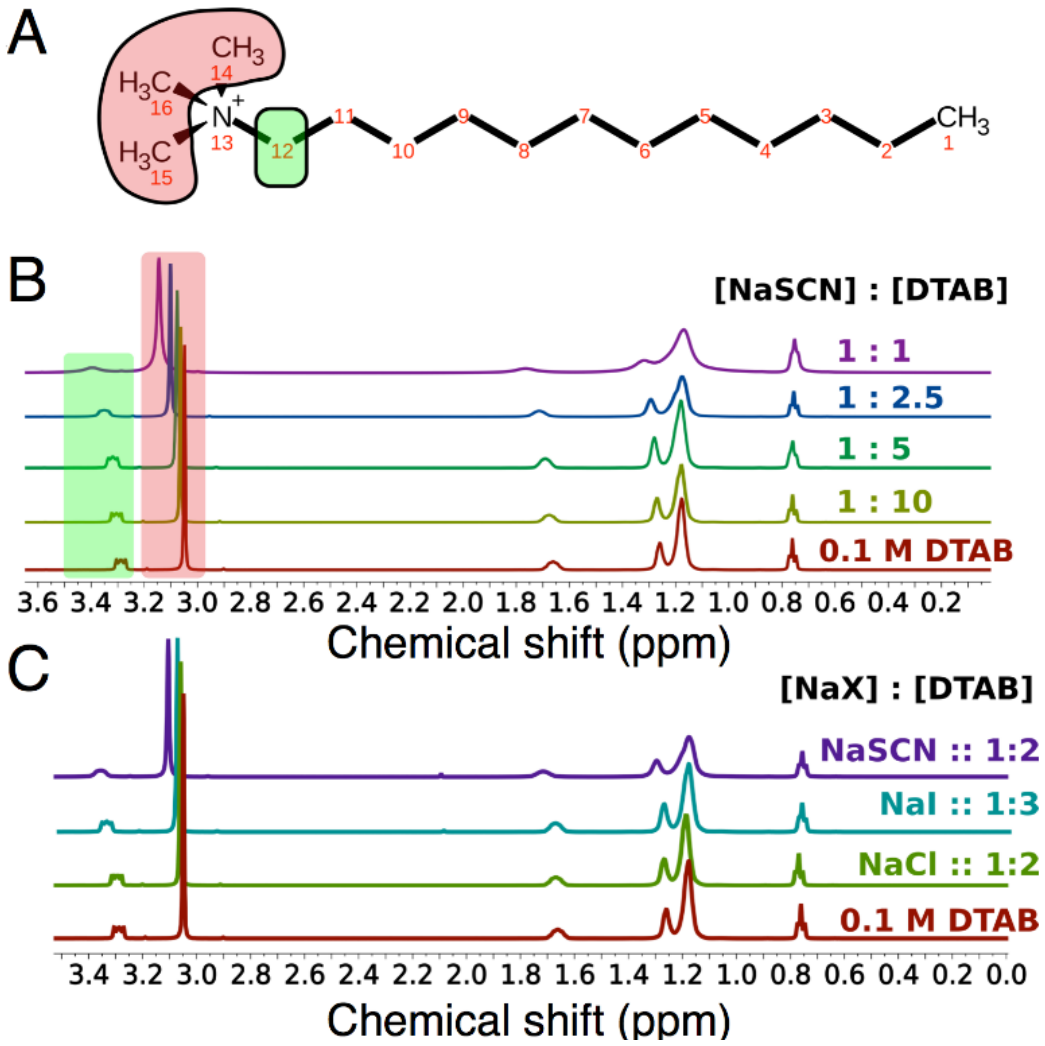

Figure 2.13. (A) Molecular structure of the DTAB surfactant used in this study for preparing micelles. Protons attached to the trimethylamine headgroup and adjacent carbon is highlighted in red and green. (B) ^{1}H NMR spectrum of DTAB only and in presence of different sodium thiocyanate concentrations in D_2O. Each peak in the spectrum corresponds to specific protons in the surfactant molecule. Highlighted peaks correspond to protons at (red) or near (green) the surfactant headgroup. Integration values and a spectrum prediction algorithm have been used to perform assignments. Increasing the ratio of sodium thiocyanate to DTAB concentration correlates with perturbation of the headgroup protons. (C) Proton NMR spectra for the regular micelles as in (B) but here studied by varying the identity of counter anions. The ratio of salt to surfactant is kept constant with iodide being the exception because iodide tends to cause precipitation of the micellar self-assembly. Increasing perturbation to the head group protons in DTAB clearly follows the chaotropicity ordering of chloride, iodide and thiocyanate in the Hofmeister series.

Figure 2.5(B) shows proton NMR spectra for a titration experiment performed using varying amounts of NaSCN relative to surfactant in normal phase micelles. Thiocyanate-to-surfactant ratios in the range 1-10 were chosen to cover the concentration ratios in our FT-

IR and 2D-IR experiments. Protons attached to the headgroup carbon (atoms labeled as 12, 14, 15 and 16) which appear at >3 ppm exhibit the greatest perturbation due to addition of sodium thiocyanate. The shifts are also dependent on the concentration of the thiocyanate added, which is consistent with direct interaction with the headgroup protons. Marginal shifts are observed for protons buried slightly into the non-polar trail of the surfactant (carbon labeled 11), and these perturbations also correlate with thiocyanate concentration. Along with the chemical shift perturbations for the protons attached to the headgroup surfactant, the spectral bands of those protons are also broadened with increased concentration of thiocyanate. For DTAB solution with the highest concentration of thiocyanate, due to salting-in effects, the sample solution had a viscous appearance. The viscosity increase as a function of thiocyanate concentration appears to be responsible for slower tumbling of the surfactant mixture in D_2O, resulting in a broadening of the linewidth as a function of increasing thiocyanate concentration. More characterization of solution viscosity with concentration of thiocyanate and different identity of salts is needed to provide insight into the complex salt-water-surfactant interaction. These NMR results support both the conclusion that SCN^- associates directly with the head groups and that the ions are slightly buried.

Figure 2.5(C) shows the proton NMR spectra for the surfactant alone and in the presence of different anions of sodium salts (NaSCN, NaCl, and NaI). The ratio of anion to surfactant was kept consistent with the only exception of iodide, which was kept at lower concentration to prevent breaking of the micellar self-assembly. The perturbation to the headgroup protons in this case occurs in the order of $Cl^- < I^- < SCN^-$, which follows the ordering of chaotropicity in the Hofmeister series, and can be linked to the surface adsorbability of those anions studied using surface-specific nonlinear spectroscopy.[60] The inability of chloride and iodide to displace thiocyanate from the cationic head group region supports the direct association view of the Hofmeister effect for ion pairing. By taking advantage of the strong preference for SCN^-/cation interactions, the strong IR transition and long-lived vibrational excitation holds great promise as an interface-specific probe of cationic membranes.

2.4. Conclusion

The SCN^- vibrational probe preferentially associates with the cationic headgroups of DTAB reverse and normal phase micelles, yielding very similar dynamical timescales regardless of the reverse micelle size factor or even the sign of the surface curvature. The 3-4-fold factor of dynamical slowdown suggests the probe is buried to some extent within the headgroup region, and that the water responsible for the spectral diffusion is more depleted of potential hydrogen bonding partners than would be expected for a simple flat interface. The SCN^- is so strongly associated with the trimethylammonium headgroups that it cannot be dislodged by either Cl^- or I^- competitors, which is consistent with the Hofmeister ordering, but highlights the magnitude of the direct interaction between SCN^- and the headgroups. NMR chemical shift perturbation measurements show that the SCN^- alters the environment of the headgroup as well as the first carbon in the alkyl chain of the surfactant, indicating some degree of embedding within the membrane. Despite this partially buried location, the 2D-IR spectral diffusion measurements show that a 3-4 ps time scale dominates, suggesting the SCN^- probe is primarily sensitive to hydration dynamics rather than the slower motions of the surfactants, at least within the accessible dynamical window. This work offers the promise of leveraging the very strong SCN^-/cation interaction to probe biomolecule interfaces even under realistic conditions where there are competing ions. Biological membranes, for the most part, are anionic, so an anionic probe such as SCN^- would not likely exhibit the exact same degree of association with a real biological membrane. Nevertheless, many of the lipids in biomembranes are zwitterionic, and a key cell membrane component is phosphatidylcholine (PC), for which the cationic part is the same trimethyl ammonium moiety found in DTAB. If the association of the SCN^- with the cationic part is not neutralized by the presence of the anionic phosphate, we would expect SCN^- to be a probe of more realistic biological membranes. Indeed, at elevated concentrations, SCN^- is known to interact with zwitterionic lipids, altering the solvent-solute and solvation environments.[83-87] Hence, it is likely that SCN^- can serve as a power probe of reconstituted biological membranes.

2.5. References

1. Fayer, M. D.; Levinger, N. E., Analysis of Water in Confined Geometries and at Interfaces. *Annu. Rev. Anal. Chem.* **2010,** *3*, 89-107.
2. Fenn, E. E.; Wong, D. B.; Giammanco, C. H.; Fayer, M. D., Dynamics of Water at the Interface in Reverse Micelles: Measurements of Spectral Diffusion with Two-Dimensional Infrared Vibrational Echoes. *J. Phys. Chem. B* **2011,** *115* (40), 11658-11670.
3. Moilanen, D. E.; Fenn, E. E.; Wong, D.; Fayer, M. D., Geometry and Nanolength Scales Versus Interface Interactions: Water Dynamics in AOT Lamellar Structures and Reverse Micelles. *J. Am. Chem. Soc.* **2009,** *131* (23), 8318-8328.
4. Piletic, I. R.; Tan, H. S.; Fayer, M. D., Dynamics of Nanoscopic Water: Vibrational Echo and Infrared Pump-Probe Studies of Reverse Micelles. *J. Phys. Chem. B* **2005,** *109* (45), 21273-21284.
5. Costard, R.; Levinger, N. E.; Nibbering, E. T. J.; Elsaesser, T., Ultrafast Vibrational Dynamics of Water Confined in Phospholipid Reverse Micelles. *J. Phys. Chem. B* **2012,** *116* (19), 5752-5759.
6. Costard, R.; Heisler, I. A.; Elsaesser, T., Structural Dynamics of Hydrated Phospholipid Surfaces Probed by Ultrafast 2D Spectroscopy of Phosphate Vibrations. *J. Phys. Chem. Lett.* **2014,** *5* (3), 506-511.
7. Stevenson, P.; Tokmakoff, A., Ultrafast Fluctuations of High Amplitude Electric Fields in Lipid Membranes. *J. Am. Chem. Soc.* **2017,** *139* (13), 4743-4752.
8. Kel, O.; Tamimi, A.; Fayer, M. D., Size-dependent Ultrafast Structural Dynamics Inside Phospholipid Vesicle Bilayers Measured with 2D IR Vibrational Echoes. *Proc. Natl. Acad. Sci. U. S. A.* **2014,** *111* (3), 918-923.
9. Osborne, D. G.; Dunbar, J. A.; Lapping, J. G.; White, A. M.; Kubarych, K. J., Site-specific Measurements of Lipid Membrane Interfacial Water Dynamics with Multidimensional Infrared Spectroscopy. *J. Phys. Chem. B* **2013,** *117* (49), 15407-15414.
10. Kundu, A.; Verma, P. K.; Ha, J. H.; Cho, M., Studying Water Hydrogen-Bonding Network Near the Lipid Multibilayer with Multiple IR Probes. *J. Phys. Chem. A* **2017,** *121* (7), 1435-1441.
11. Laage, D.; Hynes, J. T., A Molecular Jump Mechanism of Water Reorientation. *Science* **2006,** *311* (5762), 832-835.
12. Fenimore, P. W.; Frauenfelder, H.; McMahon, B. H.; Parak, F. G., Slaving: Solvent Fluctuations Dominate Protein Dynamics and Functions. *Proc. Natl. Acad. Sci. U. S. A.* **2002,** *99* (25), 16047-16051.
13. Williams, G., Use of Dipole Correlation-Function in Dielectric-Relaxation. *Chem. Rev.* **1972,** *72* (1), 55-69.
14. Laage, D.; Elsaesser, T.; Hynes, J. T., Water Dynamics in the Hydration Shells of Biomolecules. *Chem. Rev.* **2017,** *117* (16), 10694-10725.
15. Setny, P.; Baron, R.; Michael Kekenes-Huskey, P.; McCammon, J. A.; Dzubiella, J., Solvent Fluctuations in Hydrophobic Cavity-ligand Binding Kinetics. *Proc. Natl. Acad. Sci. U. S. A.* **2013,** *110* (4), 1197-1202.
16. Guha, S.; Sahu, K.; Roy, D.; Mondal, S. K.; Roy, S.; Bhattacharyya, K., Slow Solvation Dynamics at the Active Site of an Enzyme: Implications for Catalysis. *Biochemistry* **2005,** *44* (25), 8940-8947.
17. Silva, J. L.; Vieira, T. C.; Gomes, M. P.; Bom, A. P.; Lima, L. M.; Freitas, M. S.; Ishimaru, D.;

Cordeiro, Y.; Foguel, D., Ligand Binding and Hydration in Protein Misfolding: Insights from Studies of Prion and p53 Tumor Suppressor Proteins. *Acc. Chem. Res.* **2010,** *43* (2), 271-279.
18. Szyc, L.; Yang, M.; Nibbering, E. T.; Elsaesser, T., Ultrafast Vibrational Dynamics and Local Interactions of Hydrated DNA. *Angew. Chem., Int. Ed.* **2010,** *49* (21), 3598-3610.
19. Garczarek, F.; Gerwert, K., Functional Waters in Intraprotein Proton Transfer Monitored by FTIR Difference Spectroscopy. *Nature* **2006,** *439* (7072), 109-112.
20. Mrazkova, E.; Hobza, P.; Bohl, M.; Gauger, D. R.; Pohle, W., Hydration-induced Changes of Structure and Vibrational Frequencies of Methylphosphocholine Studied as a Model of Biomembrane Lipids. *J. Phys. Chem. B* **2005,** *109* (31), 15126-15134.
21. Dutta, P.; Sen, P.; Haider, A.; Mukherjee, S.; Sen, S.; Bhattacharyya, K., Solvation Dynamics in a Protein-surfactant Complex. *Chem. Phys. Lett.* **2003,** *377* (1-2), 229-235.
22. Sasmal, D. K.; Ghosh, S.; Das, A. K.; Bhattacharyya, K., Solvation Dynamics of Biological Water in a Single Live Cell under a Confocal Microscope. *Langmuir* **2013,** *29* (7), 2289-2298.
23. Martin, D. R.; Matyushov, D. V., Dipolar Nanodomains in Protein Hydration Shells. *J. Phys. Chem. Lett.* **2015,** *6* (3), 407-412.
24. Ebbinghaus, S.; Kim, S. J.; Heyden, M.; Yu, X.; Heugen, U.; Gruebele, M.; Leitner, D. M.; Havenith, M., An Extended Dynamical Hydration Shell around Proteins. *Proc. Natl. Acad. Sci. U. S. A.* **2007,** *104* (52), 20749-20752.
25. King, J. T.; Arthur, E. J.; Brooks, C. L., 3rd; Kubarych, K. J., Crowding Induced Collective Hydration of Biological Macromolecules over Extended Distances. *J. Am. Chem. Soc.* **2014,** *136* (1), 188-194.
26. Novelli, F.; Pour, S. O.; Tollerud, J.; Roozbeh, A.; Appadoo, D. R. T.; Blanch, E. W.; Davis, J. A., Time-Domain THz Spectroscopy Reveals Coupled Protein−Hydration Dielectric Response in Solutions of Native and Fibrils of Human Lysozyme. *J. Phys. Chem. B* **2017,** *121* (18), 4810-4816.
27. Shen, Y. N.; Wu, T. M.; Jiang, B.; Deng, G. H.; Li, J. B.; Chen, H. L.; Guo, X. M.; Ge, C. Q.; Chen, Y. J.; Hong, J. Y.; Yang, X. M.; Yuan, K. J.; Zhuang, W.; Zheng, J. R., Comparison Studies on Sub-Nanometer-Sized Ion Clusters in Aqueous Solutions: Vibrational Energy Transfers, MD Simulations, and Neutron Scattering. *J. Phys. Chem. B* **2015,** *119* (30), 9893-9904.
28. Li, J. B.; Bian, H. T.; Chen, H. L.; Wen, X. W.; Hoang, B. T.; Zheng, J. R., Ion Association in Aqueous Solutions Probed through Vibrational Energy Transfers among Cation, Anion, and Water Molecules. *J. Phys. Chem. B* **2013,** *117* (16), 4274-4283.
29. Chen, H. L.; Zhang, Q.; Guo, X. M.; Wen, X. W.; Li, J. B.; Zhuang, W.; Zheng, J. R., Nonresonant Energy Transfers Independent on the Phonon Densities in Polyatomic Liquids. *J. Phys. Chem. A* **2015,** *119* (4), 669-680.
30. Chen, H. L.; Wen, X. W.; Li, J. B.; Zheng, J. R., Molecular Distances Determined with Resonant Vibrational Energy Transfers. *J. Phys. Chem. A* **2014,** *118* (13), 2463-2469.
31. Chen, H. L.; Wen, X. W.; Guo, X. M.; Zheng, J. R., Intermolecular Vibrational Energy Transfers in Liquids and Solids. *Phys. Chem. Chem. Phys.* **2014,** *16* (27), 13995-14014.
32. Bian, H. T.; Wen, X. W.; Li, J. B.; Chen, H. L.; Han, S. Z.; Sun, X. Q.; Song, J. A.; Zhuang, W.; Zheng, J. R., Ion Clustering in Aqueous Solutions Probed with Vibrational Energy Transfer. *Proc. Natl. Acad. Sci. U. S. A.* **2011,** *108* (12), 4737-4742.
33. Bian, H.; Chen, H.; Zhang, Q.; Li, J.; Wen, X.; Zhuang, W.; Zheng, J., Cation Effects on Rotational Dynamics of Anions and Water Molecules in Alkali (Li^+, Na^+, K^+, Cs^+) Thiocyanate (SCN^-) Aqueous Solutions. *J. Phys. Chem. B* **2013,** *117* (26), 7972-7984.
34. Camardo, M.; D'Angelo, M.; Mannaioli, S.; Onori, G.; Santucci, A., Effect of Surfactant

Counterion on Spectroscopic Properties of Water in Oil Microemulsions. *Colloids Surf., A* **1996,** *119* (2-3), 183-187.
35. Bardez, E.; Vy, N. C.; Zemb, T., Counterion-driven Sphere to Cylinder Transition in Reverse Micelles: A Small Angle X-ray Scattering and Conductometric Study. *Langmuir* **1995,** *11* (9), 3374-3381.
36. Moilanen, D.; Fenn, E.; Wong, D.; Fayer, M., Water Dynamics in Large and Small Reverse Micelles: From Two Ensembles to Collective Behavior. *J. Chem. Phys.* **2009,** *131* (1), 014704.
37. Martinez, A. V.; Dominguez, L.; Malolepsza, E.; Moser, A.; Ziegler, Z.; Straub, J. E., Probing the Structure and Dynamics of Confined Water in AOT Reverse Micelles. *J. Phys. Chem. B* **2013,** *117* (24), 7345-7351.
38. Czurlok, D.; Gleim, J.; Lindner, J.; Vohringer, P., Vibrational Energy Relaxation of Thiocyanate Ions in Liquid-to-Supercritical Light and Heavy Water. A Fermi's Golden Rule Analysis. *J. Phys. Chem. Lett.* **2014,** *5* (19), 3373-3379.
39. Kuo, C.; Hochstrasser, R., Two Dimensional Infrared Spectroscopy and Relaxation of Aqueous Cyanide. *Chem. Phys.* **2007,** *341* (1-3), 21-28.
40. Heilweil, E.; Doany, F.; Moore, R.; Hochstrasser, R., Vibrational-Energy Relaxation of the Cyanide Ion in Aqueous Solution. *J. Chem. Phys.* **1982,** *76* (11), 5632-5634.
41. Hamm, P.; Lim, M.; Hochstrasser, R., Vibrational Energy Relaxation of the Cyanide Ion in Water. *J. Chem. Phys.* **1997,** *107* (24), 10523-10531.
42. Zhong, Q.; Baronavski, A. P.; Owrutsky, J. C., Vibrational Energy Relaxation of Aqueous Azide Ion Confined in Reverse Micelles. *J. Chem. Phys.* **2003,** *118* (15), 7074-7080.
43. Zhong, Q.; Baronavski, A. P.; Owrutsky, J. C., Reorientation and Vibrational Energy Relaxation of Pseudohalide Ions Confined in Reverse Micelle Water Pools. *J. Chem. Phys.* **2003,** *119* (17), 9171-9177.
44. Singh, P. K.; Kuroda, D. G.; Hochstrasser, R. M., An Ion's Perspective on the Molecular Motions of Nanoconfined Water: A Two-Dimensional Infrared Spectroscopy Study. *J. Phys. Chem. B* **2013,** *117* (33), 9775-9784.
45. Nibbering, E.; Fidder, H.; Pines, E., Ultrafast Chemistry: Using Time-Resolved Vibrational Spectroscopy for Interrogation of Structural Dynamics. *Annu. Rev. Phys. Chem.* **2005,** *56*, 337-367.
46. King, J. T.; Kubarych, K. J., Site-specific Coupling of Hydration Water and Protein Flexibility Studied in Solution with Ultrafast 2D-IR Spectroscopy. *J. Am. Chem. Soc.* **2012,** *134* (45), 18705-18712.
47. King, J. T.; Arthur, E. J.; Brooks, C. L., 3rd; Kubarych, K. J., Site-specific Hydration Dynamics of Globular Proteins and the Role of Constrained Water in Solvent Exchange with Amphiphilic Cosolvents. *J. Phys. Chem. B* **2012,** *116* (19), 5604-5611.
48. King, J. T.; Baiz, C. R.; Kubarych, K. J., Solvent-Dependent Spectral Diffusion in a Hydrogen Bonded "Vibrational Aggregate". *J. Phys. Chem. A* **2010,** *114* (39), 10590-10604.
49. Ashihara, S.; Huse, N.; Espagne, A.; Nibbering, E.; Elsaesser, T., Ultrafast Structural Dynamics of Water Induced by Dissipation of Vibrational Energy. *J. Phys. Chem. A* **2007,** *111* (5), 743-746.
50. Ramasesha, K.; De Marco, L.; Horning, A. D.; Mandal, A.; Tokmakoff, A., A Phenomenological Approach to Modeling Chemical Dynamics in Nonlinear and Two-Dimensional Spectroscopy. *J. Chem. Phys.* **2012,** *136* (13), 134507.
51. Perakis, F.; Hamm, P., Two-Dimensional Infrared Spectroscopy of Supercooled Water. *J. Phys. Chem. B* **2011,** *115* (18), 5289-5293.

52. Piletic, I.; Gaffney, K.; Fayer, M., Structural Dynamics of Hydrogen Bonded Methanol Oligomers: Vibrational Transient Hole Burning Studies of Spectral Diffusion. *J. Chem. Phys.* **2003,** *119* (1), 423-434.
53. Kiefer, L. M.; Kubarych, K. J., Solvent-Dependent Dynamics of a Series of Rhenium Photoactivated Catalysts Measured with Ultrafast 2DIR. *J. Phys. Chem. A* **2015,** *119* (6), 959-65.
54. Kiefer, L. M.; King, J. T.; Kubarych, K. J., Dynamics of Rhenium Photocatalysts Revealed through Ultrafast Multidimensional Spectroscopy. *Acc. Chem. Res.* **2015,** *48* (4), 1123-1130.
55. Kiefer, L. M.; King, J. T.; Kubarych, K. J., Equilibrium Excited State Dynamics of a Photoactivated Catalyst Measured with Ultrafast Transient 2DIR. *J. Phys. Chem. A* **2014,** *118* (42), 9853-9860.
56. Zhang, Y.; Cremer, P. S., Interactions Between Macromolecules and Ions: The Hofmeister Series. *Curr. Opin. Chem. Biol.* **2006,** *10* (6), 658-663.
57. Collins, K. D.; Washabaugh, M. W., The Hofmeister Effect and the Behavior of Water at Interfaces. *Q. Rev. Biophys.* **1985,** *18* (4), 323-422.
58. Kunz, W.; Lo Nostro, P.; Ninham, B. W., The Present State of Affairs with Hofmeister Effects. *Curr. Opin. Colloid Interface Sci.* **2004,** *9* (1-2), 1-18.
59. Schwierz, N.; Horinek, D.; Sivan, U.; Netz, R. R., Reversed Hofmeister Series-The Rule Rather than the Exception. *Curr. Opin. Colloid Interface Sci.* **2016,** *23*, 10-18.
60. Nihonyanagi, S.; Yamaguchi, S.; Tahara, T., Counterion Effect on Interfacial Water at Charged Interfaces and its Relevance to the Hofmeister Series. *J. Am. Chem. Soc.* **2014,** *136* (17), 6155-6158.
61. Onorato, R. M.; Otten, D. E.; Saykally, R. J., Adsorption of Thiocyanate Ions to the Dodecanol/water Interface Characterized by UV Second Harmonic Generation. *Proc. Natl. Acad. Sci. U. S. A.* **2009,** *106* (36), 15176-15180.
62. Rankin, B. M.; Hands, M. D.; Wilcox, D. S.; Fega, K. R.; Slipchenko, L. V.; Ben-Amotz, D., Interactions Between Halide Anions and a Molecular Hydrophobic Interface. *Faraday Discuss.* **2013,** *160*, 255-270.
63. Silber, J. J.; Biasutti, A.; Abuin, E.; Lissi, E., Interactions of Small Molecules with Reverse Micelles. *Adv. Colloid Interface Sci.* **1999,** *82* (1-3), 189-252.
64. Rodenas, E.; Dolcet, C.; Valiente, M.; Valeron, E. C., Physical Properties of Dodecyltrimethylammonium Bromide (DTAB) Micelles in Aqueous Solution and Their Behavior as the Reaction Medium. *Langmuir* **1994,** *10* (7), 2088-2094.
65. Oh, K. I.; Choi, J. H.; Lee, J. H.; Han, J. B.; Lee, H.; Cho, M., Nitrile and Thiocyanate IR Probes: Molecular Dynamics Simulation Studies. *J. Chem. Phys.* **2008,** *128* (15), 154504.
66. Choi, J.-H.; Oh, K.-I.; Lee, H.; Lee, C.; Cho, M., Nitrile and Thiocyanate IR Probes: Quantum Chemistry Calculation Studies and Multivariate Least-Square Fitting Analysis. *J. Chem. Phys.* **2008,** *128* (13), 134506.
67. Yuan, R.; Yan, C.; Tamimi, A.; Fayer, M. D., Molecular Anion Hydrogen Bonding Dynamics in Aqueous Solution. *J. Phys. Chem. B* **2015,** *119* (42), 13407-13415.
68. Okuda, M.; Ohta, K.; Tominaga, K., Comparison of Vibrational Dynamics Between Non-ionic and Ionic Vibrational Probes in Water: Experimental Study with Two-Dimensional Infrared and infrared Pump-Probe Spectroscopies. *J. Chem. Phys.* **2016,** *145* (11), 114503.
69. Park, S.; Ji, M.; Gaffney, K. J., Ligand Exchange Dynamics in Aqueous Solution Studied with 2DIR Spectroscopy. *J. Phys. Chem. B* **2010,** *114* (19), 6693-6702.
70. Kiefer, L. M.; Kubarych, K. J., NOESY-Like 2D-IR Spectroscopy Reveals Non-Gaussian

Dynamics. *J. Phys. Chem. Lett.* **2016,** *7* (19), 3819-3824.
71. Roberts, S. T.; Ramasesha, K.; Tokmakoff, A., Structural Rearrangements in Water Viewed Through Two-Dimensional Infrared Spectroscopy. *Acc. Chem. Res.* **2009,** *42* (9), 1239-1249.
72. Elsaesser, T., Two-dimensional infrared spectroscopy of intermolecular hydrogen bonds in the condensed phase. *Acc. Chem. Res.* **2009,** *42*, 1220-1228.
73. King, J. T.; Ross, M. R.; Kubarych, K. J., Water-assisted Vibrational Relaxation of a Metal Carbonyl Complex Studied with Ultrafast 2D-IR. *J. Phys. Chem. B* **2012,** *116* (12), 3754-3759.
74. Brookes, J. F.; Slenkamp, K. M.; Lynch, M. S.; Khalil, M., Effect of Solvent Polarity on the Vibrational Dephasing Dynamics of the Nitrosyl Stretch in an Fe-II Complex Revealed by 2D IR Spectroscopy. *J. Phys. Chem. A* **2013,** *117* (29), 6234-6243.
75. Boisson, J.; Stirnemann, G.; Laage, D.; Hynes, J. T., Water Reorientation Dynamics in the First Hydration Shells of F^- and I^-. *Phys. Chem. Chem. Phys.* **2011,** *13* (44), 19895-19901.
76. Laage, D.; Stirnemann, G.; Hynes, J. T., Why Water Reorientation Slows without Iceberg Formation around Hydrophobic Solutes. *J. Phys. Chem. B* **2009,** *113* (8), 2428-2435.
77. Long, J. A.; Rankin, B. M.; Ben-Amotz, D., Micelle Structure and Hydrophobic Hydration. *J. Am. Chem. Soc.* **2015,** *137* (33), 10809-10815.
78. Goh, G. B.; Eike, D. M.; Murch, B. P.; Brooks, C. L., 3rd, Accurate Modeling of Ionic Surfactants at High Concentration. *J. Phys. Chem. B* **2015,** *119* (20), 6217-6224.
79. Skinner, J. L.; Pieniazek, P. A.; Gruenbaum, S. M., Vibrational Spectroscopy of Water at Interfaces. *Acc. Chem. Res.* **2012,** *45* (1), 93-100.
80. Tang, X. M.; Koenig, P. H.; Larson, R. G., Molecular Dynamics Simulations of Sodium Dodecyl Sulfate Micelles in Water-The Effect of the Force Field. *J. Phys. Chem. B* **2014,** *118* (14), 3864-3880.
81. Aoun, B.; Sharma, V. K.; Pellegrini, E.; Mitra, S.; Johnson, M.; Mukhopadhyay, R., Structure and Dynamics of Ionic Micelles: MD Simulation and Neutron Scattering Study. *J. Phys. Chem. B* **2015,** *119* (15), 5079-5086.
82. Yuan, R.; Yan, C.; Nishida, J.; Fayer, M. D., Dynamics in a Water Interfacial Boundary Layer Investigated with IR Polarization-Selective Pump-Probe Experiments. *J. Phys. Chem. B* **2017,** *121* (17), 4530-4537.
83. Viswanath, P.; Aroti, A.; Motschmann, H.; Leontidis, E., Vibrational Sum Frequency Generation Spectroscopic Investigation of the Interaction of Thiocyanate Ions with Zwitterionic Phospholipid Monolayers at the Air-Water Interface. *J. Phys. Chem. B* **2009,** *113* (44), 14816-14823.
84. McLaughlin, S.; Bruder, A.; Chen, S.; Moser, C., Chaotropic Anions and Surface-Potential of Bilayer Membranes. *Biochim. Biophys. Acta* **1975,** *394* (2), 304-313.
85. Cunningham, B. A.; Shimotake, J. E.; Tamuralis, W.; Mastran, T.; Kwok, W. M.; Kauffman, J. W.; Lis, L. J., The Influence of Ion Species on Phosphatidylcholine Bilayer Structure and Packing. *Chem. Phys. Lipids* **1986,** *39* (1-2), 135-143.
86. Cunningham, B. A.; Lis, L. J.; Quinn, P. J., The Influence of Mono-Valent Anions on Dipalmitoylphosphatidylcholine Bilayer Phase-Transitions - A Time Resolved X-Ray-Diffraction Study. *Mol. Cryst. Liq. Cryst.* **1986,** *141* (3-4), 361-367.
87. Cunningham, B. A.; Lis, L. J., Thiocyanate and Bromide Ions Influence the Bilayer Structural Parameters of Phosphatidylcholine Bilayers. *Biochim. Biophys. Acta* **1986,** *861* (2), 237-242.
88. Frisch, M. J.; Trucks, G. W.; Schlegel, H. B.; Scuseria, G. E.; Robb, M. A.; Cheeseman, J. R.; Scalmani, G.; Barone, V.; Mennucci, B.; Petersson, G. A.; Nakatsuji, H.; Caricato, M.; Li, X.;

Hratchian, H. P.; Izmaylov, A. F.; Bloino, J.; Zheng, G.; Sonnenberg, J. L.; Hada, M.; Ehara, M.; Toyota, K.; Fukuda, R.; Hasegawa, J.; Ishida, M.; Nakajima, T.; Honda, Y.; Kitao, O.; Nakai, H.; Vreven, T.; Montgomery Jr., J. A.; Peralta, J. E.; Ogliaro, F.; Bearpark, M. J.; Heyd, J.; Brothers, E. N.; Kudin, K. N.; Staroverov, V. N.; Kobayashi, R.; Normand, J.; Raghavachari, K.; Rendell, A. P.; Burant, J. C.; Iyengar, S. S.; Tomasi, J.; Cossi, M.; Rega, N.; Millam, N. J.; Klene, M.; Knox, J. E.; Cross, J. B.; Bakken, V.; Adamo, C.; Jaramillo, J.; Gomperts, R.; Stratmann, R. E.; Yazyev, O.; Austin, A. J.; Cammi, R.; Pomelli, C.; Ochterski, J. W.; Martin, R. L.; Morokuma, K.; Zakrzewski, V. G.; Voth, G. A.; Salvador, P.; Dannenberg, J. J.; Dapprich, S.; Daniels, A. D.; Farkas, Ö.; Foresman, J. B.; Ortiz, J. V.; Cioslowski, J.; Fox, D. J. *Gaussian 09*, Gaussian, Inc.: Wallingford, CT, USA, 2009.

A.2. APPENDIX

A.2.1. ^{1}H NMR spectral assignments

Proton NMR spectra were recorded for 100 mM concentration of DTAB samples in D_2O alone and in the presence of different concentrations of thiocyanate and other counter anions chloride and iodide are described in the main text.

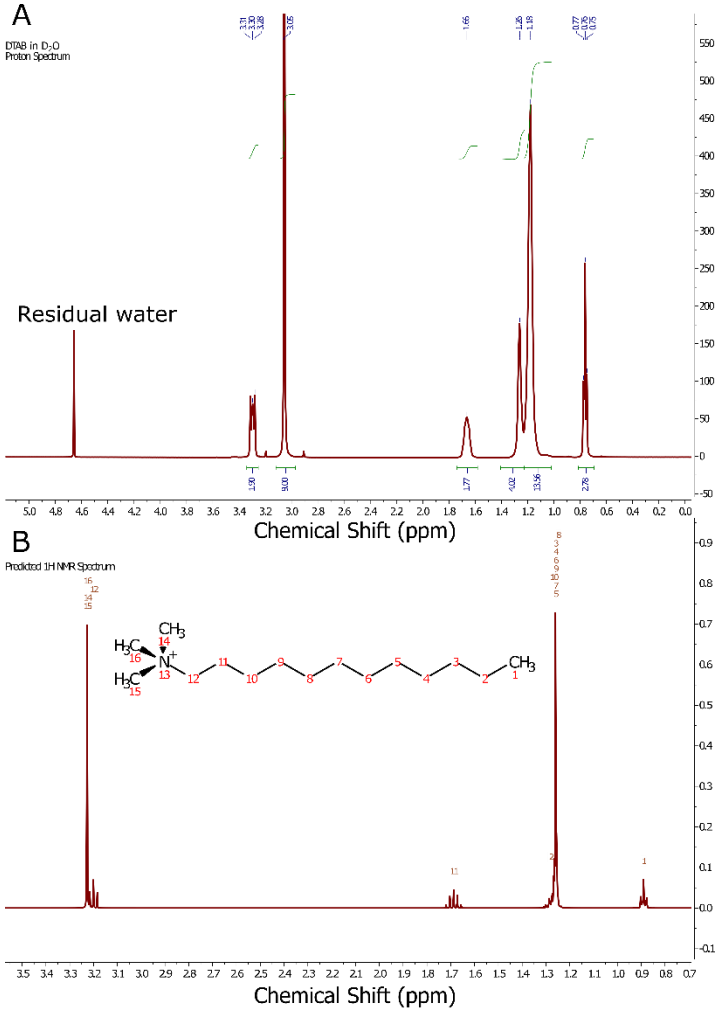

Figure A.2-1. (A) ^{1}H NMR spectra of 100 mM DTAB in D_2O. Also shown are integration values for protons attached to all the carbons in the surfactant molecule. The integration values have been referenced using the 9 trimethyl protons in the surfactant headgroup. Spectra were obtained by averaging 16 scans, baseline and phase corrected to yield absorptive lineshapes. (B) Predicted NMR spectra for the surfactant molecule using Mnova NMRPredict algorithm. The algorithm captures the major chemical shifts for the protons corresponding to the surfactant tail and headgroup regions. Peak positions for protons in the trimethyl amine and the alpha carbon appear swapped due to close chemical shifts values, but the splitting pattern predicted matches well with the experimental data (singlet for trimethyl protons and triplet for the alpha carbon). The quintet splitting pattern and chemical shift values are especially well predicted for carbon #11, which contains 4 neighboring protons. Chemical shift values for protons in the alkyl surfactant tail region are in excellent agreement with the experimental data.

Figure A.2-1(A) shows the ^{1}H NMR spectrum of DTAB surfactant only in D_2O.

Integration values obtained have been referenced to the most intense 9 trimethyl protons at 3.05 ppm attached to the tertiary amine. Integration values for protons along the surfactant hydrocarbon chain are in good agreement with the actual number of attached protons. A singlet is obtained for the trimethyl amine protons, which lack coupling due to the presence of the highly electronegative nitrogen bridge. For carbon #12 containing 2 secondary protons, an integration value of 1.9 is obtained and appears as a triplet due to vicinal coupling from 2 protons attached to the adjacent carbon. Being attached directly to the amine group, significant deshielding causes them to appear downfield at 3.3 ppm. For the 2 protons attached to carbon #11 at 1.66 ppm, integration value of 1.77 is obtained and the spectra is split into multiplets. Specifically, a quintet is expected due to the presence of a total of 4 vicinal coupling protons (2 on each adjacent side). Protons from carbon #10 to #2 at ~1.2 ppm correspond to 18 secondary protons along the surfactant tail with a total integration value of 17.58. Due to slight differences in the magnetic environment and numerous splitting patterns result in two distinct peaks around 1.2 ppm. For 3 protons attached to the end of the surfactant tail at carbon #1 at 0.76 ppm, an integration value of 2.78 is obtained which appears as triplet, again due to 2 vicinal coupling protons.

Figure A.2-1(B) shows the predicted NMR spectrum of DTAB using the Mnova NMRPredict algorithm. The prediction method captures the major chemical shifts for protons corresponding to the surfactant tail and the headgroup. The assignment agrees well with the experimentally obtained spectrum.

A.2.2. Frequency calculations for thiocyanate in different environments

Normal mode analysis was performed in Gaussian 09[88] using the B3LYP functional and a 6-31G(d,p) basis set on each atom. All calculations were done in vacuum since we are seeking primarily trends in vibrational frequencies. The following cases were calculated: thiocyanate anion only; thiocyanate hydrogen bonded to water; thiocyanate near a bare positive charge; and thiocyanate near a trimethylalkylammonium cation. The trend in red shift of CN stretching frequency observed in our experiments are reproduced using these calculations which highlight the proximity of our probe to the interface.

A detailed comparison for the thiocyanate's CN stretching frequency by itself and in different hydration and electrostatic environments (also reported are shifts relative to bare

thiocyanate anion) is tabulated in **Table A.2-1.**

Table A.2-1. DFT calculated CN stretching frequency of thiocyanate alone and in different environments mimicking the positive electrostatic environment near the DTAB surfactant interface. A blue shift (value of shift reported in parentheses) in CN stretching frequency is observed when thiocyanate hydrogen bonds with one water molecule. Near a bare positive charge and in two different truncated alky(trimethyl)ammonium cation, the CN stretching frequency red shifts (values of the shift are reported in parentheses).

Thiocyanate system	CN frequency (cm^{-1})
Only thiocyanate	2175
Thiocyanate + 1 water	2184 (**+9**)
Thiocyanate + ethyl(trimethyl) ammonium cation	2120 (**-55**)
Thiocyanate + butyl(trimethyl) ammonium cation	2120.35 (**-54.65**)
Thiocyanate + bare positive charge	1904.18 (**-270.82**)

DFT calculated CN stretching frequency of thiocyanate when hydrogen bonded with water is blue shifted by 9 cm^{-1} compared to free thiocyanate. Blue shifts are commonly observed for alkylthiocyanates due to the donation of electron density into a bonding orbital of the CN unit.[10, 65] In presence of a bare positive charge, on the other hand, and in alkylammonium cations, we find a red shift in the thiocyanate vibrational frequency, which agrees with previous measurements.[33, 69] Our experimental observation of 10-12 cm^{-1} red shift in the thiocyanate stretching frequency appears to be due to combination of factors including breaking of hydrogen bond facilitated by the interface, as well as the introduction of a significant electrostatic environment by the positive nature of the surfactant headgroup. Either way the proximity of the thiocyanate probe to the interface seems unambiguous. Frequencies calculated for thiocyanate near the alkyl(trimethyl)ammonium cation shows insensitivity to the length of the non-polar surfactant tail (**Fig. A.2-3**).

From charge density analysis of the surfactant, shown in **Figure A.2-2**, it is apparent that the positive charge is concentrated at the headgroup amine.

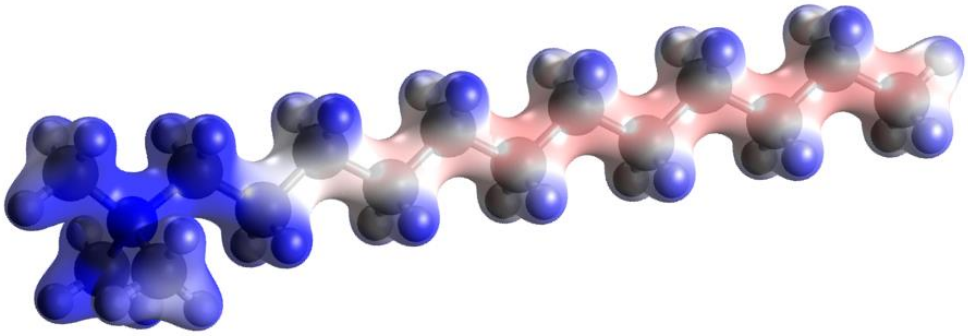

Figure A.2-2. Computed electron density map for the surfactant studied in this work. Electron density is color coded using the electrostatic potential. Blue color represents lack of electron density while red corresponds to increased electron density. The positive charge in the molecule can be seen to be localized at the trimethylamine group.

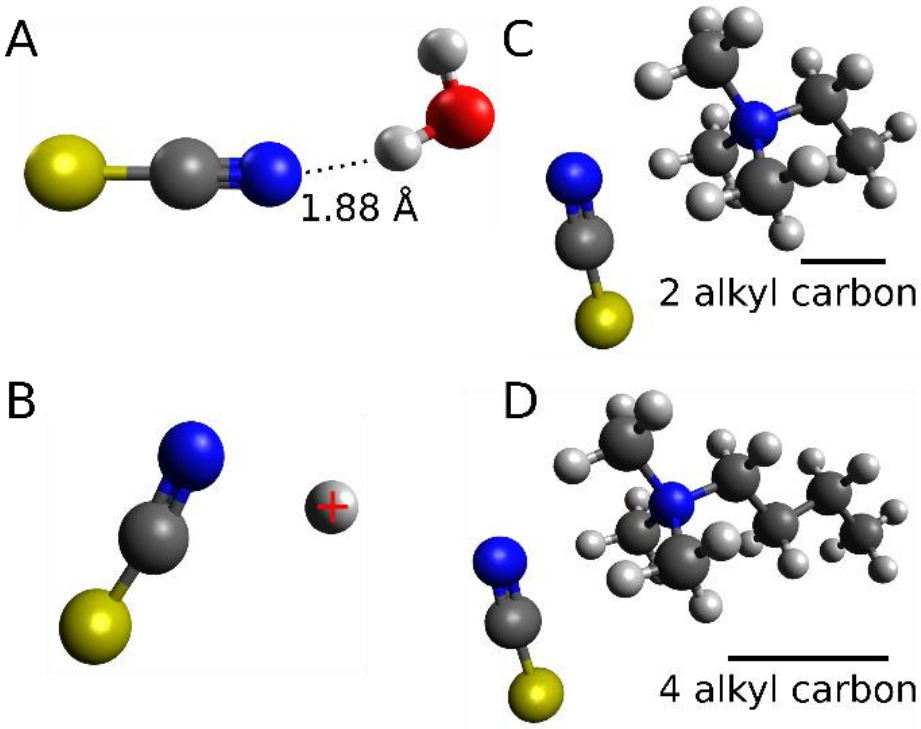

Figure A.2-3. (A) Optimized geometry for thiocyanate in the presence of one H_2O molecule. Formation of a hydrogen bond between the nitrogen in thiocyanate and water blue shifts the CN stretching frequency. (B) Optimized thiocyanate structure in the presence of a single unit of positive charge. The positive charge near the thiocyanate was chosen to mimic the charged environemnt that thiocyanate experiences near the cationic surfactant interface. (C) A more realistic model of the environment in micelles was considered by replacing the bare positive charge with ethyl(trimethyl) ammonium cation and (D) butyl(trimethyl) ammonium cation. The spectral shifts of thiocyanate CN stretching frequency in the presence of these bulky cations also show a trend that is consistent with those determined experimentally in micelles.

Chapter 3

Water in Crowded Protein Solutions Has Robust Bulk-like Hydrogen Bonding Network Topology

3.1. Introduction

The long-standing quest to develop a molecular picture of how interfaces perturb hydration dynamics remains to be explored using both theoretical as well as surface selective spectroscopy experiments. As mentioned in previous chapters, graph theoretical analyses of molecular dynamics simulations offer promising approach to map topological network characteristics of water hydrogen bond network in bulk water and in crowded proteins.

In this work, we attempt to determine a quantitative characterization of the magnitude, nature, and extent of hydration shell perturbations around and between protein interfaces using molecular dynamics simulations. Based on the predictions from network analysis, 2D-IR spectral diffusion measurements are also carried to out to test the validity of retardation in protein surface residues fluctuations and the degree of such coupling in influencing hydration dynamics.

Previous measurement using 2D-IR have validated theoretical models of water rearrangement in the vicinity of an isolated interface.[1-4] The surface topology plays a decisive role in the degree of hydration slowdown based on the excluded volume of potential hydrogen bonding partners.[5] For example, simulations of water near an armchair carbon

nanotube conclude that a concave geometry is more hydrophobic than convex geometry.[6] Different surface patterning of functional groups have also been shown to alter macroscopic hydrophobicity.[7] In general, the Lum-Chandler-Weeks description identifies a length scale dependence to the thermodynamics of hydration,[8-13] though it remains a challenge to discern the degree to which molecular dynamics follows a similar trend.

Reduced tetrahedral order parameter, diffusivity, and hydrogen bond switching dynamics near an interface might have the potential to propagate beyond the first hydration shell.[14] Experimental methods using site-specific protein labeling and 2D-IR spectroscopy to probe water dynamics in different levels of crowding have provided some evidence of this actively debated long-range perturbation.[2, 15-17] It is well known that an interface alone can perturb water in the immediate vicinity, but hydration dynamics in various confined geometries have been found to exhibit assorted levels of retardation, due to variations in protein surface topology and chemical heterogeneity.[18, 19] Previous work[2] employing 2D-IR has shown that merely increasing the access of water to an interface further slows water dynamics, even undergoing a dynamical transition. Despite appreciable evidence favoring long-range perturbation to hydration dynamics at ultrafast timescales, it is not yet clear what functional consequences result from the constraints on crowded hydration dynamics.[20, 21] Slowed water has a reduced dielectric constant, leading to enhanced Coulomb interactions arising from reduced screening.[22] In fact, a recent simulation study has found artificial box size dependent protein conformational distributions, suggesting that periodic boundary conditions and water dielectric properties can have unexpected thermodynamic consequences even in the absence of physical crowding.[23] Experimentally, Cho et al.[24] have highlighted that the water dynamics in chemically similar crowding scenarios depend on the size of the crowding agent, which is consistent with our previous studies using surface-labeled lysozyme.[3] Recent attention to strongly hydrophilic crowding agents such as PEG has provided mounting evidence that water can remain "bulk" like even when the overall solution viscosity is very high.[25, 26] Still, the central question of whether the very presence of interfaces alone can collectively induce dramatic hydration slowdown in crowded environments remains to be completely explored.

Network concepts have been applied to protein hydration largely from the perspective of percolation, where above a critical level of hydration (h = grams of

water/grams of protein), contiguously hydrogen bonded waters span nearly the entire protein surface.[27, 28] Winter *et al*. estimated the average number of water-water hydrogen bonds at the percolation transition to be 2.0-2.3.[29] From a molecular perspective, this transition corresponds to the depletion of nearly half of the available water molecules, implying significant disruption in hydrogen bond connectivity. Recently Sterpone *et al.* have also examined the role of water in dictating protein flexibility using simulations performed at very low hydration factor of $h = 0.39$.[30] This coupling of water and protein motions has only been studied experimentally in protein powders and never in well-hydrated environments ($h > 1$). For reference, an almost saturated solution of HEWL (200 mg/ml) has a hydration factor of 5.0. This work adapts ideas from network science to hydrogen bonding network of water in crowded, but well hydrated protein solutions that resemble realistic biological conditions.

Despite extensive research on hydrogen bonding networks, and their putative disruption by macromolecules and crowding,[14, 31] there has yet to be a study that directly analyzes crowded water using the theoretical constructs of network theory. Our goal is to identify network topology changes accompanying crowding to learn specifically how the network is perturbed. Lacking any changes, we can propose that dynamical perturbations are largely or entirely astructural, such as those encountered in the glass transition, where dynamical slowdown does not have clear structural correlates. Experimentally it is challenging to probe hydration dynamics as a function of protein distances while simultaneously decoupling protein and water motions. Using molecular dynamics simulation supplemented by graph theoretical analysis, we characterize structure, dynamics, and network topologies of water upon crowding. Among the key findings of this work is the quantitative observation that crowded HEWL exhibits constrained structural fluctuations even though there is no apparent perturbation to the interstitial water's network topology. We also find that the delocalized collective hydrogen bond stretching motions are perturbed at most up to two hydration shells from the protein interface. Simulations of real proteins contain significant heterogeneity and complexity, and it is not obvious the degree to which such details are essential to the fundamental perturbations of hydrogen bond switching dynamics. In parallel with the present atomistic simulation, we also implemented a simple lattice model of confined water which we treated with a Monte Carlo simulation.[32] That

lattice model is devoid of surface structural or chemical heterogeneity, yet it recapitulates the main findings of the present study regarding the spatial extent of hydrogen bonding slowdown under varying degrees of crowding.

3.2. Results and discussion

3.2.1. Average hydrogen bond number with and without crowding

Before performing any topological network analysis on water selections in different environments, it is imperative to ensure that we have a reasonable hydrogen bond geometric cutoff criterion. Water molecules in crowded protein environments are selected in a cylindrical geometry as shown in **Figure 3.1**(A). Analogous control analysis is also performed from a bulk water simulation, using droplets of spatial diameter (**Fig. 3.1**(B))

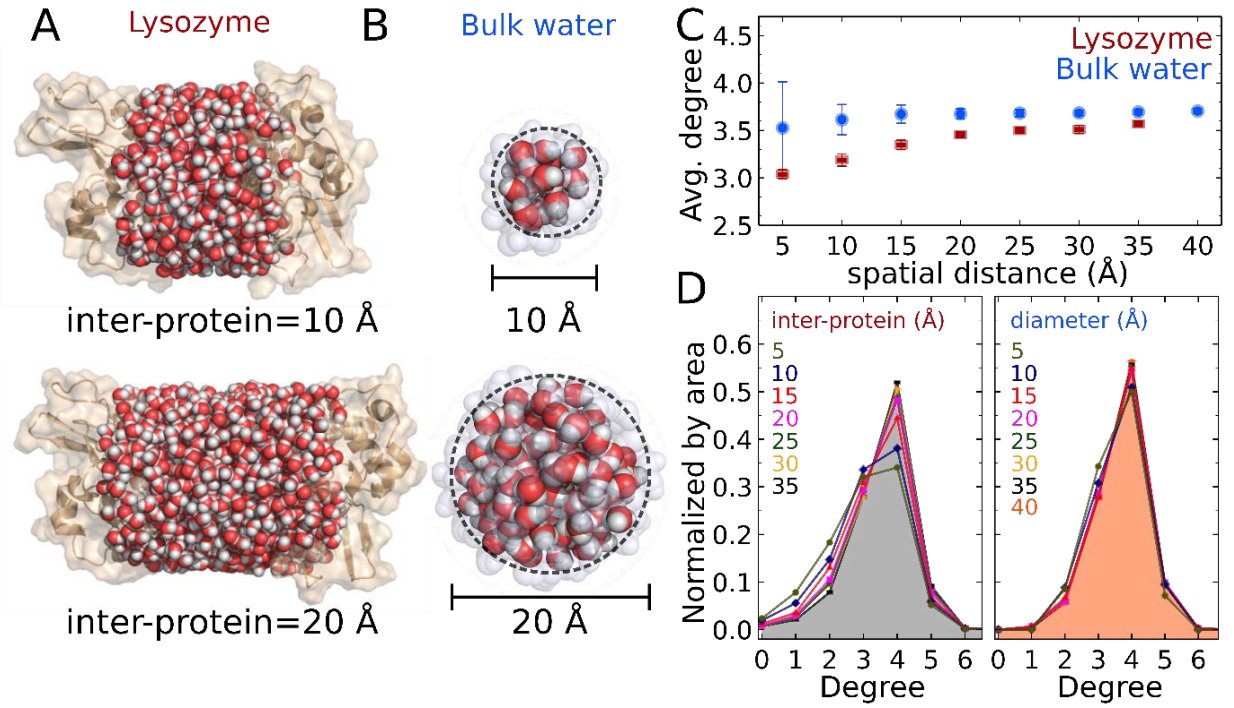

Figure 3.1. (A) Two simulated hen egg while lysozyme (HEWL) proteins constraining water molecules at inter-protein distances of 10 and 20 Å. Cylindrical water selections simulate hydration dynamics in slow, crowded environments relative to fast, bulk-like environments. (B) Spherical droplets of bulk water with diameters of 10 and 20 Å. To eliminate edge effects in spherical droplets, one layer of water molecules (~2.5 Å) is excluded and the remaining inner sphere is used for analysis. Similar rejection of the interface was also performed in the case of binary protein simulations along the lateral surface. (C) Average hydrogen bond numbers for waters in between two HEWL proteins and within the spherical droplets of bulk water. The error bars represent one standard deviation from mean values. (D) Hydrogen bond coordination distribution (i.e. the degree distribution) for crowded (left) and bulk (right) water. Degree distributions for crowded water shift to a higher degree with increased inter-protein distance, whereas in bulk water droplets, the average degree remains constant with increasing diameter.

equal to inter-protein separations. The average coordination number for each water molecule (hydrogen bond number or "degree") is determined from the adjacency matrix, whose ij^{th} element contains a 1 if molecules *i* and *j* are hydrogen bonded, and zero otherwise (see appendix A.3.6.2). We also determine the degree distribution of hydrogen bonds. Average hydrogen bond degrees for water molecules in bulk droplets and in between crowded HEWL proteins is shown in **Fig. 3.1**(C). In water droplets, a constant mean value of ~3.6 hydrogen bonds per molecule is obtained for diameters between 5-40 Å. This average degree is consistent with having roughly 10% hydrogen bond defects in liquid water.[33] The error bars are large for small water droplets, where only few water molecules can be selected. For comparison, at most 2 water molecules can be stacked along any axis in a sphere of 5 Å dimeter. Waters molecules in the highest crowding case show a slight shift in the degree distribution. The average coordination number increases gradually to the bulk degree by 10-15 Å. At small inter-protein distances, the proximity of water to macromolecular interfaces results in the sacrifice of some hydrogen bonds. The reduction in average water-water hydrogen bonds does not negate the presence of protein-water hydrogen bonds. Although the average degree at 5 Å inter-protein separation is ~15 % less compared to that of bulk water, it is still well above the percolation threshold (2.0 - 2.3) for forming spanning clusters.[29] This further confirms that no significant breakage of hydrogen bonds occurs when more than one shell of hydrating water is present.

Hydrogen bond degree distributions shown in **Fig. 3.1**(D) compare bulk and crowded water with different spatial dimensions. In bulk, most of the water molecules are involved in 4 hydrogen bonds with a small fraction of them forming three and two hydrogen bonds. Crowded water in between two proteins also exhibit similar distributions, except for the 5 Å and 10 Å inter-protein separations. At small protein separation, only a few layers of water molecules are present, thus reducing the fraction of 4 coordinated water molecules and increasing the population of 1 and 2 coordinated waters.

It is important to note that any hydrophobic interface will likely disrupt the hydrogen bond network, consistent with the excluded volume picture. Based on average coordination numbers and degree distributions of water between crowded interfaces, it can be inferred that protein surfaces may alter water's local connectivity appreciably up to 15 Å of inter-protein separation. Reduction in local connectivity is simply due to the presence of an

interface, as no protein-water hydrogen bonds have been considered in our analysis.

3.2.2. Crowded and bulk water have similar network topologies

Topological network analysis using graph theory is a well-established field of study.[34-38] Its applications include, but are not limited to, extracting key network characteristics in artificial (world wide web, telephone connections, rail and road), biological (metabolic pathways, neural circuit) or social (friendship, dating, actors) networks. Ideas from network science have previously been applied to understand hydrogen bonding characteristics in bulk water,[39-41] concentrated salt and alcohol solutions[42-45] as well as in polymer solutions.[46]

The observed reduction in average coordination of water near an interface correlates with the depleted number of available partners. Does this slight change in coordination number force water molecules to adopt a different connectivity, potentially also affecting neighboring shells? To address this question, we applied the metric of clustering coefficient as defined in network theory. Clustering coefficient measures how well any node is connected in the network, providing a quantitative measure of its connectivity pattern. We have used both local and global metrics of clustering coefficient to characterize HB network. **Figure 3.2**(A) shows the dependence of local network structure on varying spatial distances of the protein and bulk water droplets. For comparison, the clustering coefficient in a model random network ($C_{random} \sim \langle k \rangle / N$) is also plotted (dashed grey curve in **Fig. 3.2**(A)) with the number of nodes (N) and average degree (k) comparable to that of crowded water. Clearly, the clustering coefficients of water HB networks have a different dependence on varying spatial distance relative to that of a random network. From a network perspective, the local topology of hydrogen bonds is not altered due to the presence of nearby interfaces. The global clustering coefficient (**Fig. 3.2**(A)) of water counts the occurrences of three-membered rings in the network, enabling the determination of the local connectivity pattern of hydrogen bonds. Formation of three membered water rings inherently has low probability except during the transient hydrogen bond switching event[47]. An average value of ~0.02 is consistent with work previously published by Cho *et al.*[43] for water in highly concentrated aqueous salt solutions. The small value of the clustering coefficient also confirms that loops and rings are not dominant species at room temperature in water[48] as previously claimed.[49, 50] We have also calculated the local clustering coefficient of water (see appendix A.3.1.1),

defined slightly differently in the network science literature.[51] Briefly, the local clustering coefficient counts the number of mutual connections neighbors form with a given node,

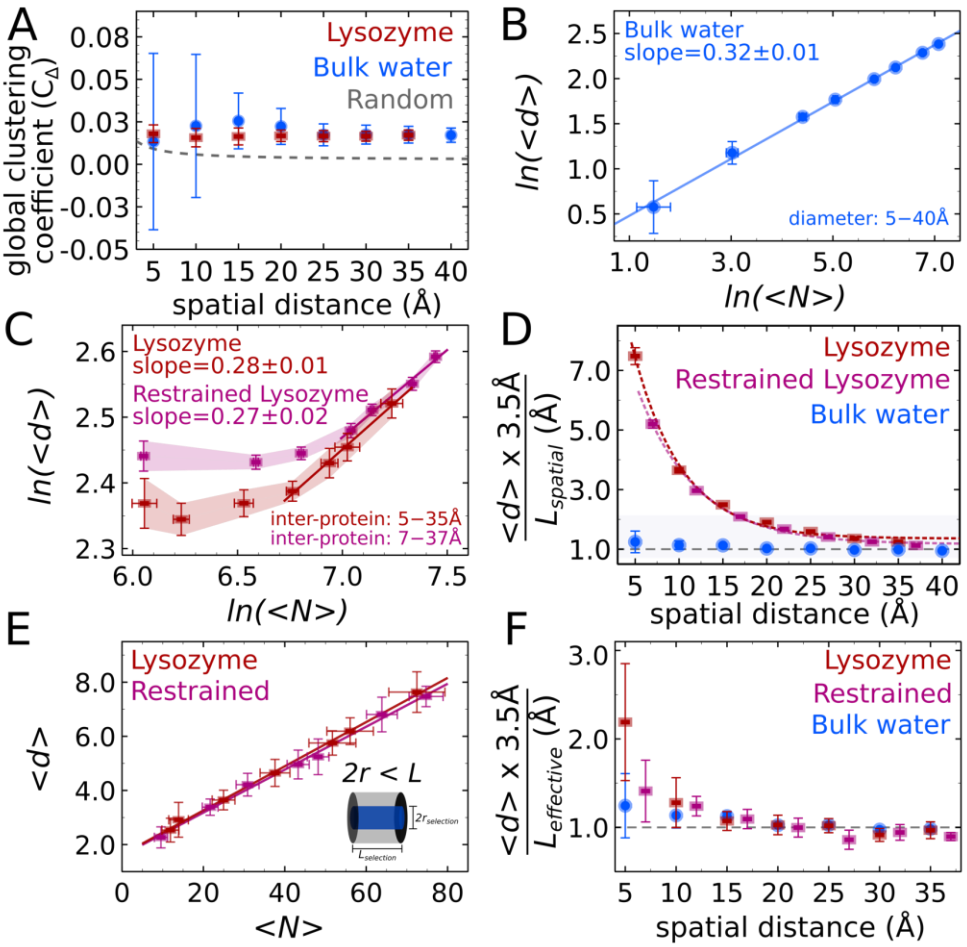

Figure 3.2. (A) Global clustering coefficient values for water simulated in crowded (binary protein) and bulk (pure water) environments. Error bars represent one standard deviation obtained using simulation snapshots separated by 15-20 ps. Large fluctuations arise from small water droplets (5 and 10 Å) with few molecules. Clustering coefficient values do not show any dependence on spatial distance, either in crowded or bulk environments, indicating local network characteristics are unaltered due to crowding. (B) Log-log plot for the average path length <*d*> versus the average number of network nodes <*N*> for different water droplet diameters (5 – 40 Å). This global network characteristic shows a linear dependence for bulk water, indicating that the average path length is proportional to a non-linear power of the number of nodes. Error bars for both the abscissa and ordinate are one standard deviation for the corresponding variables averaged over all simulation snapshots. A perfectly crystalline 3D-lattice has an exponent of 0.33, which is indistinguishable from our measured slope of 0.32 ± 0.1. (C) Average path length analysis for waters in between two HEWL proteins at separations of 5 – 35 Å (without protein position restraints) and 7-37 Å (with restraints). The reduced error bars <*N*> with position restraints reflects the impact that protein fluctuations have on the volume of the crowded region. (D) Distance-normalized average path lengths for water in crowded and bulk-like environments. Average network distances were obtained by multiplying the average path length by a constant distance of 3.5 Å. In the case of bulk water, no variation is observed whereas crowded water fits well to an exponential decay function. (E) Average path length as a function of the number of nodes in the network for crowded water. A smaller cylindrical selection was used to compute topology, such that the diameter of cylinder < inter-protein distances. The linear dependence is consistent with a 1D lattice model. (F) Average path length normalized by "effective" distance for the selected water volumes becomes roughly constant beyond 2-3 water shells.

indirectly measuring the number of loops and triads in a network. In our analysis, local clustering coefficients also remain invariant with system size for both crowded and bulk water, further confirming that the local topology remains unaltered by the interfaces.

Average path length is a measure of the global topology of a network that counts the number of hops between any pair of nodes in the network. Large path lengths characterize a sparse and broken network, while dense ("small-world") network path lengths are smaller. A log-log plot of average path length versus the number of nodes in different diameters (5 – 40 Å) of bulk water droplets (**Fig. 3.2**(B)) exhibits a linear slope, indicating a power law dependence of path length on the number of nodes. A linear fit yields a slope of 0.32 ± 0.01, which is in good agreement with a model network where nodes are arranged in a 3-dimensional crystalline lattice.[51] The degree distribution (**Fig. 3.1**) and measured diffusion constant (see appendix A.3.4) do not point towards an amorphous ice like property of liquid phase water in our selection. Rather, it is the topological network properties of water that show lattice-like behavior.

Average path length analyses for crowded water with and without protein fluctuations turned on (i.e. "position restrained") (**Fig. 3.2**(C)) show a different dependence. The average path length remains constant for inter-protein distances up to 20 – 22 Å, becoming linear afterwards. The linear region can be fitted to a straight line that yields a slope of ~0.28 with and without position restraints, appreciably different from the case of bulk water (0.32 ± 0.01). It is important to note that the average path length values for water crowded between restrained proteins are greater by one node (e.g. one water molecule) relative to the unrestrained case. Based on our analysis, we believe that the observed difference does not have any significant contribution from the protein fluctuations, but rather that the different values are consistent with the different spatial extents of the crowded region. For our restrained simulations the minimum inter-protein distance was chosen to be 7 Å and subsequent distances are ~2 Å larger than in the simulation without restraints. The mean average path length for inter-protein distances up to 20 Å differs by 1 node ($e^{-(2.45\,-\,2.35)} \sim 1$). Having an additional 2 Å separation may result in accommodating an additional water molecule (node) along the inter-protein axis.

To gain insight into the effective global size of the network, we normalize the average pathlength by the spatial distance (**Fig. 3.2**(D)). The average network path lengths are

converted into approximate physical distances by multiplying by a constant size of water molecule using the first minimum in the radial distribution function, (3.5 Å). These distances are then normalized by the spatial distance of the system ($L_{spatial}$). For bulk water, the average size of the network scales well with the diameter of the droplet further reinforcing the lattice-like network topology for bulk water. The network size for the crowded water, however, shows an exponential decay that eventually becomes bulk-like at large inter-protein distances. Data points for simulations with and without position restraints agree well with each other, further confirming that the difference in spatial extent of the restrained and unrestrained proteins accounts for the differences in the measured path lengths.

The observed ~7-fold increase in average path length for 5 Å inter-protein separation should imply dramatic disruption of the hydrogen bond network due to crowding. Since we did not observe a significant reduction in average coordination number, we wanted to explore its origin. By restricting the cylindrical water selection diameter in the crowded region to be less than the inter-protein distance ($2r < L$), a linear dependence is observed for the average path length with the number of nodes, as shown in **Fig. 3.2**(E). This dependence is consistent with the lattice model where network nodes have a single degree of freedom for expansion. A corrected version of the normalized average size of the network with "effective" distance (equivalent cuboid length) is shown in **Fig. 3.2**(F). From analyzing path length distributions of water between proteins, we find two populations of short and long paths representing lateral and axial dimensions of the cylinder (see appendix A.3.1.2).

Although the average connectivity of water is appreciably altered due to crowding (particularly at small inter-protein distances, **Fig. 3.1**) the hydrogen bond networks show similar linking patterns and topologies in crowded and bulk-like environments. We also find no preference in connecting to nodes of any degree in the hydrogen bond network regardless of crowding extent (see appendix A.3.3). From a molecular perspective, this indicates homogeneous spatial density distribution without formation of low- and high-density patches of water.

3.2.3. Extent of collective vibrational modes of water from protein interfaces

In previous sections, we established that the overall topology of the hydrogen bond network remains unaltered upon crowding. Based on our previous measurements of hydrogen bond

correlation times,[2] we next turn to an analysis of the extent of collective motions of water near HEWL interfaces in between the crowded regions of the proteins. Experimental evidence for extended hydration shells has been obtained using THz spectroscopy and was found to be sensitive to the distance between proteins.[52]

Figure 3.3 shows computed vibrational density of states (VDOS) of water in different shells of HEWL in crowded and dilute environments from 0 - 1000 cm^{-1}. Ultrafast infrared

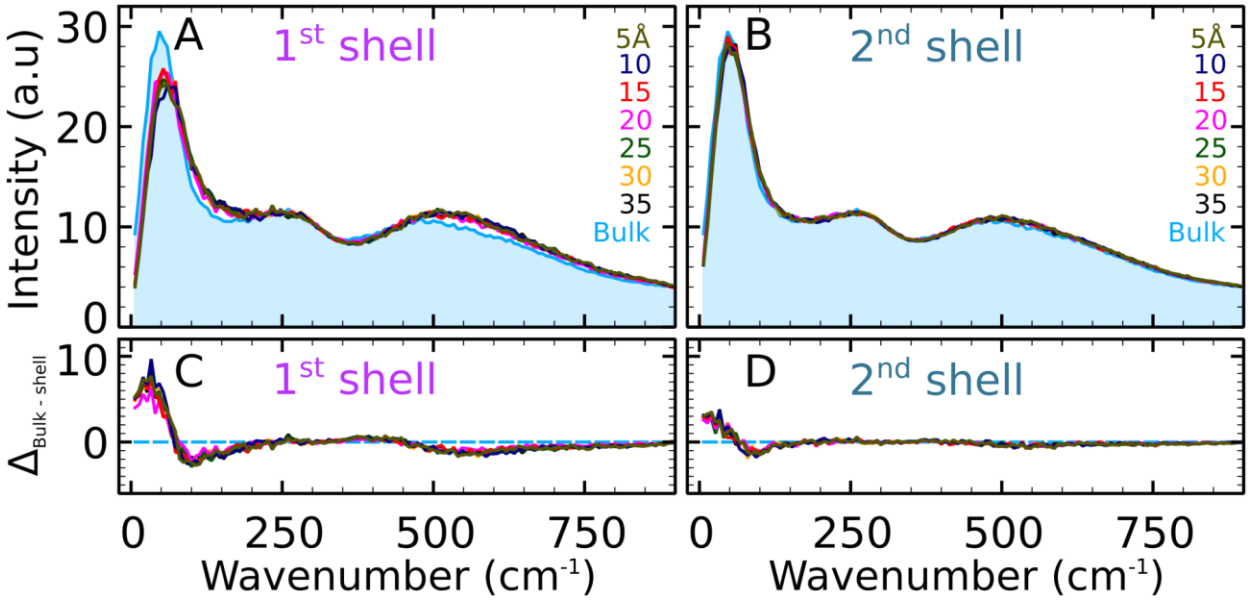

Figure 3.3. (A) Vibrational density of states (VDOS) spectra for the first shell of water molecules around binary HEWL proteins in the crowded region. Varying the inter-protein distances from 5 Å to 35 Å mimic different degrees of crowding which has no influence on the VDOS spectra. Relative to bulk water, the first shell water molecules show depleted intensity in the hydrogen bonded stretching region. (B) VDOS spectra for water molecules in the second shell in the crowded region. The second shell spectra agree well with the spectrum of bulk water indicating that the collective dynamical motion of water in the second hydration shell is bulk-like. (C) Difference spectra for first shell waters with different inter-protein distances relative to the VDOS spectrum of bulk water. (D) Difference VDOS spectrum for water molecules in the second hydration shell.

spectroscopy has established ~1 ps as the time scale for hydrogen bond rearrangements in the bulk liquid.[53] Collective modes of water contributing to this dynamical time scale lie roughly between 0 – 100 cm^{-1}, a frequency range also accessible with THz spectroscopy. Modes below 100 cm^{-1} are due to bending and stretching of the hydrogen bond (HB), while those above 200 cm^{-1} correspond to librational motion (centered at 500 cm^{-1}). [54] **Figure 3.3**(A) shows VDOS spectra for water in the first hydration shell (within 2.8 Å from the protein surface) in the crowded region of the proteins. While the librational band shows an increased amplitude compared to bulk water, a reduction in the kinetic energy (i.e. amplitude of the VDOS spectrum) is observed for bands corresponding to the HB stretch.

This redistribution of the kinetic energy for first-shell water molecules also remains insensitive to different degrees of crowding. Similar insensitivity to inter-protein distances is also observed for second-shell water molecules (2.8 – 5.6 Å from the interface) (**Fig. 3.3**(B)), which show bulk-like behavior. In case of first-shell water molecules, the presence of an interface reduces the slow HB stretch entropy while at the same time increasing the many-body fast libration motion within the same shell.[55, 56] It is known from previous work[47, 57] that librations play an important role during hydrogen bond switching via the three-body angular jump mechanism. Difference spectra (**Figure 3.3**(C, D)) highlight the insensitivity of collective motions of water to different inter-protein distances. VDOS calculations for different shells of water near an interface imply that the collective motion only gets perturbed to a maximum of two to three hydration shells. Different degrees of crowding do not influence the extent of this perturbation. This modest perturbation of water's collective motions was also observed recently using MHz to THz dielectric spectroscopy in aqueous bovine serum albumin protein solutions.[58] Recently, Halle *et al.*[59] have shown that various kinetic and configurational properties decay to bulk-like behavior within one hydration shell of the protein. The alignment order parameter calculated for globular proteins with net explicit charge (–6) show short-range exponential dependence of calculated water dipole moments. On the other hand, proteins with a net dipole moment were shown to exhibit long range, power-law influence (R^{-3}). Such long-range perturbation can only be observed in proteins with sufficiently large dipole moment. To examine the effect of the interface and crowding on the orientational motion of water, we also calculated dipole auto correlation functions (see appendix A.3.5) for water in different shells of the protein and found decay times significantly different from bulk at the second hydration shell. Despite this extended distance penetration of the interface, we find no dependence on protein-protein separation, suggesting that crowding does not dramatically alter the hydration shell-dependent slowdown of orientational motion.

3.2.4. Influence of protein fluctuations on measured hydration dynamics

Our current results, using topological network analysis and VDOS calculations, suggest that the extent of perturbation to the hydrogen bond network structure is short ranged (within 10 Å from the interface). A key finding of this work is to discern the direct influence of protein

fluctuations on the measured hydration dynamics as applicable to experimental site-specific labeling approaches. Instead of analyzing exclusively the water molecules, we now focus on characterizing the perturbation of protein conformational fluctuations induced by crowding, an approach that has been taken previously.[31] **Figure 3.4**(A, B) show snapshots of the binary

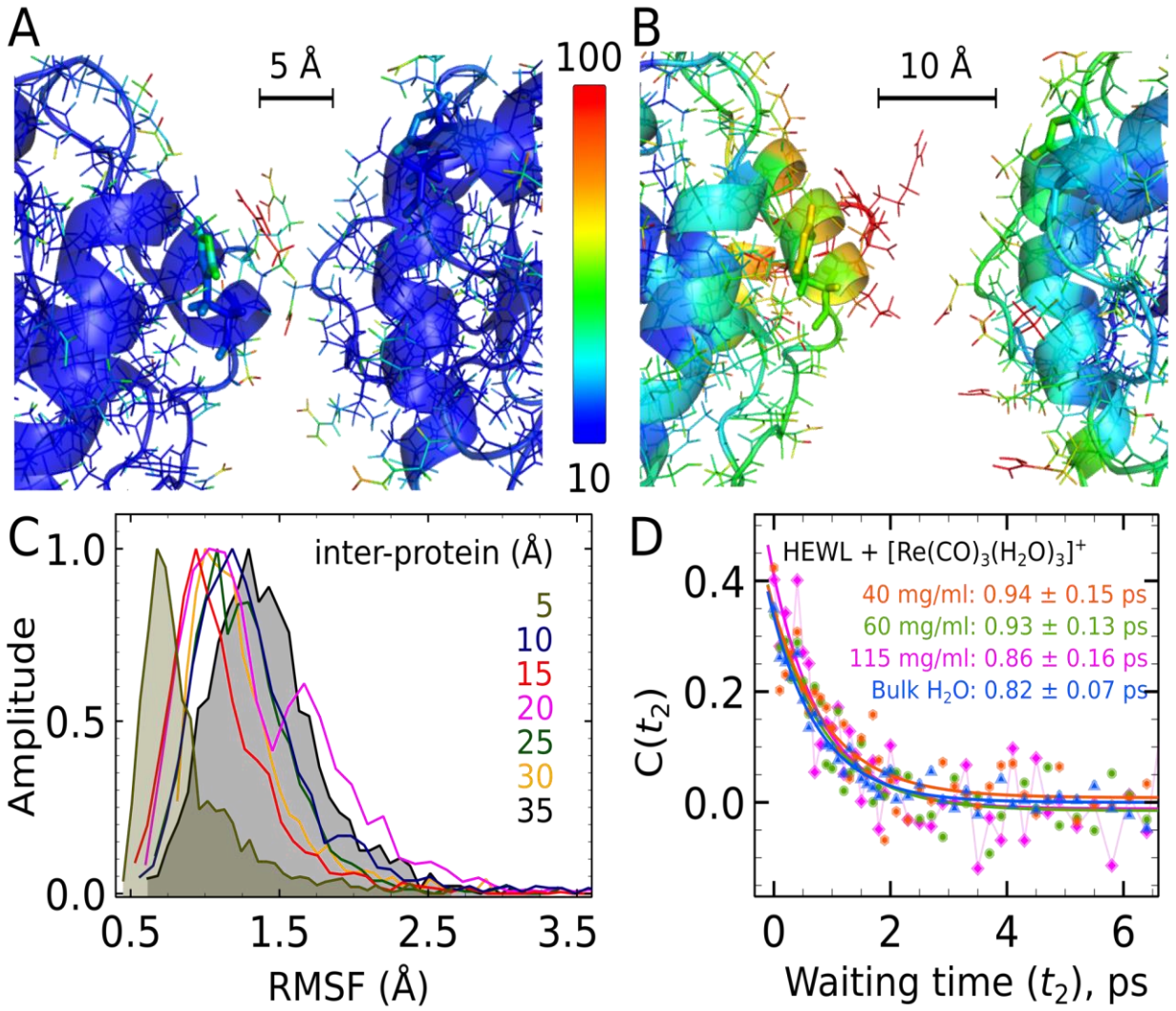

Figure 3.4. (A) Snapshot of the crowded region at 5 Å inter-protein distance. The residues are color coded by B-factor (Å^2) as a measure of their structural fluctuations. For the 5 Å case, nearly all the atoms are constrained. (B) At 10 Å separation, the side chain fluctuations are increased as well as those of the backbone atoms of the helices. (C) Histogram comparing the root mean square fluctuations (Å) for every protein atom in the crowded region. There is a gradual increase in the degree of atomic fluctuations with increasing inter-protein distances. (D) Experimental 2D-IR frequency-fluctuation correlation function measurements using $[Re(CO)_3(H_2O)_3]Br$ as a vibrational probe without labeling the HEWL. The decay, arising from spectral diffusion, show bulk-like hydration dynamics (~1 ps), even at a concentration (115 mg/ml) near the dynamical transition point observed previously using surface-labeled HEWL.

protein structure for inter-protein distances of 5 and 10 Å respectively. The protein residues have been colored based on calculated B-factor values. B-factors quantify mean squared

fluctuations of the atoms in the protein sequence ($B = 8\pi^2\langle u^2\rangle$, *where u is the displacement*). At 5 Å separation (**Fig. 3.4**(A)), the entire backbone of the protein shows reduced flexibility, except for a few residues in the interstitial region. Slightly reduced crowding (10 Å separation), however, results in a pronounced increase in the atomic fluctuations, particularly in the crowded region (**Fig. 3.4**(B)).

To quantify these fluctuations, we plot the distributions of root mean square fluctuations (RMSF) for all the surface atoms facing the crowded region (**Fig. 3.4**(C)). The most probable fluctuations of atoms in the crowded region of the binary protein increases gradually with decreasing degree of crowding. For nearly all the inter-protein distances, fluctuations of atoms on the surface have a unimodal distribution. For an inter-protein distance of 20 Å, a slight shoulder appears around 1.7 Å which can be attributed to releasing strain for a surface lysine residue in the protein.

The most probable fluctuation for 10 Å is observed to be greater than that of 15 Å. Although this may appear to be an outliner, it is still valid to conclude that for intermediate protein separations, the most probable fluctuations lie between the two crowding extremes. Overall, we do observe a trend in protein fluctuations with different degrees of crowding, and fully converging the protein fluctuations is beyond the scope of this study. It might be argued that reduced availability of conformational sampling of residues might not directly contribute dynamics. To address this issue, we computed the ratio of mean square displacements to the average correlation time; this measure represents a form of diffusion constant. A sharp reduction in "diffusivity" of surface residues for 5 Å inter-protein distance is observed (see appendix A.3.7.2) which plateaus to a constant value (within error) for large separation. This crowding dependent slowdown of protein surface residues suggests that protein fluctuations may contribute significantly to the hydration dynamics observed in experiments, though our study does not identify the origin of the protein flexibility changes. Although overall collective motions of water may not be directly perturbed beyond the second hydration shell, protein fluctuations do appear to be more constrained due to crowding. This picture is consistent with THz spectroscopy of concentrated protein solutions. This interplay between the surface fluctuations of macromolecules and collective water motions is likely to play key role in governing the overall free energy landscapes between protein-protein and protein-substrate interactions.

Finally, we test experimentally the hypothesis that protein fluctuations do not substantially influence hydration dynamics when probed without a site-specific vibrational probe. Instead of site-specifically labeling the protein, we used a metal carbonyl probe ($[Re(CO)_3(H_2O)_3]Br$) in bulk H_2O. The frequency-frequency correlation function for a CO stretching mode was measured using 2D-IR spectroscopy (see appendix A.3.6) with increasing HEWL concentrations. 2D-IR spectroscopy (**Fig. 3.4**(D)) of the rhenium probe in bulk H_2O and in the presence of up to 115 mg/mL HEWL shows similar time constants. Experimental data points were fitted using a single exponential. For the rhenium probe in H_2O, the spectral diffusion time constant of 0.82 ± 0.07 ps is consistent with bulk-like dynamics. With increasing concentrations of protein (40, 60 and 115 mg/mL), spectral diffusion time constants remain unaltered within error (0.94 ± 0.15, 0.93 ± 0.13 and 0.86 ± 0.16 ps respectively), thereby indicating the preservation of bulk-like hydration dynamics. Hence, we observe spectral diffusion time constants for high HEWL concentrations of up to 8 mM to be bulk-like. Previously, a transition in the spectral diffusion time constants for surface-labeled protein was observed at the maximum concentration of protein used here.[2]

3.2.5. Protein fluctuations are uncorrelated with hydration dynamics

Coupling between protein and water motions has previously been proposed to be determined chiefly by slow solvent shell rearrangements. This interpretation has been used to explain dynamic fluorescence stokes shift measurements.[60, 61] It is therefore of interest to investigate whether fluctuations of protein surface residues can possibly also influence the fast picosecond dynamics of its hydration shell and beyond.

In order to observe true dynamics of water solely due to an interface it is imperative to separate possible contributions from protein fluctuations and hydrophilic interactions. To observe the influence of protein fluctuations, we computed hydrogen bond correlation times for water molecules constrained between proteins that were modeled as being either fully flexible or as having position restraints. Hydrogen bond correlation functions (**Figure 3.5**(A, B)) of water molecules in between two lysozyme proteins show pronounced differences only for the closest protein-protein distances. The flexible protein simulations have inter-protein separations between 5 and 35 Å in steps of 5 Å while restrained proteins have minimum separations of 7 Å up to 37 Å in steps of 5 Å. The hydrogen bond correlation decay is fitted

to a biexponential with a constant offset (see appendix A.3.8). Librational motion of hydrogen bonded water molecules is responsible for the fast time constant while hydrogen bond switching dynamics is encoded in the slow component (<10 ps) of the correlation function.[62] At an inter-protein separation of 5 Å, we do observe a pronounced slowdown in the hydrogen bonding dynamics, where the retardation factor of ~3 can likely be attributed mostly to the excluded volume effect (**Fig. 3.5**(C)). Moreover, due to interactions between the protein interface and the water molecules, there are certainly other sources of dynamical retardation beyond the statistical excluded volume contribution. Hydrogen bond correlation

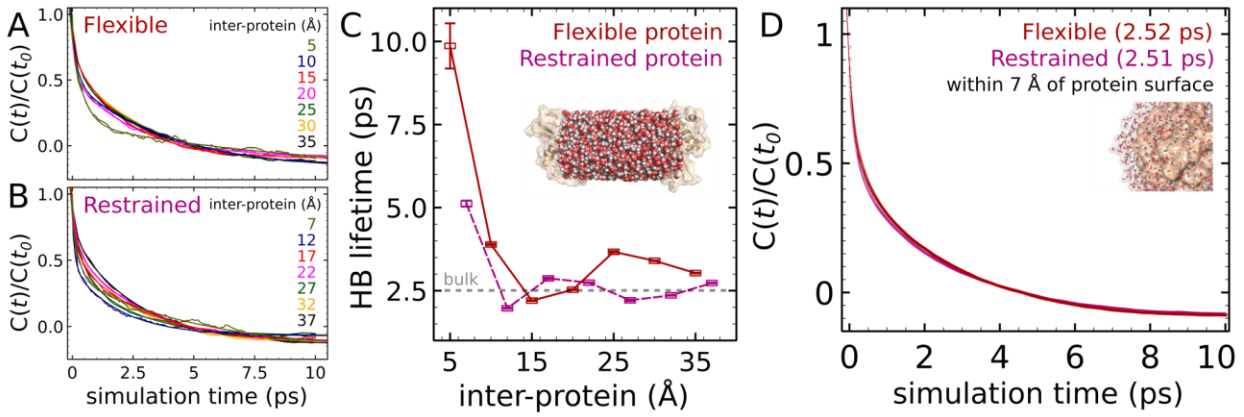

Figure 3.5. Time correlation functions for hydrogen bond switching dynamics of water confined between (A) flexible and (B) restrained proteins. (C) Hydrogen bond lifetime is determined by the long-time component of biexponential fits to the curves in (A) and (B). Error bars represent deviations of fits from the correlation data. We attribute the short time component to fast librational motion of water which appears to remain invariant with inter-protein separation, as observed in our VDOS analysis. At very small inter-protein separations (5-7 Å) substantial (< 3.5) slowdown in dynamics is observed, likely attributable to the excluded volume effect and hydrophilic interactions with the surface residues. With a slight increase in protein separation, the dynamical timescale falls sharply to ~3 ps (the bulk value is shown as a dashed line). (D) Under dilute conditions, analysis of the hydrogen bond correlation function shows that when considering the water molecules within 7 Å of the protein, there is no difference between flexible and restrained protein molecules, indicating a lack of dynamical coupling between the water and protein dynamics on this time scale.

times for large inter-protein separations (>12 Å) converge to the bulk time constant (~2.5 ps) quickly. We observe the perturbations of hydrogen bond switching not to extend beyond the third shell. Interestingly, protein simulations with and without surface residue fluctuations reveal nearly identical H-bond correlation time scales at similar distances, though there are some differences at the closest separations. Under dilute conditions (**Fig. 3.5**(D)), protein flexibility has no influence at all on the hydration water (<7 Å). Our results affirm that protein fluctuations and hydration dynamics remain largely decoupled, at least on the 2-10 ps time scale captured by hydrogen bonding rearrangements. In the context of a jamming transition in viscous protein solutions, where translational motion of particles

spaced more closely than the solvent diameter become essentially frozen (as in the "mayonnaise effect"), our results support the hypothesis that solvent dynamics should remain largely unaltered near the critical concentration. [63, 64]

3.3. Conclusion

From all-atom molecular dynamics and experimental 2D-IR measurements, we find a relatively short-range perturbation to the hydration networks in crowded protein solutions. A key finding from our work is that water forms a robust hydrogen bond network whose topology is preserved even at small inter-protein distances. The unique nature of the water hydrogen bond network to favorably form nearly four hydrogen bonds likely prevents the failure of its network even at extreme crowding. Hydrogen bonding degree distributions of water at the smallest inter-protein separations (5 – 10 Å) yield a slight decrease in the fraction of 4 bonds and increase in 1 or 2 hydrogen bonded fractions. Analyzing the vibrational density of states, which encodes the collective hydration dynamics of water near the protein interface, shows a similar extent of perturbation irrespective of whether it is in crowded or dilute conditions. Considering the protein in addition to the water, we find a pronounced influence of crowding on the degree and dynamics of protein fluctuations. This finding is surprising due to the very minor crowding induced variations in the water hydrogen bonding network topology. Nevertheless, since we do find that first and second shell water molecules exhibit significantly slower translational and orientational diffusion (relative to bulk), that may be sufficient to explain the altered inter-protein structural dynamics owing to the altered local dielectric screening. One area where this study cannot be conclusive is in determining precisely the spatial range of hydration shell structural dynamics perturbations near varying hydrophilic surface residues. Real proteins have rough surfaces that fluctuate, and the overlapping time scales for translational and orientational diffusion make it virtually impossible to study shell-by-shell properties without inevitable transit among these shells. Our Monte Carlo simulations of a lattice model lacking these complications nevertheless recapitulate the main findings of the modest slowdown and relatively short-ranged extent of the perturbations.[32] Our findings indicate that in analyzing experiments, particularly those using site-specific labeling approaches either with fluorophores[60, 61, 65-73] or infrared probes, one must consider sources of anomalous behavior

in hydration dynamics as arising from the direct manifestation of modulated fluctuations of protein residues. It is not clear whether or not these protein structural dynamics will also manifest in the same way when studied by surface bound spin labels via ODNP NMR.[74] Future work to elucidate the nature of the crowding-induced protein dynamical coupling will be needed to establish a more complete understanding of the complex interactions between biomacromolecules and the role played by hydration water.

3.4. References

1. Osborne, D. G.; Dunbar, J. A.; Lapping, J. G.; White, A. M.; Kubarych, K. J., Site-Specific Measurements of Lipid Membrane Interfacial Water Dynamics with Multidimensional Infrared Spectroscopy. *Journal of Physical Chemistry B* **2013,** *117* (49), 15407-15414.
2. King, J. T.; Arthur, E. J.; Brooks, C. L.; Kubarych, K. J., Crowding Induced Collective Hydration of Biological Macromolecules over Extended Distances. *Journal of the American Chemical Society* **2014,** *136* (1), 188-194.
3. King, J. T.; Kubarych, K. J., Site-Specific Coupling of Hydration Water and Protein Flexibility Studied in Solution with Ultrafast 2D-IR Spectroscopy. *J. Am. Chem. Soc.* **2012,** *134* (45), 18705-18712.
4. Yang, M.; Szyc, L.; Elsaesser, T., Decelerated Water Dynamics and Vibrational Couplings of Hydrated DNA Mapped by Two-Dimensional Infrared Spectroscopy. *J. Phys. Chem. B* **2011,** *115* (44), 13093-13100.
5. Laage, D.; Stirnemann, G.; Hynes, J. T., Why Water Reorientation Slows without Iceberg Formation around Hydrophobic Solutes. *J. Phys. Chem. B* **2009,** *113* (8), 2428-2435.
6. Xi, E.; Venkateshwaran, V.; Li, L.; Rego, N.; Patel, A. J.; Garde, S., Hydrophobicity of proteins and nanostructured solutes is governed by topographical and chemical context. *Proceedings of the National Academy of Sciences* **2017,** *114*, 201700092.
7. Giovambattista, N.; Debenedetti, P. G.; Rossky, P. J., Enhanced surface hydrophobicity by coupling of surface polarity and topography. *Proc. Natl. Acad. Sci. U. S. A.* **2009,** *106* (36), 15181-15185.
8. Patel, A. J.; Varilly, P.; Jamadagni, S. N.; Acharya, H.; Garde, S.; Chandler, D., Extended surfaces modulate hydrophobic interactions of neighboring solutes. *Proc. Natl. Acad. Sci. U. S. A.* **2011,** *108* (43), 17678-17683.
9. Lum, K.; Chandler, D.; Weeks, J. D., Hydrophobicity at small and large length scales. *J. Phys. Chem. B* **1999,** *103* (22), 4570-4577.
10. Chandler, D., Interfaces and the driving force of hydrophobic assembly. *Nature* **2005,** *437* (7059), 640-647.
11. Huang, D. M.; Chandler, D., Temperature and length scale dependence of hydrophobic effects and their possible implications for protein folding. *Proc. Natl. Acad. Sci. U. S. A.* **2000,** *97* (15), 8324-8327.
12. Giovambattista, N.; Rossky, P. J.; Debenedetti, P. G., Computational Studies of Pressure, Temperature, and Surface Effects on the Structure and Thermodynamics of Confined Water. *Annual Review of Physical Chemistry, Vol 63* **2012,** *63*, 179-200.
13. Bagchi, B., Water dynamics in the hydration layer around proteins and micelles. *Chem. Rev.* **2005,** *105* (9), 3197-3219.
14. Harada, R.; Sugita, Y.; Feig, M., Protein Crowding Affects Hydration Structure and Dynamics. *J. Am. Chem. Soc.* **2012,** *134* (10), 4842-4849.
15. Winther, L. R.; Qvist, J.; Halle, B., Hydration and mobility of trehalose in aqueous solution. *J Phys Chem B* **2012,** *116* (30), 9196-207.
16. Heyden, M.; Schwaab, G.; Havenith, M., Comment on "Hydration and mobility of trehalose in aqueous solution". *J Phys Chem B* **2014,** *118* (36), 10802-5.
17. Halle, B., Reply to "Comment on 'Hydration and mobility of trehalose in aqueous solution'". *J Phys Chem B* **2014,** *118* (36), 10806-12.
18. Fogarty, A. C.; Laage, D., Water dynamics in protein hydration shells: The molecular

origins of the dynamical perturbation. *Journal of Physical Chemistry B* **2014,** *118*, 7715-7729.
19. Laage, D.; Elsaesser, T.; Hynes, J. T., Water Dynamics in the Hydration Shells of Biomolecules. *Chemical Reviews* **2017,** *117* (16), 10694-10725.
20. Jungwirth, P., Biological Water or Rather Water in Biology? *Journal of Physical Chemistry Letters* **2015,** *6*, 2449-2451.
21. Mondal, S.; Mukherjee, S.; Bagchi, B., Protein hydration dynamics: Much ado about nothing? *Journal of Physical Chemistry Letters* **2017,** *8*, 4878-4882.
22. Despa, F.; Fernandez, A.; Berry, R. S., Dielectric Modulation of Biological Water. *Physical Review Letters* **2004,** *93* (22), 228104.
23. El Hage, K.; Hedin, F.; Gupta, P. K.; Meuwly, M.; Karplus, M., Valid molecular dynamics simulations of human hemoglobin require a surprisingly large box size. *Elife* **2018,** *7*, e35560.
24. Verma, P. K.; Kundu, A.; Cho, M., How Molecular Crowding Differs from Macromolecular Crowding: A Femtosecond Mid-Infrared Pump-Probe Study. *J. Phys. Chem. Lett.* **2018,** *9* (22), 6584-6592.
25. Daley, K. R.; Kubarych, K. J., An "Iceberg" Coating Preserves Bulk Hydration Dynamics in Aqueous PEG Solutions. *J. Phys. Chem. B* **2017,** *121* (46), 10574-10582.
26. Verma, P. K.; Kundu, A.; Ha, J. H.; Cho, M., Water Dynamics in Cytoplasm-Like Crowded Environment Correlates with the Conformational Transition of the Macromolecular Crowder. *J. Am. Chem. Soc.* **2016,** *138* (49), 16081-16088.
27. Oleinikova, A.; Smolin, N.; Brovchenko, I.; Geiger, A.; Winter, R., Formation of spanning water networks on protein surfaces via 2D percolation transition. *Journal of Physical Chemistry B* **2005,** *109*, 1988-1998.
28. Smolin, N.; Oleinikova, A.; Brovchenko, I.; Geiger, A.; Winter, R., Properties of spanning water networks at protein surfaces. *Journal of Physical Chemistry B* **2005,** *109*, 10995-11005.
29. Oleinikova, A.; Brovchenko, I.; Smolin, N.; Krukau, A.; Geiger, A.; Winter, R., Percolation transition of hydration water: from planar hydrophilic surfaces to proteins. *Phys Rev Lett* **2005,** *95* (24), 247802.
30. Rahaman, O.; Kalimeri, M.; Katava, M.; Paciaroni, A.; Sterpone, F., Configurational Disorder of Water Hydrogen Bond Network at the Protein Dynamical Transition. *The Journal of Physical Chemistry B* **2017**, 6792–6798.
31. Heyden, M.; Tobias, D. J., Spatial dependence of protein-water collective hydrogen-bond dynamics. *Physical Review Letters* **2013,** *111*, 16-20.
32. Roy, V. P.; Kubarych, K. J., A simple lattice Monte Carlo simulation describes interfacial and crowded water rearrangements. *submitted*.
33. Lee, H. S.; Tuckerman, M. E., Dynamical properties of liquid water from ab initio molecular dynamics performed in the complete basis set limit. *J. Chem. Phys.* **2007,** *126* (16).
34. Newman, M. E. J., The structure and function of complex networks. *Siam Review* **2003,** *45* (2), 167-256.
35. Watts, D. J.; Strogatz, S. H., Collective dynamics of 'small-world' networks. *Nature* **1998,** *393* (6684), 440-2.
36. Pavlopoulos, G. A.; Secrier, M.; Moschopoulos, C. N.; Soldatos, T. G.; Kossida, S.; Aerts, J.; Schneider, R.; Bagos, P. G., Using graph theory to analyze biological networks. *Biodata Mining* **2011,** *4*, 1-27.
37. Newman, M. E. J., Assortative mixing in networks. *Phys. Rev. Lett.* **2002,** *89* (20).
38. Newman, M. E. J., Mixing patterns in networks. *Physical Review E* **2003,** *67* (2).

39. Geiger, A.; Stillinger, F. H.; Rahman, A., Aspects of the Percolation Process for Hydrogen-Bond Networks in Water. *Journal of Chemical Physics* **1979,** *70* (9), 4185-4193.
40. Stillinger, F. H.; Rahman, A., Improved simulation of liquid water by molecular dynamics. *J. Chem. Phys.* **1974,** *60*, 1545-1557.
41. Rao, F.; Garrett-Roe, S.; Hamm, P., Structural inhomogeneity of water by complex network analysis. *Journal of Physical Chemistry B* **2010,** *114*, 15598-15604.
42. Choi, J.-H.; Cho, M., Ion aggregation in high salt solutions. II. Spectral graph analysis of water hydrogen-bonding network and ion aggregate structures. *The Journal of Chemical Physics* **2014,** *141*, 154502.
43. Choi, J.-H.; Cho, M., Ion aggregation in high salt solutions. IV. Graph-theoretical analyses of ion aggregate structure and water hydrogen bonding network. *The Journal of Chemical Physics* **2015,** *143*, 104110.
44. Bakó, I.; Bencsura, A.; Hermannson, K.; Bálint, S.; Grósz, T.; Chihaia, V.; Oláh, J., Hydrogen bond network topology in liquid water and methanol: a graph theory approach. *Pccp* **2013,** *15*, 15163-15171.
45. da Silva, J. A. B.; Moreira, F. G. B.; dos Santos, V. M. L.; Longo, R. L., On the hydrogen bond networks in the water-methanol mixtures: topology, percolation and small-world. *Physical Chemistry Chemical Physics* **2011,** *13*, 6452-6461.
46. Sumpter, B. G.; Noid, D. W., Neural networks and graph theory as computational tools for predicting polymer properties. *Macromolecular Theory and Simulations* **1994,** *3* (2), 363-378.
47. Laage, D.; Hynes, J. T., A Molecular Jump Mechanism of Water Reorientation. *Science* **2006,** *311* (5762), 832-835.
48. Ozkanlar, A.; Clark, A. E., ChemNetworks: a complex network analysis tool for chemical systems. *J Comput Chem* **2014,** *35* (6), 495-505.
49. Keutsch, F. N.; Cruzan, J. D.; Saykally, R. J., The water trimer. *Chemical Reviews* **2003,** *103* (7), 2533-2577.
50. Liu, K.; Cruzan, J. D.; Saykally, R. J., Water clusters. *Science* **1996,** *271* (5251), 929-933.
51. Barabási, A.-L. s.; Pósfai, M. r., *Network science*. Cambridge University Press: Cambridge, United Kingdom, 2016; p xviii, 456 pages.
52. Ebbinghaus, S.; Kim, S. J.; Heyden, M.; Yu, X.; Heugen, U.; Gruebele, M.; Leitner, D. M.; Havenith, M., An extended dynamical hydration shell around proteins. *Proceedings of the National Academy of Sciences of the United States of America* **2007,** *104* (52), 20749-20752.
53. Roberts, S. T.; Ramasesha, K.; Tokmakoff, A., Structural Rearrangements in Water Viewed Through Two-Dimensional Infrared Spectroscopy. *ACCOUNTS OF CHEMICAL RESEARCH* **2009,** *42* (9), 1239-1249.
54. Zelsmann, H. R., Temperature-Dependence of the Optical-Constants for Liquid H_2O and D_2O in the Far Ir Region. *J Mol Struct* **1995,** *350* (2), 95-114.
55. Bohm, F.; Schwaab, G.; Havenith, M., Mapping Hydration Water around Alcohol Chains by THz Calorimetry. *Angew. Chem., Int. Ed.* **2017,** *56* (33), 9981-9985.
56. Persson, R. A. X.; Pattni, V.; Singh, A.; Kast, S. M.; Heyden, M., Signatures of Solvation Thermodynamics in Spectra of Intermolecular Vibrations. *Journal of Chemical Theory and Computation* **2017,** *13*, 4467-4481.
57. Moilanen, D. E.; Fenn, E. E.; Lin, Y. S.; Skinner, J. L.; Bagchi, B.; Fayer, M. D., Water inertial reorientation: Hydrogen bond strength and the angular potential. *Proc. Natl. Acad. Sci. U. S. A.* **2008,** *105* (14), 5295-5300.

58. Charkhesht, A.; Regmi, C. K.; Mitchell-Koch, K. R.; Cheng, S.; Vinh, N. Q., High-Precision Megahertz-to-Terahertz Dielectric Spectroscopy of Protein Collective Motions and Hydration Dynamics. *J Phys Chem B* **2018,** *122* (24), 6341-6350.
59. Persson, F.; Söderhjelm, P.; Halle, B., The spatial range of protein hydration. *J. Chem. Phys.* **2018,** *148*, 215104.
60. Furse, K. E.; Corcelli, S. A., The dynamics of water at DNA interfaces: Computational studies of Hoechst 33258 bound to DNA. *J. Am. Chem. Soc.* **2008,** *130* (39), 13103-13109.
61. Furse, K. E.; Corcelli, S. A., Dynamical Signature of Abasic Damage in DNA. *J. Am. Chem. Soc.* **2011,** *133* (4), 720-723.
62. Hunt, N. T.; Kattner, L.; Shanks, R. P.; Wynne, K., The dynamics of water-protein interaction studied by ultrafast optical Kerr-effect spectroscopy. *J. Am. Chem. Soc.* **2007,** *129* (11), 3168-3172.
63. Wynne, K., The Mayonnaise Effect. *J. Phys. Chem. Lett.* **2017,** *8* (24), 6189-6192.
64. Goncalves, A. D.; Alexander, C.; Roberts, C. J.; Spain, S. G.; Uddin, S.; Allen, S., The effect of protein concentration on the viscosity of a recombinant albumin solution formulation. *Rsc Advances* **2016,** *6* (18), 15143-15154.
65. Zhang, L. Y.; Wang, L. J.; Kao, Y. T.; Qiu, W. H.; Yang, Y.; Okobiah, O.; Zhong, D. P., Mapping hydration dynamics around a protein surface. *Proceedings of the National Academy of Sciences of the United States of America* **2007,** *104* (47), 18461-18466.
66. Qin, Y. Z.; Zhang, L. Y.; Wang, L. J.; Zhong, D. P., Observation of the Global Dynamic Collectivity of a Hydration Shell around Apomyoglobin. *Journal of Physical Chemistry Letters* **2017,** *8* (6), 1124-1131.
67. Li, T.; Hassanali, A. A.; Kao, Y. T.; Zhong, D.; Singer, S. J., Hydration dynamics and time scales of coupled water-protein fluctuations. *Journal of the American Chemical Society* **2007,** *129*, 3376-3382.
68. Yang, J.; Wang, Y. F.; Wang, L. J.; Zhong, D. P., Mapping Hydration Dynamics around a beta-Barrel Protein. *Journal of the American Chemical Society* **2017,** *139* (12), 4399-4408.
69. Qin, Y. Z.; Wang, L. J.; Zhong, D. P., Dynamics and mechanism of ultrafast water-protein interactions. *Proc. Natl. Acad. Sci. U. S. A.* **2016,** *113* (30), 8424-8429.
70. Hochstrasser, R. M.; Negus, D. K., Picosecond Fluorescence Decay of Tryptophans in Myoglobin. *Proc. Natl. Acad. Sci. U. S. A.* **1984,** *81* (14), 4399-4403.
71. Halle, B.; Nilsson, L., Does the Dynamic Stokes Shift Report on Slow Protein Hydration Dynamics? *J. Phys. Chem. B* **2009,** *113* (24), 8210-8213.
72. Andreatta, D.; Lustres, J. L. P.; Kovalenko, S. A.; Ernsting, N. P.; Murphy, C. J.; Coleman, R. S.; Berg, M. A., Power-law solvation dynamics in DNA over six decades in time. *J. Am. Chem. Soc.* **2005,** *127* (20), 7270-7271.
73. Sen, S.; Andreatta, D.; Ponomarev, S. Y.; Beveridge, D. L.; Berg, M. A., Dynamics of Water and Ions Near DNA: Comparison of Simulation to Time-Resolved Stokes-Shift Experiments. *J. Am. Chem. Soc.* **2009,** *131* (5), 1724-1735.
74. Huang, K. Y.; Kingsley, C. N.; Sheil, R.; Cheng, C. Y.; Bierma, J. C.; Roskamp, K. W.; Khago, D.; Martin, R. W.; Han, S., Stability of Protein-Specific Hydration Shell on Crowding. *J. Am. Chem. Soc.* **2016,** *138* (16), 5392-5402.
75. Choi, J. H.; Cho, M., Ion aggregation in high salt solutions. IV. Graph-theoretical analyses of ion aggregate structure and water hydrogen bonding network. *J. Chem. Phys.* **2015,** *143* (10), 104110.
76. Wang, J. H., Self-Diffusion Coefficients of Water. *Journal of Physical Chemistry* **1965,** *69*

(12), 4412-4412.
77. Matsumoto, M.; Ohmine, I., A new approach to the dynamics of hydrogen bond network in liquid water. *J. Chem. Phys.* **1996,** *104* (7), 2705-2712.
78. Choi, J.-h.; Lee, H.; Choi, H. R.; Cho, M., Graph Theory and Ion and Molecular Aggregation in Aqueous Solutions. *Annual Review of Physical Chemistry* **2018**, 1-25.
79. Berendsen, H. J. C.; Vanderspoel, D.; Vandrunen, R., Gromacs - a Message-Passing Parallel Molecular-Dynamics Implementation. *Comput Phys Commun* **1995,** *91* (1-3), 43-56.
80. Pearlman, D. A.; Case, D. A.; Caldwell, J. W.; Ross, W. S.; Cheatham, T. E.; Debolt, S.; Ferguson, D.; Seibel, G.; Kollman, P., Amber, a Package of Computer-Programs for Applying Molecular Mechanics, Normal-Mode Analysis, Molecular-Dynamics and Free-Energy Calculations to Simulate the Structural and Energetic Properties of Molecules. *Comput Phys Commun* **1995,** *91* (1-3), 1-41.
81. Wang, J. M.; Wolf, R. M.; Caldwell, J. W.; Kollman, P. A.; Case, D. A., Development and testing of a general amber force field. *Journal of Computational Chemistry* **2004,** *25* (9), 1157-1174.
82. Berendsen, H. J. C.; Postma, J. P. M.; Vangunsteren, W. F.; Dinola, A.; Haak, J. R., Molecular-Dynamics with Coupling to an External Bath. *Journal of Chemical Physics* **1984,** *81* (8), 3684-3690.
83. Schrodinger, LLC, The AxPyMOL Molecular Graphics Plugin for Microsoft PowerPoint, Version 1.8. 2015.
84. Schrodinger, LLC, The PyMOL Molecular Graphics System, Version 1.8. 2015.
85. Michaud-Agrawal, N.; Denning, E. J.; Woolf, T. B.; Beckstein, O., Software News and Updates MDAnalysis: A Toolkit for the Analysis of Molecular Dynamics Simulations. *Journal of Computational Chemistry* **2011,** *32* (10), 2319-2327.
86. Kumar, R.; Schmidt, J. R.; Skinner, J. L., Hydrogen bonding definitions and dynamics in liquid water. *J. Chem. Phys.* **2007,** *126* (20), 204107.
87. Nepusz, G. C. a. T., The igraph software package for complex network research. *InterJournal* **2006,** *Complex Systems*, 1695.
88. Lazarova, N.; James, S.; Babich, J.; Zubieta, J., A convenient synthesis, chemical characterization and reactivity of $Re(CO)_3(H_2O)_3Br$: the crystal and molecular structure of $Re(CO)_3(CH_3CN)_2Br$. *Inorg. Chem. Commun.* **2004,** *7* (9), 1023-1026.
89. King, J. T.; Arthur, E. J.; Brooks, C. L., III; Kubarych, K. J., Site-Specific Hydration Dynamics of Globular Proteins and the Role of Constrained Water in Solvent Exchange with Amphiphilic Cosolvents. *Journal of Physical Chemistry B* **2012,** *116* (19), 5604-5611.

A.3. APPENDIX

A.3.1. Graph theoretical metrics for characterizing topological network properties

A.3.1.1. Local vs global clustering coefficient (C_i)

Clustering coefficient, in the context of network science, is defined in two different ways. Both definitions capture information regarding the local connectivity in any given network. Local and global clustering coefficients were computed in our molecular dynamics simulations for water hydrogen bonds (HB) in between two hen egg white lysozyme (HEWL) proteins to mimic crowding conditions, as well as in spherical droplets of bulk water with

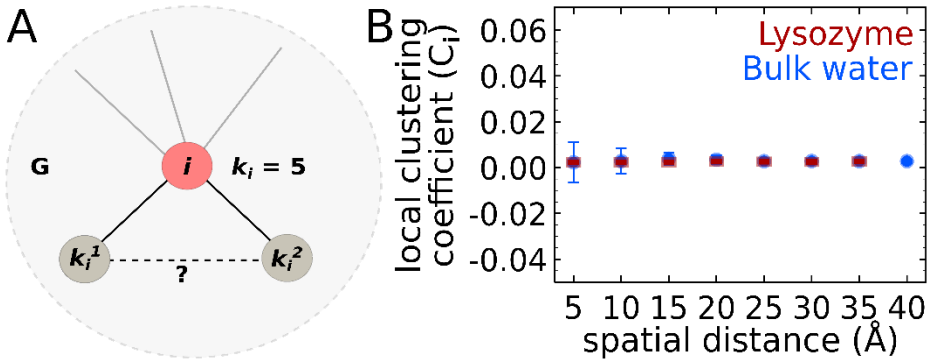

Figure A.3-1. (A) Local clustering coefficient of a node in a graph, G which is based on counting the number of links its neighbors can make with each other. For a node to have a high clustering coefficient, large populations of three-body constrained geometries need to be present. From our geometric criteria a constrained 60° angle is difficult and is only likely to be present during the transition state of hydrogen bond switching. (B) Plot showing local clustering coefficient for water in between the two Lysozyme protein and in different spherical droplets with diameters equal to the various inter-protein distances.

spatial extent comparable to the crowding cases. In the main text we presented the global clustering coefficient data which is based on counting the number of triangles (3-bonded water molecules) in a network.

The mean values for local clustering coefficients (C_i) are smaller in magnitude than the global clustering coefficients (C_Δ, as shown in main text). This difference stems from the definition of the local clustering coefficient (see **Fig. A.3-1**(A)), which counts the number of links (L_i) that neighbors (total k_i) of any given node form relative to how many theoretically can be formed ($\langle C_i \rangle = 2L_i/[k_i(k_i-1)]$). Based on any hydrogen bond definition criteria, it is almost impossible to bond the immediate adjacent neighbors of any given node (forming a triangle). **Figure A.3-1**(B) shows the calculated global clustering for hydrogen bond networks in crowded and in bulk water environements. It may be argued that the clustering

coefficient cannot be used as a good metric for characterizing HB networks.[43, 75] Having consistent values for the clustering coefficeint with different spatial dimensions implies that the local network properties remain unaltered even when there is observed to be a slight reduction in the probability of forming four hydrogen bonds, as is the case for the degree distribution plots shown in the main text.

A.3.1.2. Path length (*d*) distributions for HB networks in bulk and crowded environments

As discussed in the main text, the average path length of water droplets with different diameters led to the understanding that the topological HB network of bulk water is lattice-like. We have mentioned in the main text that it is the network topology of hydrogen bonds exhibiting lattice like behavior, not the hydrogen bond geometry itself (i.e. bulk water is not a perfect 3D lattice). The diffusion coefficient of water in the simulation box (analyzed in detail below) from which water droplets were selected was determined to be 2.69 ± 0.006 cm^2/s which agrees well with experimental value at 300 K, as would be expected for a liquid and the fact that we use the SPC/E water model.[76] The average path length in our binary

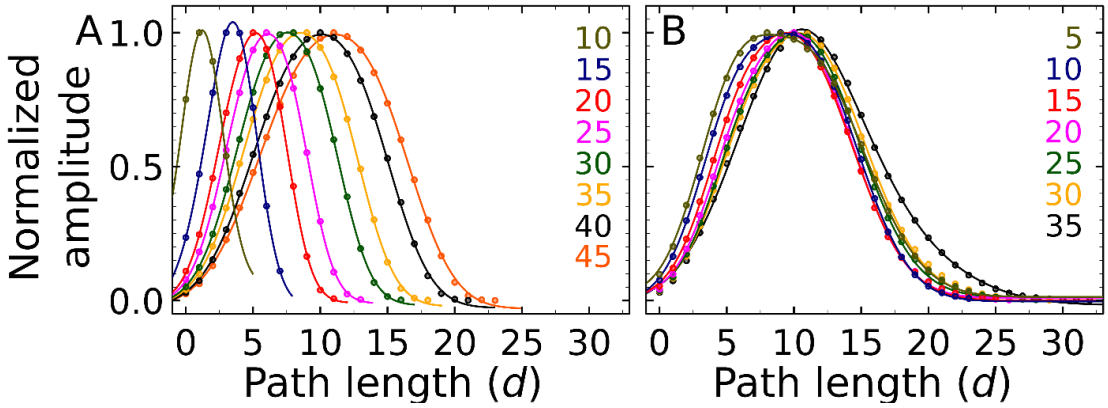

Figure A.3-2. (A) Distributions of path lengths calculated for hydrogen bond (HB) networks in bulk water droplets. Spatial dimensions in the range 10 - 45 Å have been used. Obtaining a distribution for the 5 Å diameter containing only few water molecules was not feasible so original selection is used which does not discard the lateral interface. (B) Path length distributions for HB networks in between two lysozyme proteins. A bimodal population distribution can be seen that has been fitted using sum of two gaussian where the path length was parametrized.

HEWL proteins was also observed to show similar topological variation with system size. In this supplementary section we explore additional information that path length distributions encode about the network.

Path length (*d*) distributions for bulk water droplets are computed without removing the contributions from edges formed due to selecting a finite number of water molecules. A

minimum diameter of 10 Å is used as shown in **Fig. A.3-2**(A). This approach improves statistical significance of the distribution, since data points using only 3-4 water molecules (as in case of 5 Å diameter droplet) cannot be fitted to a gaussian function without ambiguity. We observe that with increasing system size, the width of the distributions for bulk water droplets increases. The distributions for nearly all diameters of the droplets (20 Å and above) can only be fitted well using a sum of two Gaussians with individual positions as fit parameters. The observed increase in the width of the distribution, particularly at large diameters, indicates the presence of short and long paths. It is important to note that with an increasing number of nodes in the network, as in case of larger diameter of droplets, the path length distributions tend to converge.

Figure A.3-2(B) highlights the distribution of path lengths for hydrogen bond networks between the two HEWL proteins. Path length distributions have similar center positions, around 10 nodes. Path lengths for large inter-protein distance are consistent with bulk water network distributions with similar numbers of nodes (i.e. water molecules). Like bulk hydrogen bonds, path length distributions of HB networks in the crowded region of the two proteins show an equilibrium containing two populations. Short path lengths obtained using a Gaussian fit are roughly consistent with average path lengths, which is discussed in the main text. The presence of large path lengths in small inter-protein distances is due to contribution from the lateral dimension of the cylindrical water selection (i.e. around the cylinder). In the main text, we described how we were able to remove this constant path length contribution.

The fitting function (*f(x)*) used to model the HB network path length distributions in between two proteins and in bulk waters is a sum of two Gaussians where amplitudes (*a* and *d*), positions (*b* and *e*), widths (*c* and *f*) and offsets (*g*) are adjustable parameters.

$$f(x) = ae^{-(x-b)^2/c} + de^{-(x-e)^2/f} + g$$

Table A.3-1. Fit parameters obtained for sum of gaussians used to fit the path length distributions of HB network in between crowded protein environments.

Inter-protein	*a*	*b*	*C*	*d*	*e*	*f*	*g*
5 Å	0.46	**5.15**	13.59	0.90	**10.84**	37.63	0.01
10 Å	0.51	**5.31**	14.66	0.91	**10.98**	29.26	0.00

15 Å	0.24	**5.38**	11.54	0.96	**10.17**	34.35	-0.10
20 Å	0.20	**5.38**	10.50	0.97	**10.26**	32.06	0.01
25 Å	0.18	**5.79**	10.84	0.96	**10.63**	35.10	0.01
30 Å	0.16	**6.02**	11.26	0.96	**10.86**	37.76	0.01
35 Å	0.86	**9.98**	39.34	0.25	**15.47**	64.26	-0.02

Table A.3-2. Fit parameters for sum of gaussians used to model path length distributions of HB network in bulk water droplets.

Diameters	***a***	***b***	***c***	***d***	***e***	***f***	***g***
10 Å	0.96	1.22	4.70	0.05	-	-	-
15 Å	0.54	4.14	4.41	0.63	2.61	6.93	-0.01
20 Å	0.35	6.57	4.58	0.84	4.35	9.41	-0.01
25 Å	0.29	8.08	5.21	0.91	5.38	12.32	-0.01
30 Å	0.91	6.58	17.01	0.36	10.15	8.24	-0.02
35 Å	0.89	7.28	20.22	0.42	11.39	10.73	-0.02
40 Å	0.87	8.39	26.21	0.47	13.28	15.04	-0.03
45 Å	0.86	9.12	30.75	0.50	14.51	18.32	-0.03

A.3.1.3. Calculations of "effective" length for hydrogen bond network in binary proteins.

The volumes of water selected in between the two proteins were determined. Total volume equals the volume of cylinder of radius 5 Å (sub-selection, $2r < L$) plus the end cap volume excluded by the proteins. Below is the tabulation of effective distance calculations.

Protein diameter (approximate) ~ 12.5 Å

Effective distances calculated as,

Volume of water selection = $L_{effective}$ (2×2.5Å)^2

The effective distance calculated by projecting the water selected in the inter-protein region

to a cuboid geometry as shown in **Table A.3-3**

Table A.3-3. Effective length of networks for water in flexible and restrained proteins.

Flexible proteins		**Restrained proteins**	
$L_{spatial}$ (Å)	$L_{effective}$ (Å)	$L_{spatial}$ (Å)	$L_{effective}$ (Å)
5	4.05	7	5.62
10	7.98	12	9.55
15	11.90	17	13.47
20	15.83	22	17.40
25	19.76	27	21.33
30	23.68	32	25.25
35	27.61	37	29.18

A.3.2. Undirected graphs for representing hydrogen bond networks

Although hydrogen bonding between two molecules can be argued to have directionality (donor vs. acceptor molecules), in this work, we represent connectivity patterns of hydrogen bonds between water molecules in crowded and bulk environments using undirected graphs. Each water molecule can accept and donate equal numbers of hydrogen bonds (two for each case), provided the geometric criteria for bond definition is satisfied (section S6). To investigate any structural aspects of the network, non-directional connectivity information alone should be sufficient to quantify and characterize hydrogen bonding. Undirected graphs so far have successfully been applied to represent hydrogen bond networks in dense and highly crowded environments, though not yet in the context of macromolecular crowding.[77, 78] Water molecules that are spatially isolated or are at the edges of the geometric selection can only have either in or out degrees. Using directed graphs, one is likely to undercount the connectivity of those nodes since the path between an arbitrary node A to B in the network is likely to be different than from B to A.

A.3.3. Degree correlations for water in crowded and bulk environments

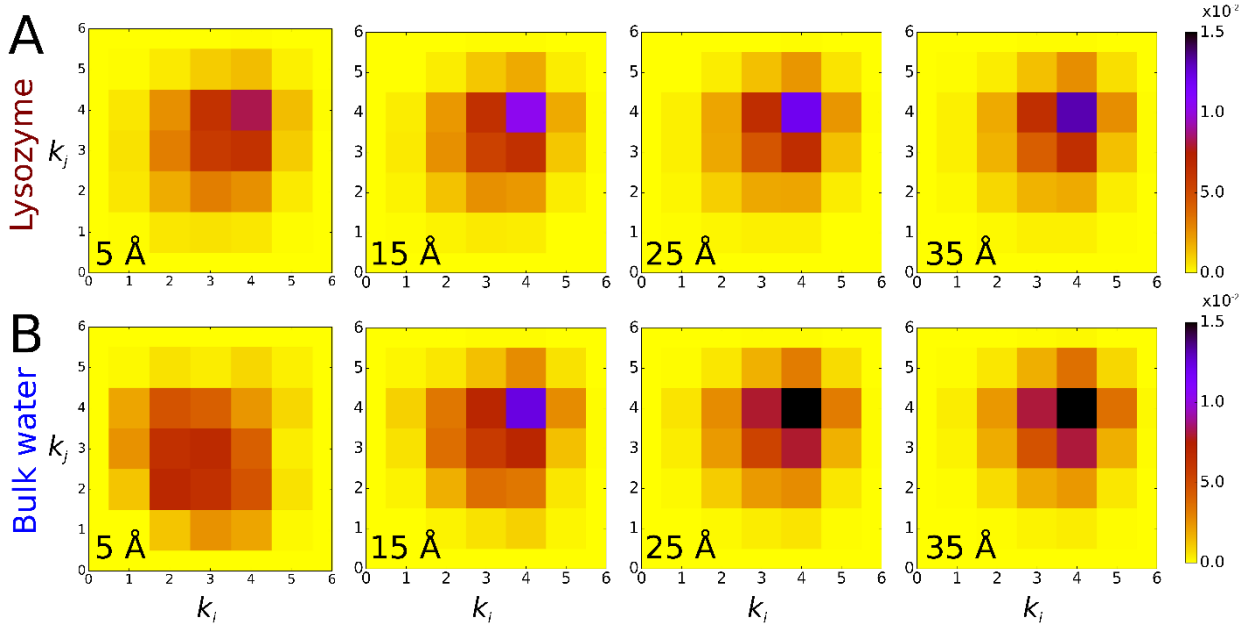

Figure A.3-3. (A) Degree correlation matrix for water in the crowded region between two lysozyme proteins. The correlation matrix is normalized by area. The symmetric nature of the degree correlation matrix indicates that HB networks across different dimensions of the system lack any correlation in linking nodes of varying degree. The HB network does not show any assortative or disassortative characteristics implying that high degree nodes have equal preference for connecting to smaller nodes and vice-versa. Water molecules inherently can form a maximum of 4 bonds and the correlation map also shows a maximum at four coordination number between donor and acceptor degree. (B) Degree correlation map for bulk water droplets studied in this work. The average degree (number of hydrogen bonds) shows slight variations between the lysozyme and bulk water cases at small spatial dimensions, particularly for the 5 Å distance. For this dimension we are looking at only 3-4 water molecules, hence a broad distribution is expected. The intensity magnitudes for the bulk water and binary proteins are slightly different but consistent with each other across different spatial distances. Overall, the distribution pattern does not show any variation between the crowded and bulk water.

An additional metric that we used to characterize the HB network in crowded and bulk like environment was using the degree correlation matrix. **Figure A.3-3** shows the degree correlation matrix, computed by counting how many occurrences of node of degree (k_i) connect with another node of degree (k_j) from our adjacency matrix. No additional network structural changes can be observed from our correlation matrix. Overall the HB network has neutral preference for connecting with nodes of any given degree.

A.3.4. Diffusion constant of water in crowded protein and bulk

In addition to hydrogen bond network topological analysis, transport properties of water in crowded and bulk like environments were also performed. **Figure A.3-4**(A) shows the mean

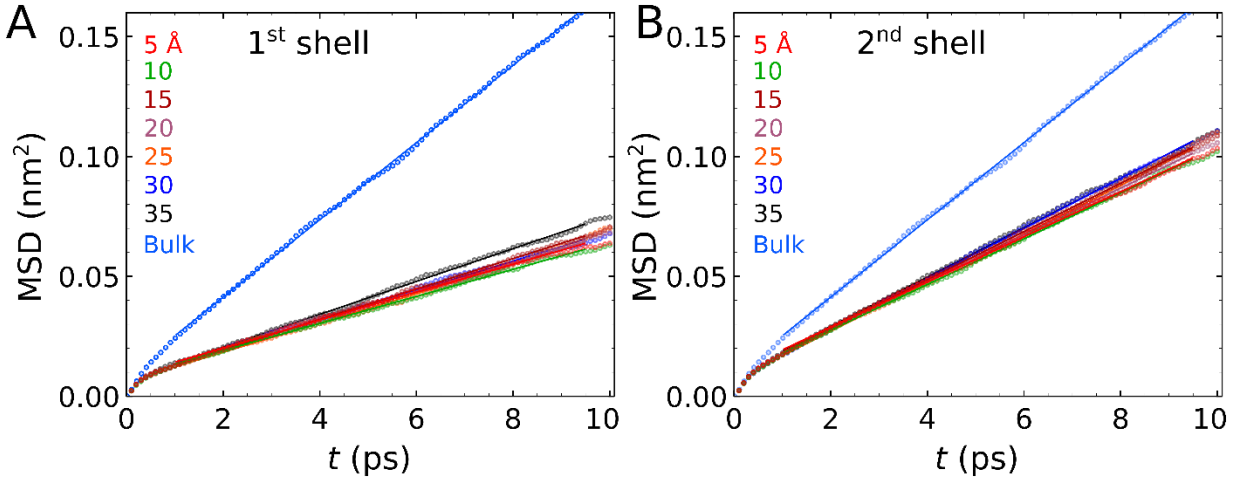

Figure A.3-4. (A) Mean square displacements (MSD) as a function of time for water molecules in the crowded region that start within the first hydration shell. For comparison, also shown is the bulk water MSD. Our results corroborate the expectation that due to the restricted degree of freedom in either one or two dimensions, the first shell water molecules should have reduced diffusivity compared to the bulk liquid. (B) MSD curves for the second shell water molecules in the crowded region. Also, for comparison is shown MSD curve for bulk water. The second shell diffusion speeds up compared to that of bulk but still experiences overall retardation compared to bulk.

square displacement (MSD) of water molecules in the first and second hydration shells of the proteins facing the crowded region. The first hydration shell of the protein encompasses all water molecules within 2.8 Å of the protein interface, while the second shell contains waters from 2.8 Å to 5.6 Å. During our defined 10 ps time window, most of the water remains in the starting shells with a relatively small fraction switching shells. Remaining in the shells is consistent with the diffusivity of water, where the root-mean-square displacement in 10 ps is 3.7 Å.

Fit parameters for calculating the diffusion constant are tabulated in **Table A.3-4**.

Table A.3-4. Parameters obtained from fitting mean square displacement of water in different shells of protein facing the crowded region representing diffusion constant of water for random walk in 3-dimension.

	Spatial distance (Å)	D (x 10^{-5} cm^2/s)	Fit Error (x 10^{-5} cm^2/s)
	5 Å	0.97	0.005
	10 Å	0.94	0.004
	15 Å	1.06	0.003

First shell	20 Å	0.99	0.006
	25 Å	1.02	0.006
	30 Å	1.02	0.006
	35 Å	1.14	0.004
Second shell	5 Å	1.57	0.005
	10 Å	1.59	0.004
	15 Å	1.67	0.003
	20 Å	1.62	0.004
	25 Å	1.69	0.007
	30 Å	1.74	0.004
	35 Å	1.72	0.006
	Bulk SPC/E	2.69 (300 K)	0.006
	Experiment[76]	2.57 (298.15 K)	0.022

A.3.5. Dipole correlation function of water in hydration shells and the bulk

We did not observe any long-range collective motions of water using vibrational density of states (VDOS) calculations in different shells of water between proteins. Also, the HB networks did not show any quantifiable differences in network topology between crowded and bulk conditions. Using the dipole correlation function of water in different shells of the protein facing the crowded region, we find some shell dependence in orientational correlation times as shown in **Figure A.3-5**. The first shell water molecules are significantly slowed compared to more distant shells (second and third). We know there is a shell dependence, but we cannot say at this point whether there is a protein-protein distance dependence as well. Overall, we can comfortably conclude that at small inter-protein distances (5 - 15 Å) we see additional slowdown for the dipole correlation data. But for larger inter-protein distances, no substantial trend could be observed in the timescale. We attribute the lack of observing any meaningful trends to the fact that we cannot sample our dipole correlation function in different shells for longer times. Running a long trajectory for dipole

correlations will scramble the water molecules, losing the association of water molecules with distinct shells. On the other hand, averaging short time windows limits convergence in our 50 ps simulation. Even if we were to average the dipole correlation functions, we would expect to see the effect of waters switching different shells.

For inter-protein distances of up to 15 Å (7.5 Å from the center to protein interfaces, which

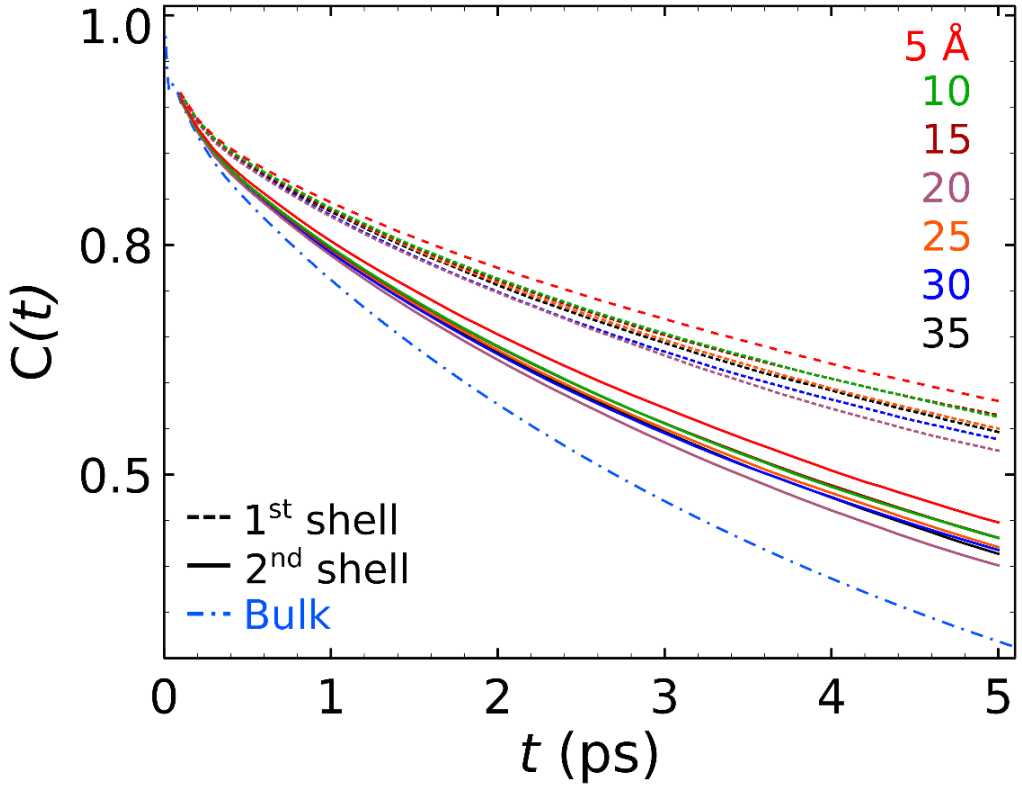

Figure A.3-5. Dipole correlation function for water molecules in the crowded region of the protein in different hydration shells and with varying inter-protein distances. Also, for comparison is shown the dipole correlation for bulk water (blue, dot dash). Overall, we see a clear trend in the dipole correlation slowing down for the first hydration shell while the second hydration shell is faster, but not bulk like. Variation with inter-protein distances does have slight effect on the correlation times but no clear trend can be observed in during our observation window of 10 ps.

fits 2 shells) we do not see this switching behavior in our dipole correlation plot shown in **Figure A.3-5**. Previously from our MSD data, we found that the maximum displacement of water molecules during 10 ps time is 3.8 Å (agrees with experiment since we use SPC/E water), which is slightly greater than the first shell of water molecules. For small inter-protein distances (up to 15 Å), during this time water molecules remain in either the first or second shell, while for larger separations water molecules can readily jump to more distant shells. Hence, we have observed a minimum impact of shell switching for small inter-protein

distances, which is not observed to be significant in large protein separations.

A.3.6. Simulation and Experimental details

A.3.6.1. Molecular dynamics simulation

Different degrees of crowding in Hen Egg White Lysozyme (PDB code 3IJU) protein were simulated by systematically varying the minimum distance between the surfaces of two protein, ranging from 5 – 35 Å in steps of 5 Å. These distance gradients were simulated using GROningen MAchine for Chemical Simulations (GROMACS)[79], first by solvating with SPC/E water molecules incorporating periodic boundary conditions and later neutralizing with 16 chloride anions. The simulation box size along the inter-protein axis was varied from 108 to 133 Å to minimize the overall computation time. Comparison of protein-water simulations with bulk water is also performed in this study. All configurations of the two proteins and a 50 Å periodic box containing only SPC/E water molecules were simulated using GROMACS (version 4.5.5 for the binary protein simulations and 5.0.5 for pure water) with the AMBER99[80, 81] all-atom force field. The isobaric-isothermal ensembles were maintained at 1 atm and 300 K using the Berendsen barostat and thermostat respectively[82]. Time coupling constant of 1 ps was used for both pressure and temperature, and the system compressibility was set to 4.5 x 10^{-5} bar. Particle-mesh Ewald (PME) summation was used to determine electrostatic energies with a Fourier- transform grid width of 1.2 Å, and real-space Coulomb and Lennard-Jones cutoffs of 9 Å. The PME-shifted potential cutoff was set to 10^{-5}. The Leapfrog Verlet integrator was used with an integration time step of 1 fs. Energy minimization of the simulations were performed using steepest-descent algorithm for 500 steps which had a tolerance of 10 kJ mol^{-1} nm^{-1} followed by an equilibration run of 50 ps. The final production run was performed for 300 ps in case of the protein and bulk water simulation for which the coordinates were saved every 10 fs.

A.3.6.2. Topological network analysis for bulk and crowded waters

Topological analysis of hydrogen bond networks was performed for water within the crowded region of the binary protein system. A control experiment using pure water droplets having diameters equal to the inter-protein distances was also carried out. Geometric selection of water molecules was executed using PYMOL's *select bymolecule* command[83, 84]. This selection algebra in PYMOL selects whole water molecules (one oxygen

and two hydrogens) within a specified radius from the center of two proteins.

This spherical water droplet was further trimmed using a simple python script to yield a cylinder of water molecules. Only those water molecules in between two proteins were selected whose geometric centers lie within the cylinder of radius 19 Å (38 Å total lateral diameter) with the center of the selection passing through a line connecting the two proteins. The radius of the cylinder was chosen to include water molecules that cover the protein interface maximally. The geometrical shape of a cylinder was preferred over a sphere in the case of the binary protein simulations to minimize contributions from bulk water in our analysis. Spheres of water with diameters equivalent to inter-protein distances were

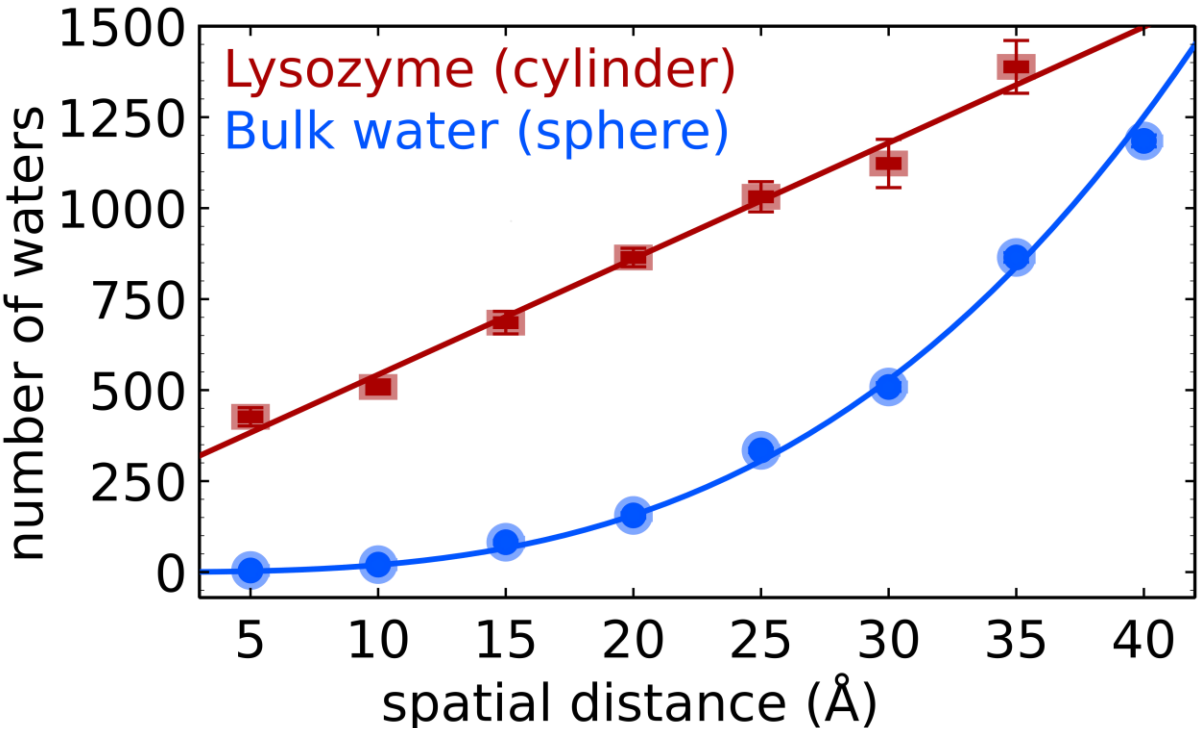

Figure A.3-6. Plot showing the number of waters in the region of interest averaged over all the simulation snapshots. Error bars indicate the spread of values within one standard deviation from the mean. For protein simulations, the number of waters scales linearly (solid maroon line is the fit) with spatial distance as indicated by the cylindrical geometry. In the case of bulk water, the number of waters in the selection scales with the third power of the spatial distance (spherical geometry) as indicated by the solid blue curve.

generated from a separate simulation of SPC/E water alone to represent bulk-like properties. The number of selected water molecules either shows a linear or cubic dependence with spatial distances, consistent with the dimensions of selections as shown in **Figure A.3-6**.

The determination of hydrogen bonds between pairs of water molecules was performed using the MDAnalysis[85] python package. The geometric distance and angle cutoff criteria were used as defined by Skinner and co-workers[86] also graphically represented in **Figure A.3-7**(A). Hydrogen bond determinations and network topology calculations were averaged every 15 ps in our 300 ps simulation (a total of 20 frames) for the binary protein simulations. The computed maximum hydrogen bond correlation time constant of ~12 ps ensures that each snapshot is uncorrelated and only structural effects dominate our analysis. For the bulk

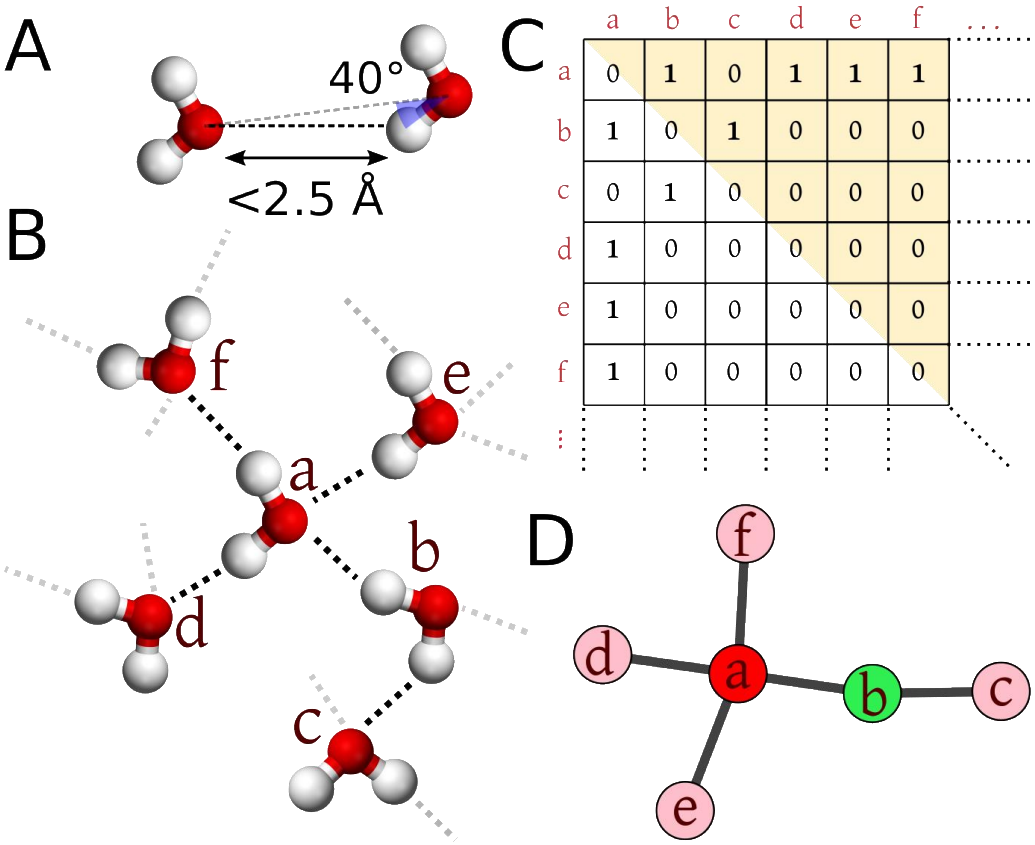

Figure A.3-7. (A) Hydrogen bonded water dimer showing geometrical criteria used in this study for defining a hydrogen bond between oxygen atom of first water molecule (*i*) and hydrogen atom of second water molecule (*j*). Two water molecules are hydrogen bonded if oxygen(*i*)-hydrogen(*j*) bond distance is less than 2.5 Å and oxygen(*i*)-oxygen(*j*)-hydrogen(*j*) bond angle is less than 40°. (B) An example cluster of six water molecules (labeled randomly) are shown representing a sub-selection in the simulation box. Water molecules in the cluster can hydrogen bond with molecules within (black dashed lines) or outside (grey dashed lines) the selected region. (C) The labeling scheme used in (B) is used to map hydrogen bond between any two water molecules using adjacency matrix. A value of 1 in adjacency matrix corresponding to a given row and column representing the water labels represents formed hydrogen bond while a value of 0 represents no hydrogen bond between those water molecules. Adjacency matrix is symmetric for our case (upper triangle equal lower triangle). (D) A graph object is created using the adjacency matrix in (C) where water molecules are represented using nodes and hydrogen bonds using edges.

water simulations, snapshots were averaged every 20 ps (for a total of 15 frames). For

selected sub-ensemble of waters, it was needed to determine whether any given pair (i, j) is hydrogen bonded or not. This hydrogen bond connectivity information between every water molecule pair was used to construct an adjacency matrix (M_{ij}) as shown in **Figure A.3-7**(C). The matrix elements M_{ij} are assigned either a value of 1 if a pair is hydrogen bonded or 0 if it's not. The adjacency matrix in our case is symmetric for all water selections. The adjacency matrix for selected waters is used to map hydrogen bond connectivity, which is then used to calculate local and global topological network parameters. Average hydrogen bond numbers ("degree") and degree distributions are determined by counting the number of hydrogen bonded partners for every water molecule from an adjacency matrix. Local and global network topologies are characterized using metrics of clustering coefficient (C_Δ) and average path length ($<d>$) using the Python igraph[87] package. All our network analysis is based on undirected graphs.

A.3.6.3. Vibrational density of states calculations

Water molecules within the crowded region of the binary protein simulations are selected at specified distances from the surfaces of the two proteins. Water molecules within 2.8 Å are defined as the first shell, from 2.8 Å to 5.6 Å is referred to as the second shell and so on. Computation of the vibrational density of states (VDOS) for each shell from 0 to 1000 cm^{-1} was performed by Fourier transforming the velocity autocorrelation function of individual atoms (hydrogens and oxygens separately) within a shell. The final spectrum is obtained by adding the individual hydrogen and oxygen VDOS spectrum in their stoichiometric ratio. To minimize diffusion of waters within shells, only 50 ps simulation was used for analysis. This short simulation was further split into 10 ps trajectories and individual VDOSs were averaged to yield the final spectrum. VDOS spectra were computed using the *velacc* function in GROMACS.

A.3.6.4. Synthesis of Rhenium probe, Lysozyme sample preparation and FT-IR spectra

A metal carbonyl molecule, ($[Re(CO)_3(H_2O)_3]Br$) was used to probe spectral diffusion of water in high concentrations of lysozyme. Synthesis of the rhenium probe was carried out using an established method[88]. Briefly, commercially available water insoluble $[Re(CO)_5]Br$ was refluxed for 24 hr in H_2O. After the reaction was over, the solution was dried using a rotatory evaporator until dryness. FT-IR spectra for the synthesized compound was acquired

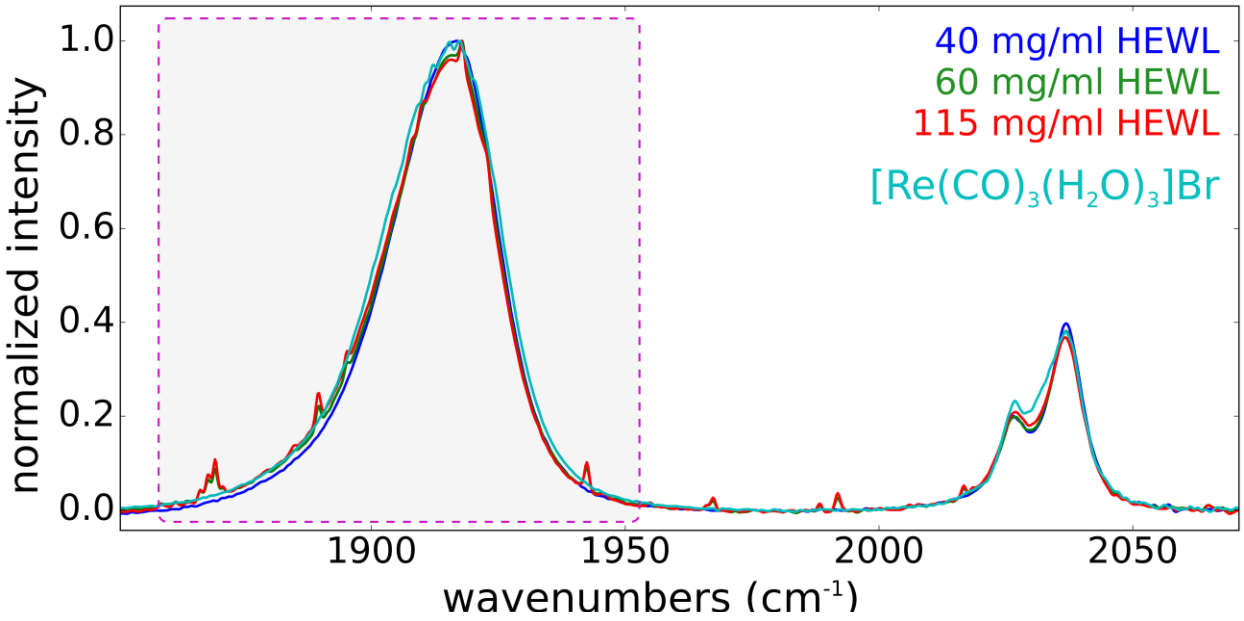

Figure A.3-8. Experimental FT-IR spectra for rhenium metal carbonyl probe ($[Re(CO)_3(H_2O)_3]Br$) in different concentrations of HEWL in H_2O at room temperature (298 K). The intense asymmetric carbonyl stretch mode at ~1910 cm^{-1} was probed in 2D-IR spectral diffusion measurements (highlighted). Metal carbonyl probe is stable even at high protein concentrations. Intermittent sharp peaks correspond to ambient water absorption.

in H_2O. Lysozyme samples were prepared by dissolving respective mass of protein in a constant 25 mM concentration of our probe in H_2O. The mixture was stirred before placing 75 µL of solution between two CaF_2 windows. FT-IR spectra were acquired before 2D-IR measurements as shown in **Figure A.3-8**. The amplitude of the rephasing 2D-IR spectrum at the diagonal peak corresponding to the asymmetric mode of the probe yields a measure of the vibrational relaxation. Vibrational lifetime measurement shown in **Figure A.3-9** confirms that our rhenium probe remains well hydrated in different crowding environments. This conclusion is based on the fact that water induces very rapid vibrational relaxation, and dehydration of water leads to significant slowdown in vibrational relaxation.[89]

Rephasing amplitudes obtained are fitted to a bi-exponential function representing spectral diffusion and vibrational lifetime of our probe in different hydration environments. Fit parameters obtained are tabulated in **Table A.3-5**.

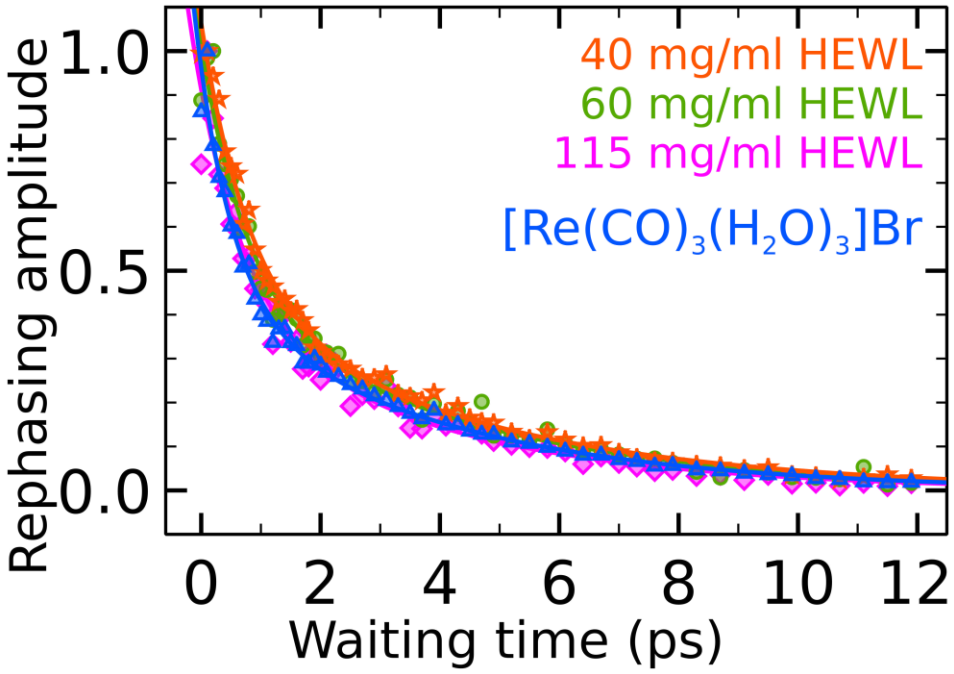

Figure A.3-9. Normalized rephasing peak amplitude corresponding to the mode at ~1910 cm^{-1}. The decay in amplitude represents vibrational lifetime of our probe in different environments. From the decay time constant (tabulated below) it can be inferred that the probe remains well hydrated.

Table A.3-5. Fit parameters along with fit errors, obtained using bi-exponential [a*exp(-x/b) + c*exp(-x/d)] fits of experimental data points corresponding to rephrasing amplitudes of our rhenium vibrational probe in different hydration environments.

Experiment	*a*	*error*	*b (ps)*	*error*	*c*	*error*	***d (ps)***	*error*
Bulk water (H_2O)	0.54	0.04	0.60	0.07	0.42	0.04	**3.97**	0.36
40 mg/ml HEWL	0.62	0.04	0.80	0.07	0.45	0.04	**4.37**	0.35
60 mg/ml HEWL	0.57	0.06	0.77	0.12	0.44	0.07	**4.22**	0.57
115 mg/ml HEWL	0.51	0.10	0.82	0.20	0.40	0.11	**3.81**	0.77

A consistent value of fitting parameter representing vibrational lifetime of our probe (*'d'*) obtained indicates a well-hydrated environment of the probe up to the highest concentration of protein studied in this work.

A.3.7. Effect on collective protein motions upon crowding

A.3.7.1. VDOS for Lysozyme residues experiencing crowding and no crowding

The vibrational density of states for hydrogen bonded water presented in the main text does

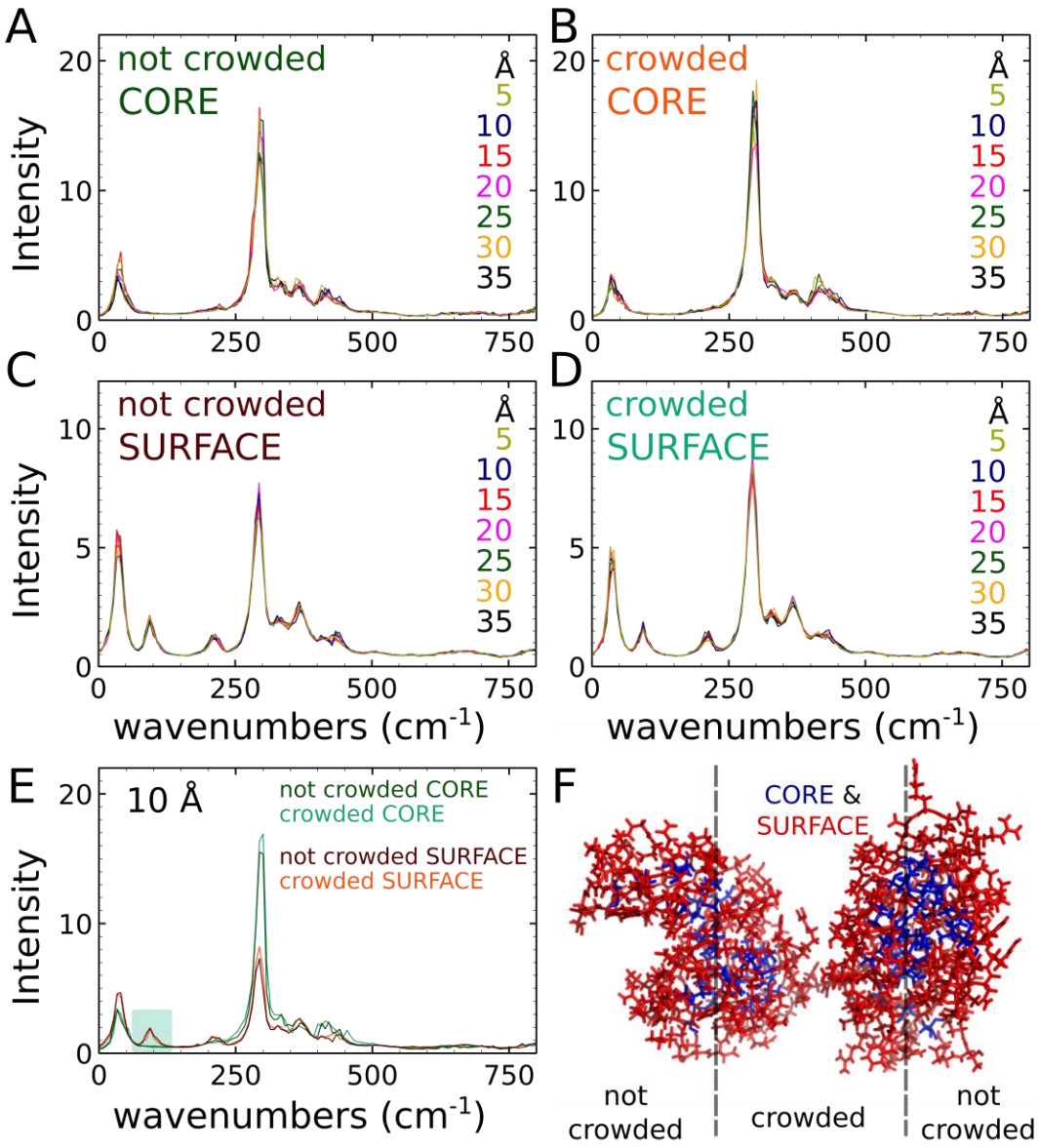

Figure A.3-10. Vibrational density of states (VDOS) spectra for atoms in the core region of the protein (A) with and (B) without crowding, respectively, with varying degrees of crowding (inter-protein distances in angstroms). VDOS spectra for atoms in the surface of the protein (A) with and (B) without crowding, respectively, with varying degree of crowding (inter-protein distances in angstroms). (E) Comparison of VDOS spectra for protein atoms in different scenarios considered in figure (A) – (D), at a fixed inter-protein distance of 10 Å. The intensity variations in crowded and uncrowded regions of the protein are consistent with the positions of atoms either in the CORE or SURFACE regions. Notice the small feature around 100 cm^{-1} corresponding to the protein librational motions. (F) Configurations corresponding to 5 Å inter-protein distance highlighting the CORE and SURFACE residues. The dashed line approximately represents the cutoff for selecting crowding and not crowded residues which passes through the center of each protein chain.

not reveal any significant perturbation to the collective motions of water beyond the second hydration shell. In the regime of extreme crowding, we nonetheless found significant reduction in the protein flexibility, particularly for the residues facing the crowded regions. It can well be argued that protein flexibility should not be the only cause for observing additional slowdown in water dynamics probed using site-specific labeling approaches. In order to address this issue, we also computed vibrational density of states (**Fig. A.3-10**) for residues facing the crowded region and compared that with those residues exposed to the bulk water environment. Residue selections in different protein configurations where performed first by identifying SURFACE and CORE residues in single lysosome protein using PYMOL's *findSurfaceResidues* extension with a cutoff area of 2.5 $Å^2$. Atoms in the protein that face each other are defined to be crowded while those facing away are defined to be not crowded. We find that the vibrational density of states for protein atoms in both the core and surface residues do not exhibit any significant dependence on the inter-protein separation. The only significant conclusion that we can make at this point is that between the surface and core residues, new modes appear around 100 cm^{-1} which indicates flexibility of the surface protein atoms distinct from the core atoms.

A.3.7.2. Surface fluctuation correlation and hindered sampling rate upon crowding

We have shown in the main text that the magnitude of atom fluctuations becomes reduced when the protein surfaces come very close together. In the case of two proteins with a negative enthalpy of binding, such spontaneous process may show a gradual reduction in side chain fluctuation correlation times. In the previous section, we observed no dramatic dependence of the velocity autocorrelations on the protein-protein distance, but this finding does not imply identical side chain fluctuation correlation times. To address the dynamical aspect, we calculate each atom's fluctuation correlation on the side which faces the crowded region. For each atom we computed the displacement from its starting position ($R(t) = r(t) - r(0)$) and then determine the fluctuation correlation function, $C(t) = \langle R(0)R(t) \rangle$ as shown in **Fig. A.3-11**(A). For small inter-protein distances (i.e. a higher degree of crowding), we find short average correlation times, indicating not only hindered motion but also retardation in the dynamics of protein fluctuations during our observation window. To further validate our hypothesis of slowed dynamics of protein fluctuations we show a plot in **Fig. A.3-11**(B) of

diffusion for sampling different environments. Using the root mean square fluctuation (MSD = RMSF^2) which indicates the mean displacement of atoms during the average correlation times. We find that for the smallest inter-protein distance of 5 Å, the rate of sampling different microenvironments by the surface protein residues (dynamics) is distinctly slower compared to large separations (no crowding). Hence, at extreme crowding we show that the overall sampling rate of protein side chains is significantly retarded.

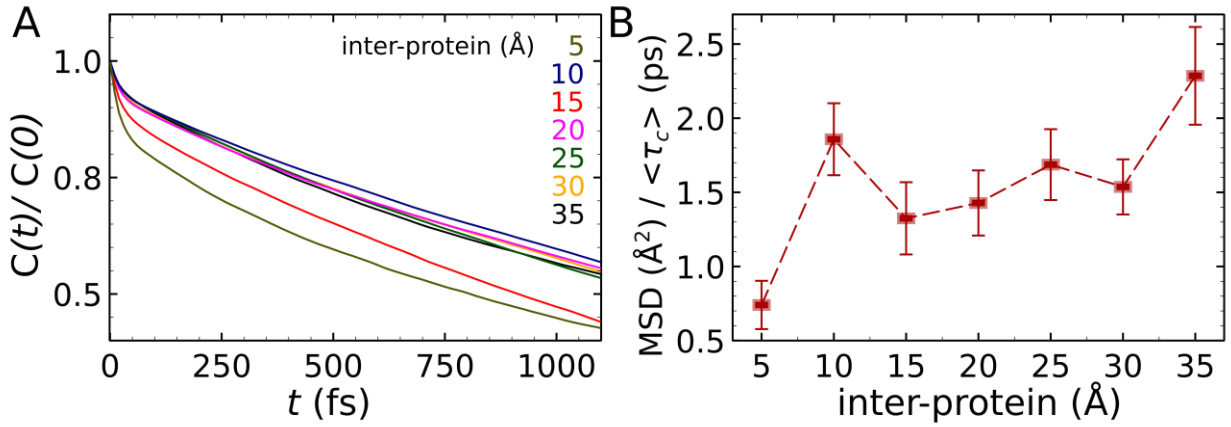

Figure A.3-11. (A) Atom position fluctuation correlation function for atoms facing the crowded region of the protein in different degrees of crowding (inter-protein distances). (B) Average sampling rate computed based on the most probable root mean square fluctuation and average fluctuation correlation times.

The observed transition between 5-10 Å of inter-protein separation is also consistent with the "dewetting" transition of water near hydrophobic surfaces[10].

Table A.3-6 .Tabulation of fluctuation parameters obtained using atoms selected on Lysozyme surface

Inter-protein	RMSF(Å)	<τ> (ps)	error	RMSF/<τ>	error	**MSD (Å²)/<τ>**	error
5	0.68	619.7	13.62	1.09	0.24	**0.74**	0.16
10	1.18	753.9	9.84	1.57	0.20	**1.86**	0.24
15	0.94	666.3	12.25	1.41	0.26	**1.323**	0.24
20	1.03	738.6	11.36	1.39	0.21	**1.43**	0.22
25	1.12	737.2	10.44	1.51	0.21	**1.67**	0.24
30	1.07	738.8	8.94	1.44	0.17	**1.54**	0.19
35	1.30	731.7	10.55	1.77	0.25	**2.29**	0.33

A.3.8. Fit parameters for hydration dynamics with and without protein fluctuations

Hydrogen bond correlation times representing the timescale for switching were obtained using fluctuations in the degree number for each water ($<n(t)n(0)>$) in the crowded region of the protein-water simulations. **Table A.3-7** shows obtained fit parameters for the biexponential function with an offset used to fit the hydrogen bond time correlation function.

Table A.3-7 . Tabulation of fit parameters obtained from fitting hydrogen bond time correlation functions using a biexponential function, a*exp(-x/b) + c*exp(-x/d) + e.

Inter-protein (Å)	a	Error (a)	b (**short time**)	Error (b)	c	Error (c)	d (**long time**)	Error (d)	e	Error (e)
Flexible proteins										
5	0.641	0.004	0.447	0.006	0.389	0.012	**9.866**	0.678	-0.220	0.015
10	0.390	0.003	0.200	0.002	0.669	0.001	**3.894**	0.020	-0.179	0.001
15	0.256	0.003	0.106	0.002	0.779	0.001	**2.195**	0.005	-0.099	0.000
20	0.369	0.003	0.122	0.002	0.602	0.001	**2.529**	0.010	-0.085	0.000
25	0.328	0.002	0.288	0.004	0.717	0.001	**3.671**	0.018	-0.177	0.001
30	0.310	0.002	0.212	0.002	0.762	0.001	**3.398**	0.010	-0.171	0.001
35	0.321	0.002	0.224	0.003	0.731	0.001	**3.028**	0.011	-0.150	0.001
Restrained proteins										
7	0.444	0.005	0.268	0.005	0.557	0.002	**5.118**	0.088	-0.185	0.004
12	0.440	0.004	0.096	0.002	0.515	0.001	**1.971**	0.010	-0.071	0.000
17	0.348	0.004	0.193	0.004	0.648	0.002	**2.870**	0.018	-0.120	0.001
22	0.296	0.002	0.204	0.003	0.721	0.001	**2.737**	0.009	-0.121	0.000
27	0.391	0.004	0.333	0.006	0.544	0.004	**2.206**	0.018	-0.068	0.001
32	0.289	0.003	0.118	0.002	0.762	0.001	**2.362**	0.007	-0.121	0.000
37	0.245	0.002	0.181	0.003	0.816	0.001	**2.725**	0.007	-0.141	0.000

Chapter 4

A Simple Lattice Monte Carlo Simulation Describes Interfacial and Crowded Water Rearrangements

4.1. Introduction

Understanding structural and dynamical fluctuations of water near hydrophobic interfaces poses challenges of practical and fundamental importance in chemistry, biology, and physics.[1-4] The hydrophobic effect can generally be understood as arising from the disruption of hydrogen bonding among water molecules upon addition of a solute.[5, 6] The structural consequences of solute hydration have been understood for many years, but there is considerably less consensus on the nature and degree of the solute's perturbation of water dynamics. There are two interrelated issues that must be addressed in fully characterizing interfacial hydration dynamics. The first is the degree and nature of a single interface's influence over the motion of water molecules, as well as the spatial extent of this perturbation as a function of the distance from the interface. The second challenge is to understand how multiple interfaces modulate the dynamics of interstitial water molecules, and the degree to which there is, or is not, any collective, non-additive behavior.

An extensive interdisciplinary effort has been directed at this problem, combining spectroscopy, simulations and theoretical methods, but there are still open questions and contradictions.[2, 3, 7] A significant fraction of existing experimental literature and simulations,

focus on biomacromolecular interfacial hydration for systems such as proteins[8-10], lipids[11, 12], micelles[13, 14] and nucleic acids[15]. Experiments typically make use of spectroscopic probes that may be intrinsic components of macromolecules, or covalently attached to specific sites. While the site-selective approach may have the advantage of enhancing signals arising from the interface, it is almost impossible to discern experimentally whether the observed dynamics results from the water alone or contains contributions from fluctuations of atoms or residues at the site of labeling. Alternatively, it is possible to use careful difference methods that isolate the interfacial contribution to steady-state Raman and THz spectra,[16-23] even at lower solute concentrations. Some of these approaches depend on complex models to deconvolve the interfacial signal from that due to the bulk.[24] When relative concentrations of the macromolecular component are high, it becomes possible to use water's local vibrational modes to sense dynamics near an interface, but only under conditions corresponding to significant crowding.[25] Studies using small reverse micelles effectively bridge these two regimes: the water is automatically confined to the nanoscale vesicle, but studies of the water necessarily average over both interfacial and bulk-like water in micelles large enough to consist not entirely of interfacial water molecules.[1, 26, 27] Understanding how interfaces impart slowdown of water dynamics is crucial for modeling the effect of crowding and understanding various biochemical process including but not limited to ligand binding to an enzyme, protein-protein interactions, and targeted drug delivery.

4.1.1. Summary of the Extended Jump Model and Interfacial Perturbations

In the immediate vicinity of an interface, water hydrogen bond switching dynamics is perturbed due to the reduced fraction of available partners (*f*), which increases the free energy barrier for the large angular jump mechanism, which is a three-body, termolecular elementary reaction.[28, 29] Based on this purely entropic constraint, the retardation factor can be predicted to be two-fold near a planar interface, and increasing nonlinearly with excluded water fraction (**Fig. 4.1**(A)). Within this model, to achieve an order-of-magnitude slowdown requires a 90% depletion of hydration water, which is limited to highly constrained geometries such as clefts, pockets, or grooves. Nevertheless, studies using dynamic fluorescence Stokes shift spectroscopy find evidence for extremely slow water, which would demand nearly full dehydration within the excluded volume picture.[10, 30-32]

One aspect of the excluded volume model apparent from **Fig. 4.1**(A) is the intrinsic locality of the perturbation. Although the water molecules directly in contact with the

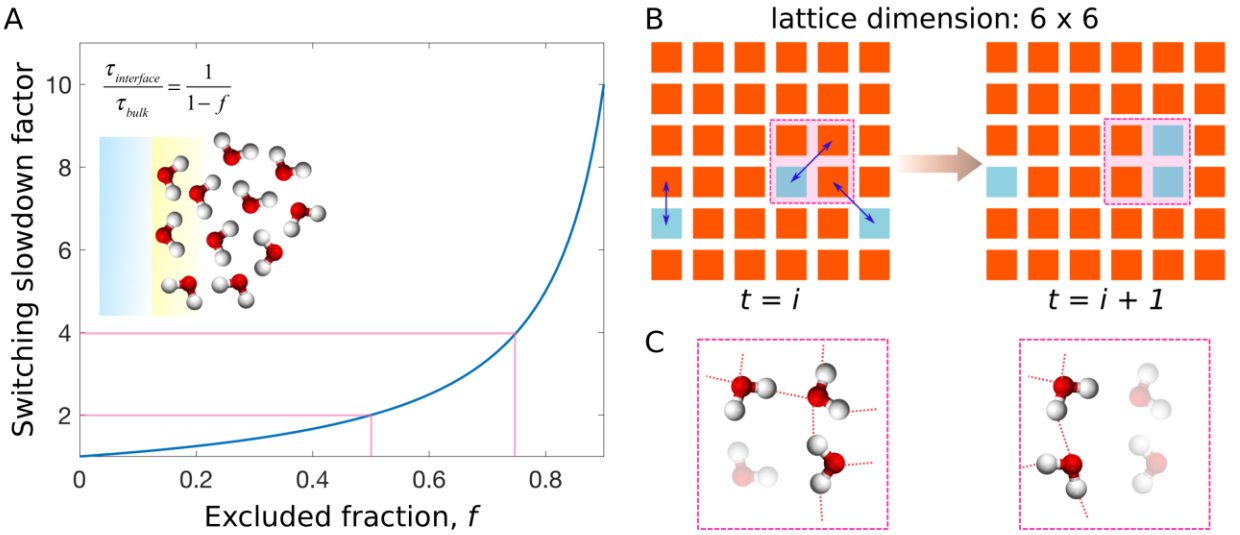

Figure 4.1. (A) The predicted slowdown of hydrogen bond switching within the entropic, excluded volume model of Laage et al. shows a highly nonlinear dependence on excluded water fraction. The cartoon highlights the local nature of this model, which would predict explicit perturbations for only those water molecules in the first solvation shell. This work aims to test whether there are any indirect, longer-range perturbations. (B) Schematic representation showing implementation of Monte Carlo simulation in 6x6 lattice. Occupied sites are represented in orange while empty sites are shown in blue. Each filled lattice sites can form maximum of 4 bonds with its immediate neighbors. A filled site can swap its position with a neighboring vacant site along any of the eight directions. Metropolis algorithm is used to determine whether move for a void is accepted or not. A move is taken only if the overall energetic cost of the swap is favorable or the Boltzmann factor is greater than a random number between 0 and 1. (C) Site switching dynamics in square lattices is analogous to the hydrogen bond switching event where bulk water molecules constantly exchanges its hydrogen bonding partner. A sub-selection of the lattice is shown originally containing 3 water molecules while after rearrangement contains 2 water molecules with different configuration of connectivity. Such fluctuation in the local coordination number of lattice sites mimics hydrogen bond switching event.

interface experience the full depletion of hydrogen bonding partners, the second hydration shell has the same number of neighboring water molecules as would be found in the bulk. Thus, the purely entropic slowdown can only apply to the first shell. The expectation is that the slowed first shell will somehow transmit its retardation to the second shell dynamically, but that coupling is mechanical rather than entropic. Significant experimental effort continues to be made to test the validity of the anticipated retardation of water dynamics at distances beyond the first hydration layer.[33]

The surface of any biological interface, such as a protein or membrane, consists of rugged topology and chemical heterogeneity. Although it is expected that concave and convex curvature slowdown and speed up water dynamics, respectively,[3, 34-36] it is not clear

to what extent the perturbation of dynamics extends from any arbitrary surface. Simulation studies of water dynamics near proteins and nucleic acids necessarily include structural and chemical heterogeneity of the interface, and the measured overall retardation factor may have contributions from a variety of influences. Hence, it may be important to understand how surface ruggedness contribute to the overall slowdown.

Remarkable progress in treating water with ever more sophistication, aided both by theoretical and computational advances, has led to the explicit representation of water polarization[37], many-body interactions,[38] electron correlation[39] and nuclear quantum effects.[40] These new physical models are able to account for phenomena that are generally missing from the fixed charge classical force fields popular in molecular dynamics simulations. It is certainly an important goal to simulate water accurately in biologically relevant systems using the most sophisticated level of theory. But remarkably, many usual and unusual properties of water emerge from simulations using very simplistic models,[41] such as the two-dimensional Mercedes-Benz,[41-43] fixed three-point charge force fields (SPC, TIP3P),[44] and even single atom models.[45]

Using a Metropolis Monte-Carlo simulation, we present a novel approach to model water's local connectivity and hydrogen bond (HB) switching dynamics in 2-D square lattices. We find that we can tune the model to give good agreement with structural (average coordination number or "degree") and dynamical properties (slowdown factor near an interface) compared to bulk water. In this work, we have also attempted to understand the switching dynamics at sites near an interface where surface topological heterogeneity is well characterized, and interactions can be eliminated. Our simple lattice model is poised to supplement the existing understanding of water dynamics near an interface. A key finding of our work is that the average switching correlation time falls off exponentially from the lattice boundary (i.e. the interface). Also, the slowdown in constrained systems can be modeled using a linear combination of individual interfaces, indicating that within this model there is no cooperative, non-additive behavior. We believe that in order to observe cooperative slowdown, a rugged surface heterogeneity is essential in addition to taking longer ranged inter-particle interactions into account.

4.2. Methods

4.2.1. Monte Carlo simulation of site switching on square lattice

Empty (all zeros) 4x4, 6x6, 8x8, 10x10, 20x20 and 25x25 square lattices (arrays) are constructed. Each site in the lattice is occupied with particles (1 for particle and 0 for voids) with a filling probability of 0.9. Two neighboring particles are understood to form a bond if they share an edge. This 4-connectivity scheme and the 0.9 filling probability ensures that the average number of bonds for each particle in the lattice mimics the average hydrogen bond number in bulk water. Bulk water is expected to have an average coordination number of 3.6, considering 10% defects.[46] Rigid boundary conditions create an interface that can be considered hydrophobic. The average coordination number of sites at flat or curved interfaces will have reduced connectivity. Vacant sites in the lattice can make random moves along any of the 8 available directions in the square lattice. Since we maintain an occupation probability of 0.9, an occupied site can only be swapped with a vacant site. The Metropolis algorithm performs particle position switching based on an energetic criterion. A move is accepted if the Boltzmann factor ($e^{-\Delta E/RT}$) is greater than a random number generated between 0 and 1. Simulations are performed for 50,000 iterations (time) and temperature is set at 298.15 K during the run. An energy of -1 kJ/mol is arbitrarily chosen as the bond energy between occupied lattice sites. An artificially low energetic barrier allows us to sample the available configurational landscape faster while also excluding enthalpic contributions (see supplementary information S5). The total energetic cost for switching a pair is determined by summing over all the energy differences that results from a new configuration. The coordination number of each site in the lattice as a function of simulation time is utilized to compute the bond correlation function $C(t)$ given by:

$$C_k(t) = \langle n_k(0) n_k(t) \rangle$$

Where $n_k(t)$ is the number of hydrogen bonds at each site, k. The average time constant is computed by integrating the normalized (i.e. $C(t=0) = 1$) correlation function for each site in the lattice. 40 trajectories with different starting configurations of the lattice were averaged to construct the correlation map.

Here, we implement a Monte Carlo simulation to investigate the effect of confinement

on site switching kinetics. The swapping of occupied sites with vacant ones captures the essence of hydrogen bond switching dynamics. In the bulk liquid, water molecules continually form and break hydrogen bonds, and a molecule completing a switch first extends its coordination with a neighboring partner thereby forming a three-body transition state. After a successful neighbor swap, the coordination number of the original partner becomes depleted by one, hence creating a vacancy. **Figure 4.1**(B) shows how this fluctuation in the position of vacant and occupied sites has been implemented in a 2-D lattice. For comparison, **Fig. 4.1**(C) shows the analogous hydrogen bond switch between water molecules in a sub-lattice between two frames.

In our simulations we have used as a time variable the number of iterations (loops) performed in the Monte Carlo simulation run. A direct relationship with absolute time (units of seconds) would require complete knowledge of the phase space being sampled by the simulation as routinely implemented by classical MD. Hence, instead of computing the absolute time scale for switching slowdown, we report the retardation factor relative to a reference bulk-like time constant (see Appendix A.4.2).

4.3. Results and Discussion

4.3.1. Spanning hydrogen bond network in bulk water

Before performing any dynamical analysis using Monte Carlo simulations, we first characterize the structural aspects of the model. Although it is common to analyze real-space atomistic structure using metrics such as radial distribution functions, in a lattice model, another useful measure of structure is the connectedness of the bonding network. Structurally, each point on the lattice represents a water molecule, which is itself a node in the network. Every occupied lattice site can form a maximum of four connections with its neighbors, which coincides with the typical maximum of 4 hydrogen bonds (2 donor and 2 acceptor) in water.[46]

The extended network of hydrogen bonds of water is thought to play an important role in the functioning of macromolecules, particularly in crowded environments. At very low hydration, the extended network of hydrogen bonds can be broken significantly, giving rise to small patches of water clusters consisting of only a few molecules. Winter and co-

workers[47] have previously shown that water clusters undergo a percolation transition at the surface of globular proteins in extremely low hydration environments. Structured water molecules in protein powders have also been shown to act as an entropic reservoir for the onset of native functioning of biomolecules.[48]

Figure 4.2 shows the largest cluster size in the square lattice with varying occupancy probabilities of the sites. A cluster is defined as any collection of occupied sites where a given site can be reached from any other site in that cluster, provided they are connected by a shared side. Having multiple disjointed clusters results in the formation of small islands of fully connected paths.

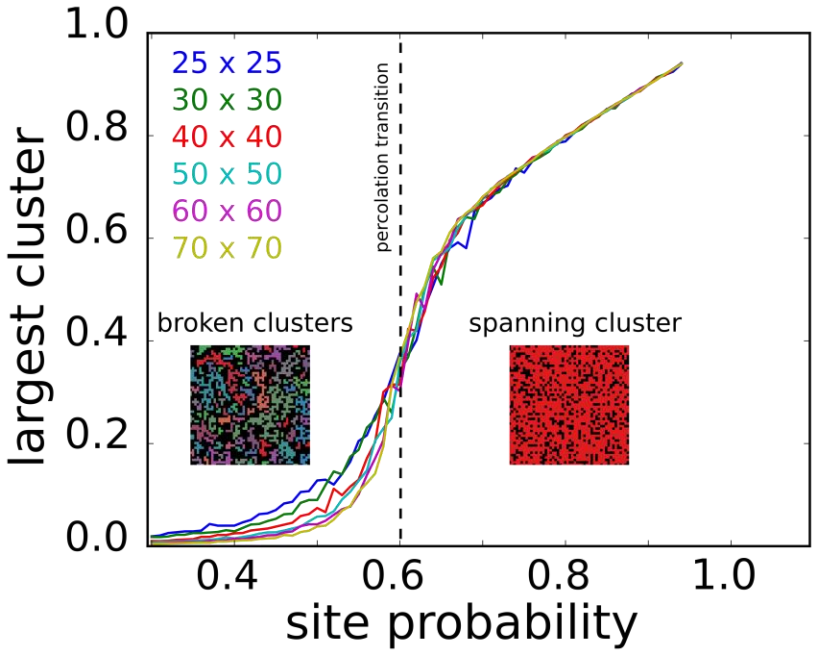

Figure 4.2. Formation of spanning (completely connected) clusters in square lattice with varying site probability. Lattice sizes from 25x25 to 70x70 have been considered where formation of spanning cluster occurs at same transition probability of 0.6. At small site probability, patches of connected cluster emerge which coalesces to form one giant cluster after percolation transition (bottom right inset). Considering 4-neighbor connectivity this probability corresponds to an average degree of ~2.4 in bulk. Below percolation threshold, lattice exhibits small patches of clusters (colored patches) as shown in the bottom left inset.

The "largest cluster" refers to the cluster with maximum number of occupied sites among all the clusters for a given configuration. The abscissa in **Fig. 4.2** has been normalized by the total number of lattice sites (N^2). Occupancy probabilities from 0.3 to 1.0 were generated for lattices of size 25x25, 30x30, 40x40, 50x50, 60x60 and 70x70.

It can clearly be observed that the onset of the percolation transition starts around a

probability of 0.5. Before the percolation transition, the lattice sites show patches of small clusters as represented in the inset of **Fig. 4.2** on the bottom left. The percolation transition occurs at the inflection point at $p \sim 0.6$ (average degree ~2.4), and is independent of the lattice dimensions, a well-known result from percolation theory.[49-51] The transition curve does appear to become steeper with increasing lattice sizes, implying that it is easier to form large clusters at the same probability in smaller square grids than in large grids. Such finite size effects are notable because rigorous theoretical values for the percolation transition are derived from infinite lattices. Beyond percolation ($p >$ ~0.7), it is apparent that most of the sites in the lattice form a giant cluster. In this regime, the largest cluster size scales linearly with occupancy probability. Previously, Winter *et al.*[52] have shown that the onset of the percolation transition in liquid water occurs around the same coordination number (degree of 2.0 – 2.3) as observed with the simplistic square lattice model. Also, the spanning water network on protein surfaces undergoes a 2-D percolation transition, also consistent with this lattice model.[53]

4.3.2. Linear scaling of average coordination number with occupation probability

In previous sections, we established that the percolation threshold in liquid water corresponds to the threshold obtained using a square lattice model. Before interpreting any dynamical observables from our simulation, it is essential to characterize the local site connectivity in the lattice relative to that of bulk water. We find a quasi-linear trend in the average coordination number for sites with varying occupation probability in square lattices as shown in **Fig. 4.3**(A). Lattice sizes of 4x4, 10x10, 20x20, 50x50, 100x100, 200x200 and 400x400 have also been compared. For the extremely small lattice size of 4x4, where the perimeter to area ratio is 1, we observe a 27% decrease in the average coordination number compared to bulk coordination number of 3.6 at 0.9 site probability as shown in **Fig. 4.3**(B). A modest percolation threshold corresponding to an average degree of ~2.4 is also shown in the plot. Although, at small lattice dimension, the average degree may appear to be smaller, we find that even at this bond connectivity only one giant cluster emerges. For all the lattice sizes, the average degree of sites studied in this work is well above the percolation threshold. **Fig. 4.3**(B) also indicates that with increasing lattice size the average connectivity converges to the bulk water coordination number of 3.6. In this work we have used square lattices with

constant occupation probability of 0.9 to mimic hydrogen bond switching dynamics in a well-understood Ising-like model. In addition, systematic variations in lattice dimensions allows us to mimic the conditions of crowding.

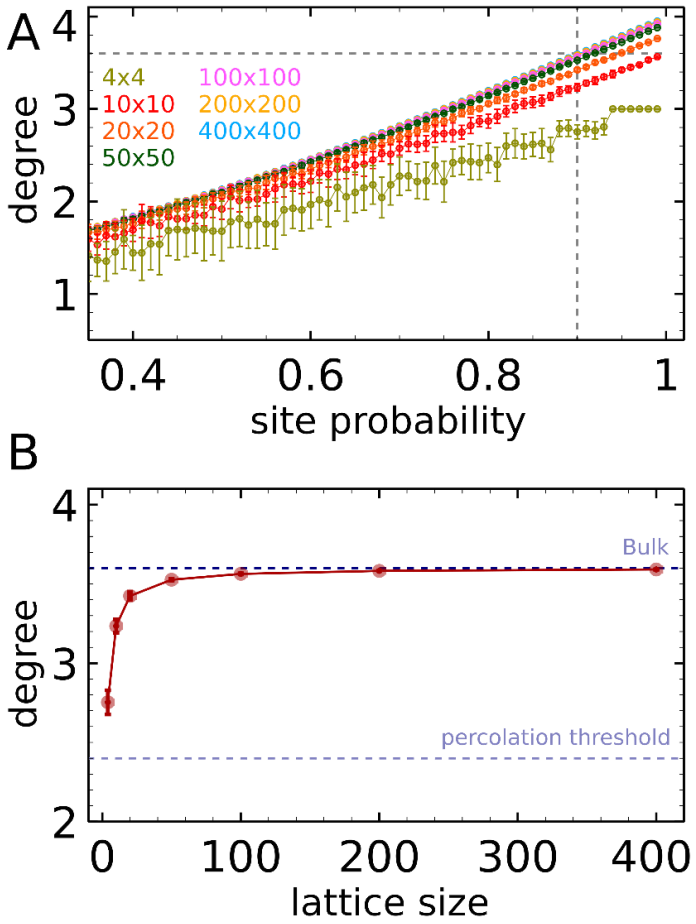

Figure 4.3. (A) Average bond number calculated for different lattice sizes from 4x4 to 400x400 with varying occupation probability. A 4-neighbor connectivity is considered for calculating coordination number of each occupied site. Clear linear trend can be observed at large occupation probabilities. For Monte Carlo simulations in this work, occupation probability of 0.9 was used to ensure that average coordination number remains ~3.6 (dashed line) mimicking bulk water coordination number. Each data points were averaged over 20 different random configuration and error bars represent one standard deviation from the mean. (B) Average coordination number in different lattice sizes shown in (A) at specific occupation probability of 0.9. Average degree converges to a value of ~3.6 with increasing lattice size mimicking similar coordination number as in bulk water.

4.3.3. Extent of hydration dynamics perturbation using square lattices

Protein interfaces do present a diversity of chemical interactions. Laage *et al.* have previously reported that such heterogeneity does not have significant impact on the average retardation factor of hydrogen bond jumps near different protein residues[35]. Overall a mean retardation factor of 2 should be expected right next to extended protein interfaces. The role

of topology, however, is more pronounced, where clefts can induce much more dramatic jump retardation factors.[34]

The swapping of empty and occupied sites in square lattices, implemented using Metropolis Monte Carlo, models hydrogen bond switching events. A filled site in the lattice represents water molecules whereas vacant sites represent an unfavorable hydrogen bonding partner (either donor or acceptor). Our MC simulation enables us to delineate contributions to dynamics arising from simple interfaces consisting of only flat sides and corners. The occupied sites at the interface have reduced coordination number since no periodic boundary is used. Small lattice sizes (4x4 or 6x6) represent higher degrees of crowding due their high surface to area ratio, while larger lattices (≥ 15x15) should be comparable to dilute, bulk-like environments.

We take as bulk-like timescales those which are obtained from the fastest average time constant in the 30x30 lattice. **Figure 4.4**(A – C) shows the retardation factor maps

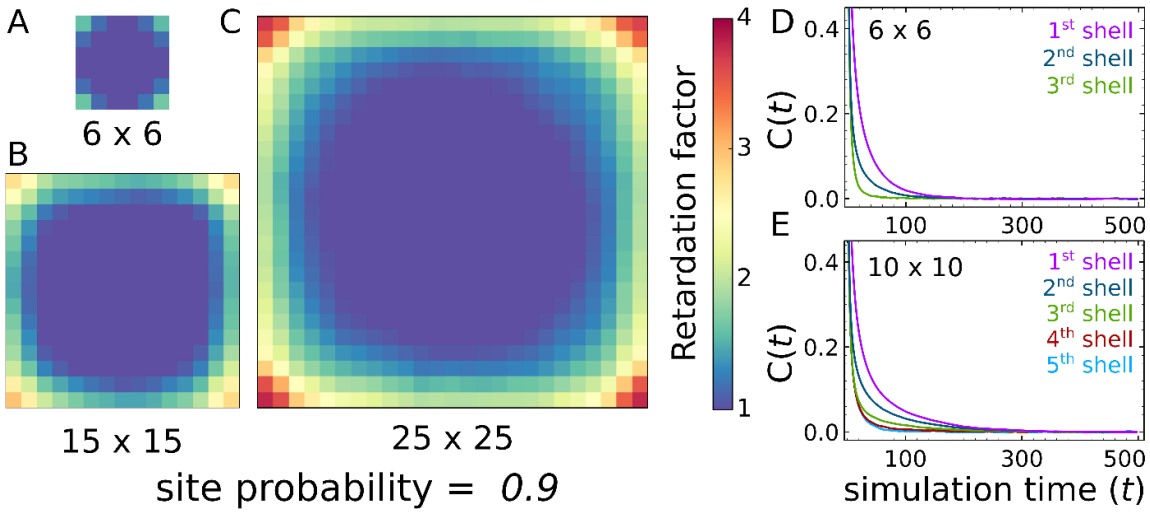

Figure 4.4. (A) Retardation factor map showing site switching dynamics in different regions of the 6x6 lattice dimension with a filling probability of 0.9. Individual pixels represent retardation factor relative to the bulk water dynamics timescale (14 simulation time) obtained using a 30x30 lattice size. Simulations were performed via switching occupied and filled site based on Metropolis-Hastings algorithm. Average bond correlation times were obtained by integrating the correlation function up to 500 simulation iterations. Difference in dynamics can be seen between the first and second shells. Retardation factor of 1 corresponds to bulk like behavior while higher value represents longer correlation times. (B) and (C) Similar retardation factor map for 15x15 and 25x25 lattice respectively. The observed retardation factor of 2 near flat interfaces is a direct manifestation of excluded volume effect. Enhanced retardation is also observed for sites near the corners consistent with reduced fraction of partners available relative to the bulk. (D) Normalized correlation function (shown up to 0.4 y-axis for clarity) in 6x6 lattice indicating maximum retardation for first shell (closest to the interface), followed by second and third shell. (E) Normalized correlation function for first to fifth shells in 10x10 lattice. Correlation decay times converge for fourth and fifth shells confirming our maximum perturbation length scale hypothesis of up to maximum third shell.

obtained by measuring average correlation times for switching vacant sites relative to bulk in 6x6, 15x15 and 20x20 size lattices, respectively. A value of 1 represents bulk-like dynamics while larger values represent longer average correlation times. In this work we find that for lattice sizes that can accommodate more than two shells, the extent of dynamical perturbation propagates, at most, to the third shell. **Figure 4.4**(D) and (E) shows calculated correlation decays for site switching dynamics in 6x6 and 10x10 lattices respectively. The 6x6 lattice (**Figure 4.4**(D)) exhibits shell-dependent time correlation functions. The slowest average correlation time is observed for the first shell, followed by the second and third shells. To determine the length scale on which dynamical perturbations propagate from the interface, we focus our attention on the larger 10x10 lattice (**Figure 4.4**(E)). 10x10 dimension provides the best chance for observing any additional contributions to the slowdown arising from the cooperative crowding conditions. This 10x10 lattice is the only size that can accommodate more than three shells while also maintaining a significantly high degree of crowding. As expected, time correlation functions for the first shell have the largest time constants (i.e. are slowest to decay) followed by the subsequent shells. The correlation times appear to converge around third shell.

Our simulations show additional slowdown in cleft like geometries near the corners of the square lattice, as is particularly evident in **Fig. 4.4**(C). This finding is in accord with the predictions from the excluded volume fraction[28] as well as calculated compressibility studies[54] of water near an armchair carbon nanotube interface which concluded that a concave geometry is more hydrophobic than a convex geometry. The 4-fold slowdown agrees quantitatively with the (1/[1-*f*], where $f = 0.75$) prediction by Laage *et al*. Apart from entropic constraints imparted by an interface, Patel *et al*. have shown that patterned patches of hydrophilic sites influence water affinity. Experiments measuring water diffusivity using NMR in different proteins exhibiting varying levels of surface topology have also found similar influences of curvature over hydrophobic interactions.[55] Enthalpic constraints imparted on water by different chemical patterns only influence molecules in the immediate vicinity of such interactions, whereas topology and patterning can be more delocalized.[56] In our lattice Monte Carlo simulations, we do not observe any additional retardation in correlation times near a flat interface, particularly in the smallest lattice dimensions.

4.3.4. Additive bond dynamics in constrained environments

Since reducing the size of the lattice effectively increases the degree of crowding, we had anticipated that the constrained geometry would show non-additive slowdown in dynamics due to collective switching dynamics. As the perimeter-to-area ratio increases in smaller lattices, however, we see a reduction in the overall average bond correlation time as shown in **Fig. 4.5**. This effect is simply based on the differences in time required to sample the

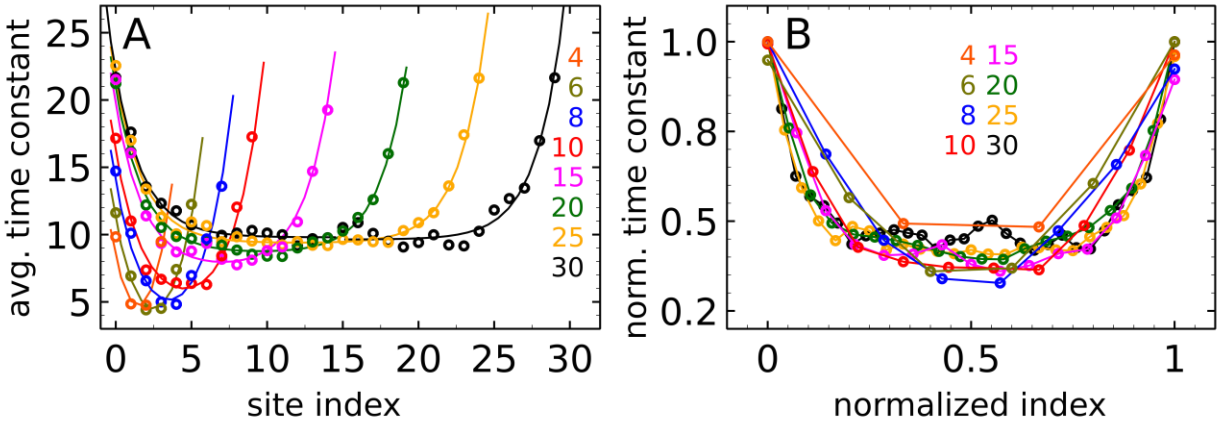

Figure 4.5. (A) Average time constant obtained from the bond correlation function along the center axis of the lattice. Projections along the X and Y axis have been averaged to minimize fluctuations. Maximum slowdown is observed for sites belonging to the first shell and decays exponentially for higher shells. Also due to finite size effect, we observe a speedup in the overall decay times for smaller lattice dimensions. (B) Normalized plot for x and y-axis for data shown in (A). The decay rates appear artificially stretched for smaller lattice dimensions.

available configurations, which is a finite-size effect common in Monte Carlo simulations. For lattices of smaller dimensions, fewer iterations are needed to completely sample the available configurations while larger lattices will require longer time to sample the entire configuration space. We find a non-linear dependence in the overall timescale for site switching along the lattice axis. It is therefore of interest to explore any possibility of non-additive behavior when interfaces come close together. We take the largest lattice dimension (30x30, black curve in **Fig. 4.5**) to obtain distance-dependent dynamics in what we assume to be the absence of crowding.

The curves are fitted with two exponential functions with a constant offset, one from 0 to 15 site index and the other from 15 to 29 site index. The constant offset parameter accounts for overall scaling of average correlation time due to finite size of the square geometry. Parameters of the fit are tabulated in **Table 4.1** which are obtained using points taken along the lattice axis passing through the center.

Table 4.1. Parameters obtained for the exponential fit for average correlation times versus site index along the center axis in 30x30 lattice as shown in **Figure 4.5**.

Site index	Fitting function	Fit parameters		
		a	τ	c
0 - 15	$f_1(x) = ae^{-x/\tau} + c$	12.21	1.87	9.80
15 - 29	$f_2(x) = ae^{-(29-x)/\tau} + c$	12.32	1.82	9.63

The fit parameters obtained for the uncrowded case are then used to fit rest of the decay constant data from 4x4 to 25x25 lattices. We use the same sum of functions $[f_1(x) + f_2(N - x)]$ to fit the smaller lattices; fixing the decay constants and its amplitude enables a direct test of the additivity in dynamics. Since the end index (N) for different lattice dimensions vary, it is set to the size of the lattice that is to be fitted. This approach leaves the offset parameter, c of the fitting function as the only adjustable term. **Figure 4.5**(A) also shows fits for the curves using solid lines. We find that all other lattice sizes could be fitted using a sum of fitting functions, which indicates a lack of any non-additive dynamics arising solely due to crowding.

In **Fig. 4.4**(C), due to increased hydrophobicity and a reduction in the availability of favorable neighbors (up to 75 %), there is additional slowdown at the corners. Based on the observed trends in the time correlation map, we can conclude that flat interfaces are ineffective in imparting any non-additive slowdown in the hydrogen bond switching dynamics within the thermodynamic model used here. Additional slowdown in dynamics near sharp concave curvatures (i.e. at the corners of the lattice) hints at the idea that a rugged topology may be essential for the observation of any non-additive contributions. This analysis is lacks explicit crowding-induced changes of the interactions between the surface and the water (e.g. due to changes in the local dielectric), as is the precise goal here, but these can certainly be expected to contribute to hydrogen bond switching perturbations.

4.4. Conclusion

A simple Monte Carlo simulation with square lattices captures the essential connectivity of hydrogen bond networks and the switching dynamics in liquid water. The main goal of analyzing such a model is to determine the spatial extent of the excluded volume perturbation of hydrogen bond dynamics in the complete absence of any interactions or

complex surface topology, which is inevitable in atomistic molecular dynamics simulations. Our approach relies on calculating the hydrogen bond time correlation function using a straightforward site swapping Metropolis method. Although our method cannot capture the orientational dynamics explicitly, the hydrogen bond switching inherently encodes the rotating water during the switching window.

By making the correspondence with the well-characterized phenomenon of percolation on 2D graphs, where there is a rigorous threshold at an occupation probability of ~0.6, we find that the connectivity in liquid water is above the percolation threshold given that accurate hydrogen bonding degree distributions require an occupation probability of 0.9. Our method also accurately describes the retardation factor for hydrogen bond switching due to an interface, which has previously been estimated using statistical mechanics and atomistic molecular dynamics simulations. The retardation factor maps for different size lattices show that the dynamical perturbation extends, at most, to the second hydration shell. Dynamical perturbation beyond this distance, which has experimental support, likely results from a mechanism not captured in the present model, or, more generally, one that is separate from the entropic excluded volume origin. The spatial dependence of the retardation factors appears to be size dependent, but we are able to reproduce results for all of the lattice sizes using only the ~2 site exponential decay found in the largest lattice. This finding is clear evidence for a lack of cooperative, non-additive behavior, and indicates that collective hydration dynamics associated with the complex coordinated rearrangements of water molecules are not captured with this model. Since our model captures quantitively the excluded volume prediction for the retardation factor in the corner regions of the lattice, the results suggest that controlled reintroduction of surface topological complexity can be used to test the origin of possible collective hydration dynamics. To the extent that there is indeed collective hydrogen bond switching slowdown caused by the influence of multiple macromolecular interfaces, these results suggest that those perturbations are intrinsically dynamic, lacking an entropic contribution to the free energy landscape change.

4.5. References

1. Fayer, M. D., Dynamics of Water Interacting with Interfaces, Molecules, and Ions. *Accounts of Chemical Research* **2012,** *45* (1), 3-14.
2. Thompson, W., Perspective: Dynamics of confined liquids. *J. Chem. Phys.* **2018,** *149*, 170901.
3. Laage, D.; Elsaesser, T.; Hynes, J. T., Water Dynamics in the Hydration Shells of Biomolecules. *Chemical Reviews* **2017,** *117* (16), 10694-10725.
4. Bagchi, B., Water dynamics in the hydration layer around proteins and micelles. *Chemical Reviews* **2005,** *105* (9), 3197-3219.
5. Lum, K.; Chandler, D.; Weeks, J. D., Hydrophobicity at small and large length scales. *Journal of Physical Chemistry B* **1999,** *103* (22), 4570-4577.
6. Hillyer, M. B.; Gibb, B. C., Molecular Shape and the Hydrophobic Effect. *Annual Review of Physical Chemistry* **2016,** *67*, 307-329.
7. Kubarych, K. J.; Roy, V. P.; Daley, K. R., Interfacial water dynamics. In *Encyclopedia of Interfacial Chemistry* Wandelt, K., Ed. Elsevier: 2018; pp 443-461.
8. King, J. T.; Arthur, E. J.; Brooks, C. L.; Kubarych, K. J., Site-Specific Hydration Dynamics of Globular Proteins and the Role of Constrained Water in Solvent Exchange with Amphiphilic Cosolvents. *J. Phys. Chem. B* **2012,** *116* (19), 5604-5611.
9. Yang, J.; Wang, Y. F.; Wang, L. J.; Zhong, D. P., Mapping Hydration Dynamics around a beta-Barrel Protein. *Journal of the American Chemical Society* **2017,** *139* (12), 4399-4408.
10. Zhang, L. Y.; Wang, L. J.; Kao, Y. T.; Qiu, W. H.; Yang, Y.; Okobiah, O.; Zhong, D. P., Mapping hydration dynamics around a protein surface. *Proceedings of the National Academy of Sciences of the United States of America* **2007,** *104* (47), 18461-18466.
11. Folpini, G.; Siebert, T.; Woerner, M.; Abel, S.; Laage, D.; Elsaesser, T., Water Librations in the Hydration Shell of Phospholipids. *Journal of Physical Chemistry Letters* **2017,** *8* (18), 4492-4497.
12. Kundu, A.; Blasiak, B.; Lim, J. H.; Kwak, K.; Cho, M., Water Hydrogen-Bonding Network Structure and Dynamics at Phospholipid Multibilayer Surface: Femtosecond Mid-IR Pump-Probe Spectroscopy. *J. Phys. Chem. Lett.* **2016,** *7* (5), 741-745.
13. Piletic, I. R.; Tan, H. S.; Fayer, M. D., Dynamics of nanoscopic water: Vibrational echo and infrared pump-probe studies of reverse micelles. *J. Phys. Chem. B* **2005,** *109* (45), 21273-21284.
14. Roy, V. P.; Kubarych, K. J., Interfacial Hydration Dynamics in Cationic Micelles Using 2D-IR and NMR. *Journal of Physical Chemistry B* **2017,** *121* (41), 9621-9630.
15. Kuchuk, K.; Sivan, U., Hydration Structure of a Single DNA Molecule Revealed by Frequency-Modulation Atomic Force Microscopy. *Nano Lett.* **2018,** *18* (4), 2733-2737.
16. Davis, J. G.; Gierszal, K. P.; Wang, P.; Ben-Amotz, D., Water structural transformation at molecular hydrophobic interfaces. *Nature* **2012,** *491* (7425), 582-585.
17. Davis, J. G.; Rankin, B. M.; Gierszal, K. P.; Ben-Amotz, D., On the cooperative formation of non-hydrogen-bonded water at molecular hydrophobic interfaces. *Nature Chem.* **2013,** *5* (9), 796-802.
18. Perera, P. N.; Browder, B.; Ben-Amotz, D., Perturbations of Water by Alkali Halide Ions Measured using Multivariate Raman Curve Resolution. *J. Phys. Chem. B* **2009,** *113* (7), 1805-1809.
19. Perera, P. N.; Fega, K. R.; Lawrence, C.; Sundstrom, E. J.; Tomlinson-Phillips, J.; Ben-Amotz, D., Observation of water dangling OH bonds around dissolved nonpolar groups. *Proc. Natl. Acad. Sci. U. S. A.* **2009,** *106* (30), 12230-12234.
20. Niehues, G.; Heyden, M.; Schmidt, D. A.; Havenith, M., Exploring hydrophobicity by THz absorption spectroscopy of solvated amino acids. *Faraday Discuss* **2011,** *150*, 193-207; discussion 257-92.
21. Bohm, F.; Schwaab, G.; Havenith, M., Mapping Hydration Water around Alcohol Chains by THz

Calorimetry. *Angewandte Chemie, International Edition* **2017,** *56* (33), 9981-9985.
22. Ebbinghaus, S.; Kim, S. J.; Heyden, M.; Yu, X.; Heugen, U.; Gruebele, M.; Leitner, D. M.; Havenith, M., An extended dynamical hydration shell around proteins. *Proceedings of the National Academy of Sciences of the United States of America* **2007,** *104* (52), 20749-20752.
23. Novelli, F.; Pour, S. O.; Tollerud, J.; Roozbeh, A.; Appadoo, D. R. T.; Blanch, E. W.; Davis, J. A., Time-Domain THz Spectroscopy Reveals Coupled Protein-Hydration Dielectric Response in Solutions of Native and Fibrils of Human Lysozyme. *Journal of Physical Chemistry B* **2017,** *121* (18), 4810-4816.
24. Fega, K. R.; Wilcox, D. S.; Ben-Amotz, D., Application of Raman Multivariate Curve Resolution to Solvation-Shell Spectroscopy. *Applied Spectroscopy* **2012,** *66* (3), 282-288.
25. Tielrooij, K. J.; Garcia-Araez, N.; Bonn, M.; Bakker, H. J., Cooperativity in Ion Hydration. *Science* **2010,** *328* (5981), 1006-1009.
26. Fenn, E. E.; Wong, D. B.; Giammanco, C. H.; Fayer, M. D., Dynamics of Water at the Interface in Reverse Micelles: Measurements of Spectral Diffusion with Two-Dimensional Infrared Vibrational Echoes. *Journal of Physical Chemistry B* **2011,** *115* (40), 11658-11670.
27. Fenn, E. E.; Wong, D. B.; Fayer, M. D., Water dynamics at neutral and ionic interfaces. *Proceedings of the National Academy of Sciences of the United States of America* **2009,** *106* (36), 15243-15248.
28. Laage, D.; Hynes, J. T., A molecular jump mechanism of water reorientation. *Science* **2006,** *311* (5762), 832-835.
29. Fogarty, A. C.; Laage, D., Water Dynamics in Protein Hydration Shells: The Molecular Origins of the Dynamical Perturbation. *J. Phys. Chem. B* **2014,** *118* (28), 7715-7729.
30. Qin, Y. Z.; Zhang, L. Y.; Wang, L. J.; Zhong, D. P., Observation of the Global Dynamic Collectivity of a Hydration Shell around Apomyoglobin. *Journal of Physical Chemistry Letters* **2017,** *8* (6), 1124-1131.
31. Li, T.; Hassanali, A. A.; Kao, Y. T.; Zhong, D.; Singer, S. J., Hydration dynamics and time scales of coupled water-protein fluctuations. *Journal of the American Chemical Society* **2007,** *129*, 3376-3382.
32. Qin, Y. Z.; Wang, L. J.; Zhong, D. P., Dynamics and mechanism of ultrafast water-protein interactions. *Proceedings of the National Academy of Sciences of the United States of America* **2016,** *113* (30), 8424-8429.
33. King, J. T.; Arthur, E. J.; Brooks, C. L.; Kubarych, K. J., Crowding Induced Collective Hydration of Biological Macromolecules over Extended Distances. *Journal of the American Chemical Society* **2014,** *136* (1), 188-194.
34. Sterpone, F.; Stirnemann, G.; Laage, D., Magnitude and Molecular Origin of Water Slowdown Next to a Protein. *Journal of the American Chemical Society* **2012,** *134* (9), 4116-4119.
35. Fogarty, A. C.; Laage, D., Water dynamics in protein hydration shells: The molecular origins of the dynamical perturbation. *Journal of Physical Chemistry B* **2014,** *118*, 7715-7729.
36. Laage, D.; Stirnemann, G.; Hynes, J. T., Why Water Reorientation Slows without Iceberg Formation around Hydrophobic Solutes. *Journal of Physical Chemistry B* **2009,** *113* (8), 2428-2435.
37. Han, J.; Mazack, M. J. M.; Zhang, P.; Truhlar, D. G.; Gao, J. L., Quantum mechanical force field for water with explicit electronic polarization. *J. Chem. Phys.* **2013,** *139* (5).
38. Cisneros, G. A.; Wikfeldt, K. T.; Ojamae, L.; Lu, J. B.; Xu, Y.; Torabifard, H.; Bartok, A. P.; Csanyi, G.; Molinero, V.; Paesani, F., Modeling Molecular Interactions in Water: From Pairwise to Many Body Potential Energy Functions. *Chemical Reviews* **2016,** *116* (13), 7501-7528.
39. Ma, Z. H.; Zhang, Y. L.; Tuckerman, M. E., Ab initio molecular dynamics study of water at constant pressure using converged basis sets and empirical dispersion corrections. *J. Chem. Phys.*

2012, *137* (4).
40. Hamm, P.; Fanourgakis, G. S.; Xantheas, S. S., A surprisingly simple correlation between the classical and quantum structural networks in liquid water. *J. Chem. Phys.* **2017,** *147* (6).
41. Silverstein, K. A. T.; Haymet, A. D. J.; Dill, K. A., A simple model of water and the hydrophobic effect. *Journal of the American Chemical Society* **1998,** *120* (13), 3166-3175.
42. Urbic, T.; Vlachy, V.; Dill, K. A., Confined water: A Mercedes-Benz model study. *Journal of Physical Chemistry B* **2006,** *110* (10), 4963-4970.
43. Xu, H. F.; Dill, K. A., Water's hydrogen bonds in the hydrophobic effect: A simple model. *Journal of Physical Chemistry B* **2005,** *109* (49), 23611-23617.
44. Skyner, R. E.; McDonagh, J. L.; Groom, C. R.; van Mourik, T.; Mitchell, J. B. O., A review of methods for the calculation of solution free energies and the modelling of systems in solution. *Physical Chemistry Chemical Physics* **2015,** *17* (9), 6174-6191.
45. Lu, J. B.; Qiu, Y. Q.; Baron, R.; Molinero, V., Coarse-Graining of TIP4P/2005, TIP4P-Ew, SPC/E, and TIP3P to Monatomic Anisotropic Water Models Using Relative Entropy Minimization. *Journal of Chemical Theory and Computation* **2014,** *10* (9), 4104-4120.
46. Lee, H. S.; Tuckerman, M. E., Dynamical properties of liquid water from ab initio molecular dynamics performed in the complete basis set limit. *Journal of Chemical Physics* **2007,** *126* (16).
47. Smolin, N.; Oleinikova, A.; Brovchenko, I.; Geiger, A.; Winter, R., Properties of spanning water networks at protein surfaces. *J. Phys. Chem. B* **2005,** *109* (21), 10995-11005.
48. Rahaman, O.; Kalimeri, M.; Katava, M.; Paciaroni, A.; Sterpone, F., Configurational Disorder of Water Hydrogen-Bond Network at the Protein Dynamical Transition. *J. Phys. Chem. B* **2017,** *121* (28), 6792-6798.
49. Shante, V. K. S.; Kirkpatrick, S., Introduction to Percolation Theory. *Advances in Physics* **1971,** *20* (85), 325-357.
50. Newman, M. E. J., The structure and function of complex networks. *Siam Review* **2003,** *45* (2), 167-256.
51. Albert, R.; Barabasi, A. L., Statistical mechanics of complex networks. *Reviews of Modern Physics* **2002,** *74* (1), 47-97.
52. Oleinikova, A.; Brovchenko, I.; Smolin, N.; Krukau, A.; Geiger, A.; Winter, R., Percolation transition of hydration water: From planar hydrophilic surfaces to proteins. *Phys. Rev. Lett.* **2005,** *95* (24).
53. Oleinikova, A.; Smolin, N.; Brovchenko, I.; Geiger, A.; Winter, R., Formation of spanning water networks on protein surfaces via 2D percolation transition. *J. Phys. Chem. B* **2005,** *109* (5), 1988-1998.
54. Xi, E.; Venkateshwaran, V.; Li, L.; Rego, N.; Patel, A. J.; Garde, S., Hydrophobicity of proteins and nanostructured solutes is governed by topographical and chemical context. *Proceedings of the National Academy of Sciences* **2017,** *114*, 201700092.
55. Barnes, R.; Sun, S.; Fichou, Y.; Dahlquist, F. W.; Heyden, M.; Han, S. I., Spatially Heterogeneous Surface Water Diffusivity around Structured Protein Surfaces at Equilibrium. *Journal of the American Chemical Society* **2017,** *139* (49), 17890-17901.
56. Arthur, E. J.; King, J. T.; Kubarych, K. J.; Brooks, C. L., Heterogeneous Preferential Solvation of Water and Trifluoroethanol in Homologous Lysozymes. *Journal of Physical Chemistry B* **2014,** *118* (28), 8118-8127.

A.4. APPENDIX

A.4.1. Correlation map for lattice of varying sizes

Time correlation function for each lattice sites were averaged 40 times and a spatial map is generated. **Figure A.4-1** shows the time correlation map for all the sites in different size lattices.

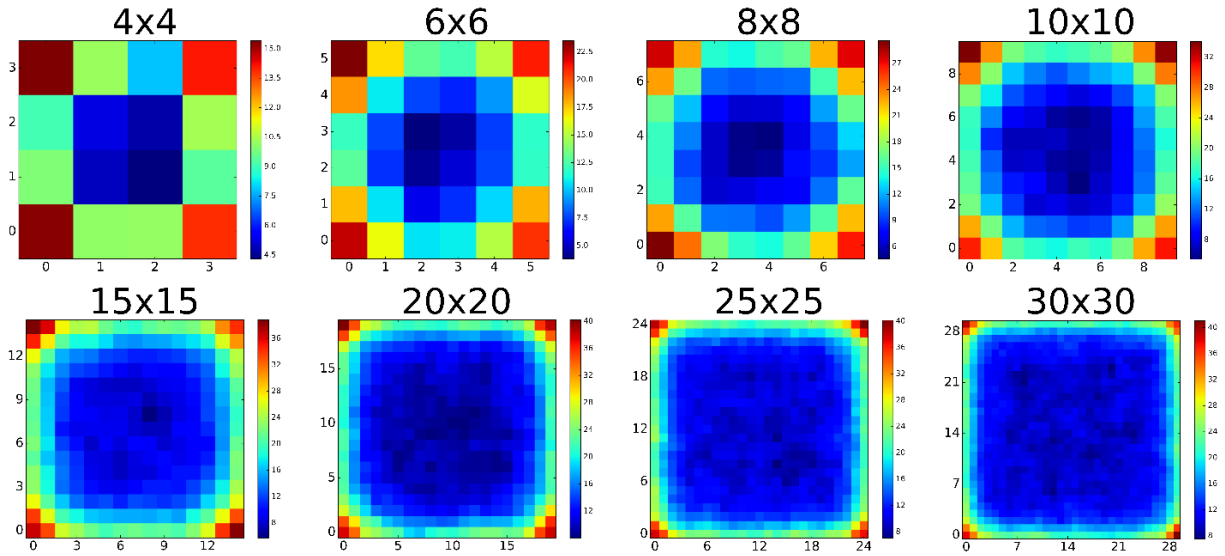

Figure A.4-1. Average bond correlation time map for every site in square lattice used for Monte Carlo simulations. Lattice dimensions from 4x4 to 30x30 are shown which covers different degree of crowding. The color maps for every lattice is different, representing time constants obtained for a give lattice size.

A.4.2. Determining 'bulk' time constant for computing retardation factor map

Although, it has earlier been stated that with increasing lattice dimension, we see an overall increase in the average time constant. Due to finite size effect, it was necessary to determine a single bulk time constant value to get a meaningful retardation factor. We circumvent, this limitation by obtaining 'bulk' time constant by performing Monte Carlo simulation in a periodic lattice where there are no restrictions for the particles to cross the edge boundary. **Figure A.4-2** shows the average time constants obtained for individual shells from first to sixth in lattices of varying sizes (4x4, 6x6, 8x8, 10x10, 15x15, 20x20, 25x25 and 30x30). The obtained time constants show a logarithmic behavior with respect to lattice dimensions. Fit constant obtained for different shells are tabulated in **Table A.4-1**. The observed 'bulk' average time constant for every lattice size is smaller than the time constant for its largest shell (least perturbation to the switching event). We could have obtained the true 'bulk' time constant using the largest shell from our largest lattice dimension (shell 15 in 30x30).

Instead, we choose to extrapolate the time constants obtained from simulations using period boundary condition. Because simulation points for all the lattice sizes are used, this method offer better statistics for computing the 'bulk' time constant. We choose extrapolated lattice size of 100x100 to determine the time constant which is 14.1 simulation units. This value also agrees very well with the sixth shell time constant for 30x30 lattice.

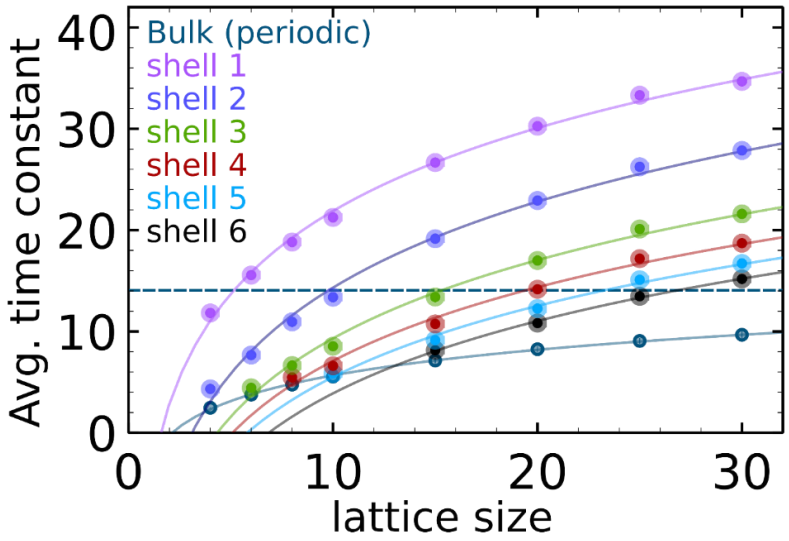

Figure A.4-2. Plot showing average time constant from first to sixth shell in lattice sizes (N x N) from 4x4 to 30x30 in our Monte Carlo simulation. Average time constants scale as a natural log of lattice size (N). To take account of the finite size effect, simulations without boundary conditions were also carried out to represent 'bulk' like dynamics. Logarithmic fits are shown as solid curves for respective shells and bulk like simulations. Dashed line represents the extrapolated time constant (14.1) for a larger lattice (100 x 100).

Fitting function used for data points shown in **Fig. A.4-2Error! Reference source not found.**, is $f(N) = a + b*ln(N)$

Table A.4-1. Fit parameters for average time constant vs lattice size in different shells as shown in **Fig. A.4-2**.

shell	a	b
1st	-5.32	11.82
2nd	-13.86	12.24
3rd	-16.35	11.14
4th	-17.05	10.49
5th	-17.81	10.13
6th	-19.82	10.30
Bulk	-2.74	3.65

A.4.3. Bond correlation time plot for all lattice dimensions in different shells

For clarity and completeness, we present the bond correlation time plots for lattice sizes ranging from 4x4 to 30x30 studied in this work. **Figure A.4-3Error! Reference source not found.** shows the time correlation decay curves for all the lattices sizes up to the fifth shells.

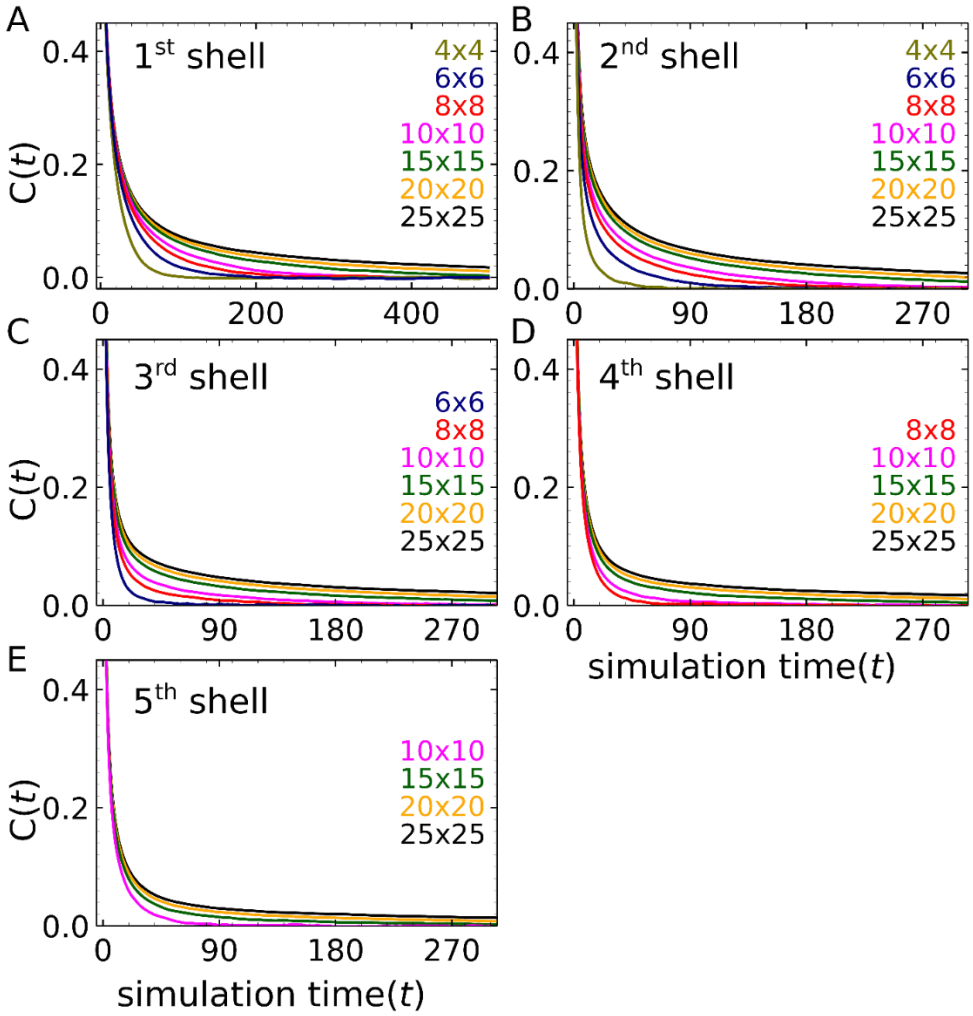

Figure A.4-3. Time correlation function plots for site switching dynamics in square lattices of all sizes studied in this work from 4x4 to 30x30. First to fifth shell correlation decays have been shown (A - E). For clarity, the x-axis range in the plots for correlation data for first shell has been trimmed to 270 simulation time.

A.4.4. Dependence of mean square displacement with lattice size

In the main text we find non-linear dependence of bond switching dynamics with the lattice sizes studied in this work. Based on our findings, we also wanted to test how transport properties of occupied sites depends in our simulation, particularly diffusion constant (mean square displacement with respect to time).

A linear fitting function was used to fit mean square displacement data shown in **Fig. A.4-4**(A). The fitting region selected was roughly estimated to avoid the ballistic and saturation regime for diffusion in a confined region.

Fits were performed in the region which excludes ballistic and saturation regime.

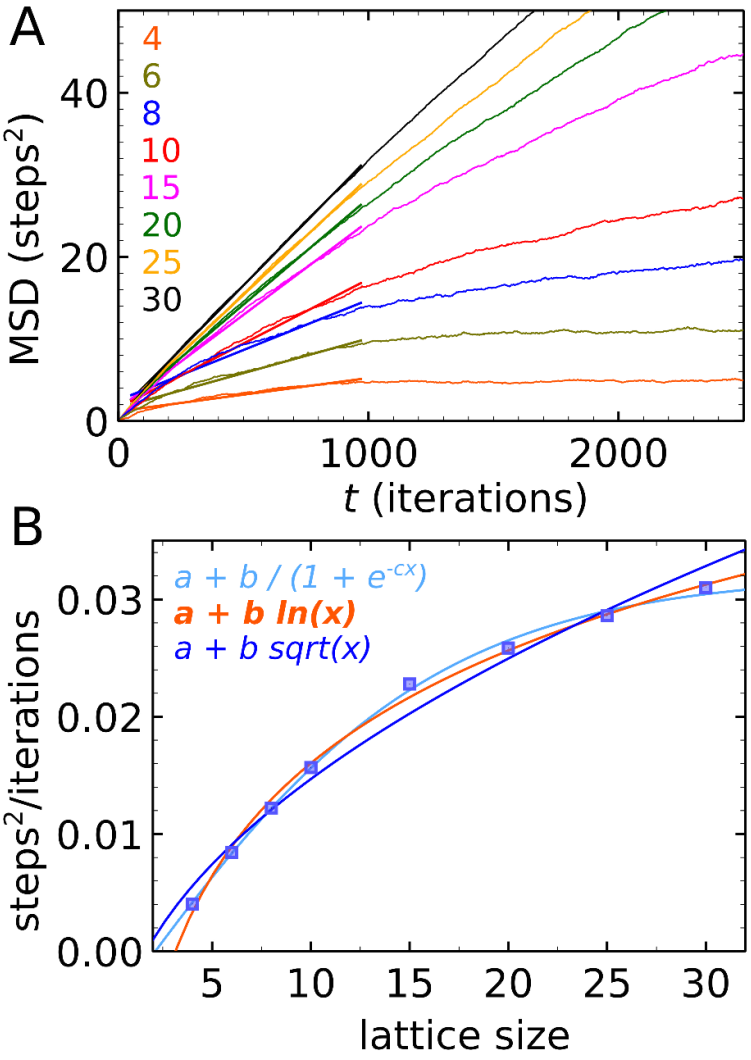

Figure A.4-4. (A) Mean square displacement vs simulation time plot for occupied sites in square lattices of sizes ranging from 4x4 to 30x30. Random walk in a confined region is expected to attain a saturation value after all the available sampling space have been explored. Linear fits were performed in the region which roughly excludes the ballistic and saturated regime. Variation in slope indicates that diffusion constant varies with lattice size indicating finite size effects. The obtained fit parameters are tabulated in **Table A.4-2**. (B) Computed "diffusion" constant for occupied lattice sites plotted as a function of lattice dimension. A nonlinear dependence is observed which is fitted to a variety of functions. The fit parameters are tabulated in **Table A.4-3**. From the fits it is observed that diffusion constant scales logarithmically as function of lattice dimension.

Fitting functions and obtained parameters for diffusion constant vs lattice sizes are tabulated in **Table A.4-2**.

Table A.4-2. Fit parameters obtained for fitting mean square displacement as a function of lattice size. A linear fitting function was used, *f(x) = a + b*x*.

Lattice size	a	Error (a)	b	Error (b)
4 x 4	1.2090	0.0176	0.0040	2.977E-05
6 x 6	1.6288	0.0222	0.0084	3.741E-05
8 x 8	2.5514	0.0405	0.0122	6.839E-05
10 x 10	1.6220	0.0321	0.0157	5.416E-05
15 x 15	1.5559	0.0291	0.0228	4.91E-05
20 x 20	1.2739	0.0237	0.0259	4E-05
25 x 25	1.0729	0.0169	0.0286	2.851E-05
30 x 30	1.0272	0.0137	0.0310	2.313E-05

Table A.4-3. Tabulation of fit parameters obtained for various fitting functions used to fit diffusion constant data as a function of lattice size.

Fitting function	Fit parameters
*a + b*log(x)*	a = -0.01586
	b = 0.013854
*a + b*sqrt(x)*	a = -0.010108
	b = 0.0078425
*a + b/(1+exp(-c*x))*	a = -0.0419049
	b = 0.07407703
	c = 0.12460364

Based on the parameters obtained for various fitting functions, we find that diffusion of the occupied sites in the lattices shows logarithmic dependence as a function of the dimension (**Table A.4-3**). In other words, this transport property scales in the same manner as do the dynamical properties. The average correlation time for bond switching (**Figure A.4-2**) also exhibits a logarithmic dependence on lattice dimension.

A.4.5. Setting bond energy between lattice sites

One may argue that since the hydrogen bond enthalpy in liquid water is about -20 kJ/mol, an arbitrary choice of bond energy (-1 kJ/mol) for lattice sites may not accurately describe

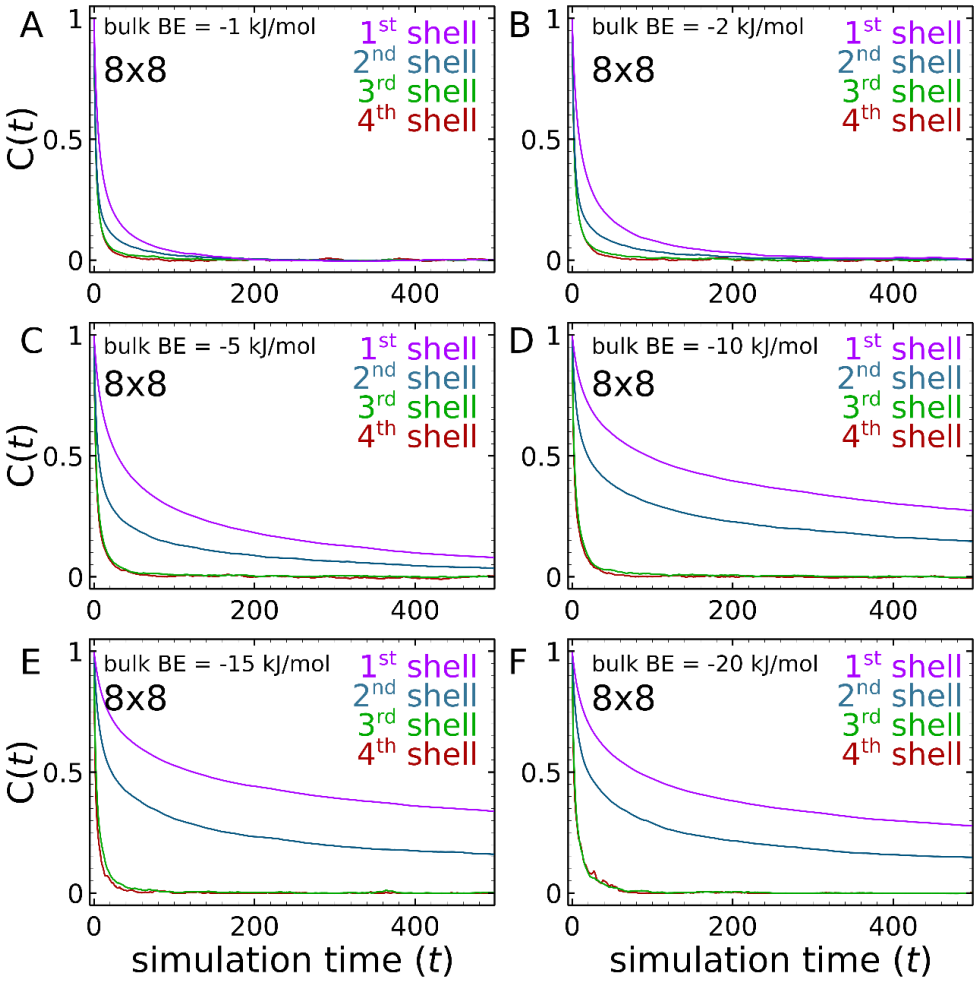

Figure A.4-5. (A - F) Time correlation function plots for site switching dynamics in different shells of 8x8 lattice gird. Binding energy for neighboring lattices sites were varied in the order -1, -2, -5, -10, -15 and -20 kJ/mol.

water. The key observable in our work is the bond correlation function of lattice sites, which is particularly sensitive to the available phase space in each system. Since we are only interested in understanding the entropic constraint imposed by an interface, different bond enthalpies should not affect the main findings of this work. Choosing a small value for bond energy chiefly provides two advantages, (a) a low energetic barrier allows one to clearly observe the entropic contribution of the interface to the perturbation of lattice-site (water) dynamics, and (b) it allows one to quickly sample the available microstates in different lattice grids, thereby considerably improving the dynamic range of the simulation window. For comparison, shown in **Fig. A.4-5** are bond correlation functions of different shells in the

lattice grid with varying binding energy for lattice sites ranging from -1 kJ/mol to -20 kJ/mol. The decay rate for the time correlation function in the bulk region of the 8x8 lattice as shown in **Fig. A.4-5**(A-F) does not appear to depend on the bond energy. While the correlation time for first and second shells are largely dependent on the pre-determined bond energy. To explain the difference in scaling between shells 1-2 relative to those in shells 3-4 we first explain the basis of obtaining the correlation function for each site in the lattice.

Figure A.4-6(A-B) shows the time correlation function of two step functions with an identical number of transitions but with different widths of the transitions (i.e. dwell times). In **Fig. A.4-6**(A) step function and its correlation function data points (below) are shown where the width of transition is 10 MC time units while **Fig. A.4-6**(B) highlights the transitions with width of 50 MC time units.

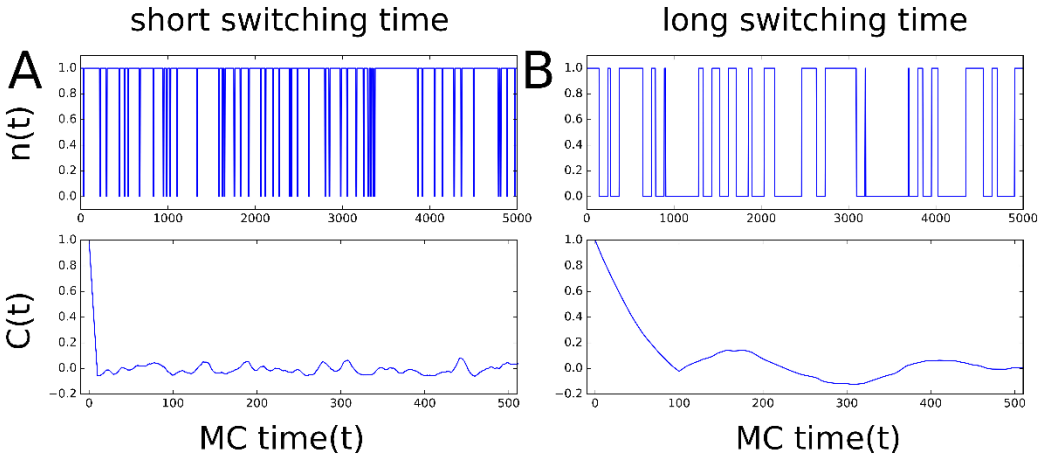

Figure A.4-6. (A) Step function and its time correlation plots where width of steps is 10 MC time units (B) Step function and its correlation plots which has width of 50 MC time units. In both the cases, the total number of transitions has been fixed to 50.

From the time correlation plot it is apparent that when the dwell time is longer, the decay of the correlation function is slower, and *vice versa*. This relationship implies that it does not matter if the transition from state A to B is more probable or not, the rate of correlation decay simply depends on how long the system stays in each state. In our simulation of an 8x8 lattice, we find that the dwell times of voids in shells 3 and 4 are much shorter than are the

void dwell times in shells 1 and 2.

From **Fig. A.4-7**(A-B) we see that with increasing binding energy of the lattice sites, the rate of switching is slowed. For shells 3 and 4, the rate of jumps shows a marked reduction. At this point, we can only comment that increasing bond energy for lattice sites results in the localization of voids (defects) at the corners and edges. We observe a

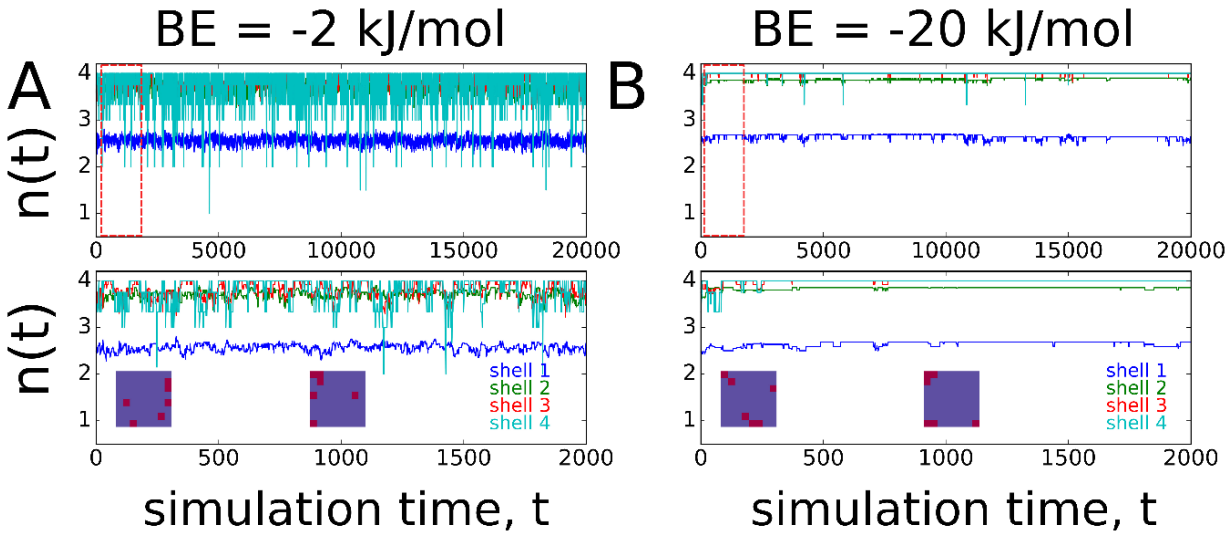

Figure A.4-7. Average coordination number for shell 1-4 in 8x8 lattice simulations with bond energy of (A) -2 kJ/mol (B) -20 kJ/mol. Inset in the bottom correlation plot shows the starting and later (~1000 simulation time) lattice configurations. Notice that for large bond energy the voids get quickly localized on the corners which are most hydrophobic compared to when bond energy is lower where voids are still scattered.

pronounced reduction in the time correlation function decay rate at large bond energy because, for the first and second shells, all the voids are simply localized in those shells. While for the second and third shells, any formation of voids quickly becomes pushed to the edges and corners primarily based on the definition of Metropolis algorithm. For nearly all switching events, the Boltzmann factor at 298 K with $\Delta E \sim -20$kJ/mol >> any random number between 0 and 1 hence the system is poised to follow the trajectory of the minimum energy path. Therefore, our choice of using an arbitrary binding energy of -1 kJ/mol is reasonable in order to allow fast and complete sampling of the available phase space of the lattices. Based on our analysis we find that our main conclusion of the paper will still hold with a larger bond energy for the lattice sites. Our results indicate that the dynamical perturbation to hydrogen bond switching can only propagate at most three shells from a hydrophobic interface if only entropic factors are considered.

Chapter 5

Aqueous Polyethylene glycols Embed Hofmeister Cations: A Hydration Dynamics Study

5.1. Introduction

Understanding the complex interplay between water and dissolved solutes such as polymers, proteins, nucleic acids, and ions holds promise to accurately model various biochemical reactions. Apart from acting as merely a passive solvent, water is essential for maintaining the optimal structures governing the function of macromolecules.[1] As mentioned in the introductory chapter, only a few hydration layers are enough to lubricate the needed conformational changes during enzymatic binding processes. Kinetics and thermodynamics of such events have been anticipated to be influenced by fast picosecond fluctuations and orientational dynamics of water, though testing this fundamental hypothesis remains a challenge.

Polar and charged components in proteins and nucleic acids not only assist in solubilizing the macromolecule but also help maintain its native structure and function in a buffered and crowded intra-cellular environment. To completely capture the timescale and perturbation to hydration dynamics near a variety of interfaces, the role of surface charges and their interactions with water cannot be excluded. Electrolytes present in the cytoplasm, apart from maintaining osmotic pressure also directly or indirectly interact with a variety of interfaces which further modulate the hydrogen bond fluctuations. It has been

experimentally reported that solvation dynamics near DNA follow a power law dependence with time and appears to be more dramatic than what has been observed near protein interfaces. Timescales as slow as 100 ps have been reported using fluorescence-based stokes shift experiments.[2, 3] This seemingly inexplicable result has been subjected to several follow up investigations regarding its nature and origin of slowdown. Berg and co-workers suggest that conjugated dyes used in fluorescence experiments can intercalate into the groves of the DNA which also show power law dependence.[4, 5] Earlier works by Zewail and co-workers[6] studied DNA with modified bases by 2-aminopurine which highlight that long time decays can be attributed to less appreciated proton and electron transfer processes. While the pursuit continues to decipher long-time dynamics in DNA primarily attributable to water, one cannot neglect the flexible and conformational freedom that DNA polymers exhibit, which may strongly couple to its hydration water. In addition, the associated counter ions in the DNA buffer can create local polarizable fields, but the extent to which such an effect can modify interfacial hydration dynamics is yet to be completely understood.[7]

In dilute salt solutions, molecular ions can moderately structure hydration water, and only at very high concentrations, the network and orientational dynamics of water is observed to get perturbed.[8-10] The ability of small ions, particularly kosmotropic cations, to structure water within the first solvation shell, has been used to partially explain the Hofmeister ordering for protein denaturation. Such electrostatic interaction is assumed to be short ranged due to its inverse length dependence. In addition, the high dielectric constant of water effectively screens the effect of an isolated charge in dilute aqueous solutions via ion-dipole interactions. But it is not clear whether the orientational dynamics of water is also significantly perturbed. One can argue that small ions lack large enough surface area to alter hydrogen bond jumping kinetics and cause water to slowdown. On the other hand, macromolecular interfaces perturb hydration dynamics primarily by altering the probability of hydrogen bond jumping processes. In addition, the presence of hydrophilic groups on macromolecular surfaces allow direct bonding with water which can significantly restrict water diffusion. Contrarily, some experimental and theoretical investigations surprisingly show that water structure can be altered even in the dilute regime where no macromolecular interfaces are present.[11, 12]

In biological environments, dissolved salts play an important role in modulating the

dielectric strength of the medium while simultaneously helping maintain osmotic balance and the structure of macromolecules. Considerable attention has been given to studying the dynamics and structure of water around macromolecules[13, 14] either in dilute or concentrated solutions, with considerable effort expended to find any collective effects. But little efforts have been expended to incorporate the role of ions[15-18], partially due to complexity of the electrostatic environment which can either speed up or slow down water dynamics. Recent spectroscopic measurements have come to a consensus that highly polarizable anions in the Hofmeister series[19-21] can directly interact with an extended interface, however, a complete picture for cation-water-interface remains elusive.

Slowing hydration dynamics by flexible polymers which lack an extended interface would require them to strongly compete with water for its hydrogen bond which reduces the probability of hydrogen bond jumping. To what extent can such strong associations propagate beyond the first solvation shell is not yet clear. Poly(ethylene oxide) or PEG is well known for its water structuring ability and bio-compatibility by forming a strong, structured hydration shell. Apart from biocompatibility considerations, PEG has also been recognized as a versatile molecule for mimicking conditions of crowding, solubilizing hydrophobic molecules[22] and facilitating protein crystallization[23]. Relatively high viscosity and gel-like appearance of some polyelectrolytes have been found to possess very slow water diffusion.[24] Surprisingly, the ultrafast dynamics of high molecular weight PEG solutions largely remains bulk-like[25] which has been attributed to forming "clathrate" type water structures around the polymer. Such static ordering of water around PEG is also supported by its high negative enthalpy of hydration.[26] Since PEG is a neutral molecule devoid of its own electrostatic effects, it serves as a good model system to understand the effect of ions on polymer. Later in this chapter we will also study the hydration dynamics of DNA biopolymers, which contain a highly charged phosphate backbone.

5.2. Materials and methods

5.2.1. PEG-200 and DNA sample preparations

Stock poly(ethylene oxide) having molecular weight of 200 g/mol and salmon sperm DNA (~2000 bp, 30 mg/mL stock) were purchased from Sigma-Aldrich and used without further

purification. DNA samples were generously provided by the research group of Prof. Nils Walter. PEG and DNA solutions were diluted in D_2O (purchased from Sigma-Aldrich) to achieve necessary volume ratios as mentioned in the results sections. Different thiocyanate salts were then added to this solution to a total concentration of 200 mM.

5.2.2. Infrared measurements of aqueous polymers

Linear Fourier transform infrared spectroscopy on solutions of PEG and DNA in D_2O were carried out by placing 75 μL of sample within a 50 μm thick Teflon spacer sandwiched between two calcium fluoride windows (3 mm thick, 1-inch diameter). All spectra mentioned in the work were background subtracted using pure D_2O. 2D-IR spectral diffusion measurements were carried out as described in the introduction chapter of this dissertation.

5.3. Results and Discussion

5.3.1. Conformational transition in PEG-200 with cations

The high solubility of poly(ethylene oxide) in water makes it an interesting candidate to study hydration dynamics near an interface which is has higher conformational flexibility. PEG is also amphiphilic so it can be expected that direct interaction with other hydrophobic/chaotropic solutes might preferentially modulate its dynamics as well. The hydrophilic oxygens on the polymer backbone can donate two hydrogen bonds to hydration water molecules. Previous studies[25] have attributed this strong association with water to be "ice-like" indicating a frozen structure during the observation timescale. If water is so strongly bound to the polymers, it can be hypothesized that any ion-polymer interaction is mediated by an indirect association of ions with water molecules in the second shell of the polymer.

In this work we use thiocyanate salts with different cations (guanidinium, calcium, potassium and ammonium) to observe any effects of ions on the polymer structure and water dynamics. Specific cations are chosen to encompass the full spectrum of the Hofmeister series which are ranked based on the ion's ability to precipitate proteins. Apart from merely acting as a counter anion, the strong thiocyanate CN stretching frequency has also been used to probe structural dynamics of the hydration environment in the polymer

solution. Previously, the CN stretch vibrations of thiocyanate[20] and selenocyanate[27] have successfully been used to probe dynamics of water near surfactant and in the bulk liquid.

A key advantage that thiocyanate offers is that its stretching frequency is very sensitive its hydration environment. **Figure 5.1**(A) shows the FT-IR spectrum of the CN stretching mode of thiocyanate in bulk D_2O which has a maximum absorption around 2065 cm^{-1}. Different cations do not appear to alter the CN stretching frequency indicating any lack

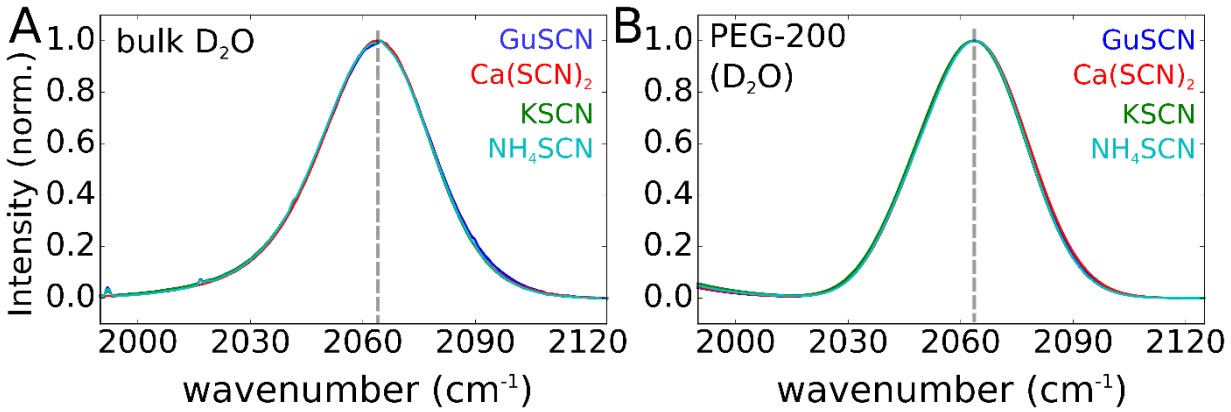

Figure 5.1. (A) FT-IR spectra of CN stretching mode of thiocyanate anion in pure D_2O. Counter cations were chosen to encompass the entire spectrum of the Hofmeister series. In bulk water counter cations have no effect on the stretching frequency which appears at ~2065 cm^{-1}. (B) FT-IR spectra of different Hofmeister thiocyanate CN stretching mode in 50 % by volume PEG-200 in D_2O. We again observe any sensitivity of different cations on vibrational stretching frequency of thiocyanate. A small shoulder in the low frequency region of the spectrum is due to residual absorption of D_2O in our polymer solutions.

of structural perturbation. This is expected since dilute concentrations of small ions are incapable of significantly breaking the hydrogen bond networks of water. Similar invariance of the CN stretching frequency is observed (**Fig. 5.1**(B)) where thiocyanate salts are dissolved in D_2O with 50 % PEG-200 by volume. The line widths for the CN stretching mode vibrations are essentially identical.

The fundamental limitations of linear FT-IR measurements to resolve underlying dynamics can be overcome using time resolved 2D-IR measurements. **Figure 5.2**(A-B) shows the frequency fluctuation correlation functions of the thiocyanate CN stretching mode in bulk water (D_2O) and with PEG-200 as a function of waiting time (t_2) between the excitation and detection pulses. The decay constant for the correlation functions were obtained by fitting the experimental data points with a single exponential function. In pure D_2O (**Fig. 5.2**(A)) a decay constant of ~1 ps is obtained which is consistent with bulk dynamics. A significant slowdown (>3.5) in the spectral diffusion time constant (**Fig. 5.2** (B))

with PEG-200 is observed. On the other hand, the high magnitude of spectral diffusion time constant in polymer solutions may be ascribed to the increased solution viscosity, and further validation is needed. Previously, a retardation factor of ~3.5 for thiocyanate in

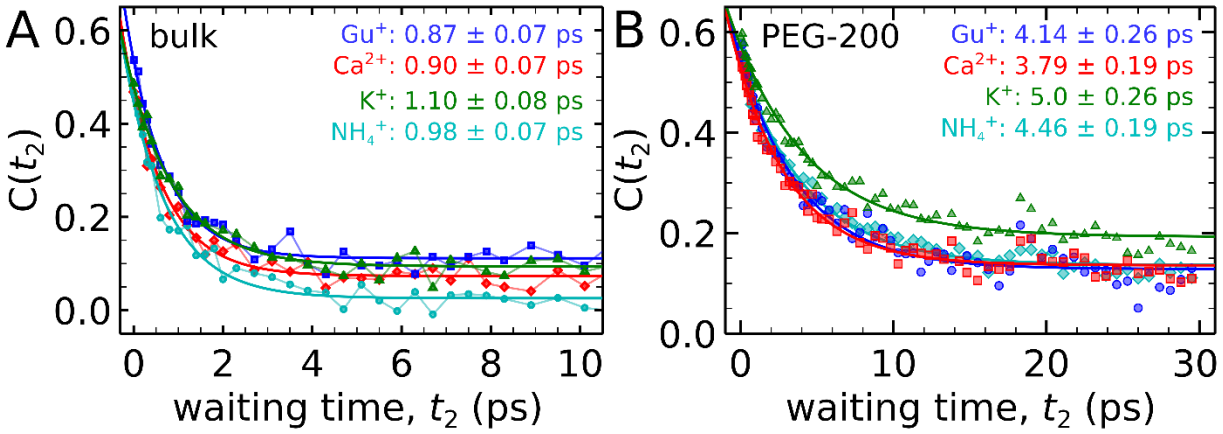

Figure 5.2. (A) Frequency fluctuation correlation function (FFCF) obtained using 2D-IR spectra diffusion measurements for different Hofmeister thiocyanates in D_2O. Experimental data points are fitted to a single exponential function with an offset. Hydration dynamics time constant of ~1ps is consistent with hydrogen bond switching timescales obtained using other methods. We do not attribute any physical interpretation to the observed differences in relative offsets. (B) FFCF of thiocyanate stretching mode for different Hofmeister cations with PEG-200 in D_2O. Data points are fitted to a single exponential function. Time constant for the dynamics in case of polymer shows significant retardation (>3.5) compared to bulk water. Guanidinium, calcium and ammonium show identical time scale for dynamics (within error) while potassium shows further slowdown (5 fold) compared to bulk.

reverse and normal phase micelles[20] was attributed to strong preference of the probe with positively charged interfaces. There we clearly found that the anion absorbability with the interface follows its Hofmeister ordering. Surprisingly, we do not find any obvious trend in the spectral diffusion time constant for different cations in PEG-200. Following experiments on DTAB with different Hofmeister cations consistently showed 3.5 times retardation in hydration dynamics. Instead, we see a clear difference in the FFCF time constant between potassium and other Hofmeister cations (guanidinium, calcium and ammonium). Within error, guanidinium, calcium and ammonium have similar retardation factors compared to bulk time scales. In the case of potassium thiocyanate, we not only observe the spectral diffusion time constant to be significantly slower, but the relative offset is also higher compared to the other ions (we think the offset for PEG experiments are meaningful, and report on slower dynamics than accessible in the lifetime-limited temporal window). The lack of any correlation for spectral diffusion timescale with Hofmeister ordering of cations indicate a very specific interaction of potassium with PEG.

Differences in correlation decay times from 2D-IR can also arise from variations in the hydration environment around a vibrational probe[28] which results in weak coupling with solvent accessible modes. The vibrational lifetime of our probe can easily be characterized using the rephasing spectrum obtained in 2D-IR experiments (**Fig. 5.3**). For Hofmeister salts

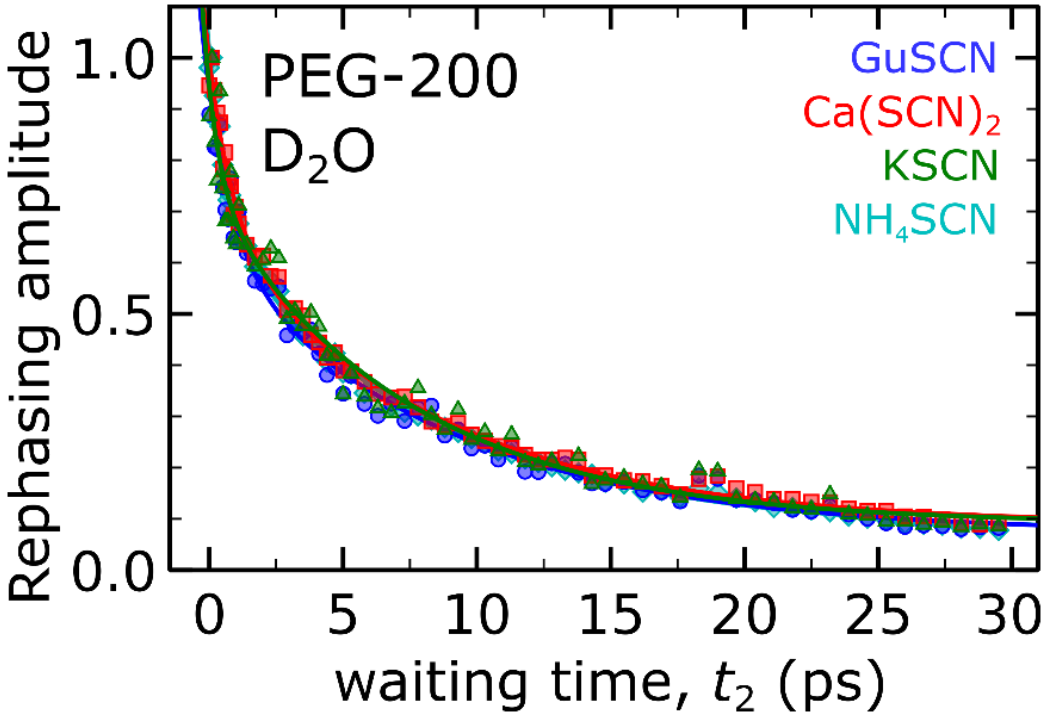

Figure 5.3. Rephasing amplitude vs waiting time showing lifetime of the vibrational CN stretching mode of different Hofmeister thiocyanate anion with PEG-200 in D_2O. For guanidinium, calcium, potassium and ammonium we find that the probe has nearly exact hydration environment.

used in the experiments, no differences in the vibrational lifetime for thiocyanate were observed with PEG-200. **Table 5.1** shows the obtained fitted time constants using a sum of exponentials.

Table 5.1. Obtained fit parameters for vibrational lifetime for CN stretching mode of different Hofmeister thiocyanate salts in PEG-200. Bi-exponential function is used for fitting, a*exp(-x/b) + c*exp(-x/d).

PEG-200 + salt	a	± a	b (ps)	±b, ps	c	± c	d (ps)	± d, ps
KSCN	0.40	0.05	2.09	0.45	0.49	0.05	15.98	1.85
$Ca(SCN)_2$	0.45	0.02	1.64	0.14	0.51	0.02	15.85	0.75
GuSCN	0.42	0.03	1.59	0.22	0.49	0.03	15.05	1.05
NH_4SCN	0.43	0.01	1.16	0.09	0.56	0.01	13.41	0.42

It can be concluded that different cations do not significantly alter the hydration

environment of the probe and the lifetime remains invariant (within error). The observed slowdown in the spectral diffusion time constant, particularly for the potassium ion (**Fig. 5.2** (B)) may be due to different fluctuating environments of water arising from varying polymer conformations.

It is known that cations can be trapped in cyclic crown ethers which also allows potassium and sodium salts to be soluble in organic solvents. Due to the amphiphilic character of crown ethers they are widely used as phase transfer catalyst[29]. Crown ethers are also incorporated extensively for the synthesis of rotaxane complexes which shuttle the ether subunit between two end groups[30]. From a molecular perspective, PEG has an identical chemical structure as that of crown ethers (oxygen atoms separated by two methylene carbons) except for the dangling hydroxyl end groups.[31] Using DFT calculations described in the next section, possible cation-PEG interactions are explored, and the origin of observed spectral diffusion slowdown will be discussed.

5.3.2. Optimized ion-PEG geometries using DFT

The hypothesis that PEG interacts directly with the counter cations of the thiocyanate salts by forming inclusion complexes will be verified using computer simulations. Experimentally, one can measure the conformational changes associated with the polymer. Such experiments and analysis probing the CH stretching vibration along the polymer backbone is currently underway. A linear chain of PEG-200 contains about 5-6 oxygen atoms which when folded have a similar cavity size to that of 18-crown-6 (1,4,7,10,13,16-hexaoxacyclooctadecane). The affinity of different crown ethers to bind a variety of ions in organic solvents is primarily dictated by its inner diameter. However, it is not clear how the hydration environment will play a role in governing the binding constant between different ions and PEG. Since water is so tightly bound to the first shell of PEG polymer, binding of cations with the polymer will involve restructuring or even displacing first shell water molecules.

Optimized geometries of PEG and thiocyanate salts were carried out using hybrid density functional theory. Starting geometries with cation and thiocyanate close to the polymer were used. In case of calcium and potassium ions, shown in **Fig. 5.4**, the optimized geometry clearly indicates binding of the cation with PEG-200. For the calcium ion, the oxygen atoms in PEG can be seen to be perfectly ordered around the cation. The side view of

the cation-PEG geometry reveal that the thiocyanate anion preferentially interacts with the polymer bound cations particularly in the calcium and potassium cases. On the other hand, for delocalized charge on cations such as guanidinium and ammonium, the optimized geometry does not indicate that the cation is bound to the polymer, partially attributable to insufficient cavity size. Further, due to highly delocalized nature of charge on the thiocyanate it remains within the proximity of the hydrophobic region of the polymer.

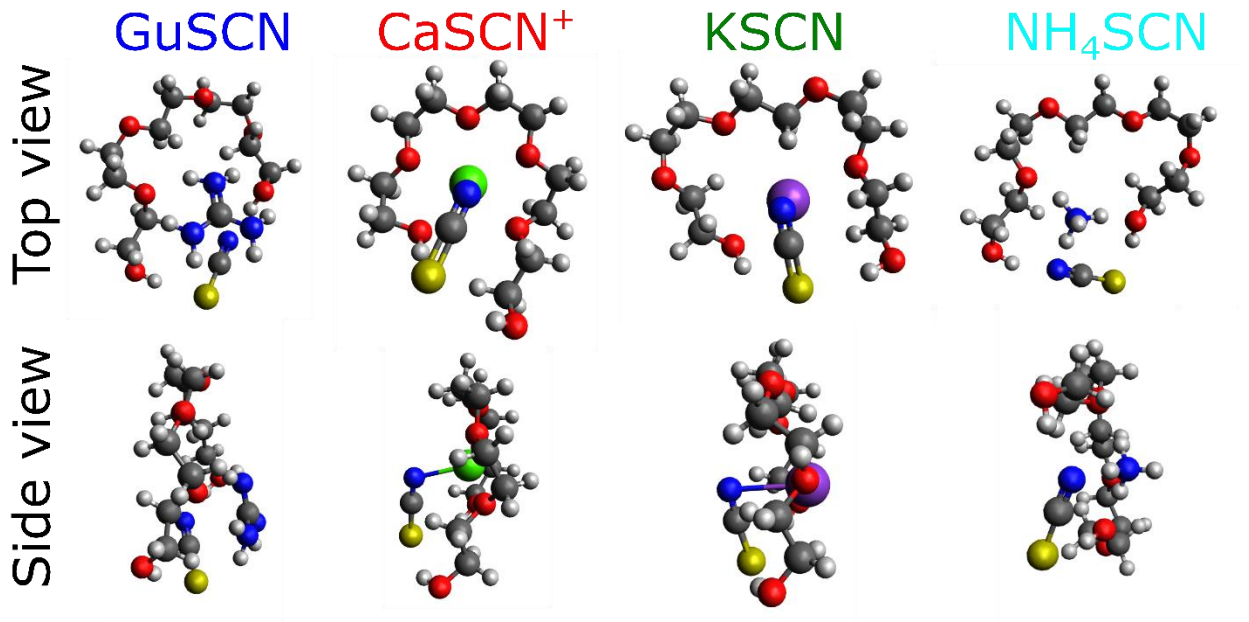

Figure 5.4. Optimized geometries for PEG with six monomer units in presence of different Hofmeister thiocyanates. DFT calculations were performed using B3LYP 6-31G(d, p) basis sets. No continuum solvent models were incorporated. Top and side view structures show that cations preferentially bind with the oxygen of the polymer. Due to negative polarizable charge of the thiocyanate counter anion it effectively neutralizes the local charge by forming an ion pair with the cations with PEG in between. For guanidinium and ammonium, the ether cavity size falls short due to large ionic radii of the cation. In case of calcium, the cavity perfectly fits the ion in the center as also seen in the side view image. Potassium ion is known to bind with 18-crown-6 which can be seen to fit perfectly well with PEG in the geometry calculations. Due to large size of potassium, it sits lopsided along the plane of the polymer.

Although the optimized geometries for calcium and potassium are similar, the dynamics of water sensed by the thiocyanate probe are distinct. Due to the small size of doubly charged calcium cation, it fits well within the PEG cavity while potassium being singly charged its ionic radii is approximately 22% larger compared to calcium. This difference in size results in potassium ion being embedded slightly away from the plane containing polymer oxygen atoms. The side view of geometry optimized structure in **Figure 5.4** confirms the observation. This slight deviation of atomic cations results in forcing the thiocyanate anion to be localized either away or very close to the cavity center. Such a small

change between the two cations have significant implications. In case of calcium which is embedded right along the center of the polymer cavity, thiocyanate anion is probably sensing second hydration shell around the polymer. Similar conclusions can be made regarding guanidinium and ammonium cations. Surprisingly, for the potassium cation, which is placed slightly away from the plane of the polymer, pulls the thiocyanate anion very close to the center of the cavity resulting in sensing tightly bound water molecules with the polymer. At this point, we can only conclude that the potassium ion is somehow only responsible for trapping the thiocyanate within the first hydration shell, while other cations do not. The experiment can also be repeated using other large cations such as cesium to further test the hypothesis. An all-atom molecular dynamics simulation is underway to explicitly capture the water and ion placement around the polymer. DFT calculations can also be performed using implicit charge models but due to high dielectric constant of water the interaction energy between nearby ions will get significantly screened. In actual experimental conditions, only a few water molecules are expected to mediate this cation-polymer-anion interaction and molecular dynamics simulations are expected to capture its underlying structural aspect.

5.3.3. Bulk-like hydration dynamics in concentrated DNA solutions

Following the observation and molecular interpretation based on spectral diffusion measurements and computational analysis of short PEG polymers with different thiocyanate

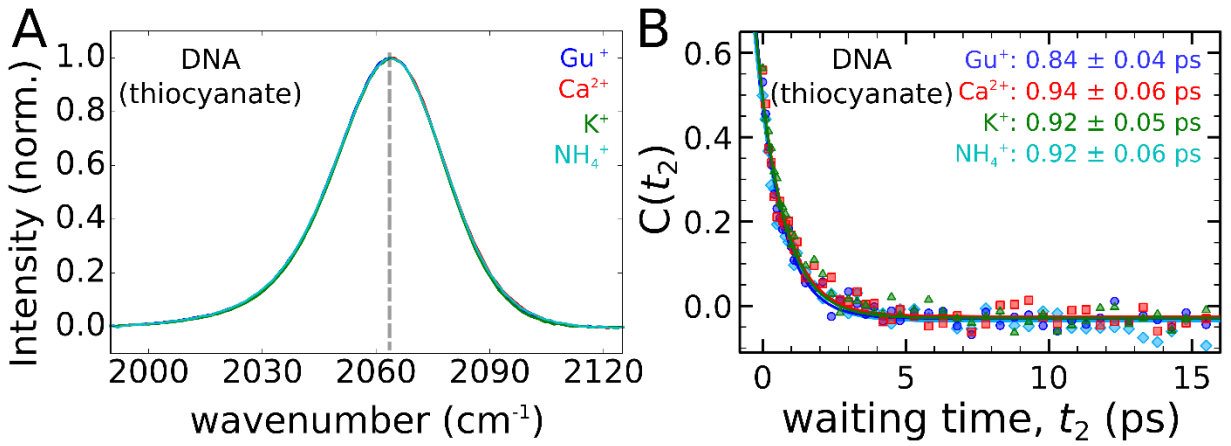

Figure 5.5. (A) FT-IR spectra showing CN stretching mode of thiocyanate for different Hofmeister cations with salmon sperm DNA solution. (B) Frequency fluctuation correlation function for CN stretching mode of different Hofmeister thiocyanates with salmon DNA. We did not observe any deviation in dynamics for thiocyanate in DNA versus when in bulk. Time constant value obtained using single exponential fits show bulk like timescales.

salts, it is of interest to explore how hydration dynamics may be altered by the presence of

biopolymers such as DNA, that are themselves polyelectrolytes. Salmon testes duplex DNA was dissolved in D_2O along with different thiocyanate salts. **Figure 5.5** (A) shows the linear FT-IR spectrum for the CN stretching band of different thiocyanate salts with salmon DNA. It should be noted that the average molecular weight of DNA base pairs far exceeds the average molecular weight of PEG used in earlier sections. The stretching frequency of thiocyanate shows the characteristic band with absorption maxima around 2065 cm^{-1} which also remains unaffected by different cations. Surprisingly, the spectral diffusion time constant as shown in **Fig. 5.5**(B) remains bulk like (~1 ps) and does not show any viscosity dependence as previously observed for PEG polymers. Also, the hydration environment does not show any significant differences for different cations as shown in **Fig. 5.6**.

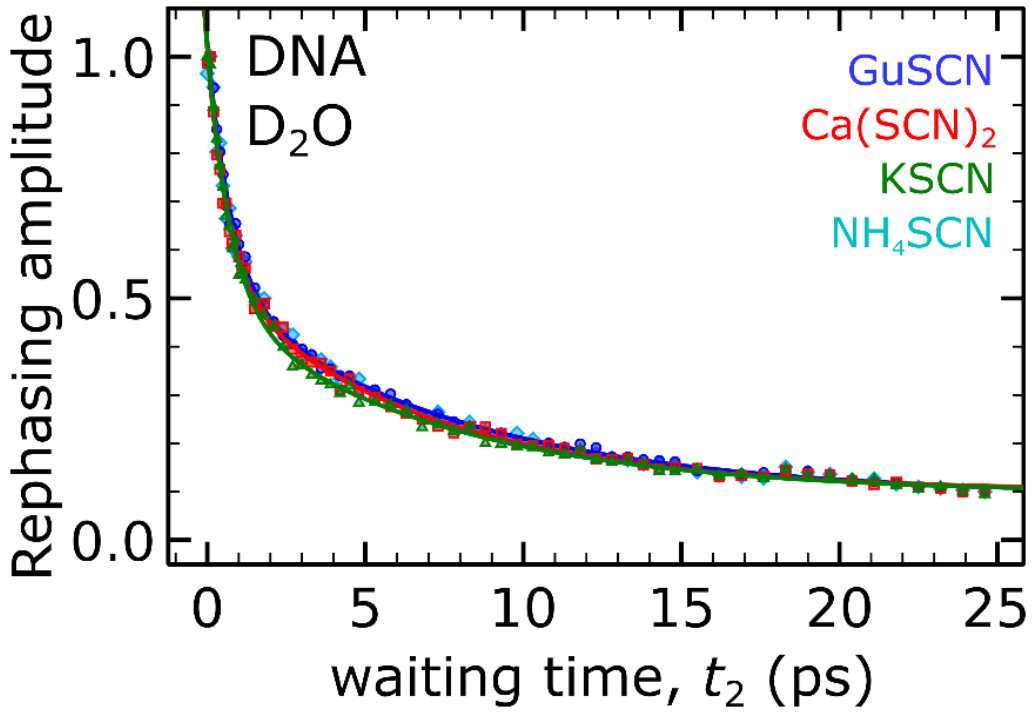

Figure 5.6. Rephasing amplitude vs waiting time showing lifetime of the vibrational CN stretching mode of different Hofmeister thiocyanate anion with salmon DNA duplex in D_2O. For guanidinium, calcium, potassium and ammonium we find that the probe has nearly identical hydration environment.

Previous measurements by Han and co-workers using spin labeled DNA duplex tethered onto a streptavidin protein complexes also reveal anomalously large water diffusion at multiple binding sites.[32] There only a 24 base pair DNA sequence was used for probing hydration in dilute conditions. The significantly high fraction of "soft" water around DNA duplexes is to be expected for short DNA duplex complexes in bulk water where small

fraction of interfacial water exists. Contrasting results from ultrafast measurements probing the phosphate backbone find significantly slow surface water molecules within the DNA minor groves.[33] The results presented in this dissertation confirm the presence of bulk-like water dynamics in significantly crowded DNA environment which has not yet been explored.

5.4. Conclusion

Significantly slow spectral diffusion (up to 5-fold) time scales were observed for hydration dynamics sensed by thiocyanate as a vibrational probe in low molecular weight aqueous PEG solutions. Although viscosity is expected to play a role in slowing water diffusion, spectra diffusion time constant probing ultrafast water rearrangements have previously been observed to be insensitive to polymer viscosity. The slowed spectral diffusion time scale in the case of potassium thiocyanate, supported by DFT optimized geometries, points towards a direct interaction between the polymer and cations. It is expected that the polymer undergoes a conformational transition in presence of specific Hofmeister cations and future work using the CH stretching vibrations shall elucidate such a mechanism. The lack of any correlation with the Hofmeister ordering of cations indicates highly specific nature of the PEG-cation interactions. While complete maintenance of bulk like dynamics in concentrated salmon DNA duplexes confirms the that water around DNA solvation shell is highly mobile.

5.5. References

1. Ball, P., Water is an active matrix of life for cell and molecular biology. *Proceedings of the National Academy of Sciences of the United States of America* **2017,** *114* (51), 13327-13335.
2. Andreatta, D.; Lustres, J. L. P.; Kovalenko, S. A.; Ernsting, N. P.; Murphy, C. J.; Coleman, R. S.; Berg, M. A., Power-law solvation dynamics in DNA over six decades in time. *Journal of the American Chemical Society* **2005,** *127* (20), 7270-7271.
3. Shweta, H.; Sen, S., Dynamics of water and ions around DNA: What is so special about them? *Journal of Biosciences* **2018,** *43* (3), 499-518.
4. Brauns, E. B.; Madaras, M. L.; Coleman, R. S.; Murphy, C. J.; Berg, M. A., Measurement of local DNA reorganization on the picosecond and nanosecond time scales. *Journal of the American Chemical Society* **1999,** *121* (50), 11644-11649.
5. Sen, S.; Andreatta, D.; Ponomarev, S. Y.; Beveridge, D. L.; Berg, M. A., Dynamics of Water and Ions Near DNA: Comparison of Simulation to Time-Resolved Stokes-Shift Experiments. *Journal of the American Chemical Society* **2009,** *131* (5), 1724-1735.
6. Fiebig, T.; Wan, C. Z.; Zewail, A. H., Femtosecond charge transfer dynamics of a modified DNA base: 2-aminopurine in complexes with nucleotides. *Chemphyschem* **2002,** *3* (9), 781-788.
7. Mukherjee, S.; Mondal, S.; Acharya, S.; Bagchi, B., DNA Solvation Dynamics. *Journal of Physical Chemistry B* **2018,** *122* (49), 11743-11761.
8. Tielrooij, K. J.; Garcia-Araez, N.; Bonn, M.; Bakker, H. J., Cooperativity in Ion Hydration. *Science* **2010,** *328* (5981), 1006-1009.
9. Bian, H. T.; Chen, H. L.; Zhang, Q.; Li, J. B.; Wen, X. W.; Zhuang, W.; Zheng, J. R., Cation Effects on Rotational Dynamics of Anions and Water Molecules in Alkali (Li^+, Na^+, K^+, Cs^+) Thiocyanate (SCN^-) Aqueous Solutions. *Journal of Physical Chemistry B* **2013,** *117* (26), 7972-7984.
10. Bian, H. T.; Wen, X. W.; Li, J. B.; Chen, H. L.; Han, S. Z.; Sun, X. Q.; Song, J. A.; Zhuang, W.; Zheng, J. R., Ion clustering in aqueous solutions probed with vibrational energy transfer. *Proceedings of the National Academy of Sciences of the United States of America* **2011,** *108* (12), 4737-4742.
11. Chen, Y. X.; Okur, H. I.; Gomopoulos, N.; Macias-Romero, C.; Cremer, P. S.; Petersen, P. B.; Tocci, G.; Wilkins, D. M.; Liang, C. W.; Ceriotti, M.; Roke, S., Electrolytes induce long-range orientational order and free energy changes in the H-bond network of bulk water. *Science Advances* **2016,** *2* (4).
12. Uematsu, Y.; Bonthuis, D. J.; Netz, R. R., Charged Surface-Active Impurities at Nanomolar Concentration Induce Jones-Ray Effect. *Journal of Physical Chemistry Letters* **2018,** *9* (1), 189-193.
13. King, J. T.; Arthur, E. J.; Brooks, C. L.; Kubarych, K. J., Crowding Induced Collective Hydration of Biological Macromolecules over Extended Distances. *Journal of the American Chemical Society* **2014,** *136* (1), 188-194.
14. Martin, D. R.; Matyushov, D. V., Terahertz absorption of lysozyme in solution. *Journal of Chemical Physics* **2017,** *147* (8).
15. Gopalakrishnan, S.; Liu, D. F.; Allen, H. C.; Kuo, M.; Shultz, M. J., Vibrational spectroscopic studies of aqueous interfaces: Salts, acids, bases, and nanodrops. *Chemical Reviews* **2006,** *106* (4), 1155-1175.

16. Winter, B.; Faubel, M., Photoemission from liquid aqueous solutions. *Chemical Reviews* **2006,** *106* (4), 1176-1211.
17. Chang, T. M.; Dang, L. X., Recent advances in molecular simulations of ion solvation at liquid interfaces. *Chemical Reviews* **2006,** *106* (4), 1305-1322.
18. Jungwirth, P.; Winter, B., Ions at aqueous interfaces: From water surface to hydrated proteins. In *Annual Review of Physical Chemistry*, 2008; Vol. 59, pp 343-366.
19. Nihonyanagi, S.; Yamaguchi, S.; Tahara, T., Counterion Effect on Interfacial Water at Charged Interfaces and Its Relevance to the Hofmeister Series. *Journal of the American Chemical Society* **2014,** *136* (17), 6155-6158.
20. Roy, V. P.; Kubarych, K. J., Interfacial Hydration Dynamics in Cationic Micelles Using 2D-IR and NMR. *Journal of Physical Chemistry B* **2017,** *121* (41), 9621-9630.
21. Rankin, B. M.; Ben-Amotz, D., Expulsion of Ions from Hydrophobic Hydration Shells. *Journal of the American Chemical Society* **2013,** *135* (24), 8818-8821.
22. Harris, J. M.; Chess, R. B., Effect of pegylation on pharmaceuticals. *Nature Reviews Drug Discovery* **2003,** *2* (3), 214-221.
23. McPherson, A., Crystallization of Proteins from Polyethylene-Glycol. *Journal of Biological Chemistry* **1976,** *251* (20), 6300-6303.
24. Kausik, R.; Srivastava, A.; Korevaar, P. A.; Stucky, G.; Waite, J. H.; Han, S., Local Water Dynamics in Coacervated Polyelectrolytes Monitored through Dynamic Nuclear Polarization-Enhanced ^{1}H NMR. *Macromolecules* **2009,** *42* (19), 7404-7412.
25. Daley, K. R.; Kubarych, K. J., An "Iceberg" Coating Preserves Bulk Hydration Dynamics in Aqueous PEG Solutions. *Journal of Physical Chemistry B* **2017,** *121* (46), 10574-10582.
26. Ng, K.; Rosenberg, A.; Bastos, M.; Wadso, I., Heat Capacity of Poly (Ethylene-Glycol) Water Mixtures - Poly (Ethylene-Glycol) Water Interactions. *Thermochimica Acta* **1990,** *169*, 339-346.
27. Yuan, R. F.; Yan, C.; Tamimi, A.; Fayer, M. D., Molecular Anion Hydrogen Bonding Dynamics in Aqueous Solution. *Journal of Physical Chemistry B* **2015,** *119* (42), 13407-13415.
28. Owrutsky, J. C.; Raftery, D.; Hochstrasser, R. M., Vibrational Relaxation Dynamics in Solutions. *Annual Review of Physical Chemistry* **1994,** *45*, 519-555.
29. Landini, D.; Maia, A.; Montanari, F.; Pirisi, F. M., Crown Ethers as Phase-Transfer Catalysts - Comparison of Anionic Activation in Aqueous-Organic 2-Phase Systems and in Low Polarity Anhydrous Solutions by Perhydrodibenzo-18-crown-6, Lipophilic Quaternary-Salts, and Cryptands. *Journal of the Chemical Society-Perkin Transactions 2* **1980,** (1), 46-51.
30. Leigh, D. A.; Marcos, V.; Wilson, M. R., Rotaxane Catalysts. *Acs Catalysis* **2014,** *4* (12), 4490-4497.
31. Poudel, L.; Podgornik, R.; Ching, W. Y., The Hydration Effect and Selectivity of Alkali Metal Ions on Poly(ethylene glycol) Models in Cyclic and Linear Topology. *Journal of Physical Chemistry A* **2017,** *121* (24), 4721-4731.
32. Franck, J. M.; Ding, Y.; Stone, K.; Qin, P. Z.; Han, S., Anomalously Rapid Hydration Water Diffusion Dynamics Near DNA Surfaces. *Journal of the American Chemical Society* **2015,** *137* (37), 12013-12023.
33. Yang, M.; Szyc, L.; Elsaesser, T., Decelerated Water Dynamics and Vibrational Couplings of Hydrated DNA Mapped by Two-Dimensional Infrared Spectroscopy. *Journal of Physical Chemistry B* **2011,** *115* (44), 13093-13100.

Chapter 6

Mid-Infrared Light Source Using Non-Collinear Difference Frequency Mixing

The work presented in this chapter has been published in the following article:
Song, Y.; Konar, A.; Sechrist, R.; **Roy, V. P.**; Duan, R.; Dziurgot, J.; Policht, V.; Matutes, Y. A.; Kubarych, K. J.; Ogilvie, J. P., Multispectral multidimensional spectrometer spanning the ultraviolet to the mid-infrared. *Rev Sci Instrum* **2019**, 90 (1), 013108

6.1. Introduction

Nearly all fundamental processes in material and biological sciences have chemical or physical molecular origin. Light matter interactions in the infrared and visible have been widely implemented to probe various mechanisms and structures of underlying molecular phenomena governing such processes. Development of targeted drugs, designing materials for renewable solar energy are some of the key areas where spectroscopy has been vital. In this pursuit, multidimensional optical spectroscopy has proven its efficacy in discerning underlying molecular dynamics which are either infeasible or difficult to access using other traditional time-resolved and one-dimensional experiments. Since the development of correlation spectroscopy[1] in the radio frequency region of the spectrum, significant efforts were made to develop an optical analogue. Major technical challenges that hindered its progress until recently was overcome by rapid advancement in higher energy ultrashort

light source and optical pulse shapers. In the infrared, two- and three-dimensional experiments have provided invaluable insight within the last two decades which otherwise could not be obtained using traditional magnetic resonance spectroscopy. Key areas where multidimensional spectroscopy is implemented include but not limited to, understanding ion and macromolecular hydration dynamics[2, 3], ultrafast charge transfer processes[4], fundamental understanding of reaction mechanism governing CO_2 reduction catalysts[5], photosynthetic energy transfer as well as nonlinear optical imaging[6, 7].

Multidimensional spectroscopy has traditionally been focused on single or few isolated bands, partially due to complex optical design and limited detection window. Transient 2D-IR spectroscopy can also be implemented to provide valuable information of molecular system under study by simply introducing an actinic pulse (typically in the UV-visible region) before 2D-IR pulse[8, 9]. It is challenging and exciting to push boundaries of cutting-edge multidimensional spectroscopy but testing its capabilities over wide range of time and frequency ranges require a cohesive understanding of independent techniques. To perform mixed pulse experiments, one needs to build an optical setup that utilizes ultrafast pulses generated from a single oscillator in order to avoid any phase instability between shot-to-shot which can easily scramble a multidimensional spectrum. While a variety of non-linear crystals and optical technique exists that can efficiently generate frequency domain pulses spanning from ultraviolet to the infrared, it is difficult to access a long-time window using a single amplifier. This problem can be circumvented by synchronizing two amplifiers seeded by a single oscillator. Such master-slave implementation of the two amplifiers offers the advantage to pick an oscillator pulse at arbitrary time delay for amplification, thus offering a large scanning time.

6.2. Dual amplifier design

In a regular chirp pulse amplified regenerative amplifier[10, 11], an arbitrary oscillator pulse is seeded into the cavity for amplification based on the repetition rate of the laser. In case of a synchronized amplifier design (**Fig. 6.1**), timing and delay (TDG) for the master laser is synchronized to the oscillator which is used to trigger the Pockel cells for that regen. For the slave regen, the TDG is synchronized when the optical pulse arrives at the PD placed right

before the regen. This allows for continuous scanning of 12.5 ns of delay between the two lasers (fine timing). While longer time delays at integral multiples of oscillator repletion rate can be set electronically using a delay generator such as one produced commercially by Stanford Research systems.

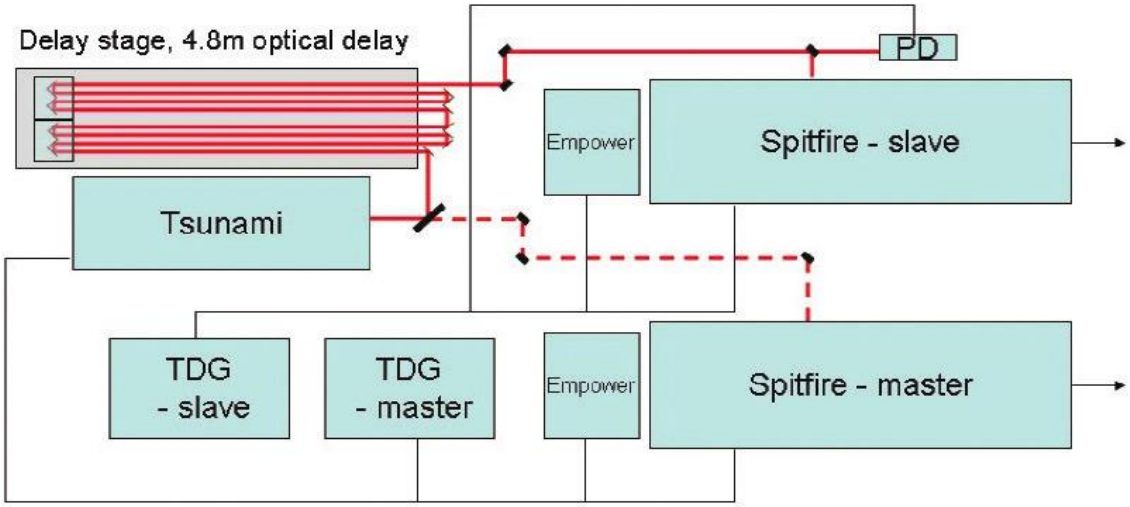

Figure 6.1. A dual amplifier setup for accessing twelve orders of magnitude in time resolution spanning femtoseconds to second timescale. A single oscillator (Tsunami in this case) output is split and a part of it is used to seed the master regen while the other half is routed through a 12.5 ns delay stage to seed the slave regen. Image reproduced from Spectra Physics-Newport Application note 43.

6.3. Multispectral Multidimensional Spectrometer (MMDS)

Previously, we discussed how one can access very high temporal ranges using dual synchronized amplifiers. To span a broad frequency ranges from ultraviolet to the mid-infrared for carrying out mixed color multidimensional experiments, light sources using the dual amplifiers are needed to be setup. This dissertation will primarily focus on the development of noncollinear mid-infrared light source for carrying out 2D-IR, transient absorption, 2DEV and other experiments which required mid-infrared light source for excitation and detection. Discussion about wide variety of experiments and method that can be implemented using MMDS is beyond the scope of this dissertation and has been described in the manuscript[12]. Results shown in previous chapters in this dissertation implemented 2D-IR at a very narrow band detection frequency of ~2000 cm^{-1}. The narrow detection window is primarily limited by the up-conversion process where bandwidth is compromised for efficiency of the phase matching process to allow better signal to noise ratio. Instead of

indirectly probing water dynamics (although it offers the advantage of cleaner signal) one can also study the OH or OD stretch mode of water beyond the detection window using a broadband mid-IR light source and MCT (mercury cadmium telluride) detectors. Future experiments studying water will take advantage of the new light source setup described in the next section of this dissertation.

6.4. Difference frequency mixing

Interaction between a low intensity light with matter results in the generation of macroscopic polarization that is linearly proportional to the electric field. Such absorption of light at characteristic frequency defined by the material have been discussed in chapter 1 of this dissertation. If the driving field is sufficiently intense, the optical material can give rise to various non-linear effects such as self-phase modulation and high harmonic generation[13]. In general, polarization for the n^{th} order mixing process can be expressed as

$$P^n(t) = \varepsilon_0 \chi^{(n)} E^n(t)$$

Where ε_0 is the permittivity of free space and $\chi^{(n)}$ is the n^{th} order electric susceptibility. Overall polarization in a material is expressed as the sum of linear and non-linear terms. Two-dimensional spectroscopy results from third order non-linear field interaction with the sample of interest. Sum frequency or second harmonic generation is one of the most studied and implemented second order non-linear technique to generate short wavelength of light ($2\omega_0$) using a long wavelength (ω_0) source. In the later part of this section we will primarily focus on second order materials for difference frequency mixing between two optical frequencies.

For any given pair of optical frequencies, a combination of frequencies can be generated in a second order crystal based on frequency matching condition which based on energy conservation between incoming and outgoing field.

$$\omega_3 = \omega_1 - \omega_2$$

In addition to frequency-matching condition, phase matching conditions also required to be satisfied, which is based on the momentum conservation for the wave. For any plane wave, its wavevector (k) is defined by the direction of its propagation.

$$k_3 = k_1 - k_2$$

Incoming plane waves of different frequencies can never have same refractive index due to inherent dispersion in any medium. Therefore, the phase matching conditions is usually achieved by combining individual frequencies at different polarization which exploits the birefringence property of the medium.

6.5. Results

6.5.1. Mid-infrared using non-collinear DFG

Broadband 100fs, 800 nm output from the slave regenerative amplifier is used to pump commercially designed optical parametric amplifier (OPA) from Light Conversion. Combined signal and idler output pulse energy of ~600 μJ is obtained which will be used in later stage difference frequency mixing process for generating broadband mid-IR light source. The signal and idler output beams are tunable from 1160 – 1600 nm and 1600 – 2600 nm respectively. Output polarization of signal and idler beams are vertical and horizontal respectively. Silver gallium sulfide (AGS) crystal has been shown to be efficient for carrying out difference frequency mixing[14] exploiting its birefringence property. Type-1 Phase matching curves for silver gallium sulfide (AGS) crystal is shown in **Figure 6.2**(A-C) which were obtained using SNLO computer program.

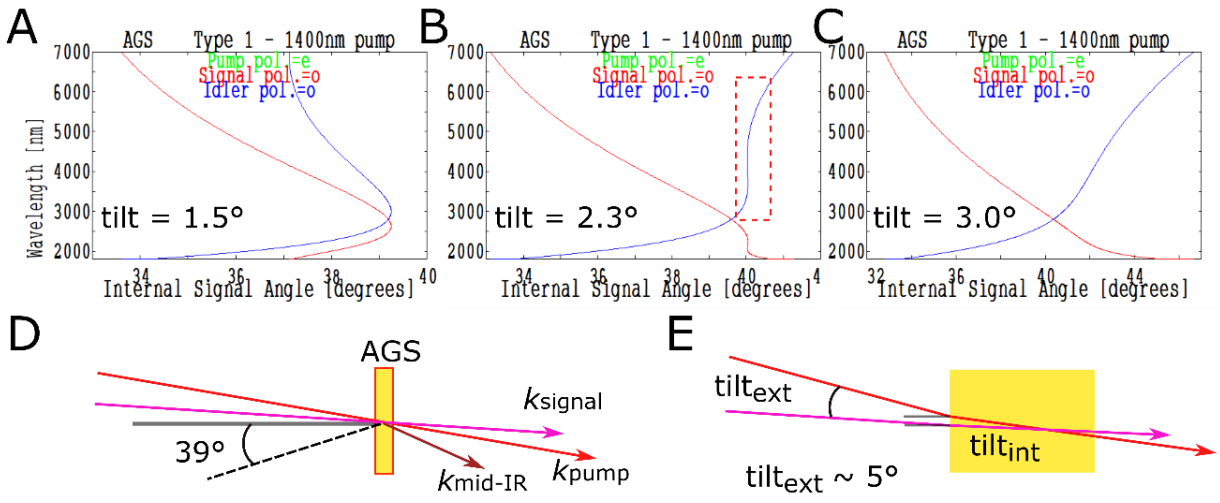

Figure 6.2. (A - C) Tuning curves for the AGS crystal at 1400 nm pump (signal output from OPA). At low (1.5°) and high (3.0°) tilt angles the tuning curve shows a very narrow band DFG mixing efficiency. Only at a critical angle of 2.3 ° separation between the signal and idler output from OPA, the DFG mixing process yields a high bandwidth mid-IR output. (D) Figure showing the beam propagation along the AGS crystal. 1° offset is needed to create a 40° internal angle for the idler beam. (E) Accounting the refractive index for the DFG crystal a precise internal tilt between the two beams can be achieved with a large external title of ~5°.

The tuning curve with low tilt angles (angle between the signal and idler beams from OPA) corresponding to collinear geometry, produces an idler output (mid-IR) from the mixing process with narrow bandwidth. Similar narrow bandwidth is obtained at high tilt angle as well. Although the crystal can be rotated, and phase matched to produce a tunable output,

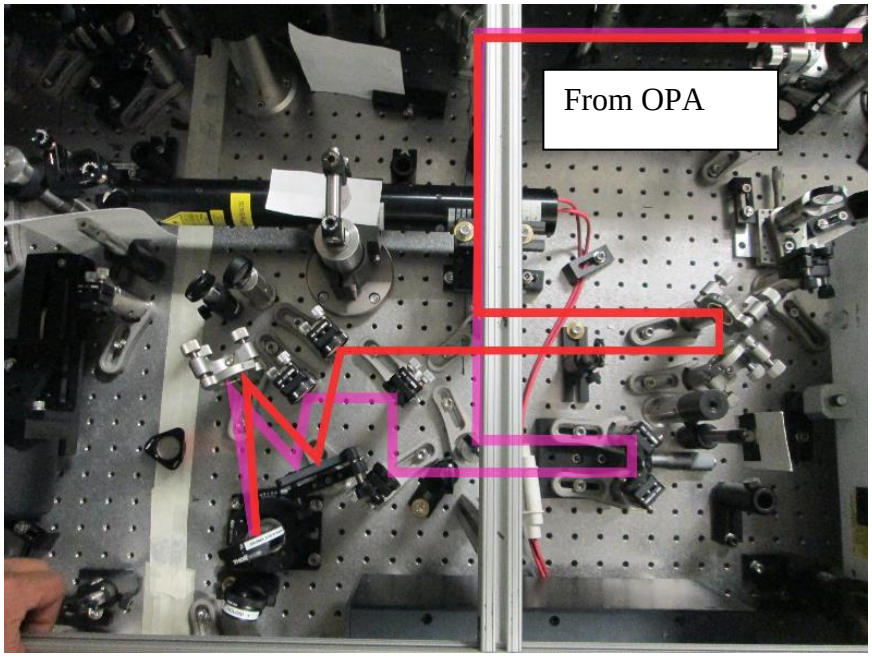

Figure 6.3. Actual optical implementation of creating non-collinear beam geometry for signal and idler output pulses from the OPA. The red and purple colors represent signal and idler beams. Due to space constraint in the working table the beams have been folded to create the optimal 5° external tilt angle.

the bandwidth at each individual internal angle will still be limited. The very fundamental goal of MMDS to perform mixed color spectroscopy experiments using broadband detection and excitation will be difficult using collinear DFG mixing geometry. It should be noted that the convention for referring outputs from different down-conversion processes will be used interchangeably. Signal output beam from the OPA becomes the pump beam for the DFG while the idler beam from OPA becomes the signal beam in the DFG. The mid-IR output from the DFG is labeled as the idler beam. In **Fig. 6.2**(B), at an optimal 2.3° tilt angle, we can observe in the tuning curve that the idler output from the DFG (mid-IR frequency) has a very broad bandwidth at an internal angle of 40°. Due to type-1 phase matching condition the mid-IR beam has the same polarization as that of the idler from the OPA which is horizontal. Commercially obtained AGS crystals are cut at internal angle of 39° which introduces additional constraint to align the idler output from the OPA at the DFG crystal. Having a large

external tilt angle allows for easier beam alignment and requires short distance for angle creation. It is therefore very critical that the optimum tilt angle is created for efficient mid-IR frequency. Actual implementation of the non-collinear geometry is shown in Figure 6.3 highlights the folded beam configuration due to space limitation. Tighter beam geometries offer advantage of improved stability and better control for walking beams to create optimal internal angles. During normal operation conditions, mid-IR pulse energy of ~10 μJ can be obtained with wide tunable wavelength in the range 3 μm to 6 μm.

Mid-Infrared out using DFG based on non-collinear geometry vs collinear geometry is compared in **Fig. 6.4**. The spectral bandwidth for the mid-IR generation is higher for pulse

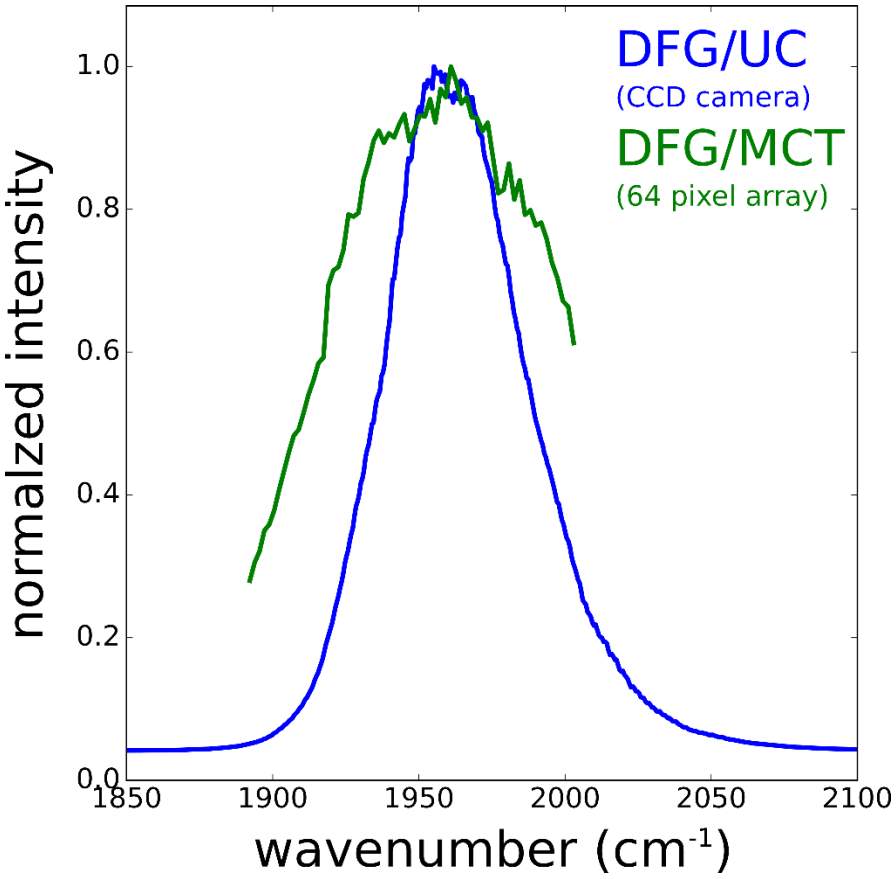

Figure 6.4. Comparing spectral bandwidth for mid-infrared light source using MCT based infrared detector (green) vs detection using chirped pulse upconversion (blue). Notice that the spectral bandwidth for the IR source using non-collinear geometry is large compared to when the mid-IR is generated using collinear geometry. The truncation in spectra for MCT array arise since only 64 pixels are present as compared to 1340 pixels in a CCD camera.

centered around 2000 cm^{-1}. In case of non-collinear geometry, the detection is carried out by upconverting the mid-IR using sum frequency generation with 800 nm chirped pulse which also contributes significantly to the overall bandwidth of the measured spectrum.

6.6. Summary

The present chapter discussed the implementation of non-collinear mid-infrared light source which can be effectively tuned from OH bending modes up to the OH stretching mode of water (3-6 micron in wavelength). This newly developed light source when integrated with other frequency sources (developed and implemented in parallel) shall allow performing mixed frequency multidimensional spectroscopy over wide range of biological, chemical and physical systems of interest. In addition, the most powerful feature of this system design is its ability to access orders of magnitude time delays which earlier has been limited to few nanoseconds due to limited length of the delay states and coherence length of various light sources.

6.7. References

1. Ernst, R. R., Nuclear-Magnetic-Resonance Fourier-Transform Spectroscopy. *Angewandte Chemie-International Edition in English* **1992,** *31* (7), 805-823.
2. Jungwirth, P.; Winter, B., Ions at aqueous interfaces: From water surface to hydrated proteins. In *Annual Review of Physical Chemistry*, 2008; Vol. 59, pp 343-366.
3. Pal, S. K.; Peon, J.; Bagchi, B.; Zewail, A. H., Biological water: Femtosecond dynamics of macromolecular hydration. *Journal of Physical Chemistry B* **2002,** *106* (48), 12376-12395.
4. Gray, H. B.; Winkler, J. R., Electron transfer in proteins. *Annual Review of Biochemistry* **1996,** *65*, 537-561.
5. Kumar, B.; Llorente, M.; Froehlich, J.; Dang, T.; Sathrum, A.; Kubiak, C. P., Photochemical and Photoelectrochemical Reduction of CO_2. In *Annual Review of Physical Chemistry, Vol 63*, 2012; Vol. 63, pp 541-569.
6. Tiwari, V.; Matutes, Y. A.; Gardiner, A. T.; Jansen, T. L. C.; Cogdell, R. J.; Ogilvie, J. P., Spatially-resolved fluorescence-detected two-dimensional electronic spectroscopy probes varying excitonic structure in photosynthetic bacteria. *Nature Communications* **2018,** *9*.
7. Baiz, C. R.; Schach, D.; Tokmakoff, A., Ultrafast 2D IR microscopy. *Optics Express* **2014,** *22* (15), 18724-18735.
8. Baiz, C. R.; McCanne, R.; Nee, M. J.; Kubarych, K. J., Orientational Dynamics of Transient Molecules Measured by Nonequilibrium Two-Dimensional Infrared Spectroscopy. *Journal of Physical Chemistry A* **2009,** *113* (31), 8907-8916.
9. Bredenbeck, J.; Helbing, J.; Behrendt, R.; Renner, C.; Moroder, L.; Wachtveitl, J.; Hamm, P., Transient 2D-IR spectroscopy: Snapshots of the nonequilibrium ensemble during the picosecond conformational transition of a small peptide. *Journal of Physical Chemistry B* **2003,** *107* (33), 8654-8660.
10. Vaillancourt, G.; Norris, T. B.; Coe, J. S.; Bado, P.; Mourou, G. A., Operation of a 1-KHz Pulse-Pumped Ti-Sapphire Regenerative Amplifier. *Optics Letters* **1990,** *15* (6), 317-319.
11. Murray, J. E.; Lowdermilk, W. H., Nd - YAG Regenerative Amplifier. *Journal of Applied Physics* **1980,** *51* (7), 3548-3555.
12. Song, Y.; Konar, A.; Sechrist, R.; Roy, V. P.; Duan, R.; Dziurgot, J.; Policht, V.; Matutes, Y. A.; Kubarych, K. J.; Ogilvie, J. P., Multispectral multidimensional spectrometer spanning the ultraviolet to the mid-infrared. *Rev Sci Instrum* **2019,** *90* (1), 013108.
13. Franken, P. A.; Weinreich, G.; Peters, C. W.; Hill, A. E., Generation of Optical Harmonics. *Physical Review Letters* **1961,** *7* (4), 118-119.
14. Rotermund, F.; Petrov, V.; Noack, F., Difference-frequency generation of intense femtosecond pulses in the mid-IR (4-12 μm) using $HgGa_2S_4$ and $AgGaS_2$. *Optics Communications* **2000,** *185* (1-3), 177-183.

Chapter 7
Conclusion

7.1. Key findings

Ideas and results presented in this dissertation can be tied using one common thread, namely, to investigate the role of hydration dynamics near a variety of macromolecular interfaces exhibiting diverse surface chemistry and topology. Experimental and simulation approaches were implemented on tunable model systems of micelles as well as on actual proteins and polymers to discern the nature and origin of the slowdown of fluctuations in hydrogen bond rearrangements. The observed dynamics reveal a variety of timescales in crowded and viscous environments indicating that biomacromolecular interfaces exhibit diverse hydration properties.

On a model system of micelles, we used the thiocyanate anion (SCN^-) as a vibrational probe chromophore in conjunction with infrared and NMR spectroscopy. It is found that SCN^- strongly associates with the cationic head group of dodecyltrimethylammonium bromide (DTAB) micelles, both in normal-phase and reverse micelles. In competition with chloride and iodide ions, we find no evidence for displacement of thiocyanate, in accord with the chaotropicity of the Hofmeister ordering, while lending support to a direct interaction picture of its origin. Ultrafast 2D-IR spectroscopy of the SCN^- probe in a range of DTAB micelle sizes (w_0 = 4 to w_0 = 12) shows little if any size dependence to the time scale for spectral diffusion, which is found to be ~3.5 times slower than in bulk water (both D_2O and H_2O). Normal-phase micelles studied with 2D-IR exhibit essentially the same spectral dynamics as do reverse micelles, indicating a lack of sensitivity to interfacial curvature. Combined with ^1H NMR chemical shift perturbations, we conclude that the SCN^- ions tightly associate with the head groups and are partially buried. The 3-4-fold slowdown in spectral

diffusion is consistent with the excluded volume model for interfacial perturbation to hydrogen bond reorientation dynamics. Based on these observations and comparisons to previous studies of zwitterionic interfaces probed with phosphate transitions, we conclude that the SCN^- spectral dynamics in both reverse and normal-phase micelles is largely dominated by hydration contributions and offers a promising probe of interfacial hydration at cationic interfaces. Addition of competitive anions alters neither the IR spectra nor the ultrafast dynamics, indicating that SCN^- is robustly associated with the head groups.

Later in the dissertation we attempted to address the long-standing quest to develop a molecular picture of how interfaces perturb hydration dynamics. Despite immense advancements in our understanding many pression questions still remains to be explored using both theoretical as well as surface selective spectroscopy experiments. We present graph theoretical analyses of molecular dynamics simulations to map topological networks of hydrogen bonds in bulk water and in confined protein (hen egg white lysozyme, HEWL) geometries. Topological network characteristics averaged over simulation runs were characterized using the metrics of network theory. The observed power-law dependence of average path length on system size reveals that the bulk hydrogen bond networks cannot be considered random, but rather essentially consists of a giant lattice-like component. At small inter-protein distances (5-10 Å) with reduced hydrogen bond connectivity, similar global network structures are observed, indicating the maintenance of a completely unperturbed network topology. From a dynamical perspective, computation of the vibrational density of states (VDOS) in the 0-25 THz spectral region for the first and second hydration shells exhibit a distinct insensitivity to the presence of the nearby macromolecular interfaces. Experimental measurements of hydration dynamics in crowded protein solutions using 2D-IR spectroscopy support the prediction of short-range perturbation. These results quantitatively indicate a lack of structural modification to the hydrogen bonding network under crowding conditions, pointing towards a purely dynamical origin for the slowdown of hydrogen bond rearrangements. Nevertheless, we do find that protein surface residues significantly slow when crowded. A detailed understanding of conformational restrictions imposed by crowding is necessary to predict protein-protein and protein-drug interactions, particularly for processes governed by induced fit.

Seeking a complete simulation model that captures the essential nearly four-coordinate hydrogen bonding network, we discussed a finite, two-dimensional lattice model of liquid water, while permitting a simple Metropolis Monte Carlo simulation in conditions ranging from crowded to dilute. This model focuses only on the consequences of excluded volume contributions to the perturbation of hydrogen bond switching dynamics by avoiding topological and chemical heterogeneity of an interface. Dynamical retardation factors (relative to bulk) for hydrogen bond switching agree with previous statistical models and atomistic molecular dynamics simulations of hydrated proteins. The model enables straightforward spatial mapping of retardation factors that are difficult to measure in atomistic simulations. The spatially-dependent retardation factors decrease exponentially from the interface. By simulating varying degrees of macromolecular crowding, we do not find any cooperative, collective contributions expected for the highly correlated hydrogen bonding rearrangements of confined water. Longer-range cooperative influences of an interface may be due to complex chemical patterning of the surface which have only recently been explored using all-atom MD simulations.

Based on 2D-IR spectral diffusion measurements, a significantly retarded hydration dynamics was observed in concentrated short polyethylene glycol polymers using the CN stretching frequency of thiocyanate as a probe. The origin of this slowdown and significant enhancement for potassium cations have been explored using DFT calculations. Based on the optimized geometry of the polymer and ions it is being hypothesized that some (particularly potassium and calcium) Hofmeister cations strongly associate with the oxygen atoms of the polymer while also inducing conformational changes to the polymer itself. Based on our previous understanding of interaction of thiocyanate with buried charge, the slowdown in hydration dynamics arises due to highly immobile first shell water on the polymer backbone.

In the last chapter, we implemented a non-collinear difference frequency mixing approach for generating broadband mid-infrared light source. Tunability range vary from 3-6 micrometer in wavelength which can effectively span vibrational frequencies between water and amide stretching, enabling simultaneous probing of interfacial and hydration dynamics. Coupled with dual synchronized amplifiers various ultrafast and slow molecular mechanisms can now be studies in single experiment accessing twelve orders of magnitude in time resolution.

7.2. Future directions

The work presented in this dissertation lays a strong foundation for performing wide range of hydration dynamics studies on a variety of macromolecular constructs, either experimentally or applying developed network analysis methods. In addition to simply extending the work on the role of ions and surface charges on different surfactant or protein molecule, one can directly utilize the high absorbability of thiocyanate anions with the interface to study interesting chemical reactions and phenomena. An immediate area of research where surface charges play a significant role but are under-researched is in understating interfacial electron and proton transfer kinetics. In addition to scientific curiosity, exploration of how charge transfer rates get influenced by constrained and interfacial solvent environments have practical implications such as developing renewable sources of electricity. Electron transfers reactions in chemistry and biology are known to undergo via a tunneling or hopping mechanism[1-3]. Depending on the distance between a donor/acceptor pair and electrochemical potential, either of the two mechanisms can get preferred.[4] Electron transfers in the bulk solution between neighboring molecules involves outer sphere rearrangements and have been studied extensively using small molecule analogues. In such dilute environment, the electron transfer rates depend significantly on solvent viscosity which determines how fast the encounter complexes form. But in biology, electron transfers occur over long distances (up to 20 Å)[5] and does not necessarily involve physical contact between the donor and acceptor moieties. A unified connection between charge transfer process and timescales for hydration dynamics near such interfaces is needed to accurately model various chemical interactions in biology.

The kinetic rate expression for electron transfer reactions based on Marcus theory[6], not only involves free energy barrier between reactants and products but also solvent reorganization. Dynamics of solvent rearrangements at ultrafast timescales and its distance dependence near macromolecular interfaces have been extensively studied in this dissertation. A recent study[7] of thiocyanate at the air-water interface found that ultraviolet excitation of the anion results in either dissociation (CN^- and S) or release of an electron ($SCN + e^-$) to the solvent medium. Electron donation to the solvent can eventually be captured by a nearby electron acceptor resulting initiating an electrochemical reaction. It is known that

the presence of hydrated electrons near a charged interface can catalyze reactions[8] while also inhibit electron transfer rates between oxidant and reductant separated between polar and non-polar phases[9]. DTAB micellar interface in presence of thiocyanate exhibits a versatile electrochemical property that offers a promising way to explore electron transfer reactions. One promising area where charge migration from micellar interface to the core can have practical implications are in redox flow batteries[10], which has potential to become high energy density and power delivery source for future electrical devices.

Another simple yet powerful experiment that can be performed using the DTAB micellar construct. By preparing a reverse phase micelle, i.e. encapsulating dichloromethane nanodroplet surrounded by an aqueous medium, one can control the electron transfer injection from thiocyanate to any electronically excited photocatalyst such as rhenium photocatalyst for CO_2 reduction embedded in the non-polar phase. By varying the surfactant tail length on can systematically vary the electron transfer rates and optimize the catalytic cycle (**Fig. 7.1**).

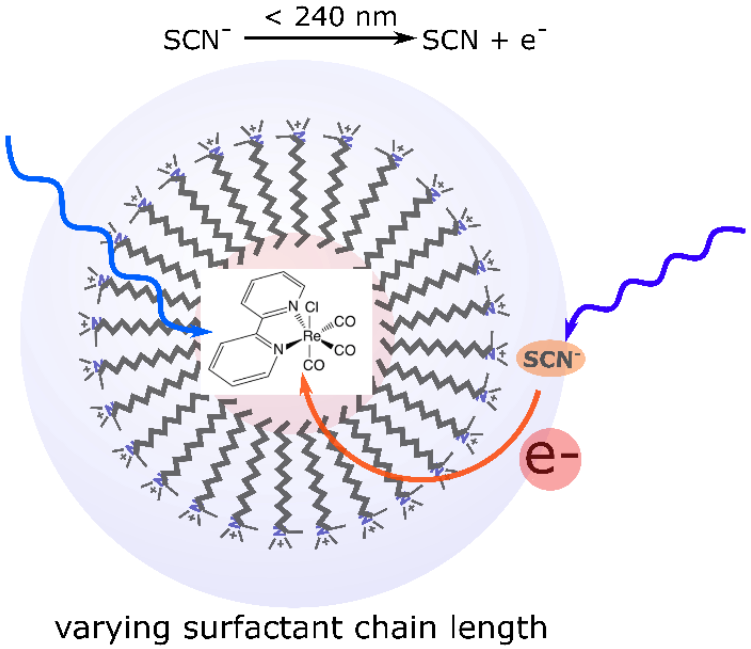

Figure 7.1. Schematic highlighting future experiments that can be performed using the micellar construct prepared and studied in this dissertation. By encapsulating a photocatalyst in the reverse phase micelles one can essentially control the electron transfer rate from thiocyanate at the surfactant interface. Thiocyanate anion is known to release an electron upon photoexcitation below 240 nm which does not overlap with the metal to ligand charge transfer absorption around 400 nm for the rhenium catalyst shown here.

Ammonium cations have recently also been shown to catalyze the formation of bromine molecule from bromide ion in ocean sea sprays.[11] In this study, the catalytic

conversion of bromine was found to be impeded due to the presence of competing chaotropic ions such as chloride by 37% only. The authors in this work only focused on the effect of one counter ion. The role of chaotropic ions to screen the active interface can directly be related to our experimental findings. Increased kinetics for the formation of halogen molecules near a surfactant/lipid interfaces containing an ammonium moiety which are abundant in the ocean water, can directly alter the global concentration of ozone in the troposphere. Therefore, it would be of scientific merit to perform future experiments to characterize the formation of molecular halogens when extremely chaotropic ion such as thiocyanate is used in competition. It can be expected that molecular bromine formation would be significantly depleted thus offering a novel approach for preventing ozone depletion near specific coastal areas.

Experimental findings mentioned in chapter 5 of this dissertation based on 2D-IR spectroscopy probing hydration dynamics near aqueous short polymers with different cations requires an immediate computational validation. Optimized geometry using DFT concluded that potassium ion favorably brings the thiocyanate anion closer to the first hydration shell of PEG thereby sensing dynamics of immobile water. Implicit solvent model can screen charges on the opposite faces of the polymer loops between the counter ions, thereby leading to a false negative result, but can be explicitly captured using all classical molecular dynamics simulations result but can be explicitly captured using all-atom classical molecular dynamics simulations. In addition, a wide range of network properties of water in the polymer hydration shell can be carried. The immobile water within the first hydration shell should display a different global characteristic such as average path length and degree correlations. The vibrational density of states calculations on first and second shell water molecule should reveal the length scale for perturbation to dynamics near a flexible interface. Previous simulations using restrained and flexible protein no coupling was observed between protein and hydration, partially attributed to the fact that water molecules do not get trapped by flat interfaces. By analyzing data on polymer simulations, one can expect to observe a significant coupling between water and polymer fluctuations.

7.3. References

1. Shih, C.; Museth, A. K.; Abrahamsson, M.; Blanco-Rodriguez, A. M.; Di Bilio, A. J.; Sudhamsu, J.; Crane, B. R.; Ronayne, K. L.; Towrie, M.; Vlcek, A.; Richards, J. H.; Winkler, J. R.; Gray, H. B., Tryptophan-accelerated electron flow through proteins. *Science* **2008,** *320* (5884), 1760-1762.
2. Gray, H. B.; Winkler, J. R., Electron tunneling through proteins. *Quarterly Reviews of Biophysics* **2003,** *36* (3), 341-372.
3. Gray, H. B.; Winkler, J. R., Electron transfer in proteins. *Annual Review of Biochemistry* **1996,** *65*, 537-561.
4. Voityuk, A. A., Long-Range Electron Transfer in Biomolecules. Tunneling or Hopping? *Journal of Physical Chemistry B* **2011,** *115* (42), 12202-12207.
5. Gray, H. B.; Halpern, J., Distant charge transport. *Proceedings of the National Academy of Sciences of the United States of America* **2005,** *102* (10), 3533-3533.
6. Marcus, R. A., Electron Transfer Reactions in Chemistry - Theory and Experiment. *Reviews of Modern Physics* **1993,** *65* (3), 599-610.
7. Mizuno, H.; Rizzuto, A. M.; Saykally, R. J., Charge-Transfer-to-Solvent Spectrum of Thiocyanate at the Air/Water Interface Measured by Broadband Deep Ultraviolet Electronic Sum Frequency Generation Spectroscopy. *Journal of Physical Chemistry Letters* **2018,** *9* (16), 4753-4757.
8. Gratzel, M.; Kozak, J. J.; Thomas, J. K., Electron Reactions And Electron-Transfer Reactions Catalyzed by Micellar Systems. *Journal of Chemical Physics* **1975,** *62* (5), 1632-1640.
9. Georganopoulou, D. G.; Strutwolf, J.; Pereira, C. M.; Silva, F.; Unwin, P. R.; Williams, D. E., Effect of nonionic surfactants on interfacial electron transfer at the liquid/liquid interface. *Langmuir* **2001,** *17* (26), 8348-8354.
10. Klaiber, A.; Kollek, T.; Cardinal, S.; Hug, N.; Drechsler, M.; Polarz, S., Electron Transfer in Self-Assembled Micelles Built by Conductive Polyoxometalate-Surfactants Showing Battery-Like Behavior. *Advanced Materials Interfaces* **2018,** *5* (8).
11. Shaloski, M. A.; Gord, J. R.; Staudt, S.; Quinn, S. L.; Bertram, T. H.; Nathanson, G. M., Reactions of N_2O_5 with Salty and Surfactant-Coated Glycerol: Interfacial Conversion of Br^- to Br_2 Mediated by Alkylammonium Cations. *Journal of Physical Chemistry A* **2017,** *121* (19), 3708-3719.